

Optimising the Operation of Renewable Energy-Driven Reverse Osmosis Desalination

Mohamed Tarek Mohamed Abdelmonem Saleh Mito

Doctor of Philosophy

Aston University

September 2021

© Mohamed Tarek Mohamed Abdelmonem Saleh Mito, 2021

Mohamed Tarek Mohamed Abdelmonem Saleh Mito asserts his moral right to be identified
as the author of this thesis

This copy of the thesis has been supplied on condition that anyone who consults it is understood to recognise that its copyright belongs to its author and that no quotation from the thesis and no information derived from it may be published without appropriate permission or acknowledgement.

Aston University

Optimising the Operation of Renewable Energy-Driven Reverse Osmosis Desalination

Mohamed Tarek Mohamed Abdelmonem Saleh Mito

Doctor of Philosophy

2021

Abstract

The integration of Renewable Energy (RE) and Reverse Osmosis (RO) is essential for sustainable water production. However, it requires large-scale RO plants to accommodate fluctuating power inputs. Variable operation of RO plants by matching their load to available power, without battery back-up, has only been implemented for small-scale systems. This thesis presents a variable operation control procedure suitable for operating large-scale RO systems using RE. The procedure consists of two techniques, i.e., variable-speed operation and modular operation, for matching the RO load to varying degrees of RE fluctuation. The solutions presented were developed using a pilot RO plant that delivers similar performance to large-scale systems to allow implementation to such scale. Wind energy was used as a representation of an intermittent and fluctuating RE source. For variable-speed operation, multiple strategies were explored for varying the operating parameters according to available power. An advanced control system based on Model Predictive Control was designed and compared to a conventional Proportional-Integral-Differential controller. For modular operation, neural networks were developed to provide long- and short-term wind speed prediction for scheduling the RO units operation. The results showed that operation at variable recovery with constant brine flowrate delivered the lowest specific energy consumption and widest operation range for a system with an isobaric pressure exchanger. For a 10% step-change in permeate flowrate, the MPC controller improved the settling time by 47%. The long-term wind speed prediction was used to estimate the number of operational RO units for a day ahead for three random days, reaching a correlation of R^2 0.78, 0.64, and 0.79 with the actual wind speed. This allowed scheduling the RO units to operate with a smooth operation profile that avoids unexpected shutdowns. By combining the optimised variable-speed and modular operations techniques, 90.9%, 91.5% and 91.4% of the available wind energy was utilised for Days 1, 2 and 3, which led to a high cumulative daily permeate production of 78 m³, 91.5 m³ and 123.4 m³, respectively. The solutions developed in this thesis showed that RO systems can be powered efficiently by RE using variable operation. This is fundamental for implementing this technology on a large-scale and decarbonising water production.

Keywords: Desalination; reverse osmosis; renewable energy; variable operation, model predictive control, wind speed prediction.

Acknowledgement

I wish to acknowledge all those who helped and advised me in finishing this research. It would not have been possible without their kind support, advice, and suggestions.

I am deeply indebted to Prof. Philip Davies, Dr Xianghong Ma and Dr Hanan Albuflasa for their mentorship, enthusiasm, immense knowledge, and constant support. Their guidance and support assisted me during all stages of this PhD.

I would like to express my highest gratitude towards my colleagues at Aston University Dr Moid Khan, Dr Kemal Masera and Mr Abdelnasir Omran for their kind cooperation and encouragement which helped me along the way.

Finally, I take this opportunity to express my deepest gratitude and sincerest appreciation to my beloved parents, brothers and friends for their love and continuous support.

I dedicate this PhD to my father.

List of publications

- 1 **Mito, M. T.**, Ma, X., Albuflasa, H., & Davies, P. A. (2019). *Reverse osmosis (RO) membrane desalination driven by wind and solar photovoltaic (PV) energy: State of the art and challenges for large-scale implementation.* Renewable and Sustainable Energy Reviews, 112, 669-685. The main content of this paper is reflected in Chapters 1 and 2.
- 2 **Mito, M. T.**, Ma, X., Albuflasa, H., & Davies, P. A. (2019). *Prospects of wind power prediction and variable operation in optimising wind-powered reverse osmosis operation.* Paper presented at the International Desalination Association (IDA), World Congress 2019, Crossroads to Sustainability, World Trade Center, Dubai, UAE. The main content of this paper is reflected in Chapters 6 and 7.
- 3 **Mito, M. T.**, & Davies, P. (2020). *Towards Energy-Efficient Reverse Osmosis.* In A. Sapalidis (Ed.), *Membrane Desalination From Nanoscale to Real World Applications* (pp. 400). Boca Raton: CRC Press. The main content of this book chapter is reflected in Chapter 1.
- 4 **Mito, M. T.**, Ma, X., Albuflasa, H., & Davies, P. A. (2021). *Variable operation of a renewable energy-driven reverse osmosis system using model predictive control and variable recovery: Towards large-scale implementation.* Manuscript submitted for publication in Desalination. The main content of this paper is reflected in Chapters 4 and 5.
- 5 **Mito, M. T.**, Ma, X., Albuflasa, H., & Davies, P. A. (2021). *Modular operation of a renewable energy-driven reverse osmosis system using wind speed prediction and operation scheduling: Towards large-scale implementation.* Manuscript to be submitted for publication in Desalination. The main content of this paper is reflected in Chapters 6 and 7.

Table of Contents

Abstract	2
Acknowledgement	3
List of publications	4
Table of Contents	5
Nomenclature	10
List of tables	13
List of figures	14
1 Chapter 1 Introduction	19
1.1 Growth of the desalination industry	19
1.2 Reverse osmosis	20
1.2.1 Background.....	20
1.2.2 Theory of operation.....	21
1.2.3 Standard RO plant configuration	23
1.2.4 Challenges to reverse osmosis desalination.....	24
1.3 Renewable energy desalination (RED)	24
1.4 Limitations of steady-state operation	26
1.4.1 Grid-connected RO systems	27
1.4.2 Energy storage	27
1.5 Variable operation	27
1.6 Thesis aims and objectives.....	28
1.7 Thesis outline and structure.....	29
2 Chapter 2 Literature review	31
2.1 Problem definition and review methodology	31
2.2 State of the art in renewable energy-driven RO	31
2.2.1 Wind-energy RO desalination.....	31
2.2.2 Solar-PV RO desalination.....	38

2.2.3	Hybrid wind-PV RO desalination.....	44
2.3	Technical challenges and potential solutions for RE driven RO plants.....	48
2.3.1	Membranes performance and lifetime.....	48
2.3.2	Energy recovery devices.....	50
2.3.3	Strategies for variable operation of RO system.....	54
2.3.4	Control system performance.....	58
2.4	Summary.....	61
3	Chapter 3 Experimental setup and procedure.....	63
3.1	Introduction.....	63
3.2	System description.....	64
3.3	Main components.....	67
3.3.1	Feed tank.....	67
3.3.2	Cartridge filter.....	67
3.3.3	Low-pressure pump.....	68
3.3.4	High-pressure pump.....	69
3.3.5	Energy recovery device.....	69
3.3.6	Brine reject valve.....	70
3.4	Instrumentations and measurements.....	71
3.4.1	Flow measurement.....	71
3.4.2	Pressure measurement.....	72
3.4.3	Concentration measurement.....	73
3.4.4	Temperature measurement.....	73
3.4.5	Power consumption measurement.....	74
3.5	Electrical power system.....	75
3.5.1	Power circuit.....	75
3.5.2	Control circuit.....	76
3.6	Data acquisition and supervisory control.....	76

3.6.1	Data logging hardware	77
3.6.2	User-interface.....	78
3.6.3	Signal processing and data logging.....	81
3.6.4	Supervisory control.....	81
3.7	Experimental procedure	81
3.7.1	System preparation.....	81
3.7.2	Start-up.....	82
3.7.3	Shutdown	82
4	Chapter 4 Reverse osmosis model development	83
4.1	Dynamic model development.....	83
4.2	Reverse osmosis system model	83
4.2.1	RO modules	85
4.2.2	Pumping system	90
4.2.3	Wind turbine	94
4.3	Model implementation	94
4.4	Model validation	95
4.4.1	Steady-state model validation	95
4.4.2	Dynamic model validation.....	98
4.5	Summary	100
5	Chapter 5 Variable-speed operation: operation strategy and control system design	102
5.1	Introduction	102
5.2	Variable-speed operation.....	104
5.2.1	Definition of an operational window	104
5.2.2	Development of an operational strategy	105
5.3	Control system design	107
5.3.1	Proportional-Integral-Differential controller	107

5.3.2	Model predictive controller.....	109
5.4	Results and discussion.....	113
5.4.1	Sensitivity analysis.....	113
5.4.2	Operational strategy	115
5.4.3	Control system performance analysis	117
5.5	Summary	123
6	Chapter 6 Wind Speed Prediction Using Neural Networks.....	125
6.1	Introduction	125
6.2	Literature review on Neural networks.....	126
6.2.1	Background.....	126
6.2.2	Wind speed prediction techniques using neural networks.....	128
6.3	Wind speed prediction for the wind-RO system	129
6.3.1	Neural Network design	129
6.3.2	Backpropagation training algorithm	130
6.3.3	Wind data.....	132
6.3.4	Long-term prediction	133
6.3.5	Short-term prediction	133
6.4	Results and discussion.....	134
6.4.1	Long-term prediction	134
6.4.2	Short-term prediction.....	137
6.5	Summary	140
7	Chapter 7 Modular operation based on wind power prediction	142
7.1	Introduction	142
7.1.1	Challenges for modular operation.....	142
7.1.2	Prospects of neural network prediction and RO operation	143
7.2	Wind speed prediction using neural networks	144
7.2.1	Long-term prediction	145

7.2.2	Short-term prediction	145
7.3	Case study	145
7.3.1	RO system description	146
7.3.2	Control system	147
7.4	Modular operation	148
7.4.1	Start-up and shutdown sequences	148
7.4.2	Rules for Modular operation	150
7.4.3	Programming the modular operation algorithm	151
7.5	Results and discussion	155
7.5.1	Standardised start-up and shutdown sequences	155
7.5.2	Operation scheduling using long-term wind speed prediction	158
7.5.3	Predictive control using short-term wind speed prediction	162
7.6	Summary	167
8	Chapter 8 Conclusions.....	169
8.1	Introduction	169
8.2	Responses to the objectives	169
8.3	Overview and original contributions	172
8.4	Recommendations for future work	174
9	References.....	176
Appendix A	RO system design drawings.....	186
Appendix B	Electrical panel design drawings	192
Appendix C	Sensors calibration	196

Nomenclature

Acronyms

ANN	Artificial neural network	MSF	Multi-stage flash desalination
CAD	Computer-aided design	MVC	Mechanical vapour compression
DMC	Dynamic matrix control	NI	National Instruments
DWEER	Dual work exchange energy recovery	NN	Neural network
ED	Electrodialysis	PID	Proportional, integral and differential control
EPA	Environmental protection agency	PPM	Part per million
ERD	Energy recovery device	PV	Photovoltaic
Exp.	Experimental study	PX	Pressure exchanger
FT	Flow transmitter	RE	Renewable energy
HPP	High-pressure pump	RED	Renewable energy desalination
HRES	Hybrid renewable energy system	RES	Renewable energy source
IMC	Internal model control	RMSE	Root mean square error
I/O	Input/output	RO	Reverse osmosis
LPP	Low-pressure pump	ROSA	Reverse osmosis system analysis
MAE	Mean absolute error	SEC	Specific energy consumption
MAPE	Mean absolute percentage error	SISO	Single input/single output
MED	Multi-effect distillation	SWRO	Seawater reverse osmosis
MIMO	Multiple input/multiple output	Theo.	Theoretical study
MLP	Multi-layer perceptron	TVC	Thermal vapour compression
MPC	Model predictive control	VFD	Variable frequency drive
MPPT	Maximum power point tracking	WHO	World health organization

Symbols

A_m	Active area, m ²	MW	Molecular weight, 58.44 kg/kmol
A_w	Water transport coefficient, m/bar.s	N	Rotational speed, rpm
B_s	Salt transport coefficient, m/s	N_p	Number of poles of a motor
C	Concentration, kg/m ³	N_{pv}	Number of pressure vessels
$C_{p,m}$	Local permeate concentration, kg/m ³	n_e	Number of modules per pressure vessel
C_v	Valve flow coefficient, m ³ /s	n_i	Number of moles
D_B	Brine diffusivity, m ² /s	n_l	Number of membrane leaves
d	Module diameter, m	P	Pressure, bar
d_h	Hydraulic diameter, m	P_{drop}	Pressure drop, bar
F	Motor frequency, Hz	P_e	Electric power, kW
H_c	Control horizon	P_{shaft}	Shaft power, kW
H_p	Prediction horizon	P_w	Wind power, kW
I_{ph}	Phase current, A	PF	Power factor
J_w	Water flux, m/s	Q	Volumetric flowrate, m ³ /s
J_s	Salt flux, kg/s m ²	R	Universal gas constant, 8.3144 × 10 ⁻² m ³ bar/K kmol
K	Conversion factor	Re	Reynolds number
K_m	Mass transfer coefficient, m/s	$Rec.$	Recovery, %
K_d	Differential controller gain	Sc	Schmidt number
K_i	Integral controller gain	SG	Seawater specific gravity
K_p	Proportional controller gain	Sh	Sherwood number
k	Sampling time	T	Temperature, °C
l_{bc}	Membrane length, m	TCF	Temperature correction factor
t	Time, s	w_{bc}	Membrane width, m

t_{bc}	Brine channel thickness, m	y	Controlled output
t_{pc}	Permeate channel thickness, m	ΔP	Differential pressure, bar
t_{sp}	Feed-spacer thickness, m	ϕ_{bc}	Brine channel void fraction
u	Manipulated input	η_m	Motor efficiency
V_{bc}	Brine channel volume, m ³	η_p	Pump efficiency
V_{bulk}	Bulk flow velocity, m/s	μ	Seawater viscosity, Pa.s
V_d	Volumetric displacement, m ³ /rev	π	Osmotic pressure, bar
V_{pc}	Permeate channel volume, m ³	ρ	Seawater density, kg/m ³
V_{ph}	Phase voltage, V	τ	Torque, N.m
V_{ws}	Wind speed, m/s	ω	Rotational velocity, rad/s

Subscripts

b	Brine stream	$shaft$	Shaft
$bulk$	Bulk stream	$total$	Total
c	Concentrate	w	Membrane wall
f	Feed stream		
HPP	Relating to the high-pressure pump		
$iSave$	Relating to the energy recovery device		
LPP	Relating to the low-pressure pump		
Lub	Lubrication stream		
p	Permeate stream		
ref	Reference value		

List of tables

Table 2.1. Summary of previous literature discussing wind-RO desalination.	36
Table 2.2. Summary of previous literature discussing PV-RO desalination.	42
Table 2.3. Summary of previous literature discussing hybrid Wind-PV RO desalination.	46
Table 2.4. Studies analysing membrane deterioration in variable operation.	50
Table 2.5. Hydraulic limitations for 8-inch (0.203 m) /37 m ² DOW-FILMTEC SW membranes with generic conventional pretreatment [142].	56
Table 3.1. RO system main specifications.	66
Table 4.1. Specifications of the SW30HRLE-400 membranes [177-180].	85
Table 4.2. Low-pressure pump specifications.	91
Table 4.3. High-pressure pump specifications.	92
Table 4.4. Energy recovery device specifications [161].	93
Table 4.5. Validation of the Steady-state model output represented by the coefficient of determination (R ²) and Root Mean Square Error (RMSE).	96
Table 5.1. Proportional-Integral-Differential (PID) controllers tuning parameters.	109
Table 5.2. Prediction accuracy of the State-Space model compared to the estimation data.	111
Table 5.3. The Model Predictive Controller tuning parameters.	113
Table 5.4. Properties of the wind speed input and disturbance signals used for assessing the control systems performance.	121
Table 6.1. Error analysis for the long-term neural network prediction during the development phase	135
Table 6.2. Error analysis for the short-term neural network prediction during the development phase	138
Table 7.1. Number of operational RO units relative to available power.	151
Table 7.2. Summary of the RO system performance for Days 1, 2 and 3.	167

List of figures

Fig. 1.1. Types of desalination processes [12].....	20
Fig. 1.2. Contribution of desalination processes to global production (adapted with permission from [16]).....	21
Fig. 1.3. Osmosis and reverse osmosis processes [20].	22
Fig. 1.4. Hollow fibre modules (reused with permission from [21]).	23
Fig. 1.5. Spiral wound modules (reused with permission from [21]).	23
Fig. 1.6. Flow diagram of a RO module [20].	23
Fig. 1.7. Standard reverse osmosis plant configuration [11, 24].	24
Fig. 1.8. Overview of renewable energy desalination [11, 14].....	26
Fig. 1.9. Current landscape of renewable energy desalination worldwide (data adapted from [47-49]).	26
Fig. 2.1. Diagram of the variable capacity plant presented by Peñate et al. (reused with permission from [40]).	34
Fig. 2.2. Connection diagram for the plant presented by Carta et al. (reused with permission from [64]).....	35
Fig. 2.3. Control system layout for the plant presented by Carta et al. (reused with permission from [33]).....	35
Fig. 2.4. PV-RO system with panel cooling and concentrator mirrors (reused with permission from [90]).....	40
Fig. 2.5. Layout of the plant presented by Thomson and Infield (reused with permission from [88]).	41
Fig. 2.6. Configuration of the RO plant used by Ntavou et al. (reused with permission from [97]). ...	41
Fig. 2.7. Configuration of RO plant presented by Spyrou and Anagnostopoulos (reused with permission from [109]).....	45
Fig. 2.8. Schematic diagram of the test rig used by Carta et al. (reused with permission from [64]).	49
Fig. 2.9. Classification of energy recovery devices discussed in this article.	51
Fig. 2.10. RO plant configuration for using a) Pelton wheel, b) Turbocharger, c) DWEER and d) Pressure exchanger.....	51
Fig. 2.11. a) RO Kinetic® working principle [134] and b) ENERCON piston-type accumulator [133] (reused with permission).	53
Fig. 2.12. Two-dimensional salinity contour of the central cylindrical surface of the ERD (reused with permission from [141]).....	54
Fig. 2.13. Operational window presented by Pohl et al. (reused with permission from [79]).	57
Fig. 2.14. Proportional-Integral-Differential controller block diagram [11].	60
Fig. 2.15. Model predictive controller block diagram [11].....	60
Fig. 3.1. Isometric projection of the RO system.	64

Fig. 3.2. RO system installed in the laboratory (front).	65
Fig. 3.3. RO system installed in the laboratory (back).	65
Fig. 3.4. Schematic diagram of the RO system.....	66
Fig. 3.5. Schematic diagram of the feed tank.	67
Fig. 3.6. Cartridge filters.....	68
Fig. 3.7. Low-pressure pump.	68
Fig. 3.8. Danfoss APP high-pressure pump	69
Fig. 3.9. Schematic diagram for the Danfoss iSave energy recovery device [163, 165].	70
Fig. 3.10. Danfoss iSave energy recovery device.	70
Fig. 3.11. Brine flow control modulation valve.....	71
Fig. 3.12. Paddlewheel flowmeter.	72
Fig. 3.13. Pressure transmitter.	72
Fig. 3.14. Conductivity transmitter.	73
Fig. 3.15. Temperature transmitter.	74
Fig. 3.16. Current transmitter.....	74
Fig. 3.17. Electric control panel.....	75
Fig. 3.18. Variable frequency drive for a) the energy recovery device motor (5.5 kW), and b) the high-pressure pump motor (11kW).	76
Fig. 3.19. Data-acquisition and control system structure.....	77
Fig. 3.20. NI-9172 compact DAQ chassis.	77
Fig. 3.21. Graphical user-interface.	79
Fig. 3.22. A segment of the LabVIEW Block Diagram.....	80
Fig. 4.1. Classification of research tasks based on the used methodology (experimental or simulation-based investigation).	83
Fig. 4.2. Schematic diagram showing the RO membrane structure.....	84
Fig. 4.3. Lubrication flow required to lubricate the iSave moving parts.	93
Fig. 4.4. Wind turbine power curve.	94
Fig. 4.5. Regression analysis showing the correlation between the experimental and simulated data for the a) permeate flowrate, b) brine flowrate, c) feed pressure, d) power consumption and e) permeate concentration.	97
Fig. 4.6. A comparison between the measured and simulated a) feed pressure and b) power consumption for the same permeate flowrate. The data is collected at a feed concentration of 35,000 mg/l and a feed temperature of 25°C.....	98
Fig. 4.7. Validation of model accuracy for predicting the permeate flowrate dynamic response. The step-response test was performed at 28°C feed temperature and 35,195 mg/l feed concentration. The permeate recovery varied from 20.7% to 22.9%.....	99

Fig. 4.8. Validation of model accuracy for predicting the feed pressure dynamic response. The step-response test was performed at 28°C feed temperature and 35,195 mg/l feed concentration. The permeate recovery varied from 20.7% to 22.9%.....	99
Fig. 4.9. Validation of model accuracy for predicting the permeate concentration dynamic response. The step-response test was performed at 27°C feed temperature and 35,429 mg/l feed concentration. The permeate recovery varied from 20.7% to 22.9%.....	100
Fig. 5.1. Safe operational window.....	105
Fig. 5.2. High-level block diagram showing the control system structure and signals between each element.....	107
Fig. 5.3. Structure of the Proportional-Integral-Differential Controller. FT represents the flow transmitters sending feedback signals to the controller.....	109
Fig. 5.4. Structure of the Model Predictive Controller.....	110
Fig. 5.5. Sensitivity analysis for the effect of feed concentration on a) feed pressure, b) specific energy consumption, and c) permeate concentration.....	114
Fig. 5.6. Sensitivity analysis for the effect of feed temperature on a) feed pressure, and b) permeate concentration.....	115
Fig. 5.7. Comparison of possible control strategies.....	116
Fig. 5.8. The developed operational strategy based on variable recovery at a constant brine flowrate.....	117
Fig. 5.9. The simulated PID and MPC controller’s response to a 10% step change in the reference signal.....	118
Fig. 5.10. The simulated PID and MPC controller’s response to a 10% step change in the reference signal.....	118
Fig. 5.11. Disturbance rejection test for a step-change in feed concentration presented by a) the permeate flowrate and b) the power consumption. The test is performed at a feed temperature of 25°C.....	119
Fig. 5.12. Disturbance rejection test for a step-change in feed concentration presented by a) the permeate flowrate response and b) the power consumption. The test is performed at a feed concentration of 35,000 mg/l.....	120
Fig. 5.13. A sample of the wind speed signal used in the medium wind-variation scenario.....	121
Fig. 5.14. Performance projection of the PID controller reference tracking capability for the input signal defined in the medium wind-variation scenario.....	122
Fig. 5.15. Performance projection of the MPC controller reference tracking capability for the input signal defined in the medium wind-variation scenario.....	122
Fig. 5.16. Improvement in cumulative permeate production for one hour of operation due to using a model predictive controller instead of a proportional-integral-differential controller, for three scenarios are detailed in Table 5.4.....	123

Fig. 6.1. A feed-forward neural network structure [213].	126
Fig. 6.2. Model of a hidden layer neuron [214].	127
Fig. 6.3. Supervised learning [217].	127
Fig. 6.4. Structure of the three-layer feed-forward backpropagation neural network.	130
Fig. 6.5. Structure of the long-term prediction neural network.	133
Fig. 6.6. Structure of the short-term prediction neural network.	134
Fig. 6.7. Regression analysis representing the correlation between the long-term neural network outputs and targets dataset during training, validation, and testing.	135
Fig. 6.8. Predicted hourly average wind speed timeseries on 18 August 2020 with respect to measured data.	136
Fig. 6.9. Predicted hourly average wind speed timeseries on 30 March 2020 with respect to measured data.	137
Fig. 6.10. Predicted hourly average wind speed timeseries on 24 November 2020 with respect to measured data.	137
Fig. 6.11. Regression analysis representing the correlation between the short-term neural network outputs and targets dataset during training, validation, and testing.	138
Fig. 6.12. Predicted 2-minute average wind speed timeseries on 18 August 2020 with respect to measured data.	139
Fig. 6.13. Predicted 2-minute average wind speed timeseries on 30 March 2020 with respect to measured data.	140
Fig. 6.14. Predicted 2-minute average wind speed timeseries on 24 November 2020 with respect to measured data.	140
Fig. 7.1. Schematic diagram of the RO plant configuration. The RO plant consists of three RO units driven by a 30 kW wind turbine.	146
Fig. 7.2. Schematic diagram of the RO unit presented previously in Chapter 3.	147
Fig. 7.3. Wind turbine power curve.	147
Fig. 7.4. Structure of the Model Predictive Controller. The input disturbances are the feed concentration and feed temperature.	148
Fig. 7.5. Control system structure after implementing the modular operation technique.	153
Fig. 7.6. Algorithm for the modular operation procedure.	154
Fig. 7.7. Initial start-up procedure.	156
Fig. 7.8. Rolling start-up procedure.	157
Fig. 7.9. Shutdown procedure.	158
Fig. 7.10. Possible number of operational RO units based on actual and predicted hourly average wind speed on 18 August 2020.	160
Fig. 7.11. Possible number of operational RO units based on actual and predicted hourly average wind speed on 30 March 2020.	161

Fig. 7.12. Possible number of operational RO units based on actual and predicted hourly average wind speed on 24 November 2020.....	162
Fig. 7.13. The RO units operation using the predicted wind power from the short-term neural network as the power input for the control system.....	164
Fig. 7.14. The RO units operation using the predicted wind power from the short-term neural network as the power input for the control system.....	165
Fig. 7.15. The RO units operation using the predicted wind power from the short-term neural network as the power input for the control system.....	166

1 Chapter 1 Introduction

1.1 Growth of the desalination industry

Water security, a global challenge that is faced by several countries, has received increasing attention from the scientific community. Global water consumption is growing at more than twice the rate of population due to improving standards of living and increasing demand from the industrial and agricultural sectors [1, 2]. It is expected to increase by 50% by the year 2030 [3]. Currently, two-thirds of the world population suffers from water shortage for at least one month per year [2]. This situation is expected to escalate to the point where half will suffer from water stress by the year 2025 [4].

Although 71% of the Earth is covered by water, 97% of this is unpotable seawater [5]. Desalination is a water treatment process that involves removing salt from saline water thus making it suitable for drinking. Growing water security challenges have led to intensive research and investments in desalination, spurring its rapid growth over the last 40 years [6]. The global online desalination capacity has been constantly increasing since 1965, especially throughout the last decade [6]. It increased significantly from 66.4 million m³/day in 2012 to 99.7 million m³/day by 2018 [7-9]. The sector continues to grow, with a yearly contracted capacity of about 4 million m³/day from 2015 to 2017 [9]. A number of countries, such as Qatar and Kuwait, already rely on desalination as their sole water supply [7].

There are various types of desalination technologies. Their principle of operation depends on membrane filtration, evaporation-condensation or crystallization, as presented in Fig. 1.1. Membrane filtration processes rely on semi-permeable membranes that allow water passage and block larger molecules, i.e., salts. Membrane filtration processes that are based on osmosis rely on hydraulic pressure to separate salt from seawater. Another approach, namely Electrodialysis (ED), relies on the electric potential to remove salt ions [10]. Evaporation-condensation processes, as the name implies, rely on evaporating seawater and then condensing its water vapour to separate water from the salt water solution. Evaporation-condensation processes can operate by heat energy, such as Multi-Stage Flash Distillation (MSF) or Multi-Effect Distillation (MED); other processes operate using electrical energy, such as Mechanical Vapour Compression (MVC). Crystallization processes can be used for salt removal; however, they have not been used for large-scale desalination. The selection of

a suitable desalination process varies according to the scale of implementation, feedwater salinity, site conditions and type of available energy [11].

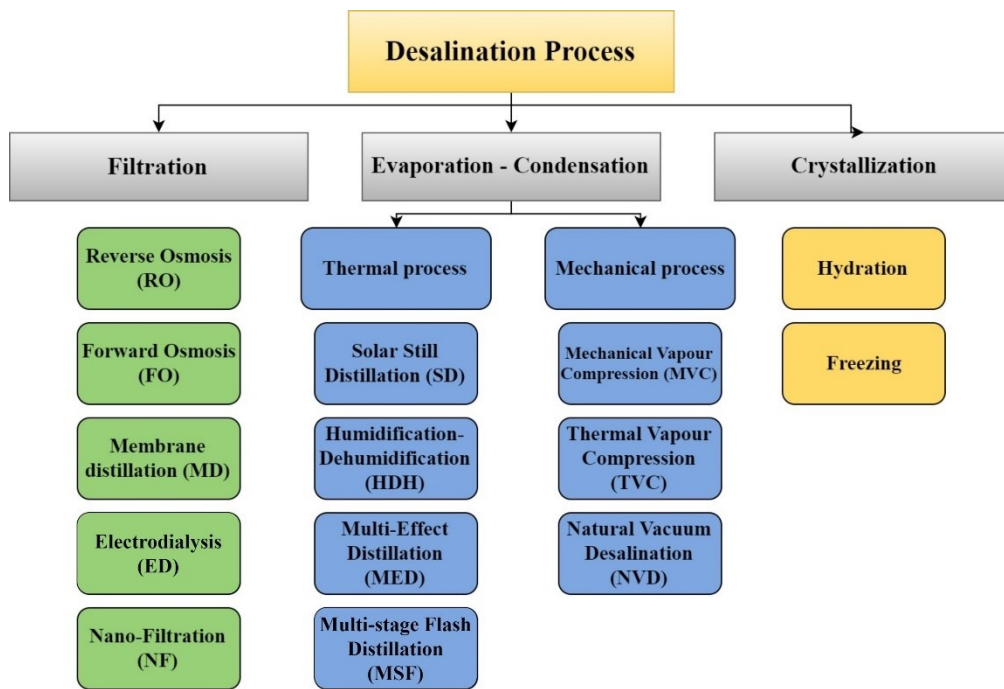


Fig. 1.1. Types of desalination processes [12].

1.2 Reverse osmosis

1.2.1 Background

Reverse osmosis (RO), a membrane-based desalination technology that depends on applying hydraulic pressure to force water through a semipermeable membrane, currently dominates the industry [10, 13, 14]. In 2016, RO represented 65% of the globally installed desalination capacity (Fig. 1.2) [15, 16]. The predominance of RO stems from several advantages. Firstly, RO can provide a wide range of production capacities, from small standalone installations delivering less than 1 m³/day to large-scale plants delivering over 500,000 m³/day [15]. Secondly, RO can handle a wide range of feedwater salinity including, brackish water and seawater. Thirdly, RO plants can provide continuous and reliable operation without shutdown for extended periods. Fourthly, RO plants operate at low Specific Energy Consumption (SEC) ranging from 2 to 4 kWh/m³, not far above the thermodynamic limit (energy released by dissolving salts in water at the respective concentration) of about 1.1 kWh/m³ for 50% recovery from seawater at 35,000 mg/l [17, 18]. Consequently, the CO₂ emission from seawater RO (SWRO) plants is the lowest compared to other desalination processes, ranging from 1.7 to 2.8 kgCO₂/m³ [19]. In contrast, the CO₂ emission for MSF

ranges from 15.6 to 25 kgCO₂/m³ and from 7 to 17.6 kgCO₂/m³ for MED [19]. Lastly, water production by RO is becoming increasingly cost-effective [8]. For large RO plants, with production capacities over 40,000 m³/day, costs ranged from 0.8–1.2 \$/m³ in 2017 and are expected to decrease further by 60% to reach 0.3–0.5 \$/m³ within the next 20 years [17].

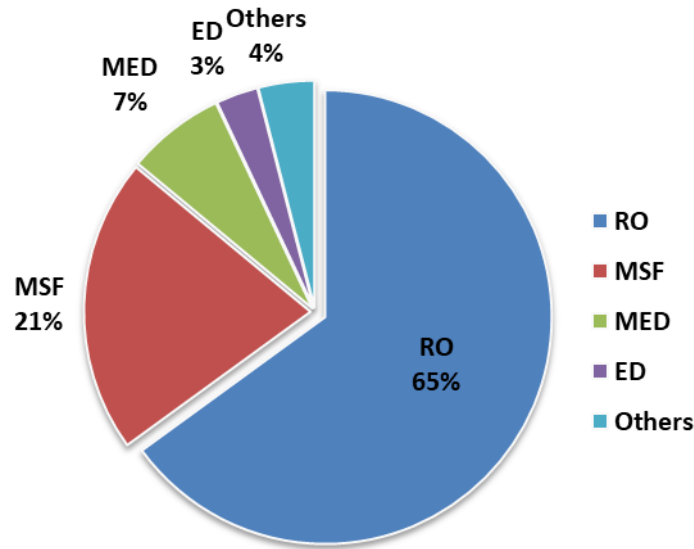


Fig. 1.2. Contribution of desalination processes to global production (adapted with permission from [16]).

1.2.2 Theory of operation

Osmosis is a naturally occurring process that happens when two aqueous solutions of different salt concentrations are separated by a semi-permeable membrane. Water will flow from the low concentration side to the high concentration side until both sides reach the same concentration. This flow is driven by osmotic pressure. The osmotic pressure is directly proportional to the difference in concentration between the two solutions, water temperature and depends on the composition of the total dissolved salts [20]. The osmotic pressure is calculated from Van't Hoff's thermodynamic law as:

$$\pi = R \times (T + 273) \times \Sigma m_i \quad (1.1)$$

where π is the osmotic pressure in bar, T is the water temperature in °C, R is the universal gas constant which is 0.082 L.atm/mol.K and Σm_i is the sum of molar concentration of all constituents of seawater in mol/L [20]. However, the process required in desalination is the opposite of the natural osmosis process. In order to transfer water from the high salinity side

to the low salinity side, the osmosis process has to be ‘reversed’, by applying pressure that is higher than the osmotic pressure. In RO this pressure is supplied by an electrical pump that pushes the water through the membrane. The difference between the osmosis and the RO processes is presented in Fig. 1.3.

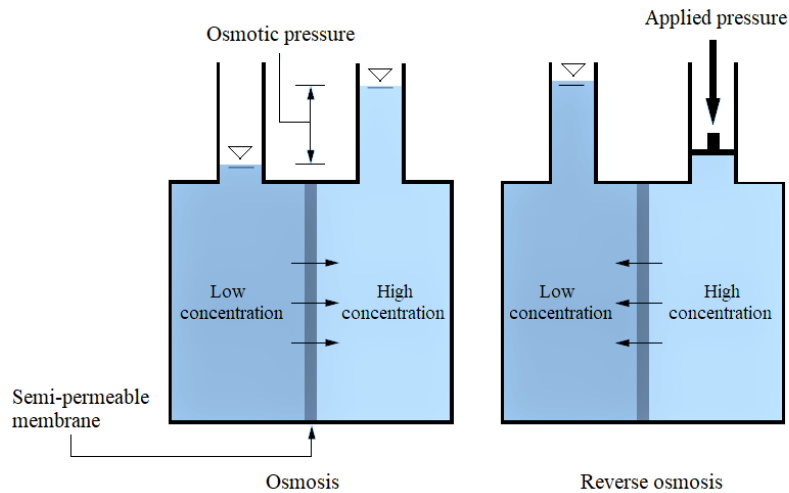


Fig. 1.3. Osmosis and reverse osmosis processes [20].

The semi-permeable membranes are packed together in a standard configuration, to provide a large surface area for water separation and to allow for commercialization. Two module configurations are widely used; either hollow fibre or spiral wound modules, presented in Fig. 1.4 and 1.5 respectively. Hollow fibre modules were mostly used until the mid-1990; however, spiral wound modules dominate the current marketplace [20]. Spiral wound modules are formed of individual flat membranes that are separated by feed and permeate spacers, allowing the feed and permeate streams to flow separately, and spirally wrapped around a permeate collecting tube. Feedwater enters the RO module and is separated into two streams, as presented in Fig. 1.6. The first stream is the clean water that passes through the membranes, called the permeate. The second stream is the highly concentrated feedwater, which is called concentrate or brine.

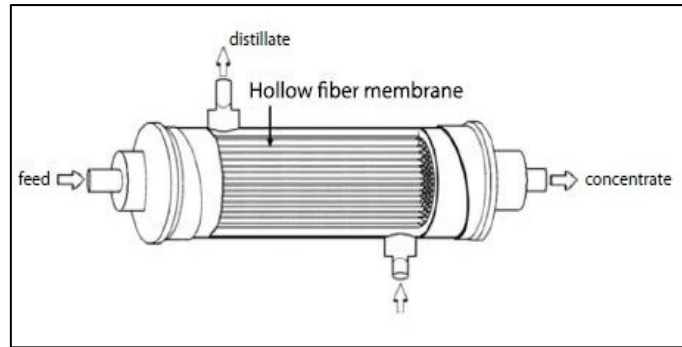


Fig. 1.4. Hollow fibre modules (reused with permission from [21]).

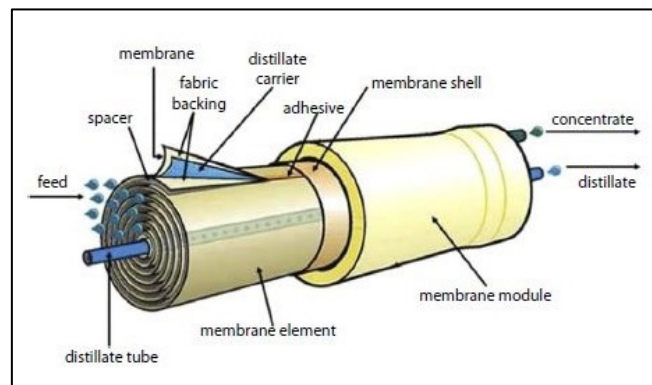


Fig. 1.5. Spiral wound modules (reused with permission from [21]).

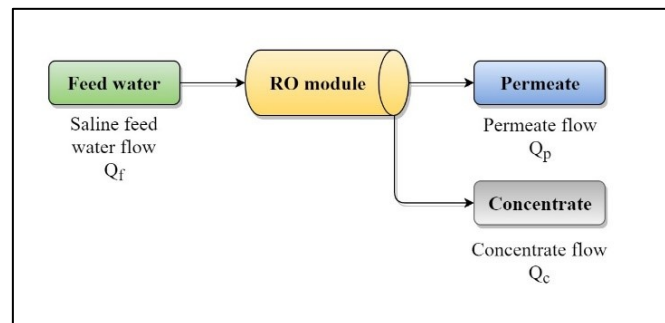


Fig. 1.6. Flow diagram of a RO module [20].

1.2.3 Standard RO plant configuration

A large-scale RO plant consists of different subsystems, as shown in Fig. 1.7. A pre-treatment system is included to remove suspended material and biological and organic contaminants from seawater before admission to the RO modules [22]. This prevents excessive membrane fouling and allows higher recovery [23]. Additionally, an after-treatment system is included for the addition of chemicals, such as lime (calcium hydroxide) to neutralise water acidity and increase hardness [20]. Also, the plant includes a pumping system that consists of a) a Low-Pressure Pump (LPP) that draws water from the feed source,

b) a High-pressure pump (HPP) that supplies pressure required for water permeation, c) an Energy Recovery Device (ERD) that recovers pressure energy from the brine, and d) a Booster Pump (BP) to account for pressure losses in the pressure vessels and ERD. Prior to using ERDs, the entire system feed was pressurised using the HPP and the brine pressure was reduced using a throttle valve. This led to using oversized HPPs to handle the entire system feed and wasting pressure energy that still resides in the brine stream. The current industry preference is to use an ERD to recover energy from the brine flow for pressurising a portion of the feed flow. This leads to reduced HPP capacities and reduced SEC. This configuration is referred to as split-feed flow configuration. Lastly, a storage tank is included to store the product water and provide it to consumers according to demand.

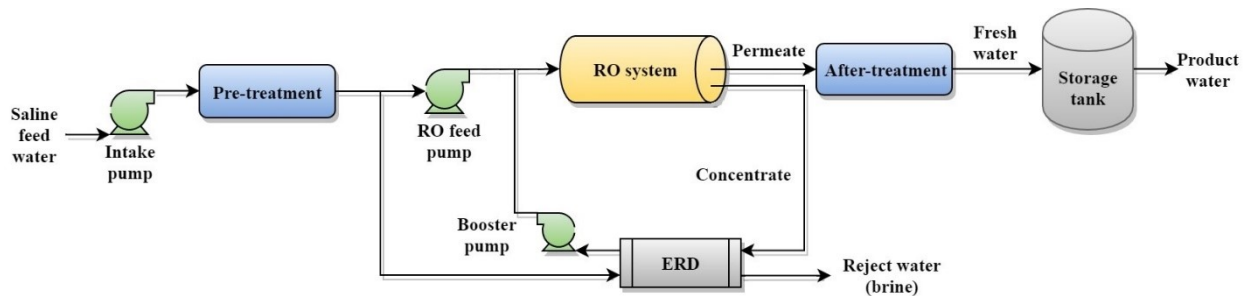


Fig. 1.7. Standard reverse osmosis plant configuration [11, 24].

1.2.4 Challenges to reverse osmosis desalination

As mentioned earlier, RO desalination plays an important role globally in providing clean water. Nevertheless, there are two major concerns about the impact of RO desalination on the environment. First, despite ongoing improvements, RO desalination remains energy intensive considering its contribution to the worldwide desalination capacity and dependency on fossil fuels [22, 25]. Second, the discharge of highly saline brine and chemicals from large plants represents a threat to the marine environment [26]. Finding alternative energy sources to drive commercial RO desalination plants is key to improving their sustainability, decarbonising water production, and making them accessible to countries with limited natural and financial resources [18, 27, 28].

1.3 Renewable energy desalination (RED)

Renewable energy (RE) is an attractive solution to reduce RO plants' carbon footprint, decrease their running costs and eliminate the link between water prices and fuel costs [22]. In general, RE is a sustainable alternative to using fossil fuels due to its abundant availability. From 2014 to 2015, the global installed capacity of wind power plants and solar photovoltaic

(PV) increased from 370 to 433 GW and from 177 to 227 GW, respectively [29]. Meanwhile, the price of RE is constantly decreasing; for example, the price of solar photovoltaic modules decreased from 33.44 \$/watt in 1979 to just 0.35 \$/watt in 2017 [30, 31]. As for wind turbines, their price in the United States decreased by one third from 2008 to 2011 [32]. Possible combinations between various Renewable Energy Sources (RES) and desalination processes are presented in Fig. 1.8.

Desalination by RO is widely considered for RED applications due to its low SEC compared to other processes [13, 33-35]. The SEC is made up of two components. Firstly, the energy required for the RO process itself, which depends on factors including water quality, membrane efficiency, pump efficiencies, recovery rate and the ERD used. It can range from 1.7 to 2.5 kWh/m³. Secondly, the energy required for secondary processes, such as feedwater pumping, pre-treatment and the plant electrical services, typically ranges from 0.3 to 1.5 kWh/m³ [28]. The SEC can vary based on plant location, size and design efficiency. While 2-4 kWh/m³ is typical for larger plants, for smaller standalone systems values tend to be higher, from 3 to 7 kWh/m³, due to unusual operating conditions, inefficiencies of scale, or sub-optimal design and operation [12].

Electrical energy to drive the RO plant, which accounts for 44% of the water cost [36], can be generated directly from RE by solar-, wind- or wave-energy converters, as shown in Fig. 1.8. Other important RE sources include hydro- and bio-energy, but these are mostly unsuitable as they rely on natural water resources that are inherently scarce in regions where desalination is needed [37]. Wind and wave energy can be used directly to produce mechanical movement to drive the HPP. However, directly-driven wind-RO systems are not recommended for SWRO due to the high osmotic pressure [38-40]. In addition, a separate electrical energy source is needed to drive the control system and data logging [41]. Another approach would be to couple a thermal energy source, such as solar-thermal or geothermal energy, to a Rankine cycle to produce mechanical energy and drive an electric generator [42]; however, this is more expensive than solar-PV or wind turbines, except in specific locations where high-grade geothermal resources are available [16, 37].

The use of wind and solar-PV to drive RO plants has been recommended by several studies, due to their affordability, availability, technological maturity, and zero water consumption compared to other RESs [13, 43-46]. PV-RO and wind-RO are the most widely deployed

technologies for RED accounting for 32% and 19% of applications respectively (Fig. 1.9) [11, 47].

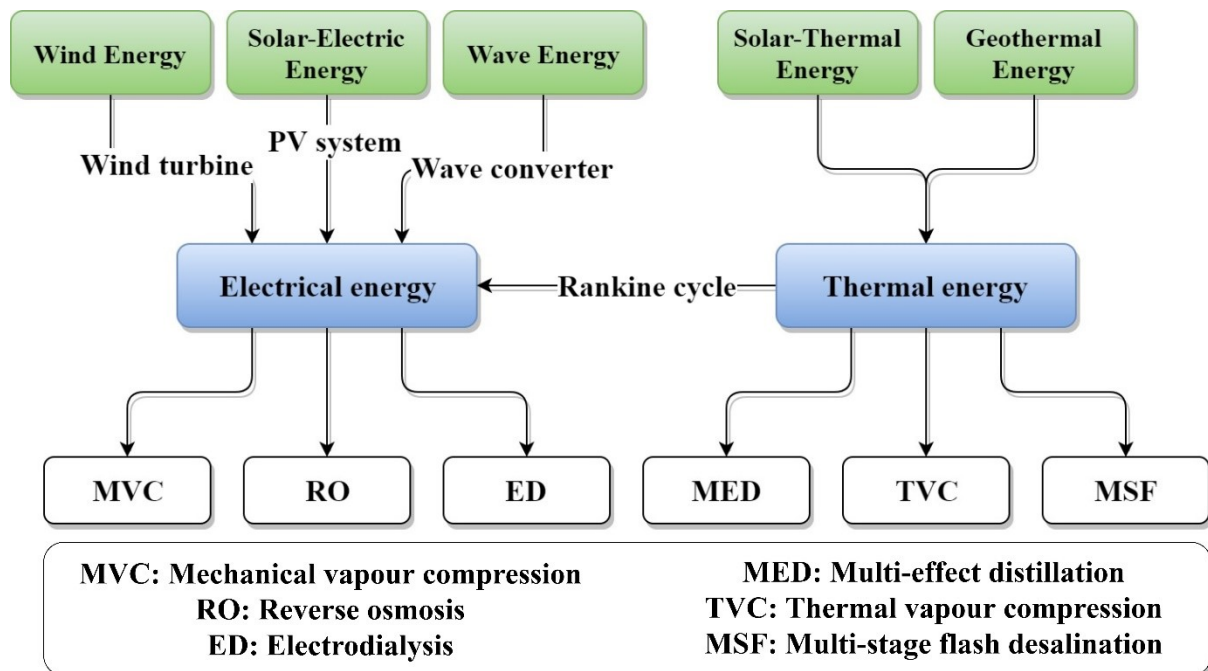


Fig. 1.8. Overview of renewable energy desalination [11, 14].

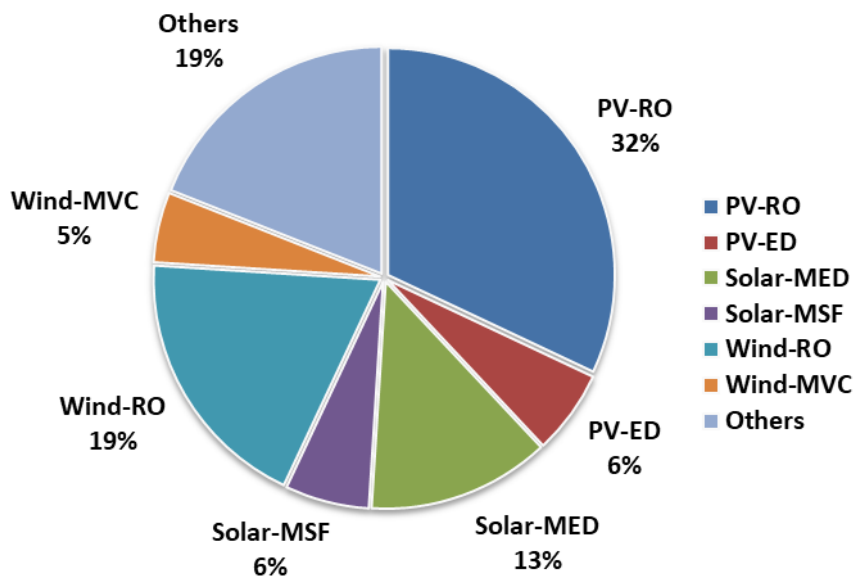


Fig. 1.9. Current landscape of renewable energy desalination worldwide (data adapted from [47-49]).

1.4 Limitations of steady-state operation

Whereas the power output of solar-PVs and wind turbines is intermittent and fluctuating, commercial RO plants are designed to work at constant flow, pressure and power level.

Steady-state operation is considered economical for grid-powered RO plants, as it maximizes production capacity and makes good use of invested capital. In addition, it is easier to maintain the product water quality and manage the membrane fouling. As such, earlier studies of renewable energy-driven RO plants often included a backup, such as a direct connection to an electric grid, an energy storage system, or a Diesel generator to operate the RO plant with constant power [50, 51].

1.4.1 Grid-connected RO systems

Current large-scale RE-powered RO plants are grid-connected to ensure constant water production, such as the Al Khafji solar-PV powered RO plant in Saudi Arabia that has a capacity of 60,000 m³/day [52]. Such plants are considered more economical than conventional fossil-fuel-powered RO plants, especially when the RES availability and the feed-in tariff are high [48]. However, grid-connected RO plants place a high load on national grids and affect grid stability. For example, in the Gulf Cooperation Council countries, desalination is estimated to consume 4–12% of the total electricity consumption, [53, 54]. It would require a high penetration of RE into the electricity grid to support these desalination plants. Such penetration would decrease the electric grid's reliability and power quality by introducing voltage rise, flicker and harmonics [55, 56]. The transition to fully renewable RO plants is desirable to allow a high fraction of RE while maintaining stable grids.

1.4.2 Energy storage

As for energy storage systems, these have been somewhat impractical for large-scale applications, as they require a large area, increase capital cost and can complicate the system due to requiring additional equipment, such as charge controllers [57]. Specifically, batteries tend to be expensive, have a short lifetime and require regular replacements - all features that cripple their economic feasibility and increase water production cost [13, 34, 57]. In [50] and [58], water production cost was compared for a SWRO system with and without battery storage. In one study, the use of batteries increased the cost from 7.8 to 8.3 €/m³ [50], and in another from 10 to 13 \$/m³ [58]. Accordingly, energy storage is limited to small standalone installations and is not economical for large-scale applications [40, 59, 60].

1.5 Variable operation

To address these difficulties, recent advances have included variable operation to directly couple the RO plant to the RES, without backup systems [33, 35, 61-65]. Firstly, directly-

coupled RO plants operate with a variable production rate and recovery ratio that follow the available power [35]. The operating pressure and flowrate are controlled to change the production rate and recovery ratio, respectively. This technique is referred to in this thesis as ‘variable-speed operation’, as it uses a Variable Frequency Drive (VFD) to change the HPP speed according to the available power. Normally, positive displacement pumps are suitable for variable-speed operation, as they offer consistent efficiency at varying flowrates. Secondly, RO trains (sets of identical modules that constitute the RO plant) can be connected/disconnected based on the available energy [66]. This technique is referred to in this thesis as ‘modular operation’. Variable operation, using the variable speed and/or modular approach, is interesting for renewable energy-driven RO plants as it omits the need for energy storage, backup systems and associated costs. It is especially attractive for islands, remote areas and countries with low energy availability from fossil fuels and lacking a regional grid interconnection to neighbouring countries [11].

1.6 Thesis aims and objectives

This thesis aims to optimise the operation of RE-driven RO to pave the way for large-scale implementation. Variable operation was used to directly connect a RO system to a RES and accommodate the variation and intermittency of available power. The study considered optimising both aspects of variable operation, i.e., variable speed operation and modular operation, to present an efficient load management technique transferable to large-scale systems. A RO pilot plant was used that delivers similar performance to large-scale systems, although at a lower production capacity (3.2 m³/h), to develop solutions suitable for such scale. The RE source considered was wind energy, as it is a good representation of a rapidly fluctuating and intermittent energy source that does not have a specific pattern. Other types of RESs, such as solar, generally vary more slowly and predictably; therefore, a solution developed for wind is expected to accommodate a range of RE types including wind, wave and solar energies. The research objectives are as follows:

- 1) Review published literature to identify state of the art regarding RE-driven RO desalination, in addition to identifying technical challenges and potential solutions for large-scale implementation.
- 2) Design, build and test a RO pilot plant at an industrial scale having comparable performance to large-scale systems to develop solutions transferable to such scale.

- 3) Develop and validate a dynamic model that predicts the dynamic behaviour of the developed RO system.
- 4) Present an optimised variable-speed operation technique to vary the RO operation parameters according to available power.
- 5) Design and implement an advanced control system based on Model Predictive Control (MPC) and compare its performance to a conventional Proportional-Integral-Differential (PID) controller.
- 6) Develop a wind speed prediction algorithm using neural networks for forecasting long- and short-term changes in wind speed.
- 7) Develop a modular operation technique to connect/disconnect RO units, while following a standardised start-up/shutdown sequence, according to changes in available power. The technique utilises wind speed prediction in scheduling the RO units' start-up/ shutdown sequence and parameters variation.

1.7 Thesis outline and structure

This thesis consists of 8 chapters. A brief outline of each chapter is provided as follows:

Chapter 1: This chapter includes the introduction and background information for this thesis. It introduces the water scarcity problem, growth of the desalination industry and the operation principle of RO systems. Also, the current landscape and modes of operation for RE-driven RO are discussed.

Chapter 2: State of the art and technical challenges for large-scale implementation of RO desalination driven by wind and solar photovoltaic energy are presented. Research gaps and potential research directions are identified.

Chapter 3: The experimental setup and procedure used throughout this study are introduced. A description of the RO system developed to imitate the operation of large-scale systems is provided. The data acquisition systems and instrumentation used in the experimental investigation are described.

Chapter 4: The development and validation of a dynamic model to predict the RO system behaviour is described. The model is used in the development and testing of the control system and the variable-speed operation technique in chapter 5, in addition to the development and testing of the modular operation technique in Chapter 7.

Chapter 5: A variable-speed operation technique using an optimised operation strategy and an advanced control system based on MPC is introduced. An investigation is performed to select the optimum operation strategy for the system configuration. The advanced MPC is compared to a conventional PID controller to quantify its effect on performance.

Chapter 6: The development of neural networks for predicting wind speed is described. Two prediction ranges are defined: a) long-term prediction to forecast a full day ahead of hourly average timeseries, and b) short-term prediction to forecast the average wind speed for the next two minutes.

Chapter 7: A modular operation technique based on wind speed prediction is introduced. A standardised start-up/ shutdown procedure for the RO system is developed. Scheduling of the RO units operation using long-term wind speed prediction is described. Modular operation guided by short-term wind speed prediction and assisted by variable speed operation is modelled for a case study incorporating three identical RO units.

Chapter 8: The findings and conclusions from this thesis are summarised by responding to the research objectives and highlighting the original contribution. Recommendations for further development are outlined.

2 Chapter 2 Literature review

2.1 Problem definition and review methodology

Chapter 1 emphasised the need for coupling RE to RO for large-scale systems as a vital step towards sustainable desalination and overcoming water security challenges. This Chapter aims to capture the current state-of-the-art and technical challenges in using wind, solar and hybrid wind-solar energies as main drivers of large-scale RO plants. Initially, studies of RO plants driven by wind and/or solar PV will be presented and analysed, to assess the current status of the technology. The technical challenges of variable operation and potential solutions will then be discussed, focussing on key elements of the RO plant – namely the membranes and energy recovery devices. Strategies for operation and control will be analysed and discussed. The chapter is concluded with recommendations for the development of RE-RO to satisfy the world’s growing water demand [11].

2.2 State of the art in renewable energy-driven RO

Over the last two decades, several research papers have discussed the variable operation of renewable energy-driven RO plants. Theoretical studies covered mostly small or medium plants (<40,000 m³/d) and experimental studies covered plants rarely exceeding 1000 m³/d. This section reviews studies of specific plants (some constructed and some only taken to the theoretical stage) that aimed to efficiently integrate RO with wind, solar or hybrid wind-solar energy. The studies are reviewed with regard to the plant configurations and the operational strategies adopted. Lessons learnt for improving the plant adaptability to fluctuating energy will be useful for application in this study [11].

2.2.1 Wind-energy RO desalination

Wind turbines are playing a major role in achieving sustainability goals in many countries [67]. Their low operating cost, high efficiency and energy availability, especially for coastal areas, make wind turbines a successful and clean choice to power RO plants [5, 68, 69], reducing both carbon footprint and water production costs [61, 70]. However, further deployment of wind turbines requires certain challenges to be addressed [71]. For example, wind turbines have to gain social acceptance and improved public perception due to their aerodynamic noise and visual impact. Wind measurement and forecasting should be enhanced for accurate prediction of power generation, which would improve the control of wind farms and their integration with local grids. Availability of lightweight materials will

allow larger turbines with improved efficiencies to be developed [72]. The fluctuating energy input of wind-powered RO plants could affect the daily production capacity and have negative effects on the plant's performance [68, 70]. Numerous studies considered the design of wind-RO plants and presented different approaches to accommodate the variable nature of wind power, as summarised in Table 2.1 [11].

2.1.1.1 Stabilisation of wind power output

Short-term energy storage devices were suggested for wind-RO plants to smooth wind power fluctuations and improve system stability [13]. They are usually selected based on their storage capacity, mode of coupling and charging/discharging rate. Common options include flywheels, compressed air storage, hydraulic accumulators and supercapacitors [59, 68, 73]. Batteries were not included in this list, as they are not suitable for stabilising wind power output due to limitations on their charging/discharging rate [59]. Flywheels and supercapacitors are promising as short-term energy storage devices as they offer high energy density and higher roundtrip efficiency of 89% and 86%, respectively, compared to 63% efficiency of lead-acid batteries [59]. Fast rotating flywheels have advantages of instantaneous response, ability to stabilise system frequency and low energy cost compared to supercapacitors [13, 35, 40, 59, 64]. For instance, Rahal [74] used a flywheel connected to a synchronous generator integrated into the wind-RO system to overcome wind power input fluctuation for an 84 m³/day RO plant. The flywheel inertia smoothed the wind turbulence and improved the stability of system frequency, which was beneficial for the RO plant as it decreased pump pressure fluctuations.

Another approach for smoothing the plant operation is by connecting it to a microgrid that includes backup systems such as Diesel generators and electricity storage. Bognar et al. [75] compared two different operation scenarios for a RO plant powered by a microgrid. The constant and variable operation of the microgrid and RO plant were compared. For constant operation, a Diesel generator and electricity storage were used to maintain a steady operation. However, for variable operation, water storage was used to meet the required production demand. Variable operation and water storage lowered electricity usage and water production costs by avoiding the fuel use of a Diesel generator [11].

2.1.1.2 Variable operation of wind-RO plants

Several studies have used variable operation to directly couple the RO plant to a wind turbine. Both modular and variable-speed operation have been used. Modular operation for wind-RO plants uses a high-power wind turbine to operate multiple RO units, such that, matching between available power and load is achieved by switching on and off RO units and trains [64]. Several research teams used this approach. Peñate et al. [40] presented a variable capacity plant, displayed in Fig. 2.1, that consists of three switchable RO trains. The variable capacity plant was compared to a fixed capacity system that operated when enough energy was available to achieve full production capacity. The variable capacity plant produced 2 – 8% less than the fixed capacity plant, which operated at a higher recovery ratio. However, the variable capacity plant operated for more hours of the year, as it adapted better to the available energy using variable-speed operation, thus showing the potential of variable operation to achieve higher permeate production subject to improvement in energy utilisation. Moreover, Carta et al. [64] presented an operational analysis of an autonomously operating RO plant in the Canary Islands. The plant, shown in Fig. 2.2, was directly coupled to a wind farm without any backup system. It consisted of 2 wind turbines and a flywheel to operate 8 identical RO units. A control strategy for the modular operation was developed to match the load to the available power. However, no other method, i.e., variable speed operation, was used to adjust the RO plant capacity to the transient power supply. Also, an ERD was not included, which reflected a high SEC of 6.9 m³/day. In another study, Carta et al. [33] designed a small-scale wind-RO plant, with a rated production capacity of 18 m³/day, using a combination of variable-speed and modular operation. A comprehensive control system was developed, presented in Fig. 2.3, to control the number of operating pressure vessels, the operating pressure and feed flowrate according to a predetermined operation strategy. Due to the inertia and sensitivity of the desalination plant towards changes in the control parameters, a perfect fit between power generated by the wind turbine and power consumed by the desalination plant was not achieved, even with constant wind speed over 2-minute intervals. This was caused by the slow response of the system in reaching reference control variables for feed flowrate and pressure. The aforementioned mismatch would have been more prominent if the RO plant included an ERD, if the constant wind speed intervals were reduced, or the wind turbine was represented by a dynamic model. A later study [63] presented the use of artificial Neural Networks (NNs) for controlling and managing the wind-RO system mentioned in [33]. The NN control system generated infrequent feed flow and

pressure setpoints that tended to drive the permeate recovery ratio over the acceptable limit. This was caused by shortcomings in the algorithms controlling the frequency converter and the proportional-solenoid throttle valve, which controlled the feed flowrate and pressure respectively. Moreover, Lai et al. recommended developing an advanced control system and strategy for directly coupled wind-RO [68]. Control systems selection, tuning and performance have a significant effect on plant performance (see Section 2.3.4).

For directly coupled wind-RO plants, the wind turbine is connected to the plant through an isolated electric grid. The grid frequency depends on the wind turbine power and plant load. A decrease in grid frequency will indicate lower power delivered by the wind turbine and the RO plant load must be decreased accordingly. On the other hand, an increase in grid frequency indicates an increase in wind turbine power, requiring activation of the blade pitch control system [35]. The creation of an isolated electric grid and load connection for a wind-powered RO plant was described in detail by Subiela et al. [35] and Carta et al. [64]. The main difficulties occurred during plant start-up, as the loads could not be connected until the frequency reached a specified range between 48 – 50 Hz.

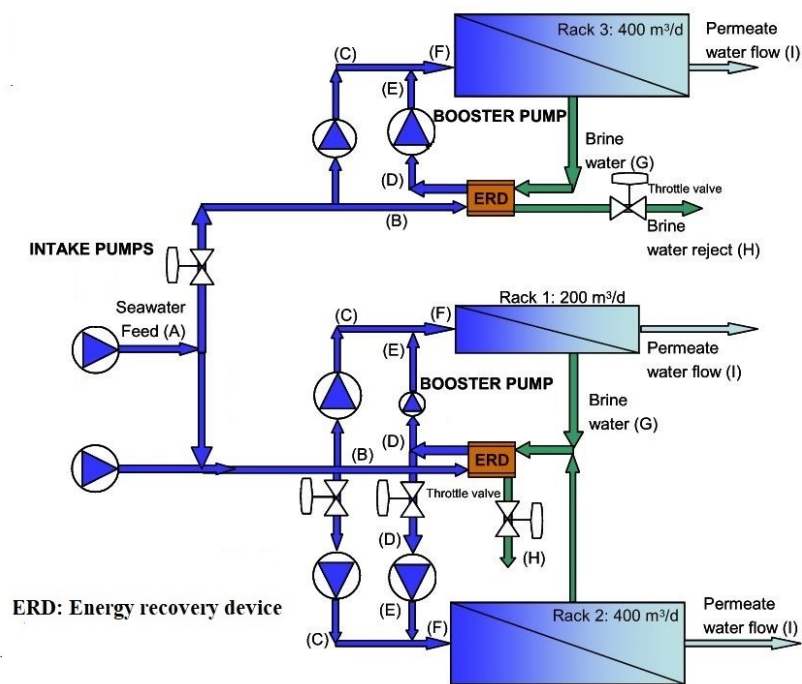


Fig. 2.1. Diagram of the variable capacity plant presented by Peñate et al. (reused with permission from [40]).

The plant consisted of three RO racks, one rack had a capacity of 200 m³/d and two racks had a capacity of 400 m³/d. The RO racks operated independently and were connected or disconnected depending on the energy available. Rack 1 and 2 shared an isobaric energy recovery device that can operate with variable capacity.

Table 2.1. Summary of previous literature discussing wind-RO desalination.

Author(s)	Year	Location	Study	Energy storage	Wind turbine power (kW)	Production capacity (m ³ /day)	S.E.C (kWh/m ³)	Feed salinity (mg/L)	Production cost	Energy recovery	Plant description
Miranda and Infield [76]	2002	Red Sea	Exp.	None	2.2	8.5	3.4	40,000	0.8 – 3 (£/m ³) [77]	Clark pump	-
Carta et al. [64]	2003	Canary Islands	Exp.	Battery and UPS for control system	2 x 230	25 x 8	6.9	Seawater	-	None	Eight identical plants connected in parallel. Each plant has three pressure vessels with three RO membranes each.
Moreno and Pinilla [78]	2004	Colombia	Exp.	None	1.5	0.4	-	35,000	-	None	One RO membrane.
Pohl et al. [79]	2009	Not based on wind data	Theo.	None	Power from main: 12.5	30.5	3.2 – 4.22	35,646	-	Presented by an 85% efficiency	Four RO membranes in series.
Peñate et al. [40]	2011	Canary Islands	Exp.	Flywheel - batteries	225	1000	2.7	38,170	-	RO Kinetic®	Three RO trains. Each train has 2, 6 and 10 pressure vessels, respectively. Each pressure vessel includes seven RO membranes in series.
Bognar et al. [75]	2012	Cape Verde	Theo.	None	275	200 - 600	4.3	Seawater	1.09 (€/m ³)	Hydraulic turbocharger	Two RO trains.
Carta et al. [33]	2015	Canary Islands	Theo.	None	15	5.2 – 19.4	10 – 14.5 11.3 – 16.9	35,200 39,800	-	None	Two pressure vessels connected in parallel. Three modules per PV.
Gökçek and Gökçek [5]	2015	Turkey	Theo.	None	30	24	4.38	43,528	2.96 – 6.46 (\$/m ³)	None	Six RO membranes in series.

Bilstad et al. [70]	2015	Norway	Exp.	None	5	7.5	4.24	35,000	-	None	Eight RO membranes in series.
Latorre et al. [62]	2015	Canary Islands	Exp.	None	Power from main 5.5 - 21.5	45.6 - 120	4 – 5.5	32,237 ppm	-	None	One pressure vessel with six RO membranes connected in series.
Cabrera et al. [63]	2017	Canary Islands	Theo.	None	11	19.4	9.73 – 14.63	29,700 – 35,600 ppm	-	None	Two pressure vessels connected in parallel. Three modules per PV.
Carta and Cabrera [80]	2021	Canary Islands	Theo.	Flywheel and UPS	2 x 2300	5000	-	Seawater	3.52 (€/m ³)	Pressure exchanger	Single-stage RO system with a pressure exchanger.

- **Acronyms:** UPS: Uninterrupted power supply.

2.2.2 Solar-PV RO desalination

Solar-PV powered RO plants are considered very promising for providing fresh water in isolated, arid and remote regions [51]. The success of solar-PV as a driver for RO plants is attributed to four factors [81]. Firstly, the modularity of PV systems offers implementation with RO on different scales and their capacity can be increased after initial installation. Secondly, PVs require low maintenance and offer a long lifetime of 20 years [51]. Thirdly, areas that demand high water consumption usually have high solar radiation intensity which makes PVs well matched to the application. Fourthly, the somewhat predictable bell-shaped diurnal solar irradiance curve, compared to the random variation of wind power, makes it easier to schedule the plant operation during daytime and use water storage instead of energy storage to meet night-time demand. Table 2.2 presents a summary of previous studies discussing solar-PV powered RO plants [11]. With the decrease in PV costs, PV-RO systems have become more feasible, depending on solar resource availability, RO system demand, water characteristics and local government policies [82]. Hence, water production cost from PV-RO systems is highly site-dependent. Numerous studies [50, 51, 82-85] discussed the feasibility of PV-RO systems and suggested different configurations that may offer high feasibility. Mohamed et al. [50] compared the performance of a RO plant using batteries for energy storage against another plant that is directly coupled to a PV array. The directly coupled plant offered less complexity since there is no need for batteries or a charge controller. Another approach to ensure a full-day operation is to assist the PV system with a conventional energy source such as a Diesel engine. This scheme was tested by Helal et al. [51] within a comprehensive techno-economic analysis for different configurations of autonomous PV-RO plants. The RO plant was alternatively driven fully by a Diesel engine, directly coupled to a PV array, or operated by both the PV array and Diesel engine. The directly coupled PV-RO plant produced water at the most competitive price. In general, PV-RO systems were found to be economically more feasible than Diesel-powered systems provided there is sufficient solar resource [82, 84, 85]. The economic feasibility of a RO plant operated by an organic-solar Rankine cycle was compared to that of a directly coupled PV-RO system by Manolakos et al. [83]. Water production cost for the PV-RO system was significantly lower than that of the organic-solar Rankine-RO system at 7.77 €/m³ compared to 12.53 €/m³.

2.1.1.3 Enhancing the PV array performance

PV array performance holds an important role in the PV-RO integration, as maximising the PV power output would lead to higher freshwater production. In previous studies, several approaches for improving the PV system performance were considered. For example, the collection of solar irradiance during daytime can be maximised by using solar trackers [86]. Richards and Schäfer suggested using single- or dual-axis trackers, which could increase water production by nearly 30% [87]. Similarly, Thomson and Infield [88] used a Matlab-Simulink® model to assess whether a single or dual-axis tracker should be used for their PV-RO system. The single- and dual-axis trackers increased annual water production, by 33% and 36% respectively, when used together with a Maximum Power Point Tracking (MPPT) algorithm [23, 88-91]. MPPT adjusts the RO plant load so that the voltage across the PV cell is equivalent to the voltage required to achieve the maximum power at the corresponding solar irradiance and cell temperature [91]. A drawback for PV-RO, which is especially marked in arid regions, is the noticeable degradation of power output due to dust and sand accumulation [92]. Scattering by dust in the atmosphere and dust accumulation over the panels can lead to an increase in panel temperature, attenuation of incoming solar radiation and may lead to physical damage [93]. Several PV cleaning techniques were suggested in the literature that includes mechanical methods, PV coating or electrostatic methods [94, 95].

Ambient temperature has a significant effect on the PV panel performance, as their conversion efficiency decreases with increasing PV temperature [90, 93]. In certain studies [90, 96], the RO system feedwater was circulated in heat exchangers to cool the PV array and increase the feedwater temperature before entering the RO system. This modification was based on the fact that solar panels' open circuit voltage and output power increase at lower temperatures, whereas RO membranes allow more permeate at higher feed temperatures [90]. A similar procedure was used by Kelley and Dubowsky [90] to improve PV-RO system productivity. However, concentration mirrors were installed to increase the solar irradiance collected by the solar panel, which alongside the solar panel cooling and feedwater heating, improved water production by 57% (see Fig. 2.4). The concentrating mirrors could not have been used without such cooling, as the panels would have overheated and their efficiency degraded [90].

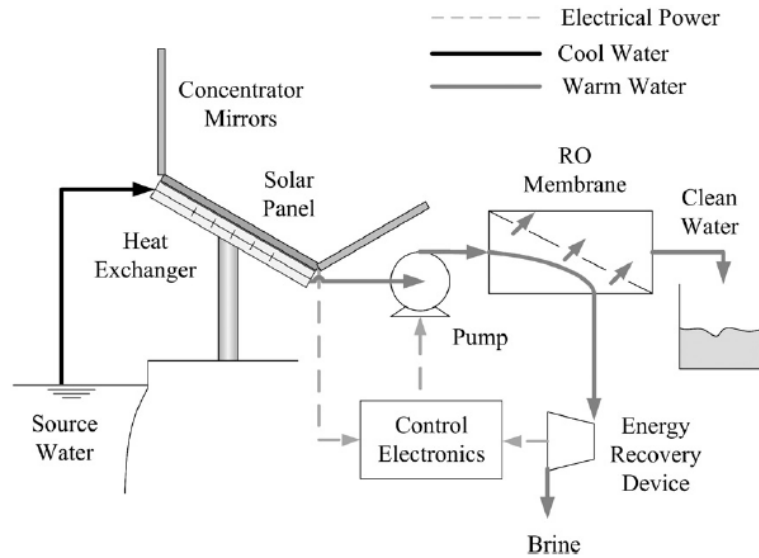


Fig. 2.4. PV-RO system with panel cooling and concentrator mirrors (reused with permission from [90]).

2.1.1.4 Variable operation of PV-RO plants

For PV-RO systems to transition to large-scale applications, a reliable operation strategy and control system is needed to allow efficient energy use despite variation in solar power. As with wind powered-RO, both modular and variable-speed operation have been used. Thomson and Infield [88] presented a variable operation PV-RO system, shown in Fig. 2.5, that can adapt to a PV array power output without using batteries. Variable-speed operation was enabled by a controller that delivers two functions. Initially, it applied MPPT, which controls the current drawn from the PV array to maximize the PV array power output at varying solar irradiance and array temperature. Then, it executed a control algorithm for two variable-speed feed pumps to operate the plant at optimum recovery ratio and minimum SEC. In another study, Ntavou et al. [97] analysed the performance of a RO plant that consists of three identical sub-units, as presented in Fig. 2.6. The RO sub-units were operated using a combination of variable-speed and modular operation. They were operated by a variable power input using a frequency inverter to control the HPPs. In addition, the number of operating units was varied depending on the available PV array power. This strategy would produce, in some cases, 4 m³/day more than a conventional system. However, a wider operation range could have been achieved by using an isobaric ERD. The ERD used was an axial piston motor coupled to an axial piston HPP that did not allow independent variation in feed pressure and flowrate, due to the linear relationship between flowrate and pump speed

for positive displacement machines. In addition, both the pump and motor had fixed volumetric displacement. These factors resulted in a linear relation between feed pressure and flowrate under varying pump speed. Therefore, the recovery ratio was fixed, which is not ideal in a variable-speed system.

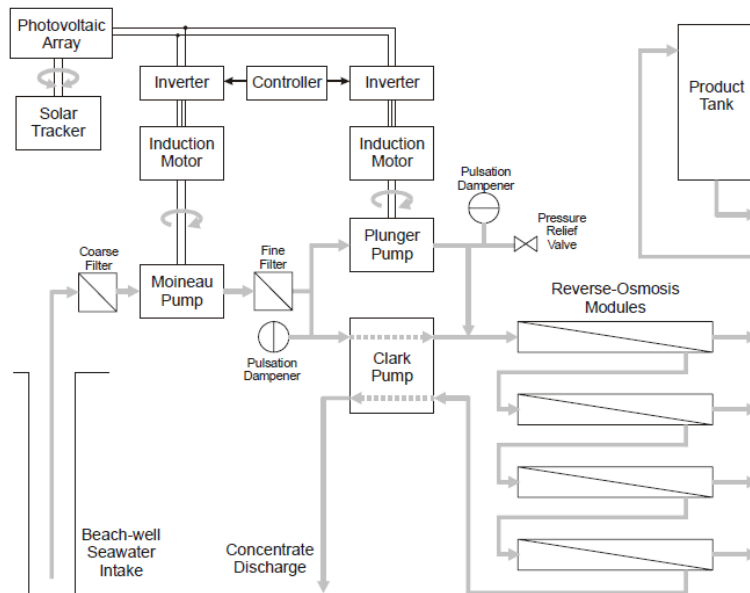


Fig. 2.5. Layout of the plant presented by Thomson and Infield (reused with permission from [88]).

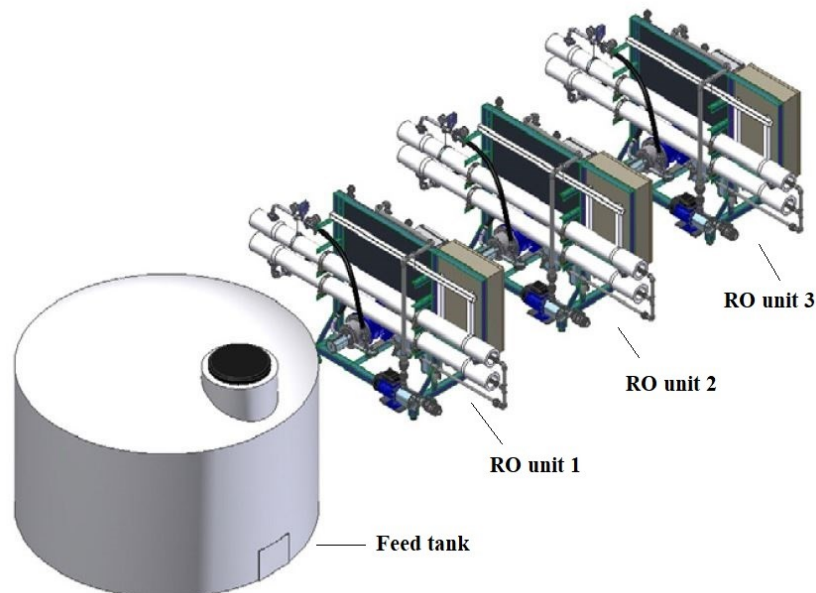


Fig. 2.6. Configuration of the RO plant used by Ntavou et al. (reused with permission from [97]).

The system included a feedwater tank and three sub-units.

Table 2.2. Summary of previous literature discussing PV-RO desalination.

Author(s)	Year	Location	Study	Energy storage	PV power (kW)	Production capacity (m ³ /day)	S.E.C (kWh/m ³)	Feed salinity (mg/L)	Production cost	Energy recovery	Plant description
Thomson and Infield [88]	2002	Massawa, Eritrea	Theo.	No	2.4	3	3.5	40,000	2 £/m ³	Clark pump	Four RO membranes in series
Mohamed et al. [50]	2007	Athens	Exp.	No	0.85	0.35	4.6	32,738	7.8 €/m ³	Clark pump	Two RO membranes in series.
Helal et al. [51]	2008	United Arab Emirates	Theo.	No	17.9	20	7.33	45,000	7.34 \$/m ³	yes	Two-stage system with booster pump between stages. Two RO membranes in series per stage.
Manolakos et al. [83]	2008	Thirasia island, Greece	Exp.	No	0.846	2.4	3.8 - 6	22,000	7.77 €/m ³	Clark pump	Two RO membranes in series.
Bilton et al. [82]	2011	USA	Exp.	Batteries to power the control electronics	0.23	0.3	4 – 2.5	35,000	4.7 – 6.62 \$/m ³	Clark pump	One RO membrane.
Soric et al. [98]	2012	Marseille, South of France	Exp.	No	0.5	0.75 – 1.02	-	25,000	-	Clark pump	Two RO membranes in series.
Clarke et al. [99]	2012	Australia	Theo.	Compare with/without batteries	0.7	With Battery: 0.054 Without battery: 0.047	-	Seawater	-	No	One RO membrane (Commercial unit).
Kelley and Dubowsky [90]	2013	USA	Exp.	No	0.23	0.3 – 0.45	-	Seawater	-	Dual-piston pressure exchanger	One RO membrane.

Kumarasamy et al. [91]	2015	India	Theo.	No	0.667	0.7	-	35,000	-	No	One RO membrane.
Ntavou et al. [97]	2016	Greece Spain UAE	Exp.	No	10 - 20	Single unit 12 – 16.8 3 identical units	5.2 – 5.8	37,500	-	Axial piston motor	Three identical units connected in parallel. Four RO membranes in series each.
Salama and Abdalla [100]	2019	Gaza strip	Theo.	No	10,000	57,600	3 – 3.5	38,400	0.56 \$/m ³	Pressure exchanger	Single-stage plant with 670 pressure vessels. Each vessel includes 8 RO elements.
Ghafoor et al. [101]	2020	Pakistan	Exp.	No	2	12	-	1720 - 1760	720 PKR/m ³	No	Two RO pressure vessels in parallel.
Saleem et al. [102]	2021	Lahore	Theo.	Battery	2.5	8	0.5 - 1	1495	-	No	Two stages each with three pressure vessels. Each vessel includes two RO elements.
		Hasil Pur			4.1			2190			Two stages each with three pressure vessels. Each vessel includes two RO elements.
		Faisalabad			11			7638			Two stages with a single pressure vessel that includes three RO elements.

2.2.3 Hybrid wind-PV RO desalination

Hybrid renewable energy systems can improve the feasibility and stability of RE-RO by exploiting the strength of one RES to overcome the weaknesses of others. For instance, wind turbines can be used with solar-PV to extend energy availability to include night-time and overcast days, providing more consistent output [45]. This will help improve system reliability and economic feasibility, as it will provide better use of capital invested in the RO plant [16]. Table 2.3 summarises previous studies of hybrid RE-powered RO plants, giving an overview of the current status and trends [11].

The selection and sizing of the hybrid RES components are not straightforward and have a significant effect on economic feasibility. Oversizing its components to overcome the intermittent power supply can lead to a wasteful increase in capital cost [51]. Hybrid RES and RO plant sizing should be based on cost optimisation as the investment cost of RESs are still high compared to conventional grid power systems [50, 103]. Several studies presented sizing models for hybrid RESs that power RO plants [104-108]. Hossam-Eldin [106] developed an optimisation procedure to optimally select and size the hybrid RES for operating a RO plant. The optimisation considered the capital cost and the excess energy generated by the hybrid RES. Similarly, Weiner et al. [107] developed a simulation code that helps in component selection and sizing of the hybrid wind-PV system and RO plant. Also, a control algorithm was developed to determine if wind and solar energy are sufficient to supply the plant load or additional energy is needed from the batteries and Diesel generator. Mokheimer et al. [108] studied the optimum component sizing for a hybrid RES-RO plant while considering the RO system performance, capital and operation costs. The optimised system achieved water production costs less than the range mentioned in literature.

The majority of studies discussing hybrid RE-RO systems focused on the theoretical aspects of sizing and performance without discussing practical operation [106, 108-110]. For, this reason the RO plant was often very simplified. In some cases, the plant was only represented by its average SEC and production capacity [104, 105, 111]. Additionally, as presented in Table 2.3, the majority of systems included energy storage to ensure the RO plant is operating at constant conditions. For example, Smaoui and Krichen [112] presented a control and energy management algorithm for a RO plant powered by a hybrid RES that includes wind turbines, PVs, a fuel cell and an electrolyser for providing hydrogen energy storage. The control algorithm optimised plant operation by considering the energy circulation among

all components. Similarly, Spyrou and Anagnostopoulos [109] operated a RO plant in Greece by a hybrid RES that included a pumped storage system. The plant, presented in Fig. 2.7, was found to be economically feasible despite having high-energy rejection.

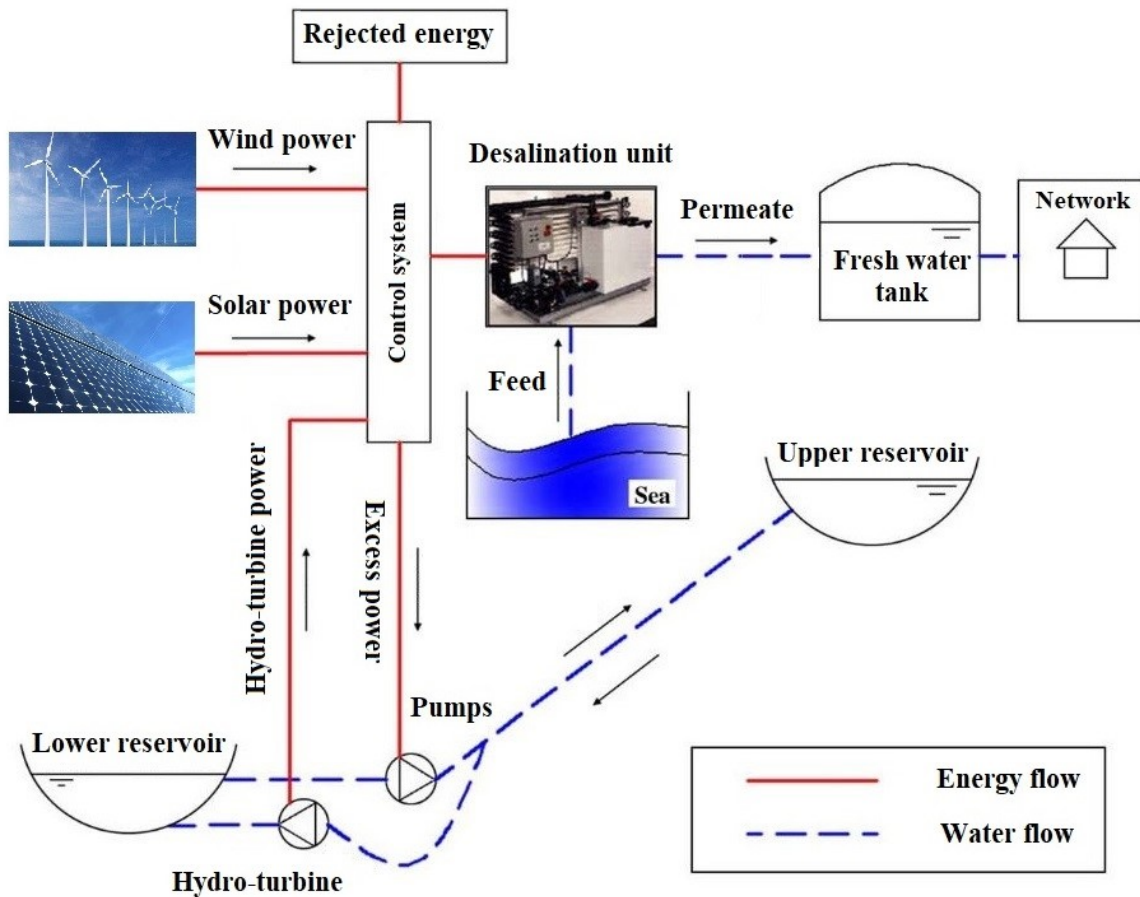


Fig. 2.7. Configuration of RO plant presented by Spyrou and Anagnostopoulos (reused with permission from [109]).

Table 2.3. Summary of previous literature discussing hybrid Wind-PV RO desalination.

Author(s)	Year	Location	Study	Backup system	Hybrid system	Production capacity (m ³ /day)	S.E.C (kWh/m ³)	Feed salinity (mg/L)	Production cost	Energy recovery	Plant description
Weiner et al. [107]	2001	Israel	Exp.	Battery + DE	WT PV	3	-	3500 - 5000	-	None	Two RO membranes in series.
Kershman et al. [110]	2002	Libya	Theo.	Grid-connected	WT PV Grid	300	5.6	Seawater	2.3 €/m ³	None	Two RO trains.
Spyrou and Anagnostopoulos [109]	2010	Greece	Theo.	Pumped storage	WT PV Hydro.	3840 Based on hourly average	3	Seawater	2.53 €/m ³	-	-
Hossam-Eldin et al. [106]	2012	Egypt	Theo.	Battery	WT DG	150	7.3	33,000	1.6 \$/m ³	None	Four pressure vessels with Three RO membranes each.
					WT PV DG	300	4.6	34,000	1.25 \$/m ³	Yes	Five pressure vessels with four RO membranes each.
Mokheimer et al. [108]	2013	Saudi Arabia	Theo.	Battery	WT PV	5	8 - 20	-	3.693 – 3.812 \$/m ³	-	-
Maleki et al. [105]	2016	Iran	Theo.	Battery	WT PV	10	4	Seawater	-	Yes	-
Li et al. [113]	2017	UK	Theo.	Battery	WT PV	240 - 2880	3	Seawater	-	-	-
Gökçek [114]	2018	Turkey	Theo.	Battery	WT PV DG	24	4.38	37,864.4	2.2	None	Single pressure vessel with six RO elements in series.

Maleki [115]	2018	Iran	Theo.	Battery + Hydrogen energy storage	WT PV	10	4	Seawater	-	Yes	-
Khiari et al. [116]	2019	Tunisia	Exp.	None	WT PV	7.2	-	4500	-	None	A single RO element.
Elmaadawy et al. [117]	2020	Egypt	Theo.	Battery	WT PV DG	1500	2.928	43,087	-	Pressure exchanger	A single-stage RO system with energy recovery.
Ibrahim et al. [118]	2020	Egypt	Theo.	Battery	WT PV DG	24	4.38	37,864.4	1.10 \$/m ³	None	Single pressure vessel with six RO elements in series.

- **Acronyms:** DG: Diesel generator - Grid: a connection to the local grid - Hydro.: Hydropower - PV: Photovoltaic - WT: wind turbine.

2.3 Technical challenges and potential solutions for RE driven RO plants

The above studies revealed numerous challenges regarding RE-RO plants, especially for the main components, operational strategy and control system design. This section analyses these aspects in detail, starting with the critical components namely membranes and energy recovery devices [11].

2.3.1 Membranes performance and lifetime

RO membranes are the heart of the desalination process. These semi-permeable membranes allow fresh water but not salts to pass, creating a concentrate (brine) and a permeate stream. Their operation depends on delivering feedwater at a pressure above the osmotic pressure for the separation process to occur. In conventional RO plants, the HPP supplies feedwater at constant pressure and flowrate. However, for variable operation, feedwater pressure and flowrate will vary according to the available RE power.

Manufacturers normally guarantee a lifetime of 5 years, if the RO membranes are operating under recommended steady conditions [64]. According to Cabrera et al. [119], continual start-ups, shutdowns, flow variation and pressure fluctuations present unusual operating conditions for the RO membranes, causing mechanical fatigue with a negative impact on the membrane lifetime and performance. Also, membrane compaction, which is the plastic deformation that leads to membrane deterioration, is expected to accelerate under variable operating conditions [120]. Accordingly, water production cost could be affected by variable operation, as it is influenced by the membrane replacements costs [64]. Hence, the economic viability of variable operation is dependent on the extent to which it affects membrane performance and lifetime.

Several studies discussed membrane performance and lifetime in plants operated with variable RE power [61, 62, 64], as summarised in Table 2.4. The study of Carta et al. [64] using 8 switchable RO units (Fig. 2.8) developed an operational strategy to examine the effect of modular operation on component lifetime. Units were connected and disconnected in reverse order, which meant that some units underwent fewer start-ups and shutdowns than others. In contrast to the claims presented by Cabrera et al. [119], Carta et al. [64] concluded that no physical deterioration was observed in the main components. Similarly, Pestana et al. [61] and Latorre et al. [62] operated a RO plant for 7000 and 6000 hours respectively, at variable flow and pressure under variable-speed operation. In both studies, no membrane

deterioration was noted. However, these test periods were insufficient to give a definitive conclusion when compared to the average 5-year (43,800 hr) lifetime of a RO membrane [64].

Performance improvements were reported in several studies [121-124] when testing the membrane performance against fluid instabilities and pulsating trans-membrane pressure. For instance, Al-Bastaki and Abbas [124] reported a maximum permeate flux improvement of 13% when testing against square wave pressure pulses at an average pressure of 50 bars. The reason for this improvement is the increased turbulence caused by the fluctuating pressure and flow instabilities. This turbulence improved the diffusion through the membrane and decreased the effect of concentration polarisation which led to increased permeate flux and quality [68]. In summary, there are mixed views about the effects of variable operation on membranes, with some authors reporting shortened lifetimes and others highlighting improvements in performance.

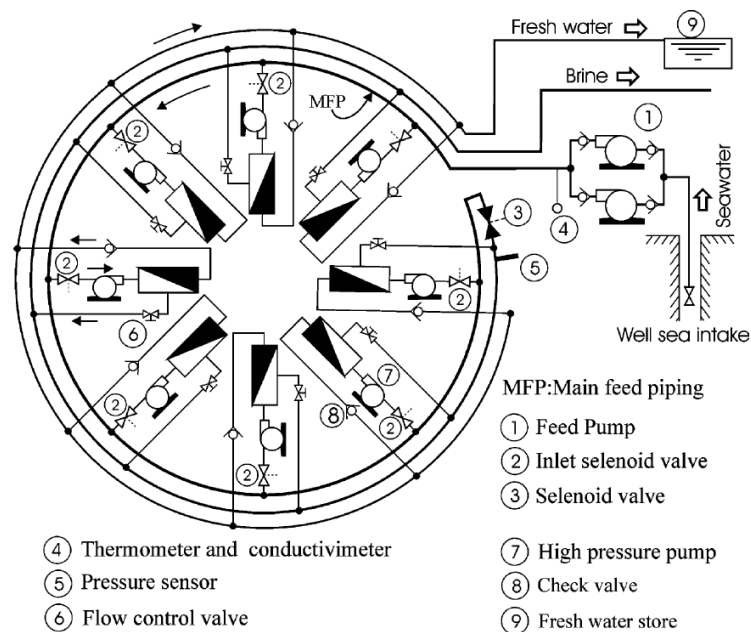


Fig. 2.8. Schematic diagram of the test rig used by Carta et al. (reused with permission from [64]).

Table 2.4. Studies analysing membrane deterioration in variable operation.

Study	Methodology	Outcome
Carta et al. [64]	Modules had a different number of start-ups and shutdowns.	No membrane deterioration was noted.
Pestana et al. [61] Latorre et al. [62]	Operated the plant for 7000 and 6000 hrs. at variable conditions.	
Rodger et al. [121] Winzler et al. [122] Al-Bastaki and Abbas [123, 124]	Effect of fluid instabilities and pulsating trans-membrane pressure.	Improvement in performance was reported.

2.3.2 Energy recovery devices

A significant amount of the pumping energy still resides in the brine stream as it exits the membrane at high pressure [125]. This energy may be recovered by a hydraulic ERD that transfers the brine energy to the feed stream, thus reducing the SEC by decreasing the HPP power. ERDs can help decrease the power consumption by as much as 60% when compared to systems operating without energy recovery [126]. Their introduction in RO desalination allowed for a SEC below 5 kWh/m³ [125, 127]. ERDs are generally classified as either centrifugal or isobaric devices. Further sub-classification of ERDs is presented in Fig. 2.9 [126]. In the early eighties, when ERDs were first introduced, centrifugal machines like the Pelton wheel or Turbocharger were mostly used, requiring system configurations as shown in Fig. 2.10 (a, b) respectively [125]. Centrifugal ERDs are characterised by their suitability for high flowrates, limited range of capacity and maximum energy transfer efficiency of around 82% [126]. On the other hand, isobaric ERDs are gaining popularity because of their higher energy transfer efficiency of nearly 97%, low power requirement, decoupled operation from the HPP and smaller size compared to centrifugal devices [126]. Many commercial RO plants that used centrifugal devices have now been retrofitted with isobaric ERDs, providing increased plant production capacity for the same power consumption [128, 129]. Two common types of isobaric ERDs are the Dual Work Exchange Energy Recovery DWEER™ and the Pressure Exchanger PX® [130-132]. Both devices are presented in Fig. 2.10 (c, d)

respectively. For commercial RO plants, the sizing and selection of ERDs are based on the plant's optimum operating point, to ensure that the ERD will operate at its optimum efficiency during normal operation [133]. The use of RE to drive RO desalination introduces new challenges regarding the variable operation of ERDs.

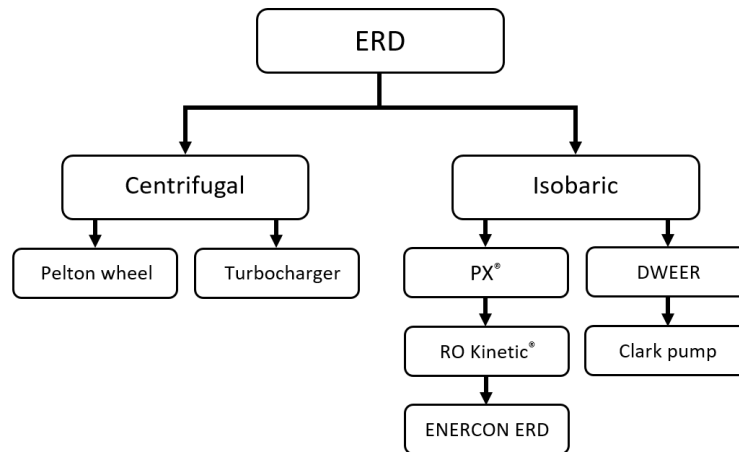


Fig. 2.9. Classification of energy recovery devices discussed in this article.

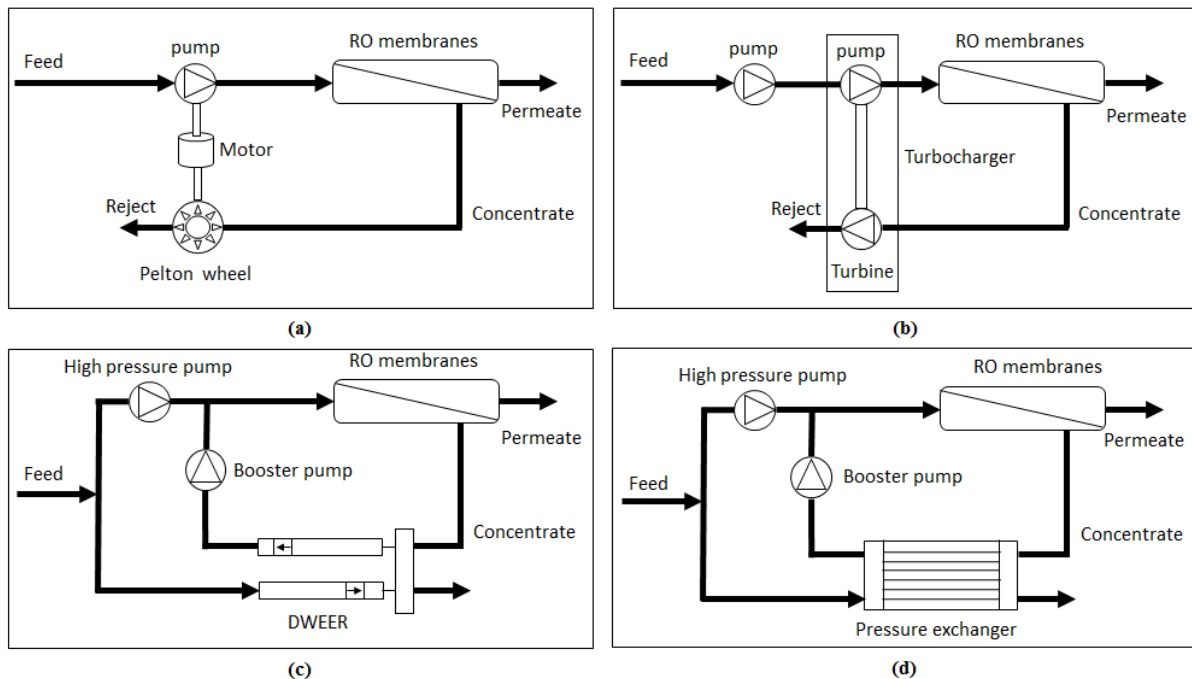


Fig. 2.10. RO plant configuration for using a) Pelton wheel, b) Turbocharger, c) DWEER and d) Pressure exchanger.

2.3.2.1 *ERD performance in variable operation*

In case of variable operation, the ERD should offer the flexibility to operate with acceptable efficiency at different flowrates, to allow for independent variation in membrane flux and recovery ratio [40]. Centrifugal devices cannot deliver this performance because their efficiency varies with changing flux and recovery ratio [40]. On the other hand, isobaric devices can operate at nearly constant efficiency with a varying flowrate which makes them more suitable for variable operation [126, 134]. Additionally, the decoupled operation of isobaric ERD from the HPP offers a great advantage for variable operation, as it allows the independent variation of membrane flux and recovery [134]. Several studies introduced isobaric ERDs that are suitable for variable operation. Peñate et al. [134] described the theory of operation and operational data of a patented isobaric ERD called RO Kinetic®, presented in Fig. 2.11 (a). The RO Kinetic® is designed in the form of a closed loop, in which, the pressure is exchanged between the brine and feedwater. The process of distributing the input feedwater and output brine is done by servo-controlled valves. The ERD delivered a robust, low maintenance operation and achieved a SEC of slightly higher than 2.2 kWh/m³. The RO Kinetic® was recommended for RO plants operating with variable conditions [40]. In another study, Paulsen and Hensel [133] presented an ERD developed by ENERCON (Aurich, Germany) specifically for RO plants operated by wind energy. The ERD, displayed in Fig. 2.11 (b), only uses a single low-pressure pump to drive the desalination process, without the need for a HPP. The ERD is a “piston-type accumulator” that operates within a range of 12.5 – 100% of plant capacity while maintaining a SEC between 2 – 2.8 kWh/m³. A follow-up study was presented in [135]. For small-scale standalone applications, the Clark pump was used by several studies, as it delivers high efficiency at low flowrates [50, 76, 82, 88, 136]. The Clark pump, manufactured by Spectra Watermakers Inc. (California, United States) [137], is described as a “positive displacement reciprocating pressure intensifier” ERD. It is referred to as a pressure intensifier because it has two pistons that allow energy from the feed to be added to the energy of the concentrate such that the output pressure is higher than that of the concentrate [138].

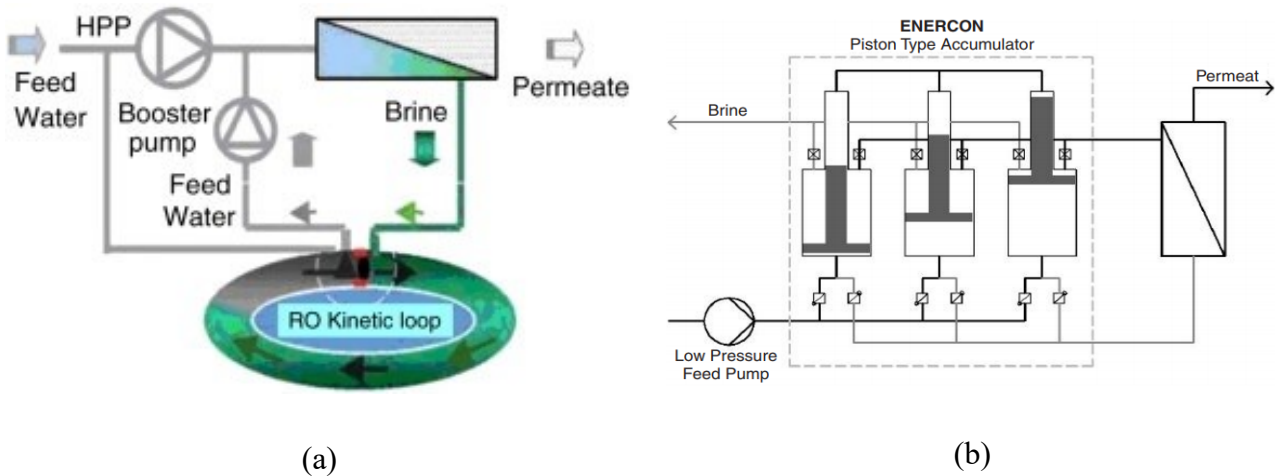


Fig. 2.11. a) RO Kinetic[®] working principle [134] and b) ENERCON piston-type accumulator [133] (reused with permission).

2.3.2.2 *Technical challenges for isobaric devices*

The main disadvantage of some isobaric ERDs is mixing between the brine and feed streams [126]. Mixing increases feed salinity thus increasing feedwater osmotic pressure and required pumping power [139]. The increase in feed salinity can range between 3 – 5%, requiring additional pressure of about 2 bar [140]. Stover [126] presented equations to describe the salinity increase due to mixing in a rotary isobaric pressure exchanger. Similarly, leakage flow occurs between the high-pressure and low-pressure sides of the brine stream. This leakage is estimated at 1 – 2.5 % of the brine flow [140]. Mixing and leakage flows depend on system pressure, temperature, feed and brine flowrate and device characteristics [126, 140]. Variable operation can lead to an increase in brine mixing and leakage due to increased fluid instabilities, resulting from changes in flow and pressure. This is especially true for the pressure exchanger (PX[®]), as there is no physical barrier between the brine and feed streams. A study was performed by Xu et al. [141] to analyse the effect of rotor speed, brine and feed flow velocities on the mixing rate for a rotary pressure exchanger. The analysis was performed using a computational fluid dynamics simulation, presented in Fig. 2.12, and an experimental model. The simulation showed clear signs of mixing.

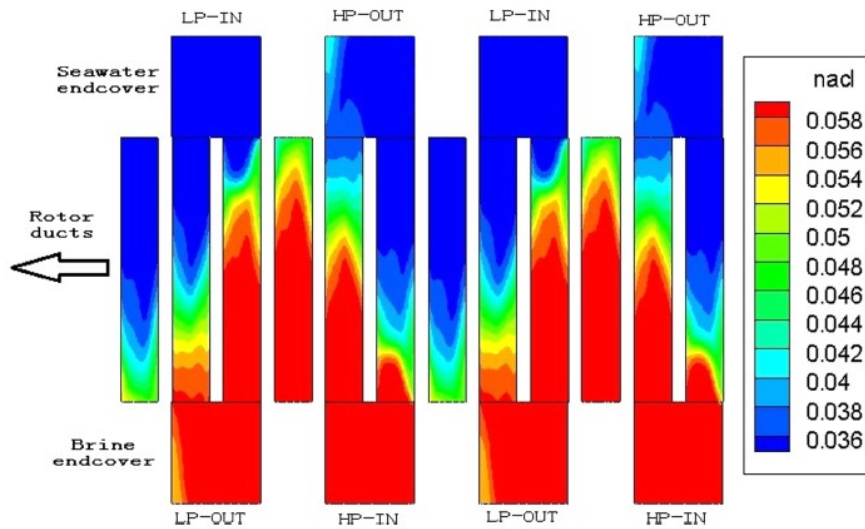


Fig. 2.12. Two-dimensional salinity contour of the central cylindrical surface of the ERD (reused with permission from [141]).

2.3.3 Strategies for variable operation of RO system

As mentioned earlier, RO plants are designed to operate at constant flow, pressure and power levels and with all modules working continuously. Specific strategies are required for the RO plant to enable variable operation. This section will review different strategies to adapt large-scale RO plants to modular and variable-speed operation [11].

2.3.3.1 *Start-up and shut down under modular operation*

For the purpose of routine maintenance in standard (non-RE) plants, manufacturers have defined operating procedures for start-up, shutdown and steady operation. With RE, modular operation will demand much more frequent start-up/shutdown of RO trains to modulate the plant according to the available power. This section will discuss the standard membrane flushing procedures during the start-up/shutdown cycle, as recommended by membrane manufacturers to deliver their claimed water quality and output and to prevent membrane fouling and damage under sudden mechanical loading [142]. The implications for variable operation are then discussed.

According to the DuPont Filmtec™ (Delaware, United States) Technical Manual [142], for a typical start-up, the system should be flushed with low-pressure clean water, between 2 to 4 bar, at a low flowrate, to purge air out of the RO elements and the pressure vessels. The concentrate and permeate should be discarded during this procedure [142]. After flushing, the feed pressure is increased gradually to reach the operation set point. Feed pressure ramping

should be limited to 0.7 and 0.5 bar per second for FILMTEC™ and TORAY (Tokyo, Japan) modules respectively, to complete a soft start [142, 143]. Otherwise, the element housing might be damaged by shock force acting in the radial or flow direction [142]. Once the set point is reached, it is suggested to disregard the permeate until it reaches the desired quality [143].

During a typical shutdown, it is recommended to flush the membrane with fresh water to prevent scaling, salt deposition and (forward) osmosis from occurring across the membrane, which can cause the membrane to swell and rupture [120, 142]. Flushing is done using low-pressure water, approximately 3 bar, at a high flowrate, to remove the brine completely from the pressure vessel [142]. Permeate water or high-quality feedwater can be used for flushing [138, 142]. This procedure should continue until the concentrate conductivity matches the feed conductivity. TORAY recommends flushing the membranes every 12 hours for shutdowns between 1 to 4 days and adding a preservative solution for shutdowns exceeding 4 days [143]. Modular operation can involve several start-ups and shutdowns of RO trains in a single day depending on RE power variation [33]. The unpredictability of RE variation can be problematic since to flush the membranes prior to shutting down, there must be enough energy to operate the flushing pumps and enough permeate water to flush the membranes [66, 138]. In terms of energy requirement, operating the flushing pumps for PV-RO systems can be scheduled at the end of peak radiation hours during the day. However, it is more challenging for wind-RO plants, as wind speed changes randomly during the day. An efficient approach would be to store water in an elevated tank for gravity-driven flushing [33]. Moderate elevation is sufficient since the pressure requirement is low. Flushing water can be obtained by storing the first batch of permeate for this purpose [66]. Feedwater is sometimes used for flushing if it is of sufficient quality [66, 138, 143].

2.3.3.2 *Variable speed operation and safe operating window*

Modular operation by switching units on and off may not be enough to accommodate the frequency and pattern of RES variation. Variable-speed operation can be used to achieve a faster and finer response. To operate a RO plant with variable speed, firstly, a safe operation window should be defined to set boundaries for the operation parameters. Secondly, an operation strategy is needed to change the operation parameter within the boundaries of the safe operation window.

The operational window defines the acceptable parameter variation range for safely operating the RO plant, providing an important guideline in control system design. The operational window is set based on operation parameters subject to hydraulic limitations such as the feed pressure and flowrate, permeate and concentrate flowrate. In several studies [76, 78, 79], the operational window was based on five parameters: 1) maximum feed pressure that the membrane can withstand based on its mechanical resistance; 2) maximum allowed feed/brine flow that is based on the membrane mechanical loading; 3) maximum permeate flow per element and the maximum recovery per element were constrained as they directly affect the concentration polarisation; 4) minimum concentrate flow to avoid precipitation and membrane fouling, as the concentrate flow is responsible for clearing the salt out of the membranes; and 5) maximum product concentration based on the recommendations of the EPA and WHO [79]. Table 2.5 includes the hydraulic limitation for a common proprietary membrane.

Table 2.5. Hydraulic limitations for 8-inch (0.203 m) /37 m² DOW-FILMTEC SW membranes with generic conventional pretreatment [142].

Maximum recovery per element	13 %
Maximum permeate flow per element	1.4 m ³ /h
Minimum concentrate flow	3.4 m ³ /h
Maximum feed/brine flowrate	14 m ³ /h

The operational limits are determined by simulating the membrane hydraulic performance while holding specific parameters constant. After defining the plant operational window, an operational strategy is used to vary the feed flow and feed pressure, according to the set boundaries. Miranda and Infield [76] established an operational window for a variable operating small-scale RO plant operating by a 2.3 kW wind turbine. Afterwards, a control strategy was developed to operate the system within the operational window. Two positive displacement pumps enabled the independent control of feed pressure and flow, to allow operation at any point within the operational window. Likewise, in [78, 79], an operational window was defined using Reverse Osmosis System Analysis (ROSA) software to vary feed flowrate and operating pressure while holding specific membrane parameters constants. The operational window set by Pohl et al. [79], for four series SW30-HR400i DOW Filmtec™ elements using feedwater at 35,646 mg/l, is displayed in Fig. 2.13.

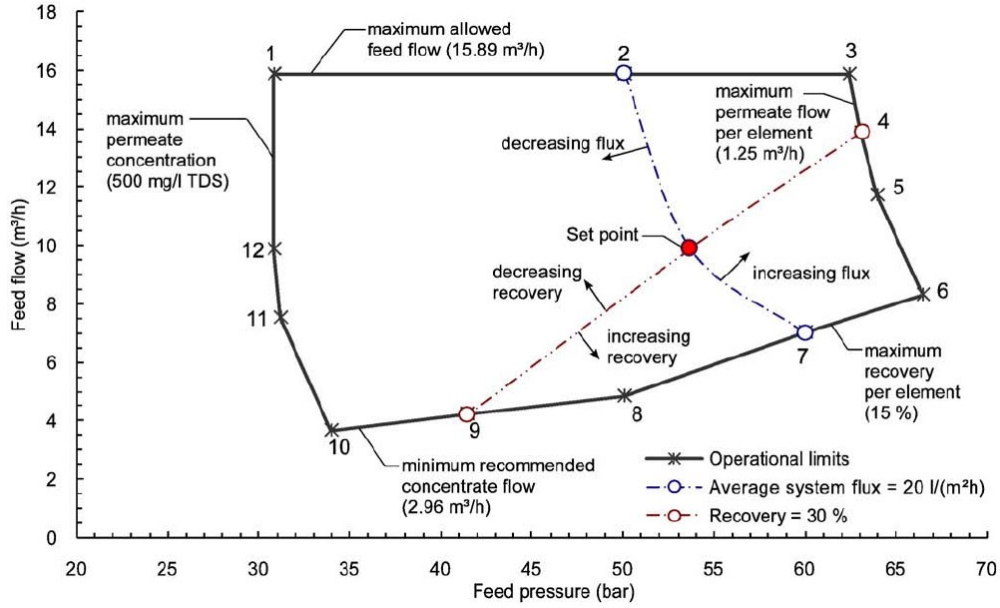


Fig. 2.13. Operational window presented by Pohl et al. (reused with permission from [79]).

Variable-speed operation requires defining an operation strategy for the plant to respond to changes in available power while remaining within the safe operation window. The operation strategy should result in feed pressure and flowrate combinations that achieve maximum water production and desired water quality while operating at the lowest SEC. Operating at the lowest SEC ensures full utilisation of available power and maximum water production [138]. The relation between feed pressure, feed and permeate flowrate, permeate recovery and SEC can be described as follows [42]:

$$Q_p = A_w * A_m * (\Delta P - \Delta \pi) \quad (2.1)$$

$$Q_s = B_s * A_m * \Delta C \quad (2.2)$$

$$Recovery = \frac{Q_p}{Q_f} \quad (2.3)$$

$$SEC = \frac{Power}{Q_p} \quad (2.4)$$

where Q_f , Q_p and Q_s are the feed flowrate, permeate flowrate and salt transport, respectively, A_w is the membrane permeability, B_s is the salt transfer coefficient and A_m is the membrane surface area. $(\Delta P - \Delta \pi)$ is the net driving pressure and ΔC is the concentration difference across the membrane.

Thomson [138] used two pumps to vary the feed pressure and flowrate individually to operate a RO plant at the lowest SEC during power fluctuation from a PV array. Pohl et al. [79] compared four different operation strategies to operate a simple RO plant connected to a wind energy source. The operation strategies relied on controlling the feed pressure, feed flowrate and permeate recovery, to operate the plant at either constant feed pressure, constant permeate recovery, constant feed flow or constant concentrate flow. Maintaining constant permeate recovery by changing feed pressure and flowrate delivered the best performance regarding SEC, permeate quality and wider load range. A study by Kumarasamy et al. [91] compared varying either the pressure or the flowrate while keeping other parameters constant. While maintaining constant pressure and varying flowrate, the recovery ratio could increase and cause increased salt diffusion through the membrane. Alternatively, operating at a constant flowrate and variable pressure increased production capacity by 5%; however, this introduced a risk of the pressure decreasing below the osmotic pressure. In general, when selecting any operation strategy, the safe operational window must be observed to ensure that there is no conflict between achieving maximum production and operating within safe limits.

Meeting the daily water demand and ensuring a suitable product water concentration are important objectives in formulating the operation strategy. Several studies suggested permeate storage to satisfy a stable water demand and allow monitoring of product water quality [51, 88, 91]. Kumarasamy et al. [91] compared operating a directly-coupled PV-RO system with and without permeate storage. For the system without permeate storage, the permeate water should meet the specified maximum concentration of 500 mg/L at all times; however, for the system using permeate storage, permeate concentration could increase above the limit temporarily as long as the concentration inside the storage tank remains below 500 mg/l. Permeate production increased significantly by 28% when using permeate storage due to a wider range of acceptable permeate concentrations. In general, permeate storage is beneficial for providing a balance between water supply and demand [51, 88, 91].

2.3.4 Control system performance

Process control is an integral part of the RO plant operation and productivity. The control strategy for grid-connected RO plants aims to fulfil a daily production demand under constant operating conditions and is relatively straightforward when compared to variably operating RO plants, which should maximize the RES power output while managing the RO plant load against energy fluctuation [40].

The control procedure for large-scale plants can be simplified into three states: start-up, shutdown, and maintenance of setpoint parameters against any disturbances. Disturbance variables – such as changes in feed temperature or concentration, reduction in permeate flow, increase in permeate concentration, increase in fouling resistance and changes in permeate demand – can interfere with the plant operation. Sensors throughout the plant monitor these disturbances and send a signal to the controller. A control signal is generated to change the manipulated variables according to the difference between the measured and the set values. The control action guides the plant towards the desired reference or set point. Systems that include supervisory control can perform an optimisation procedure to reach certain goals such as maximising daily output and water quality [144].

2.3.4.1 *Control actions for variably-operating RO plants*

The control system for variably-operating plants is a Multiple-Input Multiple-Output (MIMO) system that can handle different manipulated variables such as feed pressure, feed flowrate and recovery ratio in order to control target variables such as permeate flowrate and permeate concentration. The control is based on the available power from the discontinuous RES and water demand, in a manner that ensures proper plant operation and water quality [35, 128]. Additionally, the controller should provide fast response, high stability and minimum disturbances to adapt the RO plant against the discontinuous energy source [128].

Advanced control systems are recommended for variable operating RO plants for their ability to provide adequate control performance against the plant time-varying dynamic behaviour and RES fluctuation [33, 82]. Unfortunately, the number of studies discussing specifically RED plants control systems are low [145]. The following will introduce control systems used for RO plants control in general, which can be used for RO plants operated by RES.

2.3.4.2 *Advanced control techniques for RO plants*

PID control and MPC have been frequently described in the literature for controlling RO plants [146, 147]. A PID controller, presented in Fig. 2.14, is a common and traditional approach to process control as a result of its simplicity and effectiveness [147]. On the other hand, MPC, presented in Fig. 2.15, is an advanced optimisation-based control technique that is applicable to multivariable control problems, specifically for MIMO systems [148]. It relies on currently measured outputs from the process and future predicted outputs supplied

by a dynamic model to calculate the required change in the input variable, so the measured output reaches the set point in an optimal manner [149].

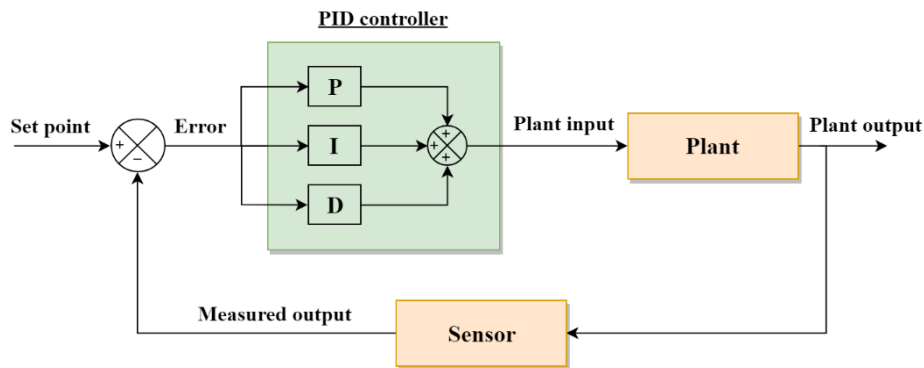


Fig. 2.14. Proportional-Integral-Differential controller block diagram [11].

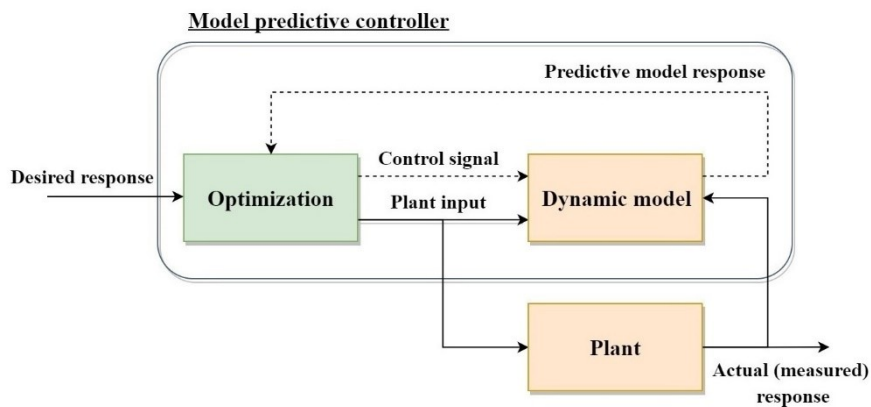


Fig. 2.15. Model predictive controller block diagram [11].

Abbas [150] used Dynamic Matrix Control (DMC), a common MPC strategy [151], to control a RO plant. The controller based on DMC was compared to a PI controller and tested against process disturbances. MPC showed faster response and robust performance as it delivered adequate response despite a $\pm 30\%$ change in the pressure-permeation rate gain. A similar study, performed by Robertson et al. [152], concluded that MPC based on DMC control algorithm offered better response and flexibility than the PI controller. The two studies used Ziegler–Nichols rule for PID tuning [150, 152]. However, another study performed by Esfahani et al. [148] used Internal Model Control (IMC) to tune a RO plant PID controller and compared it to the performance of a MPC that uses DMC and a PID controller tuned by the Ziegler–Nichols rule. The study found that the PID tuned by IMC presented better performance than both MPC and the Ziegler–Nichols tuned PID controller.

This indicates that the controller performance is dependent on its design, tuning and the control problem.

A supervisory control system based on MPC was presented by Qi et al. [153] to manage the operation of a wind-PV-RO plant. The MPC coordinated the power flow among the wind turbine, PV array, battery bank and the RO plant in order to satisfy water demand. Weather forecasts were used to predict the maximum power available from the RESs. Similar studies were presented by Palacin [145] and Salazar et al. [154] for a MPC that solves an optimisation problem at each sample step, to adjust water production based on water demand and energy available from hybrid RESs.

The application of NNs in desalination was first described by El-Hawary in 1993. Since then, NNs have been used for the RO plant modelling and performance prediction by several studies [155-159]. However, the first use of NNs to control the operation of a standalone wind-RO plant was reported by Cabrera et al. [63] in 2017. Cabrera et al. [63] implemented a NN in the control system of a wind-powered RO plant, to adapt the plant energy consumption to changes in available energy by generating feed flowrate and pressure set points while considering the wind power, feed temperature and conductivity.

2.4 Summary

The integration between RE and RO promises a cost-effective and sustainable solution to decarbonise water production. The use of RE, specifically wind and solar-PV, in driving large-scale RO plants has, however, been hampered by the inefficiency and high cost of energy storage systems with larger RED systems remaining dependent on grid connection. This review has discussed recent studies that provide innovative approaches to RED and identified technical challenges and potential solutions for the commercialization of RED in large-scale plants [11]. The main conclusions and potential improvements are as follows:

- Variable operation has been implemented in several studies by using modular ‘on-off’ operation and/or variable-speed operation. It has proven to be a successful strategy to operate small-scale RO plants and holds promise for large-scale plants with RE.
- Maintaining membrane performance and lifetime while using variable operation is economically crucial for proving RE-powered RO plants feasibility. Previous studies tested the membrane performance only for short periods compared to membrane lifetime.

Although further testing should be performed to analyse any degradation in membrane performance or lifetime due to variable operation, this was not possible due to the set duration of this research.

- Centrifugal ERDs are not recommended for variable operation, as their efficiency varies with fluid pressure and flow. On the other hand, isobaric ERDs have a stable efficient performance with varying flow and pressure which makes them preferable for variable operation. However, the negative effects of mixing and leakage on overall performance could worsen under variable operation due to increased pressure and velocity fluctuations.
- The execution of the RO operational procedure during modular operation is crucial for maintaining the lifetime and performance of the RO modules. However, if the start-up/shutdown procedures for RO trains were performed solely based on energy availability, it would be wasteful of energy and product water, both of which are valuable during variable operation. The prospect of using RES prediction to schedule the RO trains operation is examined in this research for its potential to reduce the unnecessary repetition of the start-up/shutdown cycle.
- Several studies compared advanced control systems such as MPC to classical techniques, e.g., PID control, for controlling RO plants. Different conclusions were made as to which delivers the best performance, considering response time and performance robustness. However, the number of studies discussing specifically RE driven RO plants, as opposed to fossil-fuelled RO plants, is low. This research considers the RES fluctuations in analysing the control system response, in addition to using a RO plant with a similar control structure to large-scale systems for accelerating the implementation for such scale.
- Hybrid RESs can play an important role in stabilising the operation and enhancing energy availability for RE-driven RO plants. Current studies presenting hybrid RESs to drive RO plants lack the comprehensive representation and analysis of the RO plant performance against variable power. The focus should be guided towards the RO plant performance and the benefits and challenges of using hybrid renewable energy. However, this research is focused on implementing variable operation using a single RES, i.e., wind energy, which is more challenging to achieve than using a more stable power input from a hybrid RES, thus, developing a solution that is expected to accommodate a range of RE types and their combinations.

3 Chapter 3 Experimental setup and procedure

3.1 Introduction

A fundamental objective of this study is to develop a load management technique for powering RO plants using RE that can be transferable to large-scale systems. An optimum approach would be to perform an investigation to determine the prospects of using variable operation on an existing large-scale RO system. However, large-scale RO systems are expensive to run and mostly in continuous use, such that it is difficult to access and control them purely for experimental purposes. Thus, the decision was made to design a RO pilot plant that shares the same operating principle as large-scale systems, at a lower production capacity, to develop a technology that is transferable to such scale. This enables the experimentation in any desired manner needed to validate this study.

The design and commissioning of such a pilot plant was a demanding task and required a great deal of technical and project management skills to get it completed. The design process was carried out by making initial projections of the RO plant performance using software provided by the membrane manufacturer, i.e., ROSA. The mechanical design was then performed, which included the selection and sizing of the plant's components, e.g., pumps, valves, sensors, filters, etc. In addition, a Computer-Aided Design (CAD) assembly was developed that included details on the steel frame design, pipe routing, equipment mounting and components assembly. The next step was carrying out the electrical design, which involved designing the electrical enclosure that houses the main power supply, pumps control, and the data acquisition system, in addition to preparing detailed wiring diagrams for connecting the power and control circuits. After completing the mechanical and electrical designs, the procurement process was carried out by contacting industrial suppliers and arranging the equipment purchasing and delivery. As for the system assembly, a local contractor, Aston Fitting & Flanges (Birmingham, United Kingdom), was hired to assemble the steel frame and to supply and weld the stainless-steel pipes and flanges. The rest of the system was assembled by Mohamed Mito including the PVC pipework, membranes loading, sensors assembly, and the control and electrical system wiring. Furthermore, a LabVIEW based data acquisition and control system was developed for handling the software/hardware interaction. The assembling and initial testing process were done at Aston Fitting's workshop and the plant was then transported to Aston University. A CAD drawing showing the isometric projection of the pilot plant is presented in Fig. 3.1. More CAD drawings of the RO

system are available in Appendix A. The detailed design of the developed RO system and the experimental procedure used throughout this study are presented in this Chapter.

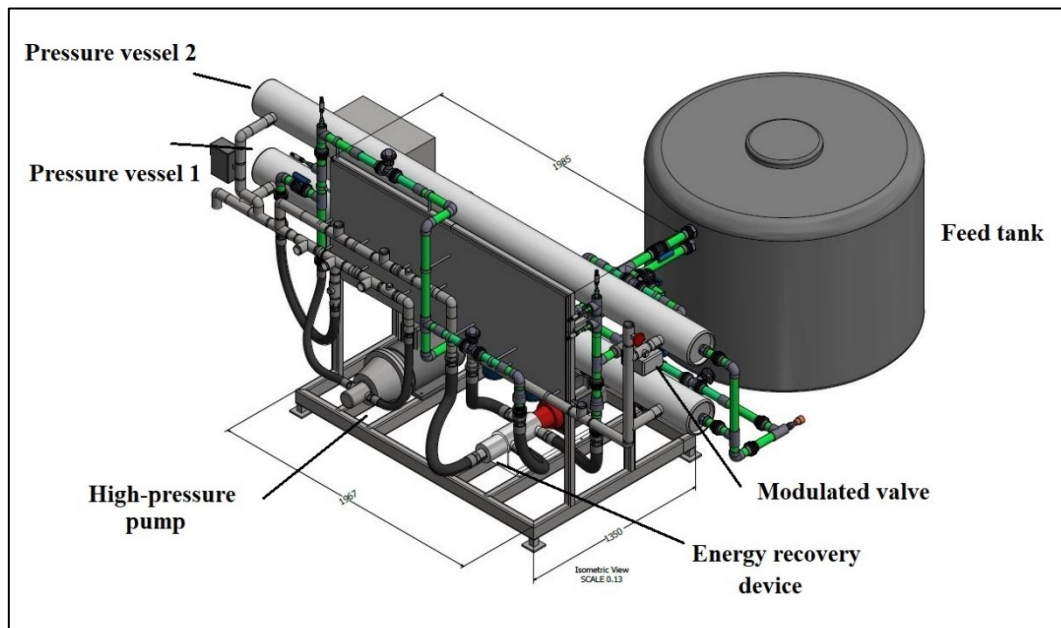


Fig. 3.1. Isometric projection of the RO system.

3.2 System description

The RO system, shown in Fig. 3.2 and 3.3, is a pilot RO plant designed for testing the operation of RE-driven RO systems. It was designed to have the essential features of large-scale systems and thus comparable performance. It includes two parallel pressure vessels, each containing three 8” RO elements arranged in series. The system is arranged in a split-feed flow configuration, following the current industry practice of splitting the feed between a HPP and an ERD. The plant’s rated production capacity is 3.2 m³/h. A schematic diagram of the system is shown in Fig. 3.4 and main system specifications are described in Table 3.1.

The HPP and ERD were selected from equipment designed for large-scale systems to investigate their ability to operate efficiently with variable power. Positive displacement devices were selected, as they offer consistent efficiency over their operational range. The HPP used is the APP 3.5 axial piston pump manufactured by Danfoss (Nordborg, Denmark) [160]. As for the ERD, isobaric pressure exchangers are favourable for large-scale systems due to their flexibility and modularity, offering high efficiency over the range of operating conditions [11]. The ERD used is the ‘Danfoss iSave 21 Plus’, which consists of an isobaric pressure exchanger coupled to a vane pump, both driven by the same motor on a single shaft, offering flexibility and precision in controlling flowrate through the ERD [161]. The HPP and

ERD motors were powered using VFD to control their speed of rotation and thus flowrate through each device. This allowed control of permeate output and recovery ratio in response to changes in available power, feed concentration and feed temperature.



Fig. 3.2. RO system installed in the laboratory (front).

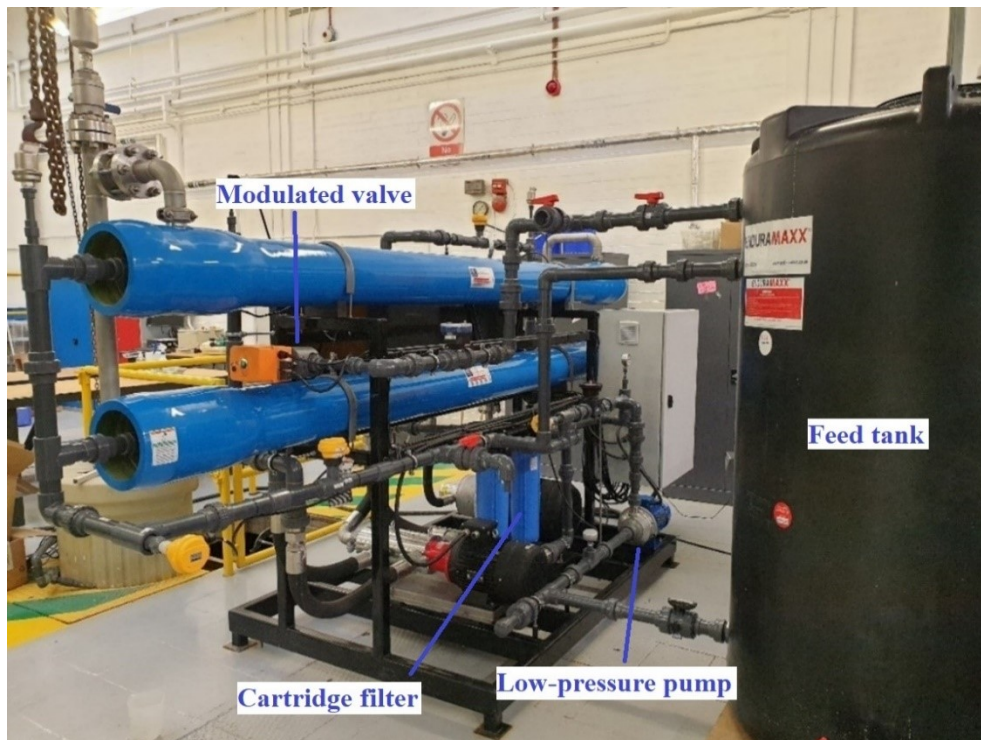


Fig. 3.3. RO system installed in the laboratory (back).

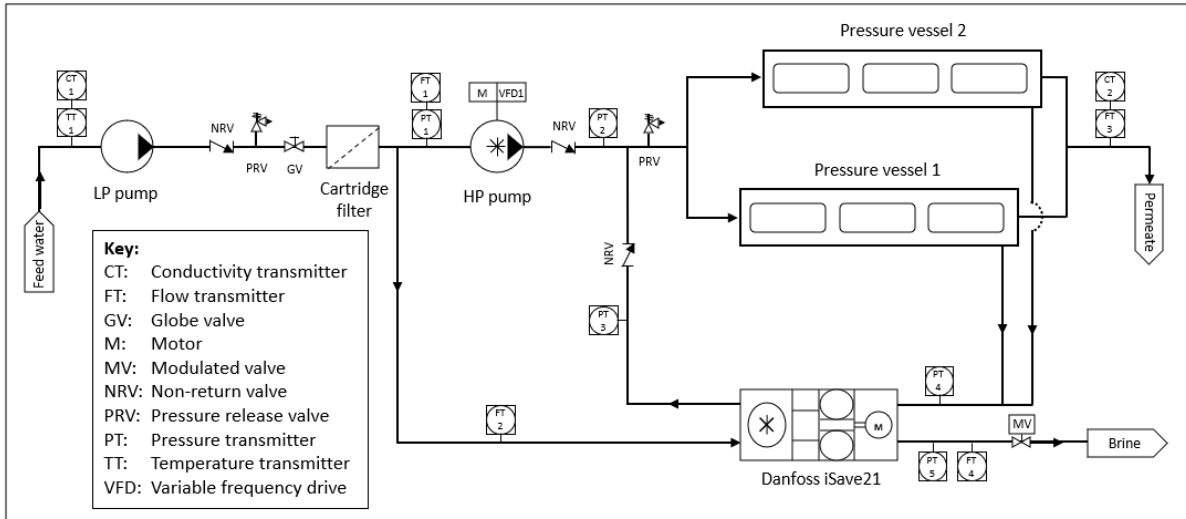


Fig. 3.4. Schematic diagram of the RO system.

Table 3.1. RO system main specifications.

Membrane type	FilmTech™ SW30HRLE-400
System arrangement	Two pressure vessels in parallel, each containing three RO elements in series
Rated permeate production	3.2 m ³ /h
Rated permeate recovery ratio	25%
Rated power consumption	7.5 kW
Rated specific energy consumption	2.34 kWh/m ³
Feedwater	Salinity 35,000 mg/l Temperature 25°C
Low-pressure pump	LOWARA CEA210/5/D-V
High-pressure pump	Danfoss APP 3.5
Energy recovery device	Danfoss iSave 21 Plus

3.3 Main components

A brief description of the RO system main components is presented in this section. Full technical specifications of each component relative to the mathematical model development are described later in Chapter 4.

3.3.1 Feed tank

The feed tank connections were configured to form a closed loop and provide a consistent supply of feedwater. As shown in Fig. 3.5, the feedwater was supplied from the bottom and the permeate and brine were returned to the feed tank where they mixed to maintain a set concentration within the tank.

The tank capacity was determined based on the amount of water required to fill the pressure vessels and piping volumes. This totalled approximately 0.3 m³. The seawater batch volume was set to 1 m³ to ensure a stable feed concentration and flow to the system. The tank was oversized to 2 m³ to aid in heat dissipation of energy added by the pumps. However, the challenge during testing was raising the temperature to the standard test condition, especially during cold days. For that purpose, submerged water heaters were installed in the tank.

The feedwater used for testing is a sodium chloride (NaCl) solution prepared from tap water at the target salinity [97]. Thus, the only solute components considered were Na⁺ and Cl⁻ and the mass concentration of total dissolved solids (TDS) was the same as that of NaCl. The standard feedwater concentration and temperature for test conditions were 35,000 mg/l. and 25°C, respectively.

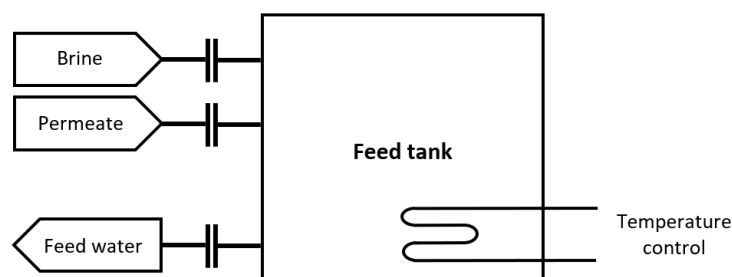


Fig. 3.5. Schematic diagram of the feed tank.

3.3.2 Cartridge filter

The RO system was fitted with two polypropylene cartridge filters arranged in parallel that offered pre-treatment for the feedwater. The cartridge filters, shown in Fig. 3.6, are

manufactured by Danfoss and can handle a flow of 10.2 m³/h each [162]. They offered prefiltration of 10µm to meet the feedwater requirement for the HPP [160].



Fig. 3.6. Cartridge filters.

3.3.3 Low-pressure pump

The LPP used was a LOWARA CEA210/5 single impeller centrifugal pump manufactured by Xylem (New York, United States). It was fitted upstream of the HPP and ERD and provided the feedwater from the feed tank. The pump's impeller and enclosure are made of stainless steel. It delivered a maximum feed flowrate of 18 m³/h using a 2.2 kW motor.



Fig. 3.7. Low-pressure pump.

3.3.4 High-pressure pump

The HPP used was the Danfoss APP 3.5 axial piston pump. It is a positive displacement pump with axial pistons specifically designed for seawater applications. The pump was powered by a 11 kW motor controlled using a VFD and delivered a maximum flowrate of 3.5 m³/h.

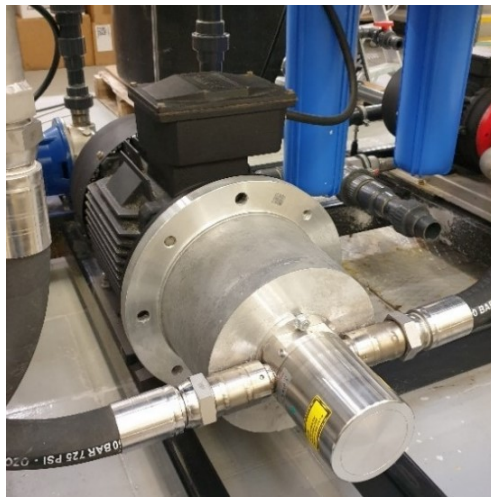


Fig. 3.8. Danfoss APP high-pressure pump.

3.3.5 Energy recovery device

The Danfoss iSave 21 consists of an isobaric pressure exchanger, a built-in BP, and an electric motor. The BP is a vane-type positive displacement pump that boosts the feed pressure to overcome pressure losses in the RO membranes and the pressure exchanger. The pressure exchanger and BP are connected on a single shaft to a 5.5 kW electric motor, which was powered using a VFD to control the iSave flow [161, 163].

The pressure exchanger transfers pressure from the high-pressure (HP) brine to the low-pressure (LP) feed by having the two streams in momentary contact with no physical barrier. The pressure transfer occurs in the ducts of a rotor that fits between two port plates. One-half of the rotor ducts are exposed to the HP stream and the other half are subjected to the LP stream, as shown in Fig. 3.9. The two streams are separated by a sealing area, which the rotor passes at each revolution to switch the duct from expelling the brine using the LP feed to pressurising the feed using the HP brine [161, 163]. The pressurised seawater then exits the BP to be mixed with the feed stream from the HPP. As a result of not having a physical barrier between the brine and seawater streams, slight mixing occurs between them. However, the design ensures that the mixing region never reaches the end of the rotor ducts

to maintain a quantity of liquid in the rotor, travelling from one end of the duct to the other, thus forming a hydraulic barrier between the brine and feedwater streams [164]. This requires a “balanced flow” between the HP and LP ducts of the pressure exchanger. During operation, the LP duct flow was matched to the flow through the HP duct and BP using a modulation valve on the brine reject line after the iSave.

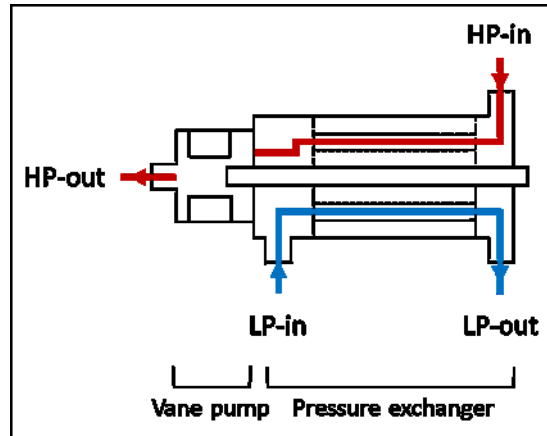


Fig. 3.9. Schematic diagram for the Danfoss iSave energy recovery device [163, 165].

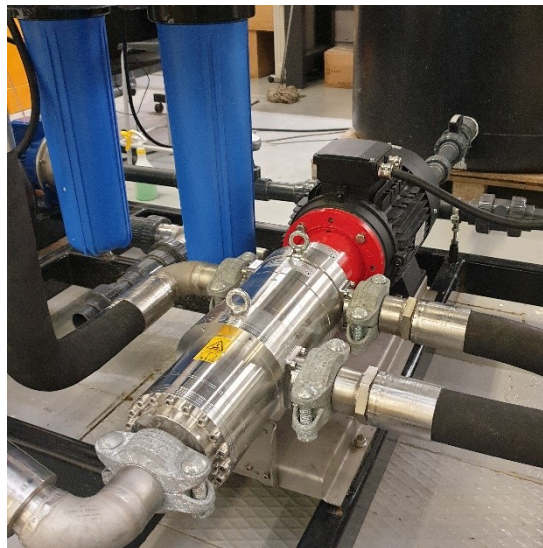


Fig. 3.10. Danfoss iSave energy recovery device.

3.3.6 Brine reject valve

The LPP flowrate was controlled using a modulated diaphragm valve installed on the brine reject line after the iSave. The valve was responsible for matching the flow on the LP side of the iSave to the flow on the HP side generated by the BP. The valve was fitted with a positioner that offered fine control of the valve opening based on a 4-20 mA signal. The

valve operated on a linear control characteristic with a flow coefficient of 27 m³/h at the fully opened position [166].



Fig. 3.11. Brine flow control modulation valve.

3.4 Instrumentations and measurements

This section describes the instrumentations used for data collection. The RO system included 16 sensors distributed across the RO test-rig to collect data for flowrate, pressure, concentration, temperature, and power consumption. The sensors were compatible for use with seawater and were selected to meet the operating range of the physical variable to be measured. The voltage required to power the sensors was provided by an external 24V DC power supply. The sensors were connected in series with the power supply forming a loop, by which, the current signal within the loop ranged from 4 – 20 mA and represented the physical reading of the sensor. This configuration is referred to as a “Loop-powered” circuit. All the sensors, except the conductivity sensors, were factory calibrated.

3.4.1 Flow measurement

The flowrates for the feed, brine and permeate streams were measured using the FPB151 flowmeter manufactured by OMEGA (Manchester, United Kingdom), shown in Fig. 3.12. It consists of a paddlewheel flowmeter mounted on a Tee and connected to a transmitter that converts the paddlewheel speed to a current signal representing the flow. The transmitter generated a 4 – 20 mA signal for a 0 - 30 m³/h flow range with an accuracy of $\pm 1\%$ of the max flowrate reading [167].



Fig. 3.12. Paddlewheel flowmeter.

3.4.2 Pressure measurement

The pressure across the RO system was measured using the RS PRO IPS series pressure sensors, shown in Fig. 3.13, manufactured by RS components (Northants, United Kingdom). They are piezo-resistive ceramic sensors with a stainless-steel housing that generated a 4 - 20 mA signal with respect to their pressure range with an accuracy of $\pm 0.25\%$ of max value [168]. The sensors fitted on the LP piping were rated from 0 to 16 bar, while the sensors on the HP side were rated from 0 to 100 bar.



Fig. 3.13. Pressure transmitter.

3.4.3 Concentration measurement

The feed and permeate concentration were measured using the OMEGA CDTX-2854 conductivity transmitter, shown in Fig. 3.14. It is an integrally mounted conductivity sensor and transmitter that delivers an accuracy of $\pm 2\%$ of reading [169]. The sensors provided a conductivity reading of 0 to 5000 $\mu\text{S}/\text{cm}$ and 0 to 100,000 $\mu\text{S}/\text{cm}$ for the feed and permeate streams, respectively, in the form of a 4 – 20 mA current signal. The conductivity reading was converted to a measurement of TDS using equation (3.1). However, the relationship between electrical conductivity and TDS varies with water salinity. The conversion factor, K , was considered as 0.64 and 0.55 for feedwater and permeate water, respectively [170]. The feed and permeate sensors were calibrated using a NIST compliant conductivity standard solution of 12,880 $\mu\text{S}/\text{cm}$. The calibration data are included in Table C.1 in Appendix C.

$$C \text{ (mg/l)} = \text{Conductivity } (\mu\text{S/cm}) \times K \quad (3.1)$$



Fig. 3.14. Conductivity transmitter.

3.4.4 Temperature measurement

The feedwater temperature was measured using a temperature transmitter installed on the feed line of the RO system. The transmitter used is the TEAT-LL fluid temperature transmitter manufactured by SYXTHSENSE (Exeter, United Kingdom), shown in Fig. 3.15. The sensor generated a 4 – 20 mA signal for a 0 to 50°C temperature range. The sensor accuracy is $\pm 0.5^\circ\text{C}$ [171].



Fig. 3.15. Temperature transmitter.

3.4.5 Power consumption measurement

The power consumption of each motor was calculated using equation (3.2), such that I_{Ph} is the current through a single phase, V_{Ph} is the phase voltage, and PF is the power factor of the respective motor. The phase voltage for each motor was constant at 240 V before the VFDs and the power factor for each motor was supplied by the manufacturers. The phase current for each motor was measured using current sensors installed on single-phase lines before the VFDs and used to calculate the power consumption from equation (3.2). The current transmitter used were the HOBUT (Walsall, United Kingdom) CT132TRAN, shown in Fig. 3.16. They generated a 4 – 20 mA signal for a current range of 0 – 10 A, 0 – 20 A and 0 – 50 A, depending on the motor power, with an accuracy of $\pm 0.5\%$ of the max current reading [172].

$$P_e = 3V_{Ph}I_{Ph}PF \quad (3.2)$$



Fig. 3.16. Current transmitter.

3.5 Electrical power system

An electric system was designed to power the LPP, HPP, ERD, sensors, data-acquisition, and control systems. It consisted of two circuits fitted in an electric enclosure, shown in Fig. 3.17, described as follows:

3.5.1 Power circuit

A 3-Phase high voltage (415V AC) power circuit was used to supply main power for the motors and panel equipment. This circuit included main switches, 3-Phase distribution blocks, residual current breakers, circuit breakers and a contactor for each motor. In addition, the circuit included a 5.5 kW and 11 kW VFDs used to control the iSave and HPP speeds respectively – shown in Fig. 3.18. The detailed wiring diagram for the power circuit is shown in Appendix B, Fig. B.1.

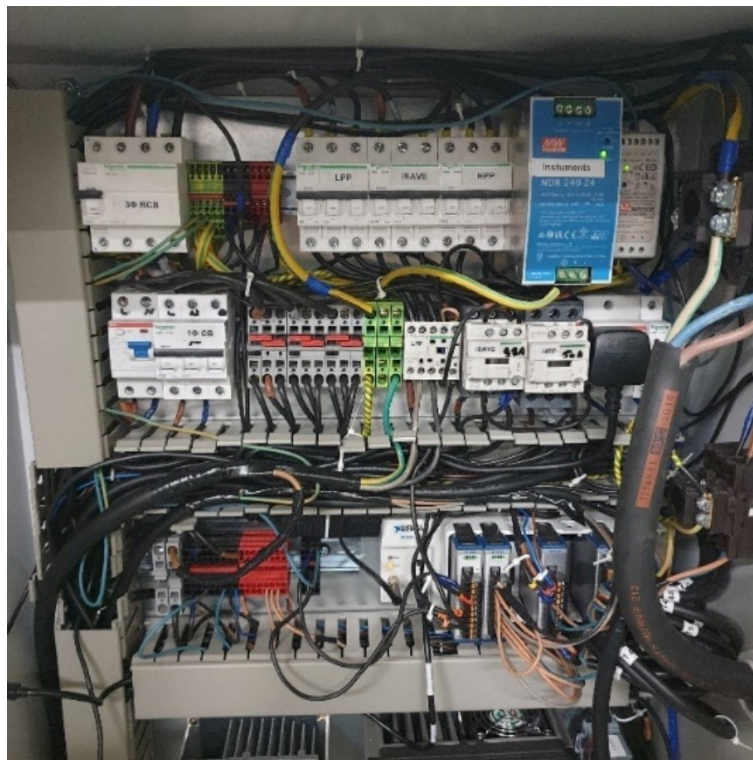


Fig. 3.17. Electric control panel.



(a)



(b)

Fig. 3.18. Variable frequency drive for a) the energy recovery device motor (5.5 kW), and b) the high-pressure pump motor (11kW).

3.5.2 Control circuit

A low voltage (24V DC) control circuit was used to power the sensors, valves, data-acquisition system, and the low-voltage circuit that energises the contactor coils for the pumps on/off control. The circuit included two 24V DC power supplies and low-voltage distribution blocks. The contactors control circuits were connected to ensure that the pumps are interconnected, such that the iSave cannot be operated without the LPP and the HPP cannot be operated without the LPP and BP. In addition, pressure switches were distributed across the system to shutdown all pumps if any pressure exceeds the set limit. The detailed wiring diagram for the control circuit is presented in Appendix B, Fig. B.2.

3.6 Data acquisition and supervisory control

A data acquisition and supervisory control system, based on hardware and software developed by National Instruments (NI) (Texas, United States), was used for logging the instrumentations readings and providing supervisory control of the system parameters. A compact DAQ chassis that includes conditioned input/output (I/O) modules processed signals from the RO system instrumentations. The processed signals are sent to a PC-based supervisory control system developed on LabVIEW for data logging and process control. The structure of the data acquisition and control system is presented in Fig. 3.19. The elements of the data acquisition and control system are described as follows:



Fig. 3.19. Data-acquisition and control system structure.

3.6.1 Data logging hardware

The data acquisition and control system was based on the Compact DAQ chassis NI-9172, shown in Fig. 3.20. The DAQ chassis provided USB connectivity to connect the sensor and electrical measurements to a PC, where the data logging and processing were performed using the LabVIEW software. The chassis housed three types of conditioned I/O modules providing different roles that are described as follows:

- NI-9208: An input module that read the current input signal (4 - 20 mA) generated by the 16 sensors distributed across the RO system.
- NI-9265: An output module that generated a current signal (4 - 20 mA) for the pumps speed control and modulated valve positioning.
- NI-9482: A relay output module used to provide on/off control for the LPP, iSave and HPP.

The connections to the terminals of the I/O modules are shown in Appendix B, Section B.3.

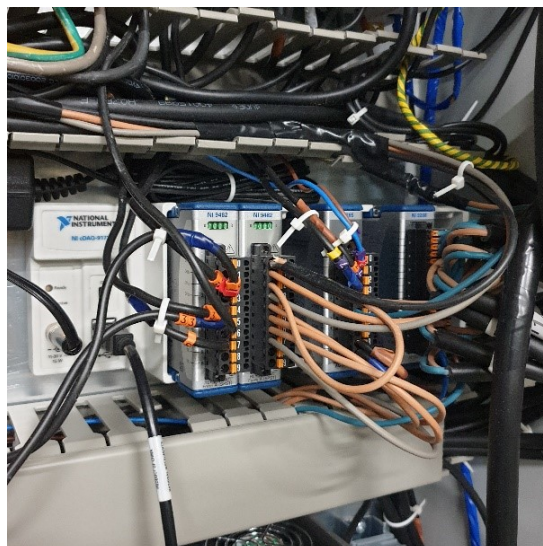


Fig. 3.20. NI-9172 compact DAQ chassis.

3.6.2 User-interface

LabVIEW is the PC-based system-design platform that handled the data acquisition, data processing and instrument control for the RO system. The software was used to develop a supervisory control system with a bespoke user-interface, shown in Fig. 3.21, that offered data monitoring, data logging and supervisory control of system parameters.

LabVIEW offered programming on two levels. The user-interface, named the Front Panel, was designed during control system development. It included data monitoring elements, i.e., graphs and indicators, and system control elements, i.e., switches and dials. The Block Diagram, shown in Fig. 3.22, included the graphical source code, where the programming and wiring for the data logging and processing was performed.

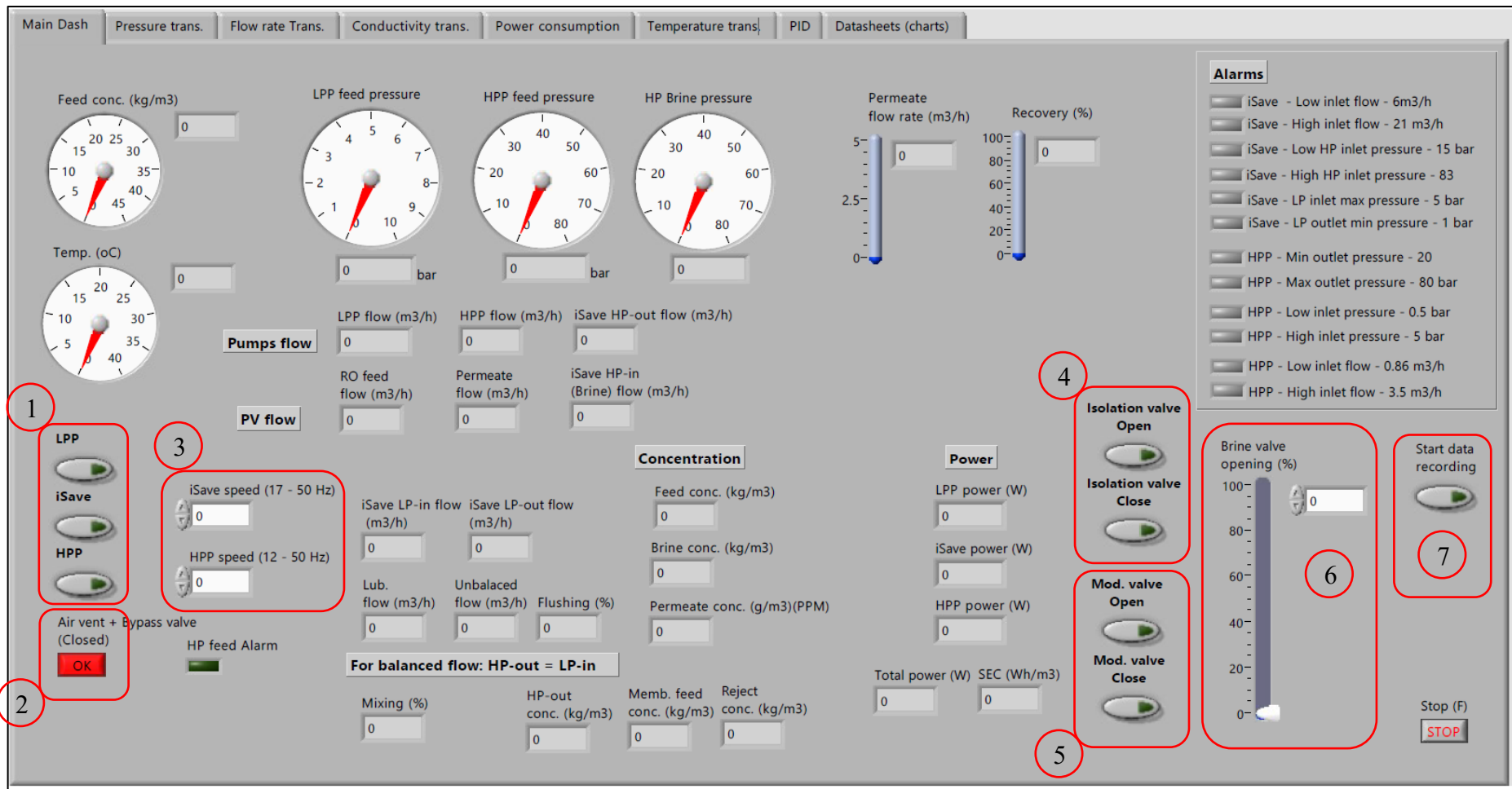


Fig. 3.21. Graphical user-interface.

Legend	Panel 1	Panel 2	Panel 3	Panel 4	Panel 5	Panel 6	Panel 7
	Pumps on/off control	Air vent closure switch	Pumps speed control	Isolation valve on/off	Modulation valve on/off	Modulation valve control	Data recording switch

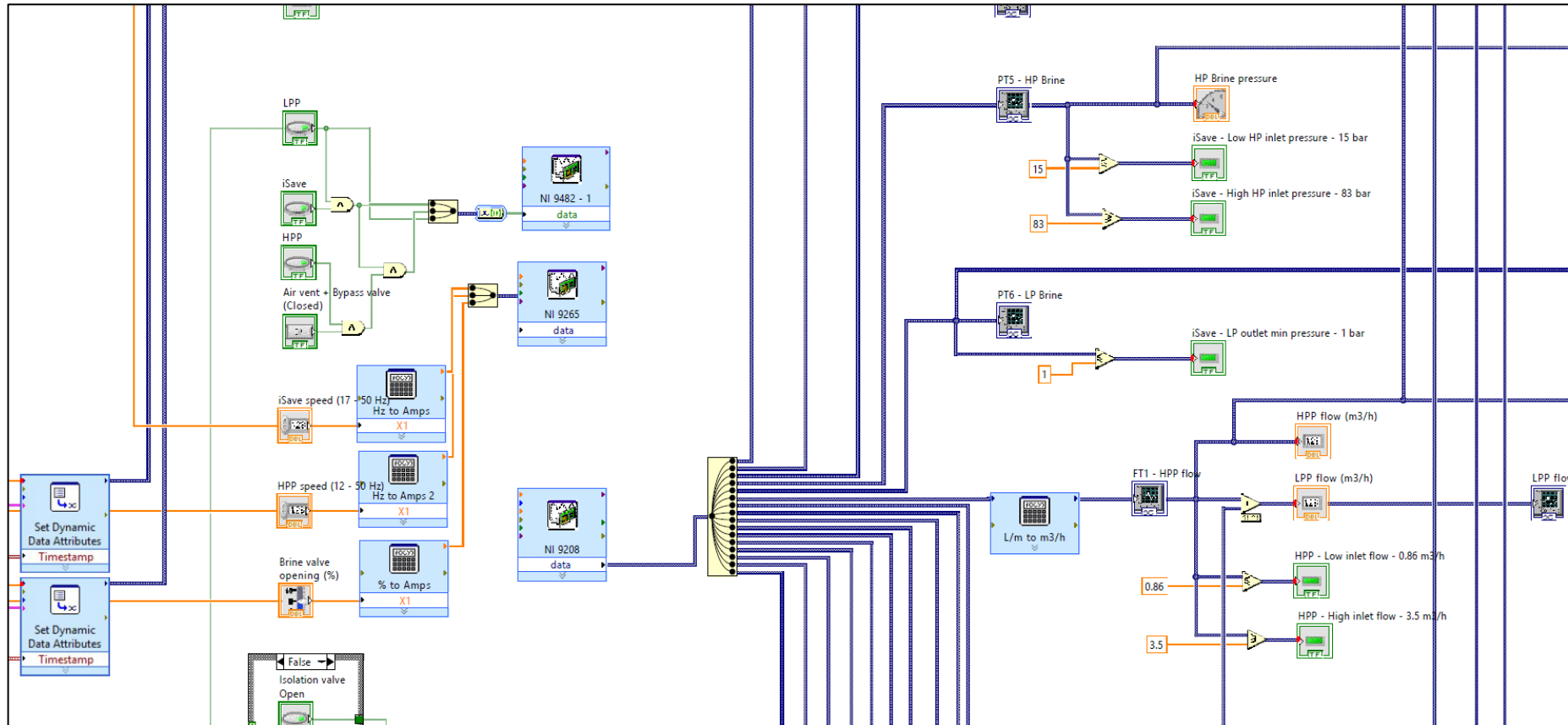


Fig. 3.22. A segment of the LabVIEW Block Diagram.

3.6.3 Signal processing and data logging

The sensors readings were sent to LabVIEW through the DAQ chassis as a current signal of 4 – 20 mA. The signal from each channel was scaled and linearised to convert into real-world units of flow, pressure, concentration, and power and then distributed for either display through the user-interface, logging in an Excel file, or used in calculating other parameters. The data were acquired at 1 Hz sampling rate, this allowed high-speed data to be collected to project the dynamic performance of the RO system.

3.6.4 Supervisory control

The data acquisition system was also used to provide open-loop supervisory control for the RO system during experimental testing. It offers on/off control for the pumps, motor speed control for the iSave and HPP through the VFDs, and position control for the modulated valve. In addition, operation constraints were integrated into the control system as a set of alarms that compare the operational boundaries to the actual measurement from the sensors and issues a warning or shuts down the system accordingly. The closed-loop control system used for controlling the operating parameters according to changes in available power was developed using MATLAB/Simulink and is described in Chapter 5.

3.7 Experimental procedure

This section provides a brief description of the experimental procedure used throughout this study. A more detailed description is presented for a standardised start-up and shutdown procedure in Chapter 7.

3.7.1 System preparation

Prior to system start-up, the RO system was flushed using freshwater to clear out any membrane preservative or left-over brine in the pressure vessels. Next, a seawater batch was prepared in the feed tank. The synthetic seawater was a NaCl solution prepared from tap water by adding NaCl at the required concentration [97]. The standard concentration for testing was 35,000 mg/l, which translated to 35 kg for a 1 m³ batch. The salt was added half a kilogram at a time while running the LPP, to circulate water from the bottom to the top of the tank. This guaranteed that the salt was properly mixed and there was no salt accumulated at the bottom of the tank, thus ensuring a consistent feed concentration during operation. The system preparation process was not included in the control system development or the

modular operation technique as it is specific to the experimental procedure of this pilot plant due to recirculating the feedwater. Generally, large-scale RO systems would have an open feedwater supply, which can be used for system flushing. In addition, it is assumed that the system is not resuming operation from a long-term shutdown.

3.7.2 Start-up

The first step of system start-up was to purge the air out of the RO system, otherwise, air left in the system during operation would lead to excessive forces on the elements causing the fibreglass shell to crack [142]. The RO system included automatic air vents distributed across the LP piping. However, for the HP side, a manual globe valve was opened to allow air to rise to an air vent connected after the pressure vessel for purging the HP piping. The manual globe valve was closed before operating the HPP to prevent damage to the air vent. The LPP and iSave were used to circulate LP feedwater through the RO system to ensure that the system was completely purged and filled with water.

After the air purge was completed and the LPP and iSave were operational, the HPP is started. The HPP speed was increased gradually to maintain a pressure ramp rate of 0.7 bar/s [142]. This was achieved by ramping the pump speed by 0.5 Hz/s until reaching the desired permeate flowrate. The permeate was discarded until it reached an acceptable concentration.

3.7.3 Shutdown

During system shutdown, the HPP was ramped down to a complete stop, then the iSave was left operational to clear the remaining brine out of the pressure vessels using feedwater. This was guaranteed by monitoring the brine concentration until it reaches the feed concentration. In case of an extended shutdown, the system was flushed using permeate water and sodium metabisulfite was added as membrane preservative. After the brine was flushed, the iSave was ramped down to a complete stop and the LPP was turned off. The system remains pressurised for approximately 30 minutes after shutdown. The pressure decreased gradually as water leaks through the iSave to the reject line.

4 Chapter 4 Reverse osmosis model development

4.1 Dynamic model development

This chapter describes the model developed to predict the RO system dynamic performance. The whole RO system model is introduced, then the modelling for each component is presented. The model has been implemented in MATLAB-Simulink and validated using experimental data from the laboratory RO system. As presented in Fig. 4.1, the dynamic model was used for tasks that require detailed analysis, such as development and testing of the control system and the variable operation procedure. Other tasks that require experimental investigation and verification, such as model validation, open-loop response, and sensitivity analysis, were performed using the pilot plant described in Chapter 3.

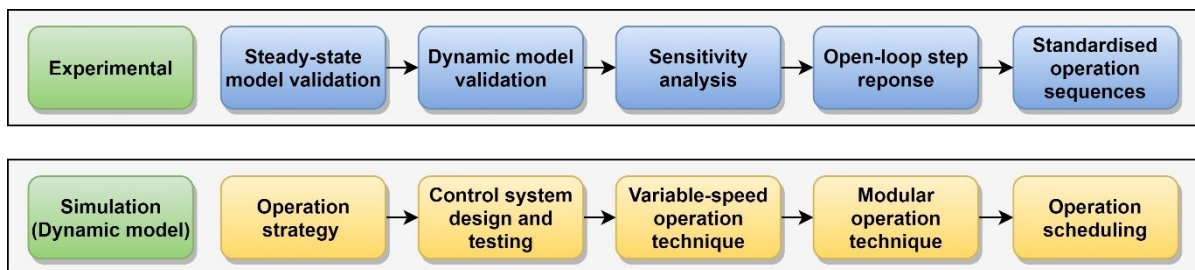


Fig. 4.1. Classification of research tasks based on the used methodology (experimental or simulation-based investigation).

4.2 Reverse osmosis system model

The dynamic model uses the solution-diffusion model to describe water and salt transport across the membrane [173]. Another alternative for modelling the permeation process is the pore-flow model, however, the solution-diffusion model has been widely accepted in recent publications [174, 175]. A detailed comparison between the solution-diffusion and pore-flow model can be found in [174]. As for the concentration polarisation, it is described using the analytical film theory to estimate the mass transfer coefficient variation along the membrane surface within the boundary layer [176, 177]. The RO modules used in this study are the DuPont FilmTec™ SW30HRLE-400 8-inch (0.203 m) membrane (see specifications in Table 4.1). A schematic diagram of the RO membrane structure is shown in Fig. 4.2. The assumptions made throughout this model are as follows:

- The solution-diffusion model is valid.

- The analytical film theory is valid for representing the effect of concentration polarisation.
- The clearances between RO elements inside a pressure vessel are neglected. This allows the in-series RO elements to be modelled as a single element having the same total length and membrane area.
- The pressure in the permeate channel is atmospheric.
- The membrane sheets are modelled as flat channels with negligible curvature.
- The flow in the spiral direction is assumed negligible.
- The feed, brine and permeate temperatures are equal and constant along the membrane.
- Despite variations in permeate concentration along the permeate channel length, the average value is regarded as the output permeate concentration.
- The feedwater is prepared using sodium chloride (NaCl) solution to achieve the same osmotic pressure as seawater [97].
- The brine channel thickness is equal to the feed-spacer thickness ($t_{bc} = t_{sp}$) and the permeate channel thickness, t_{pc} , is assumed 0.5×10^{-3} m [177, 178].

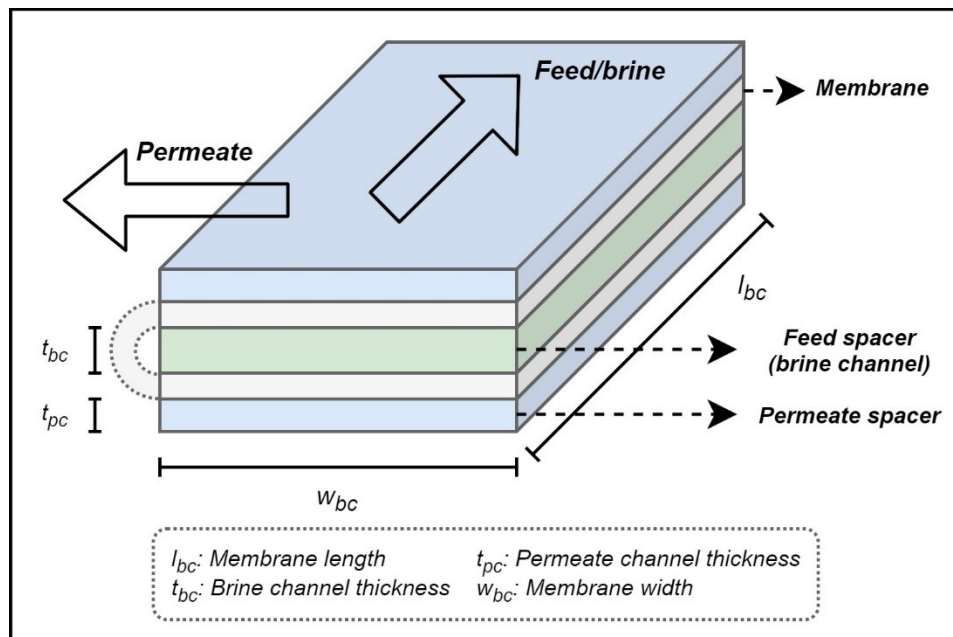


Fig. 4.2. Schematic diagram showing the RO membrane structure. Each brine channel has one membrane leaf folded into two layers and glued from the opposite side. Therefore, there are two active layers per brine channel.

Table 4.1. Specifications of the SW30HRLE-400 membranes [177-180].

Parameter	Value
Active area (A_m)	37 m ²
Module diameter (d)	0.2 m
Membrane length (l_{bc})	0.8665 m
Membrane width (w_{bc})	1.34 m
Number of membrane leaves/ brine channels (n_l)	16
Feed-spacer thickness (t_{sp})	0.7112×10^{-3} m
Brine channel thickness (t_{bc})	0.7112×10^{-3} m
Permeate channel thickness (t_{pc})	0.5×10^{-3} m
Brine channel void fraction (ϕ_{bc})	0.9
Water transport coefficient (A_w)	4.39×10^{-7} m/bar.s
Salt transport coefficient (B_s)	1.35×10^{-8} m/s

4.2.1 RO modules

The split-feed flow configuration forms two flow loops around the pressure vessels. The outer loop flow, Q_{HPP} , is pressurised by the HPP and represents the permeate portion of the feed stream. The inner loop flow, Q_{iSave} , is pressurised by the iSave and represents the brine portion of the feed stream. A defined quantity of the brine stream (0.5 – 4%), Q_{Lub} , is used in the iSave to lubricate moving parts [163]. This quantity is lost to system discharge along with the reject brine. The lubrication flow is supplied by the HPP and can be verified experimentally by subtracting the permeate flow, Q_p , from the HPP outlet flow, Q_{HPP} [163]. An empirical relation to calculate the lubrication flow can be found in Section 4.2.2.3. In steady-state condition, the flow balance per pressure vessel can be described as follows:

$$Q_f = (Q_{HPP} + Q_{iSave})/N_{pv} \quad (4.1)$$

$$Q_b = (Q_{iSave} + Q_{Lub})/N_{pv} \quad (4.2)$$

$$Q_p = (Q_{HPP} - Q_{Lub})/N_{pv} \quad (4.3)$$

where Q_f is the feed flowrate, Q_b is the brine flowrate and N_{pv} is the number of pressure vessels.

RO relies on applying pressure higher than the osmotic pressure forming a net driving pressure that pushes water through the membrane. This process is described by the solution-diffusion model as follows:

$$J_w = \frac{Q_p}{A_m} = A_w TCF(\Delta P - \Delta\pi) \quad (4.4)$$

where J_w is the permeate water flux and A_w is the membrane water permeability coefficient. A_m is the membrane active area calculated by:

$$A_m = 2n_e n_l w_{bc} l_{bc} \quad (4.5)$$

where n_e is the number of RO elements in series, n_l is the number of membrane leaves that are folded to form the feed channel, w_{bc} is the membrane width and l_{bc} is the membrane length. The pressure difference across the membrane, ΔP , is calculated using equation (4.6) as:

$$\Delta P = P_f - P_p - \frac{P_{drop}}{2} \quad (4.6)$$

where P_f and P_p are the feed and permeate pressures, respectively. P_{drop} is the pressure drop along the membrane that is given by:

$$P_{drop} = 0.01 \frac{1}{14.8} n_e \left(\frac{3600}{0.227} Q_{bulk} \right)^{1.7} \quad (4.7)$$

where Q_{bulk} is the bulk flowrate inside the brine channel. The osmotic pressure difference across the membrane, $\Delta\pi$, is calculated from equation (4.8) as follows:

$$\Delta\pi = n_i R (T + 273) \frac{1}{MW} (C_w - C_p) \quad (4.8)$$

where R is the universal gas constant, n_i is the number of moles in a NaCl molecule, MW is the NaCl molecular weight, T is the feedwater temperature in °C, C_w is the average concentration on the membrane wall and C_p is the product water concentration. The coefficients of water permeability, A_w , and salt permeability, B_s , are calculated empirically from the solution-diffusion model using data collected along the operation range at a feed temperature of 25°C. Variations in water and salt permeability due to changes in feed

temperature are accounted for using an empirical temperature correction factor, TCF , provided by the manufacturer as follows [142, 181]:

$$TCF = \begin{cases} \exp\left[2640\left(\frac{1}{298} - \frac{1}{273+T}\right)\right]; T \geq 25^\circ\text{C} \\ \exp\left[3020\left(\frac{1}{298} - \frac{1}{273+T}\right)\right]; T \leq 25^\circ\text{C} \end{cases} \quad (4.9)$$

Feed pressure after the positive displacement HPP is dependent on the system backpressure, which is caused by the osmotic pressure gradient across the membrane. Thus, the feed pressure, P_f , is calculated from a derivation of the permeate flux equation as follows:

$$P_f = \frac{1}{A_w TCF} \frac{(Q_{HPP} - Q_{Lub}) / N_{pv}}{A_m} + P_p + \frac{P_{drop}}{2} + \Delta\pi \quad (4.10)$$

where the brine pressure, P_b , is calculated according to the pressure drop along the brine channel by:

$$P_b = P_f - P_{drop} \quad (4.11)$$

Based on the concentration polarisation theory, the average seawater concentration at the membrane wall, C_w , is calculated as:

$$\frac{C_w - C_p}{C_{bulk} - C_p} = \exp\left(\frac{J_w}{K_m}\right) \quad (4.12)$$

where C_{bulk} is the bulk flow concentration and K_m is the mass transfer coefficient through the membrane, which is calculated using Sherwood analogy as follows:

$$Sh = \frac{K_m d_h}{D_B} = 0.2 Re^{0.57} Sc^{0.4} \quad (4.13)$$

where Sh is the Sherwood number, D_B is the brine diffusivity, d_h is the hydraulic diameter of the brine channel, Sc is the Schmidt number and Re is the Reynolds number in the brine channel [42, 177, 182]. The seawater diffusivity D_B and the Schmidt number are given respectively by equations (4.14) and (4.15) as:

$$D_B = 6.725 \times 10^{-6} \times \exp(0.1546 \times 10^{-3} \times C_{bulk} - \frac{2513}{T+273}) \quad (4.14)$$

$$Sc = \frac{\mu}{\rho D_B} \quad (4.15)$$

where μ is the seawater viscosity given by equation (4.16) and ρ is the seawater density calculated from equation (4.17) according to the feed concentration, C_f , as follows [42]:

$$\mu = 1.234 \times 10^{-6} \times \exp\left(0.0212 \times C_{bulk} + \frac{1965}{T+273}\right) \quad (4.16)$$

$$\rho = 498.4 \times m(T) + (248,400 \times m(T)^2 + 752.4 \times m(T) \times C_f)^{1/2} \quad (4.17)$$

where $m(T) = 1.0069 - 2.757 \times 10^{-4} \times T$

As for the Reynolds number inside the brine channel, it is given by:

$$Re = \frac{\rho d_h V_{bulk}}{\mu} \quad (4.18)$$

where V_{bulk} , the bulk flow velocity through the brine channel, is calculated as follows:

$$V_{bulk} = \frac{Q_{bulk}}{n_l w_{bc} t_{bc} \phi_{bc}} \quad (4.19)$$

where t_{bc} is the brine channel thickness and ϕ_{bc} is the void fraction that represents the reduction of void volume inside the brine channel [177, 183]. The hydraulic diameter, d_h , represents the non-circular geometry of the spacer-filled brine channels. It is calculated using the void fraction, ϕ_{bc} , and the feed spacer thickness, t_{sp} , to include the effect of the spacer's surface area on the flow as follows [177, 183]:

$$d_h = \frac{4\phi_{bc}}{\frac{2}{t_{sp}} + (1-\phi_{bc})\frac{8}{t_{sp}}} \quad (4.20)$$

As a result of high concentration difference between the brine and product water streams, salt permeates the membrane along with water molecules. This mass transport phenomenon can be described by equation (4.21), which represents the salt transport flux J_s as follows:

$$J_s = B_s T C F \exp\left(\frac{J_w}{K_m}\right) (C_{bulk} - C_p) \quad (4.21)$$

The transient characteristics of the RO module performance are associated with variation in brine concentration along the membrane length. These variations directly affect the system pressure response and permeate flowrate through changes in osmotic resistance. The change in bulk flow concentration, C_{bulk} , related to salt accumulation in the membrane channel, is

represented by the salt balance along the membrane length and through the active layer using the concentration conservation formula as follows:

$$V_{bc} \frac{dC_{bulk}}{dt} = Q_f C_f - Q_b C_b - Q_p C_p \quad (4.22)$$

where the brine channel volume, V_{bc} , and the brine concentration, C_b , are calculated respectively from equations (4.23) and (4.24) as:

$$V_{bc} = n_e n_l w_{bc} l_{bc} t_{bc} \phi_{bc} \quad (4.23)$$

$$C_b = 2C_{bulk} - C_f \quad (4.24)$$

Similarly, the transient change in the bulk permeate flow concentration, C_p , is given by:

$$V_{pc} \frac{dC_p}{dt} = Q_p C_{p,m} - Q_p C_p \quad (4.25)$$

where $C_{p,m}$ is the local permeate concentration at the membrane surface and V_{pc} is the permeate channel volume, which are given respectively by equations (4.26) and (4.27) as follows:

$$C_{p,m} = \left(\frac{J_s}{J_w} \right) \quad (4.26)$$

$$V_{pc} = n_e n_l w_{bc} l_{bc} t_{pc} \phi_{pc} \quad (4.27)$$

Although the above equations describe the output streams characteristics for a single pressure vessel, they can also be used to predict the same outputs for a RO unit containing multiple pressure vessels. Thus, the permeate flowrate, permeate concentration, brine flowrate and brine concentration from the two pressure vessels are calculated for $N_{pv} = 2$, respectively, as follows:

$$Q_p = \sum_{i=1}^{N_{pv}} Q_{p,i} \quad (4.28)$$

$$C_p = \frac{\sum_{i=1}^{N_{pv}} C_{p,i} Q_{p,i}}{Q_p} \quad (4.29)$$

$$Q_b = \sum_{i=1}^{N_{pv}} Q_{b,i} \quad (4.30)$$

$$C_b = \frac{\sum_{i=1}^{N_{pv}} C_{b,i} Q_{b,i}}{Q_b} \quad (4.31)$$

4.2.2 Pumping system

The detailed model for the LPP, HPP and iSave are presented in this section. Each subsection below outlines the flowrate and power consumption calculation of the respective pump. The total power consumption of the RO system is thus calculated as follows:

$$P_{e,total} = P_{e,LPP} + P_{e,iSave} + P_{e,HPP} \quad (4.32)$$

4.2.2.1 Low-pressure pump

Specifications of the LPP are presented in Table 4.2 [184]. The pump flowrate was controlled using a modulated diaphragm valve installed on the brine reject line after the iSave. The flowrate through the LPP and control valve, Q_{LPP} (m³/s), is calculated as follows:

$$Q_{LPP} = C_v \sqrt{\frac{\Delta P_{LPP}}{SG}} \quad (4.33)$$

where ΔP_{LPP} (bar) is the differential pressure across the LPP, SG is the feedwater specific gravity and C_v is the valve flow coefficient (m³/s) at the respective position. The valve operates on a linear control characteristic with a flow coefficient of 27 m³/h at the fully opened position. The inlet pressure to the pump was assumed atmospheric since an open-top feed tank was used. The flowrates through the suction and discharge ports were assumed equal by neglecting the leakage flow through the pump casing. The LPP discharge pressure is calculated through the pump curve in Table 4.2. The LPP power consumption, $P_{e,LPP}$, is calculated from equation (4.34) based on the pump and motor efficiency.

$$P_{e,LPP} = \frac{Q_{LPP} \times \Delta p_{LPP} \times 10^2}{\eta_{p,LPP} \times \eta_{m,LPP}} \quad (4.34)$$

Table 4.2. Low-pressure pump specifications.

	Type	LOWARA CEA210/5/D-V		
Pump	Maximum flowrate (Q_{LPP})	18 m ³ /h		
	Efficiency ($\eta_{p,LPP}$)	0.53 %		
Pump curve	$Q_{LPP} = 7.2$ m ³ /h	$Q_{LPP} = 12$ m ³ /h	$Q_{LPP} = 18$ m ³ /h	
	$\Delta P_{LPP} = 2.82$ bar	$\Delta P_{LPP} = 2.66$ bar	$\Delta P_{LPP} = 2.31$ bar	
Motor	Power ($P_{e,LPP}$)	2.2 kW		
	Efficiency ($\eta_{m,LPP}$)	0.85 %		
	Pole ($N_{p,LPP}$)	2		

4.2.2.2 High-pressure pump

Specifications of the HPP are presented in Table 4.3 [160]. The pump flowrate is directly proportional to the shaft speed regardless of discharge pressure. The pump pressure differential, ΔP_{HPP} , is the difference between the RO feed pressure and the LPP supply pressure. The pump was controlled using a VFD that varies the supply frequency and voltage to proportionally control the rotational speed. The pump's rotational speed N_{HPP} is calculated as follows:

$$N_{HPP} = \frac{120F_{HPP}}{N_{p,HPP}} \quad (4.35)$$

where F_{HPP} is the VFD supply frequency and $N_{p,HPP}$ is the number of poles of the induction motor. Accordingly, the flowrate supplied by the pump Q_{HPP} is calculated from equation (4.36) based on the volumetric displacement $V_{d,HPP}$, assuming no leakage losses in the pump casing.

$$Q_{HPP} = V_{d,HPP} \times \frac{N_{HPP}}{60} \quad (4.36)$$

The shaft power transmitted by the HPP motor, $P_{shaft,HPP}$, is calculated from equation (4.37), which is an empirical formula provided by the pump's manufacturer. The HPP power consumption, $P_{e,HPP}$, is calculated from equation (4.38) based on shaft power and motor efficiency.

$$P_{shaft,HPP} = \frac{16.7 \times Q_{HPP} \times 3600 \times \Delta P_{HPP}}{530} \quad (4.37)$$

$$P_{e,HPP} = \frac{P_{shaft,HPP}}{\eta_{m,HPP}} \quad (4.38)$$

Table 4.3. High-pressure pump specifications.

	Type	Danfoss APP 3.5		
Pump	Maximum flowrate (Q_{HPP})	3.5 m ³ /h		
	Volumetric displacement ($V_{d,HPP}$)	20.54×10^{-6} m ³ /rev		
	Power ($P_{e,HPP}$)	11 kW		
Motor	Efficiency ($\eta_{m,HPP}$)	1/1	3/4	1/2
		92.5%	92.7%	90.9%
	Pole ($N_{p,HPP}$)	2		

4.2.2.3 Energy recovery device

Specifications of the Danfoss iSave are shown in Table 4.4 [161]. The iSave's motor was controlled using a VFD for flow control. The iSave's motor speed, N_{iSave} , is calculated from equation (4.39), such that F_{iSave} is the supply frequency and $N_{p,iSave}$ is the number of poles of the induction motor. The flowrate through the iSave is calculated based on the volumetric displacement, $V_{d,iSave}$, from equation (4.40).

$$N_{iSave} = \frac{120F_{iSave}}{N_{p,iSave}} \quad (4.39)$$

$$Q_{iSave} = V_{d,iSave} \times \frac{N_{iSave}}{60} \quad (4.40)$$

The iSave power consumption $P_{e,iSave}$ is calculated from equation (4.41) based on the shaft torque τ_{shaft} , the motor efficiency $\eta_{m,iSave}$ and the rotational velocity ω (rad/s). The shaft torque and motor efficiency are presented in the iSave's datasheet [161].

$$P_{e,iSave} = \frac{\tau_{shaft} \times \omega}{\eta_{m,iSave}} \quad (4.41)$$

The lubrication flow for the iSave is presented based on the iSave flowrate Q_{iSave} and the brine pressure P_b in Fig. 4.3 [161]. Slight mixing occurs between the brine and seawater

streams due to the lack of a physical barrier between them [163]. The increase in feed concentration can be estimated by calculating the outlet feed salinity from the mixing percentage as follows [126]:

$$\text{Mixing (\%)} = \frac{C_{i\text{Save}} - C_f}{C_b - C_f} \times 100 \quad (4.42)$$

where $C_{i\text{Save}}$ is the concentration of the High-pressure (HP) feed leaving the iSave, C_f is the feedwater concentration and C_b is the HP brine concentration. The mixing volume is primarily subject to the flow balance between the HP and LP ducts of the pressure exchanger. The iSave was assumed to be operating with a balanced flow to minimise calculations, at which the volumetric mixing is estimated at 5% [161].

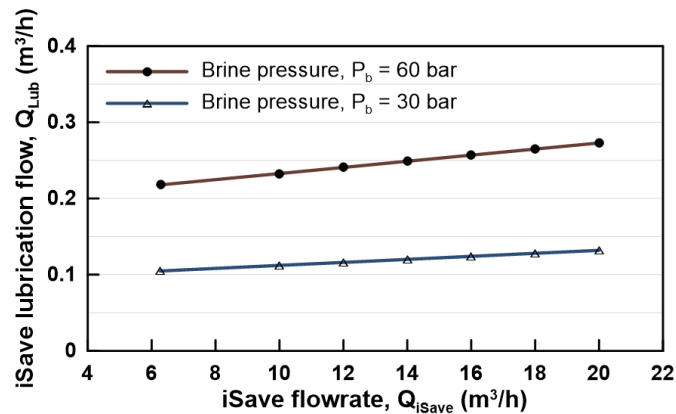


Fig. 4.3. Lubrication flow required to lubricate the iSave moving parts.

Table 4.4. Energy recovery device specifications [161].

	Type	Danfoss iSave 21 Plus		
Pump	Flowrate ($Q_{i\text{Save}}$)	6 - 22 m³/h		
	Volumetric displacement ($V_{d,i\text{Save}}$)	273×10^{-6} m³/rev		
	Power ($P_{e,i\text{Save}}$)	5.5 kW		
Motor	Efficiency ($\eta_{m,i\text{Save}}$)	1/1	3/4	1/2
		87.7%	88.2%	87.1%
	Pole ($N_{p,i\text{Save}}$)	4		

4.2.3 Wind turbine

The wind turbine used in the simulations is the Ryse Energy (Blackpool, United Kingdom) E-10, which is a 3-bladed horizontal axis wind turbine that delivers 10 kW rated power, thus matching the power requirement of the laboratory RO system [185]. Initially, the wind turbine performance was represented using a single-mass dynamic model, as in [186], which included the rotor and generator inertia in the rotor speed calculation. However, the inertial response was found to be negligible due to the low mass of the rotor and generator assembly, which showed an insignificant delay in rotor speed relative to changes in wind speed. The effect of such inertia would be more significant for larger wind turbines and would tend to smooth the power output under fluctuating wind conditions. Thus, for the selected turbine, a simple quasi-steady-state model was used to calculate the wind power using the wind turbine power curve. This quasi-steady-state model reflects the real-time wind speed fluctuations without any delays, leading to the design of a more robust control system. If the control system can accommodate the rapid fluctuations from a small, zero-inertia wind turbine, it will also be able to accommodate those from a larger turbine, and from a range of RE sources in general. The wind turbine power curve for the E-10 wind turbine is presented in Fig. 4.4 [185].

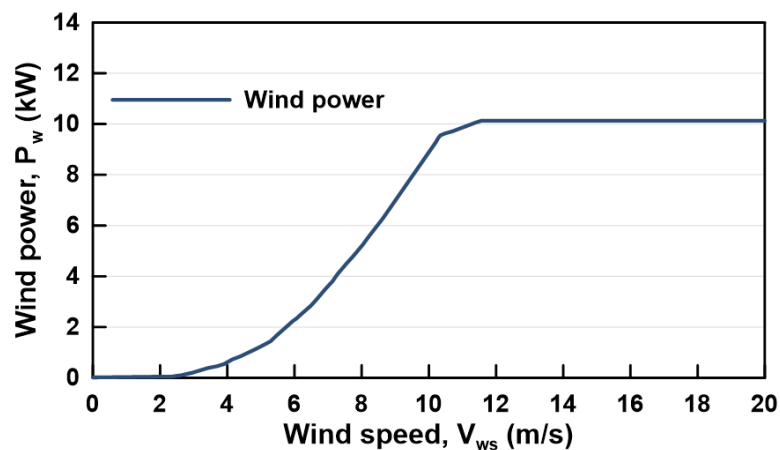


Fig. 4.4. Wind turbine power curve.

4.3 Model implementation

MATLAB-Simulink was used for implementing the RO system dynamic model. It uses a graphical programming environment for modelling, simulating, and analysing dynamic systems. The RO system was modelled in the form of interconnected blocks, with each block representing a specific component, i.e., RO pressure vessels, LPP, ERD, HPP, and wind

turbine. The component blocks were connected hierarchically by their input/output operating parameters. This modelling approach is beneficial for representing the relationship between all the components and the dependencies of operating parameters on each other. Another advantage of using MATLAB-Simulink is its ability to solve algebraic loops using Newton's method. This is important for modelling a system such as an RO plant in which the operating parameters of a component can be dependent on the states of the downstream components. For example, the flowrate through a centrifugal pump is function of the pressure downstream of the pump. This requires model states to be fed backwards for the model to converge.

The Simulink solver was set to a fixed sample time of 0.1s and it used ode14x for calculating the model's states. Ode14x uses a combination of Newton's method and an extrapolation from the current value to calculate the model's states at the next time step. The model inputs were the wind speed, HPP speed, iSave speed, feed temperature and feed concentration. The model outputs were the power consumption of the LPP, iSave and HPP, SEC, permeate recovery, and the stream characteristics (flowrate, pressure, and concentration) of the feed, brine and permeate flows.

4.4 Model validation

This section describes the model validation using measured data collected from the lab RO system. The model prediction accuracy was assessed for predicting the permeate flowrate, brine flowrate, feed pressure, permeate concentration, and power consumption, for defined inputs, i.e., the HPP and iSave speed, and input disturbances. The model steady-state output and dynamic response prediction accuracy are presented as follows:

4.4.1 Steady-state model validation

The steady-state model outputs were compared to measured data obtained with varying feed concentration (25,000 to 40,000 mg/l) and feed temperature (20 to 30°C). The data were recorded and averaged for one minute after the permeate concentration stabilised, thus indicating that the system reached steady state. Details of the measuring instruments and experimental errors can be found in Section 3.4. The dataset was simulated using the RO model at the same inputs and disturbances and compared to the experimental data. A regression analysis showing the correlation between the experimental and simulated data is shown in Fig. 4.5. The prediction accuracy was assessed using the coefficient of determination (R^2) and Root Mean Square Error (RMSE), as summarised in Table 4.5. The

model showed high accuracy for predicting the permeate flowrate, brine flowrate, feed pressure and power presented by a R^2 of 0.93, 0.97, 0.98 and 0.99 and a RMSE of 0.253 m^3/h , 0.14 m^3/h , 1.124 bar and 0.303 kW, respectively. The prediction accuracy for the permeate concentration was more modest compared to other parameters, at a R^2 of 0.77 and RMSE of 70.145 mg/l, due to an overestimation of the permeate concentration at low flowrates, as shown in Fig. 4.5 (e). To ensure that this overestimation is not a modelling error, the simulated data were compared to that of ROSA, at the same inputs and disturbances, and a correlation presented by a R^2 of 0.97 was achieved, which validated the accuracy of the model. Since the deviation between the model and actual permeate concentration is an overestimation, it should not affect the results in terms of the actual product quality exceeding 500 mg/l.

Fig. 4.6 compares the measured and simulated data of the feed pressure and power consumption for a specific permeate flowrate. The error between the measured and simulated feed pressure and power consumption remained below $\pm 2.5\%$ and $\pm 4.7\%$, respectively. The estimated experimental error for the feed pressure and power consumption based on the accuracy of measuring instruments were 0.25% and 0.5%, respectively.

Table 4.5. Validation of the Steady-state model output represented by the coefficient of determination (R^2) and Root Mean Square Error (RMSE).

	Permeate flowrate (Q_p)	Brine flowrate (Q_b)	Feed pressure (P_f)	Power ($P_{e,total}$)	Permeate concentration (C_p)
Regression analysis	$R^2 = 0.93$	$R^2 = 0.97$	$R^2 = 0.98$	$R^2 = 0.99$	$R^2 = 0.77$
RMSE	0.253 m^3/h	0.14 m^3/h	1.124 bar	0.303 kW	70.145 mg/l

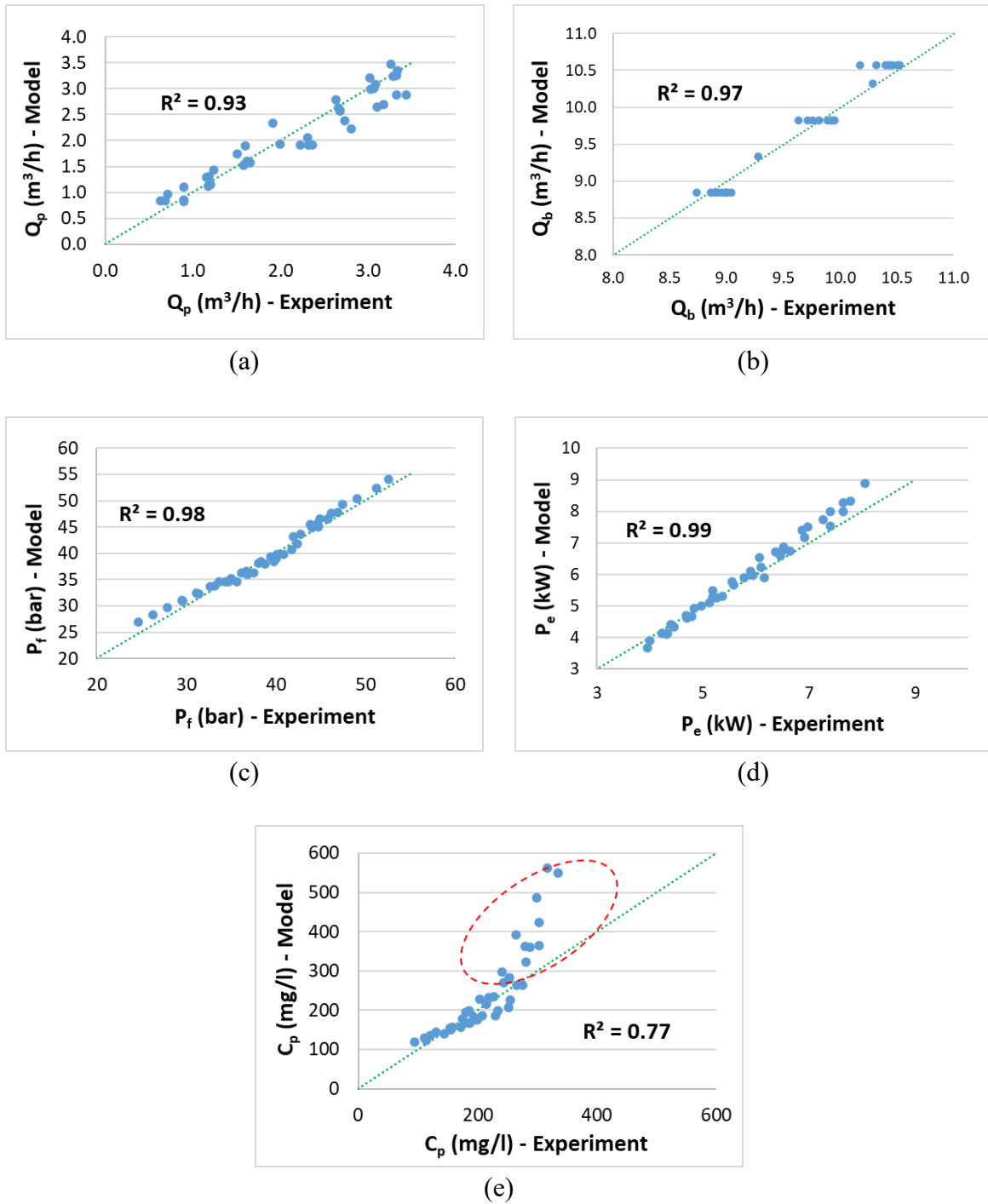


Fig. 4.5. Regression analysis showing the correlation between the experimental and simulated data for the a) permeate flowrate, b) brine flowrate, c) feed pressure, d) power consumption and e) permeate concentration.

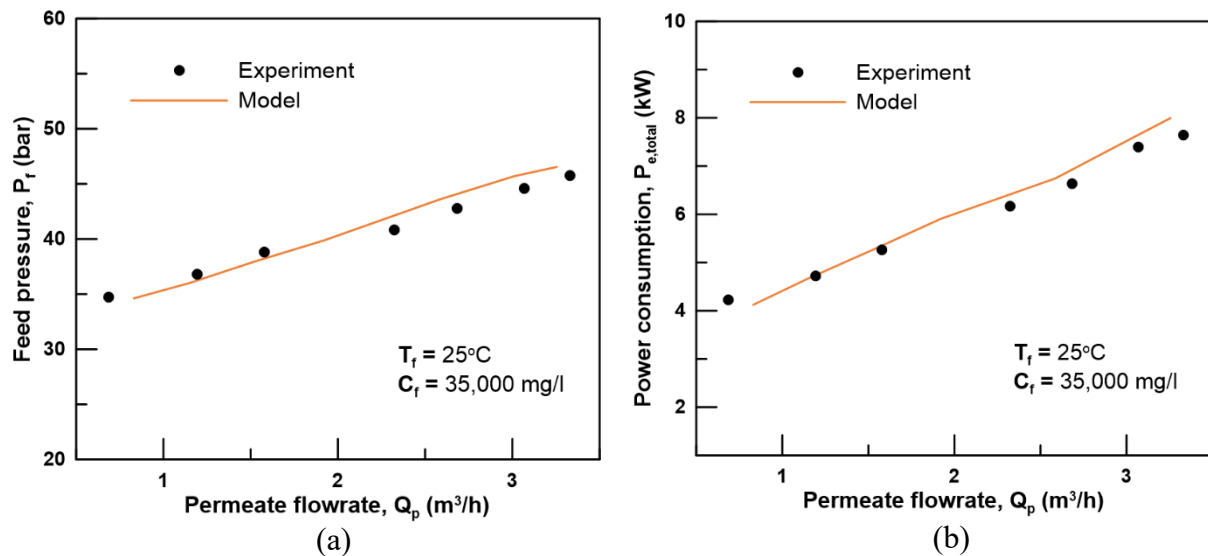


Fig. 4.6. A comparison between the measured and simulated a) feed pressure and b) power consumption for the same permeate flowrate. The data is collected at a feed concentration of 35,000 mg/l and a feed temperature of 25°C.

4.4.2 Dynamic model validation

The model prediction accuracy for the plant dynamic response was assessed by its ability to predict a transient change in permeate flowrate, feed pressure, and permeate concentration for a 10% step-change in the HPP rotational speed, N_{HPP} . As for the brine flowrate, a validation for its dynamic response was not possible due to lack of resources to install a flowrate sensor with high-pressure rating on the iSave high-pressure inlet/outlet line. Instead, the brine flowrate was calculated using mass balance via the low-pressure flowrate sensors and the developed model was validated for estimating the steady-state value, as presented in Fig. 4.5 (b). Nonetheless, this does not affect the results or accuracy of this model as the dynamic response of the brine flowrate to changes in the iSave speed is expected to be instantaneous due to using a positive displacement booster pump.

Fig. 4.7 presents the measured and simulated system response for a step-change in permeate flowrate. The model provided high accuracy in predicting the measured data, as the error remained within a $\pm 5\%$ margin along the step-test. The change in permeate production reached steady state almost instantly for the change in HPP speed. This was due to using a positive displacement HPP, where the pump discharge flow is directly proportional to the pump speed. The fluctuations in the measured flow data were due to the sensitivity of the paddle-wheel flow sensor to any turbulence or pulsation in the flow stream. The data collected from the step-test were later used in the control system design and tuning in Section 5.3.

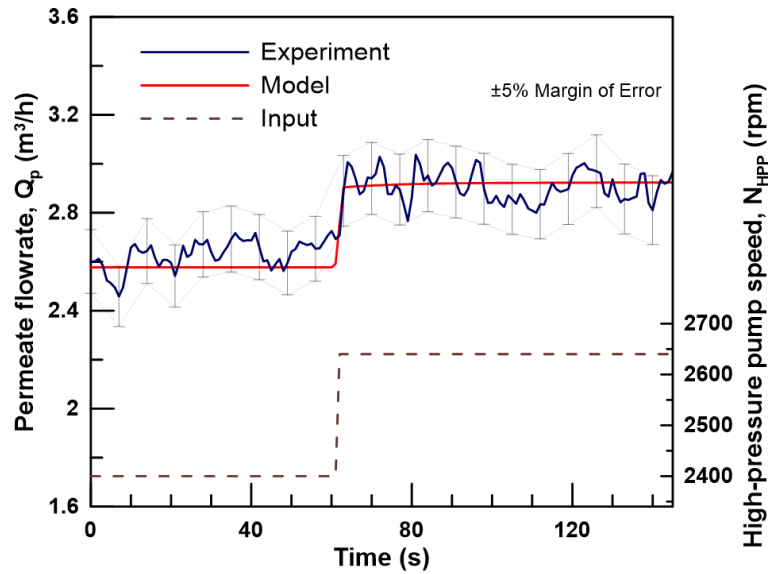


Fig. 4.7. Validation of model accuracy for predicting the permeate flowrate dynamic response. The step-response test was performed at 28°C feed temperature and 35,195 mg/l feed concentration. The permeate recovery varied from 20.7% to 22.9%.

The model also delivered high accuracy when simulating the feed pressure. As shown in Fig. 4.8, the measured and predicted data remained within a 3% error margin. The change in feed pressure due to a step-change in HPP speed exhibited two characteristic behaviours. Initially, the change in pressure was instantaneous in alignment with the change in HPP discharge flow and increased flow volume in the brine channel. The second part of the response, exhibiting the characteristics of a first-order system, was an osmotic pressure increase due to increased concentration and salt accumulation accompanying the increase in permeate flowrate.

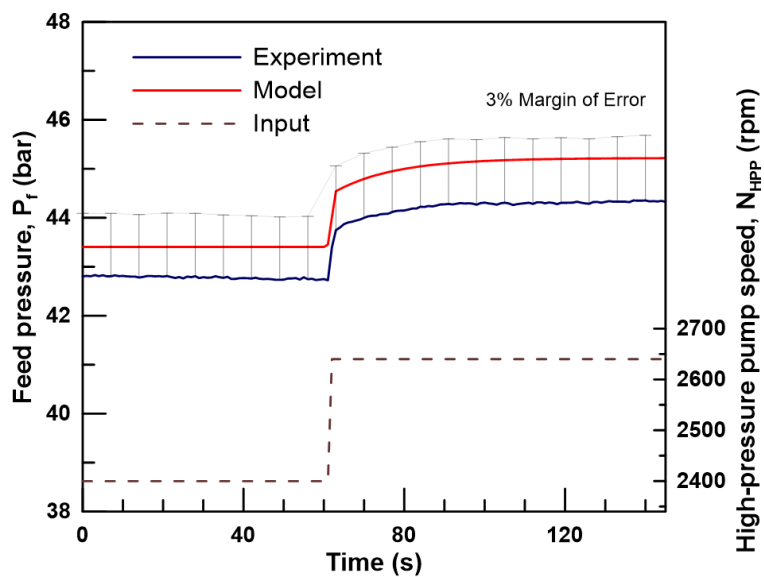


Fig. 4.8. Validation of model accuracy for predicting the feed pressure dynamic response. The step-response test was performed at 28°C feed temperature and 35,195 mg/l feed concentration. The permeate recovery varied from 20.7% to 22.9%.

The comparison between the predicted and measured permeate concentration due to a step increase in HPP speed is presented in Fig. 4.9. The model accurately predicted the decline in permeate concentration by approximating its response to a first-order system. The model showed high accuracy, such that the predicted and measured data remained within a 5% error margin. This confirmed the validity of the concentration conservation equations presented in Section 4.2.1.

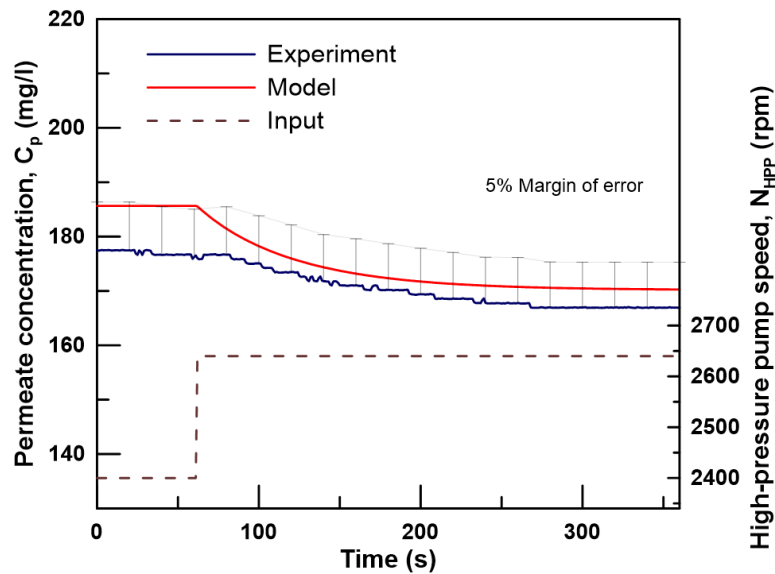


Fig. 4.9. Validation of model accuracy for predicting the permeate concentration dynamic response. The step-response test was performed at 27°C feed temperature and 35,429 mg/l feed concentration. The permeate recovery varied from 20.7% to 22.9%.

4.5 Summary

This chapter presented a bespoke dynamic model developed to predict the RO system performance. The model was based on the solution-diffusion theory and the Analytical-Film concentration polarisation theory. It has been implemented in MATLAB-Simulink and will be used in the development and testing of the control system, and the variable operation procedure. The model steady-state output and dynamic response prediction accuracy have been validated using experimental data from the RO system. The main conclusions are as follows:

- The model showed high accuracy for predicting the RO system steady-state performance. The prediction accuracy for the permeate flowrate, feed pressure, power and permeate concentration was presented by a R^2 of 0.93, 0.98, 0.99, and 0.77 and a RMSE of 0.253 m³/h, 1.124 bar, 0.303 kW, and 70.145 mg/l, respectively.

- Moreover, the model accurately predicted the transient change in permeate flowrate, feed pressure and permeate concentration for a 10% step-change in the HPP rotational speed, whereas the error between the predicted and measured data remained within a 5% margin along the step-test.

5 Chapter 5 Variable-speed operation: operation strategy and control system design

5.1 Introduction

The concept of ‘Variable Operation’ has been presented in recent studies and it has shown adequate performance compared to systems operating at constant load [11, 35]. Variable operation would allow direct operation of commercial RO plants by mature renewables, i.e., winds and solar energy, without the need for energy storage and backup systems [11, 35, 187]. Variable operation consists of two techniques, the choice of which depends on the extent of RE variation, i.e.:

- **Variable-speed operation:** The RO plant operates at variable production rate and permeate recovery to adjust its power consumption with respect to available energy [11]. This allows fine adjustment in matching RO system power consumption to RE fluctuations, but only over a limited power range.
- **Modular operation:** The RO units/trains are connected/disconnected depending on available energy. This relies on the modularity of RO systems to tackle the intermittency and considerable power variations of RE sources [66]. Though it accommodates larger variations, this technique only allows discrete changes in power input.

The possibility of combining variable-speed operation and modular operation as a load management technique for large-scale RO systems would give the greatest flexibility [187]. However, there are technical challenges in implementing variable operation in large-scale application [11]. This chapter focuses on tackling operation limitations specific to variable-speed operation.

To operate a RO system at variable speed, two steps are required. Initially, a safe operational window is defined to set the boundaries of acceptable variation in operating parameters [76, 79, 116]. Then, an operational strategy is selected that defines the control strategy for varying the operation parameters with respect to available power. This helps create a systematic approach to changing the operating parameters and thus match the RO consumption to available RE.

A study performed by Pohl et al. [79] compared the performance of four control strategies for a simple RO plant connected to a RES. The strategies controlled the feed flowrate and feed pressure to operate the system at either constant feed flow, constant feed pressure, constant concentrate flow or constant permeate recovery. The study concluded that maintaining constant permeate recovery provided the optimum performance regarding SEC, permeate quality and range of operation. Although, more recent studies [33, 188] have used constant recovery, others have used different control strategies [91, 189, 190], suggesting that the optimum control strategy depends on system design and operation requirements. This emphasizes the importance of using system configurations and components that are used in large-scale system to develop solutions that are transferable to commercial applications [11].

Another challenge is developing a control system having fast and robust performance when implementing the chosen operational strategy. Although control system performance is crucial, only a few studies have discussed this topic for RE-powered RO plants [11, 145]. An investigation by Carta et al. [33] reported a mismatch between power generated by a wind turbine and the power consumption of a small-scale RO plant, despite using a stable 2-minute resolution wind speed signal as an input. Advanced control systems were recommended for their fast response in adjusting controlled variables, despite RE fluctuations and RO system inertia [11, 33, 68, 82].

This chapter aims to improve the efficiency of variable-speed operation of RE powered RO systems to facilitate implementation for large-scale applications. The RE source considered is wind energy, as it is a good representation of a fluctuating and intermittent energy source that does not have a predictable pattern. Other types of RE, such as solar, generally vary more slowly and predictably; therefore, a solution developed for wind is expected to accommodate a range of RE types. The objectives for this chapter are to:

- Present an optimised variable-speed operation technique using a RO system having comparable performance to large-scale plants.
- Investigate and compare the performance of alternative control strategies to vary the operating parameters with respect to changes in available power from a wind turbine.
- Design and implement an advanced control system based on MPC and compare its performance to a conventional PID controller.

The chapter is structured as follows. Section 5.2 outlines the development process for an optimised operation strategy. Section 5.3 presents the PID and MPC control systems design. The results and discussion are presented in Section 5.4, where a sensitivity analysis to define the effect of input disturbances on system performance is introduced. The analysis and selection of an optimum operational strategy is also presented, and a detailed comparison between the conventional PID controller and MPC is performed. Section 5.5 summarises the findings and conclusions of this chapter.

5.2 Variable-speed operation

Variable-speed operation involves operating the RO system at varying power consumption based on available energy. The plant's power consumption is varied by changing operating parameters that affect production rate and permeate recovery [11]. The process of defining a safe operational window and operation strategy is described as follows:

5.2.1 Definition of an operational window

The operational window defines the acceptable range of parameter variation for safely operating the RO system. Several studies [76, 79, 116] have presented design specific operational windows but all using the same general concept. The operational window is defined based on the RO membrane constraints across the feed pressure and flowrate using the ROSA software. A full description of the procedure replicated in this study can be found in [79]. Constraints of the FilmTec™ SW30HRLE-400 membranes are described as follows [79, 142]:

- 1) Maximum feed pressure that the membrane can withstand (83 bar).
- 2) Maximum allowed feed flow based on the membrane mechanical loading (14 m³/h).
- 3) Maximum permeate flow per element (1.4 m³/h) and the maximum recovery per element (13%) that could lead to excessive concentration polarisation.
- 4) Minimum concentrate flow to avoid salt precipitation and membrane fouling (3.4 m³/h).
- 5) Maximum product concentration based on the recommendations of the WHO (500 mg/l).

As presented in Fig. 5.1, the operational window was defined for two pressure vessels in parallel, each containing three SW30HRLE-400 RO elements in series, for feedwater of 35,000 mg/l NaCl concentration at 25°C. During the process of RO system development, the system design and component selection reflected the limitation imposed by the operational window. More complexity can be added to the operational window development by considering variations in feed concentration and temperature, in addition to using other operation parameters such as permeate flowrate, permeate quality, power consumption and SEC [33].

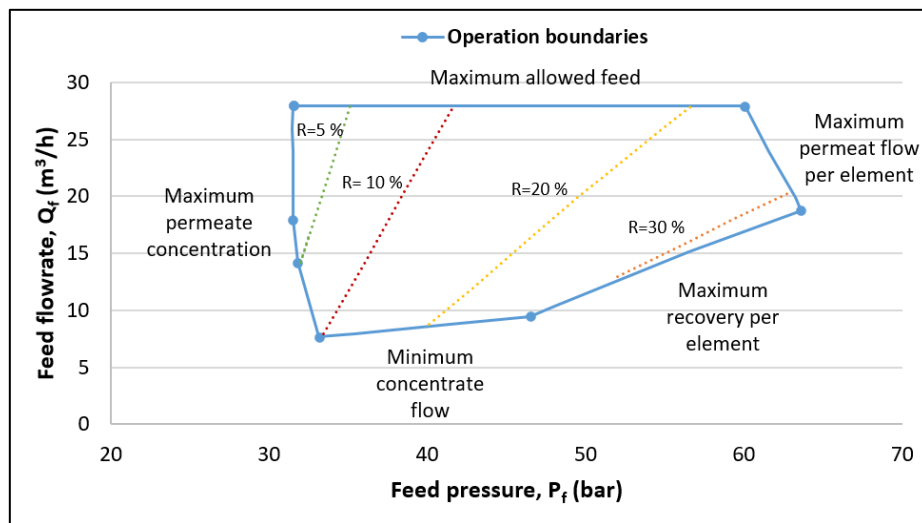


Fig. 5.1. Safe operational window.

5.2.2 Development of an operational strategy

The second step in implementing variable-speed operation is developing an operational strategy for the plant to respond optimally to wind power variation [11]. The operational strategy is developed by mapping the controlled operating parameters corresponding to the RO system power consumption over the range of operation [11]. The controlled parameters are then varied during operation depending on available power from the wind turbine.

The process of generating an operational strategy depends on two procedures. Firstly, identifying the manipulated and controlled variables that have a direct effect on the RO power consumption, which could vary depending on system design. Secondly, defining a control strategy outlining how these controlled variables will vary depending on available power.

5.2.2.1 *Identifying the manipulated and controlled variables*

The manipulated variables are independent input parameters that are varied by the control system, e.g., pump speed or valve opening, to maintain the controlled outputs, e.g., flowrate or pressure, at a reference value corresponding to specific power consumption. For RO systems, the manipulated variables and controlled outputs directly affecting the power consumption depend on system design and used equipment. Previous studies [33, 79, 97, 116] have used feed flowrate and feed pressure as controlled outputs for varying the power consumption. This concept is true for systems using a throttle valve, a Pelton wheel, or a turbocharger in the brine reject line. These systems can offer active control of the feed pressure by manipulating the throttle valve opening or changing the input nozzle valve opening in case of a Pelton turbine or a turbocharger [11]. However, for the system used in this study and for systems using split-feed flow configuration in general, their operational control is based purely on flow control, such that the variation in system pressure is a by-product of changes in permeate flux, brine flowrate, feed concentration and temperature. To further explain, the split-feed flow configuration creates two flow loops through the RO membrane. The outer loop flow is supplied by the HPP, representing the permeate portion of the feed stream, and the inner loop flow is supplied by the iSave, representing the brine portion of the feed stream. This in turn creates two independent control loops, by which the HPP speed, N_{HPP} , directly controls the permeate flowrate and the iSave speed, N_{iSave} , directly controls the brine flowrate, and both ultimately dictate the power consumption.

Fig. 5.2 presents the finalised control system structure and signals between each element. The control system generates the control signal based on available wind power and input disturbances. The control system consists of the embedded operation strategy that generates the set-points for the permeate and brine flowrates corresponding to a specific power consumption, in addition to the controller that generates the control signal depending on the error signal. The controller then sends a control signal to the RO system to vary the manipulated variables, i.e., HPP and iSave speeds, to control the controlled variables, i.e., the permeate and brine flowrates.

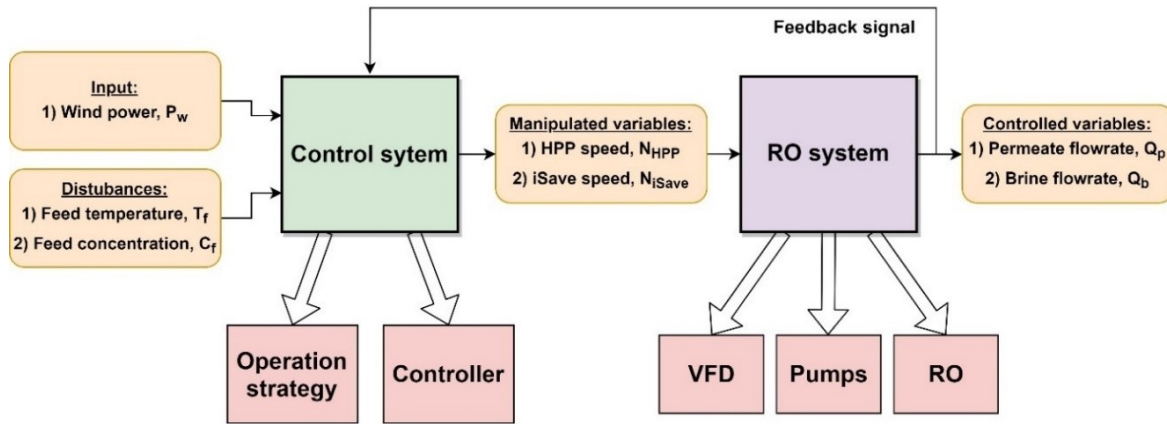


Fig. 5.2. High-level block diagram showing the control system structure and signals between each element.

5.2.2.2 Defining the control strategy

The control strategy defines the rule for changing the permeate and brine flowrates with respect to available wind power. The optimum control strategy should present a wide operation range, allowing for longer periods of permeate production, and operating at the lowest SEC, to efficiently utilize the available power [138]. An investigation was performed to determine the optimum control strategy considering, a) operation at constant recovery, b) operation at constant brine flowrate and c) operation at a constant feed flow. Operation at constant feed pressure was not considered, as it requires maintaining a constant permeate flowrate [79]. The investigation was performed by simulating the system performance along the full operation range using each control strategy. The results are presented in Section 5.4.2.

5.3 Control system design

This section presents the control system design for the PID and MPC controllers. The control system manipulated variables are the HPP speed N_{HPP} and iSave speed N_{iSave} . The controlled outputs are the permeate and brine flowrates. The input disturbances are the feed concentration and feed temperature.

5.3.1 Proportional-Integral-Differential controller

PID control is the most widely used process control technique for industrial applications, due to its simplicity and effectiveness [150]. The transfer function of a standard PID controller is presented in parallel form as follows:

$$G(s) = K_p + K_i \frac{1}{s} + K_d s \quad (5.1)$$

where K_p is the proportional gain, K_i is the integral gain, K_d is the derivative gain [191]. The proportional gain delivers a control action proportional to the present error value between plant input and the reference signal. The integral term eliminates steady-state error by summing the error over time. The derivative term adds damping and decreases overshoot by generating a control signal proportional to the rate of change of the process variable. For this study, only the proportional and integral terms were used, since the RO system open-loop response exhibited minimal overshoot and to avoid system instability that could occur due to sensors noise [33]. The derivative term is set to zero. For future investigations, a filter can be used to reduce the sensor noise when applying the derivative term, however, this is not in this study for the sake of simplicity.

The PID controller performance is dependent on the proportional, integral, and derivative gains. These tuning parameters are selected to generate a desired response based on the process dynamics [192]. Various techniques have been proposed for PID tuning that offer an educated guess for gain values for a stable system and provide a starting point for fine-tuning until the desired response is obtained [192, 193]. The PID tuning parameters were initially selected using the open loop Ziegler-Nichols tuning method, a popular PID tuning technique, and were later adjusted using the MATLAB PID Tuner to obtain an optimised performance [192, 193]. The PID Tuner allows for tuning the controller gains based on response time and transient behaviour for a step-input in the time domain [194-196]. The tuning parameters were selected to deliver the fastest rise time with minimum overshoot, while maintaining a change in pump speeds below 2 Hz/s for smooth operation [165]. The finalised PID tuning parameters are presented in Table 5.1. A schematic diagram of the PID controller developed is presented in Fig. 5.3. Depending on the wind turbine power and the selected operation strategy, the PID controllers receive reference signals for the permeate flowrate, $Q_{p,ref}$, and the brine flowrate, $Q_{b,ref}$. The controllers then generate control signals for the HPP speed, N_{HPP} , and iSave speed, N_{iSave} , which are sent to the VFDs for generating a variable frequency electric signal for the HPP, F_{HPP} , and iSave, F_{iSave} .

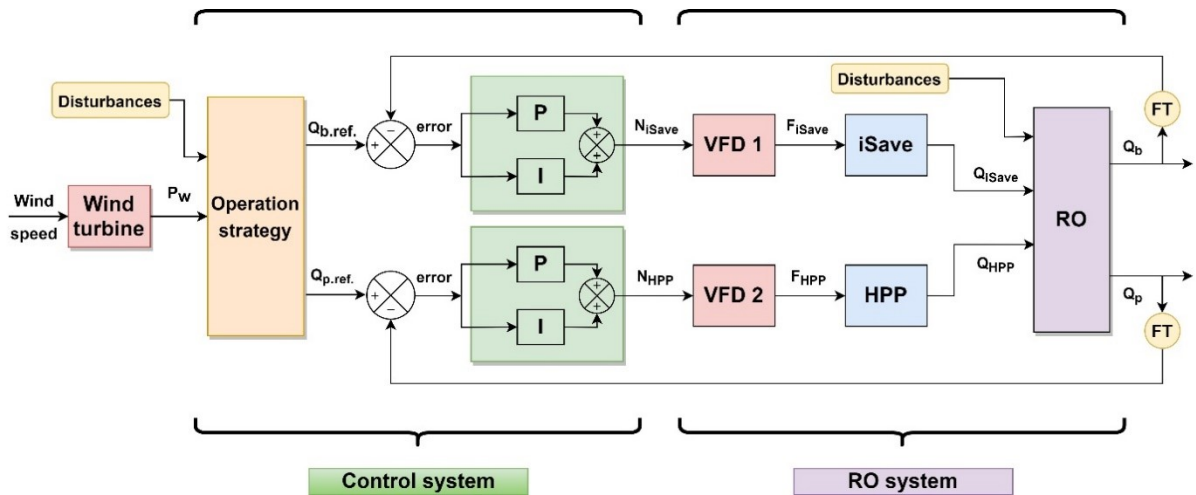


Fig. 5.3. Structure of the Proportional-Integral-Differential Controller. FT represents the flow transmitters sending feedback signals to the controller.

Table 5.1. Proportional-Integral-Differential (PID) controllers tuning parameters.

Derivative gain is set to zero for both controllers.

	Proportional gain (K_p)	Integral gain (K_i)
High-pressure pump	1.607	4.02
Danfoss iSave	0.1	0.615

5.3.2 Model predictive controller

MPC is an advanced control technique that is becoming increasingly popular for process control [197]. Unlike traditional PID control, MPC is specifically designed for multiple-input multiple-output systems and has the ability to handle system constraints such as those occurring in the RO process [150, 151].

Standard MPC comprises two components: a) a built-in dynamic model that predicts system response towards a control sequence, and b) an optimiser that calculates an optimal control sequence based on minimisation of the error between output and target values. During operation, the prediction and optimisation procedures are performed in parallel at each sample time, such that a control sequence is calculated from the optimisation problem and then tested on the prediction model for a specific prediction horizon [150]. The first control step of the control sequence is applied, and the prediction horizon is displaced one step forward to repeat the process and calculate a new control sequence. This is referred to as receding horizon approach [149]. The recalculation at each sample time is essential to

overcome inaccuracies in prediction and optimisation stages, and periodically make up for any unexpected disturbances.

The MPC controller used in this study is a direct extension of the Dynamic Matrix Control algorithm, which is a widely used MPC control algorithm [150, 198]. It uses a discrete state-space model as the prediction model and a quadratic criterion that is minimised over the prediction horizon to generate an optimal control sequence [199, 200]. The controller, presented in Fig. 5.4, receives a reference signal for the permeate flowrate, $Q_{p,ref}$, and brine flowrate, $Q_{b,ref}$, that are generated through the operational strategy, selected in Section 5.4.2, depending on the available wind power P_w . The controller generates a control signal in the form of HPP speed, N_{HPP} , and iSave speed, N_{iSave} , which are sent to the VFDs that generates an electric signal with the corresponding frequencies, F_{HPP} and F_{iSave} . The relation between the pump speeds, N , and input frequencies, F , are presented in sections 4.2.2.2 and 4.2.2.3 for the HPP and iSave, respectively. The MPC controller is developed using the MPC Designer of MATLAB-Simulink. The formulas for the prediction model and optimiser are described as follows:

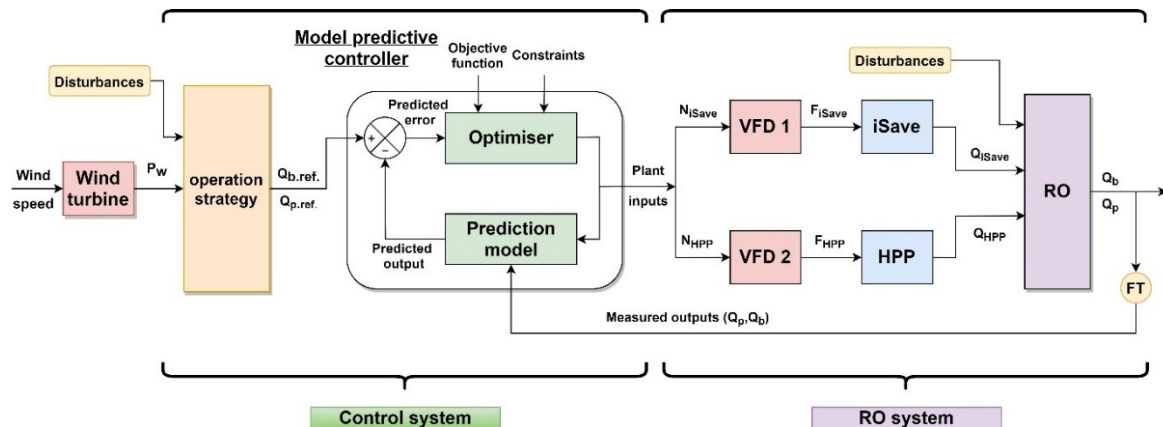


Fig. 5.4. Structure of the Model Predictive Controller.

5.3.2.1 Prediction model

The discrete linear time-invariant model used for prediction uses the following general form:

$$\mathbf{x}(k + 1) = \mathbf{A}\mathbf{x}(k) + \mathbf{B}\mathbf{u}(k) \quad (5.2)$$

$$\mathbf{y}(k) = \mathbf{C}\mathbf{x}(k) + \mathbf{D}\mathbf{u}(k) \quad (5.3)$$

where k is the sampling time, A , B , C and D are coefficient matrices for the model states, model inputs, model outputs and feedforward matrix, respectively. $\mathbf{x}(k)$, $\mathbf{u}(k)$ and $\mathbf{y}(k)$ are

vectors representing the model states, model inputs and model outputs respectively [201, 202]. The state-space prediction model was generated from input/output data using a data-driven modelling technique called System Identification [203]. System Identification is based on estimating values of the coefficient matrices by minimising the error between model output and measured response to fit the model to the input/output data [201]. The generated multi-input multi-output state-space model is as follows:

$$\begin{bmatrix} x_1(k+1) \\ x_2(k+1) \end{bmatrix} = \begin{bmatrix} -0.272 & 0 \\ 0 & -17.27 \end{bmatrix} \begin{bmatrix} x_1(k) \\ x_2(k) \end{bmatrix} + \begin{bmatrix} -0.3591 & 0 \\ 0 & 129900 \end{bmatrix} \begin{bmatrix} F_{HPP}(k) \\ F_{iSave}(k) \end{bmatrix} \quad (5.4)$$

$$\begin{bmatrix} Q_p(k) \\ Q_b(k) \end{bmatrix} = \begin{bmatrix} -0.0507 & 0 \\ 0 & 6.712 \times 10^{-5} \end{bmatrix} \begin{bmatrix} x_1(k) \\ x_2(k) \end{bmatrix} + \begin{bmatrix} 0 & 0 \\ 0 & 0 \end{bmatrix} \begin{bmatrix} F_{HPP}(k) \\ F_{iSave}(k) \end{bmatrix} \quad (5.5)$$

where the model inputs are the HPP input frequency F_{HPP} and the iSave input frequency F_{iSave} . The model outputs are the permeate flowrate Q_p and the brine flowrate Q_b . The data used for parameters estimation are time-domain input/output data recorded experimentally at 0.1s sampling interval during an open-loop step-response test of 10% deviation in the pumps' speed from the rated operating point. The model prediction accuracy is represented by its fit to the estimation data and RMSE in Table 5.2.

Table 5.2. Prediction accuracy of the State-Space model compared to the estimation data.

	Fit to estimation data	RMSE
Permeate flowrate, Q_p	86.83 %	0.00212
Brine flow, Q_b	81.25 %	0.00581

5.3.2.2 Optimiser

The MPC uses the prediction model to estimate the controlled outputs \mathbf{y} with respect to the manipulated inputs \mathbf{u} . The error between the predicted output and the reference values is minimised by generating an optimised control sequence $\mathbf{u}_k, \mathbf{u}_{k+1}, \dots, \mathbf{u}_{k+m-1}$ along the control horizon. The first element of the control sequence $\Delta\mathbf{u}(k)$ is sent to the plant as a control signal in the form of $\mathbf{u}(k) = \mathbf{u}(k-1) + \Delta\mathbf{u}(k)$. The remaining samples $\Delta\mathbf{u}(k+i)$ are discarded and a new optimisation problem is solved at the next sampling step $k+1$ based on new measurements. The control action at time k is calculated by solving the optimisation problem as follows [201, 202]:

$$\min_{\Delta \mathbf{u}(k), \dots, \Delta \mathbf{u}(k+H_c-1)} J = \sum_{i=0}^{H_p-1} \mathbf{W}_y [\mathbf{y}(k+i+1) - \mathbf{y}(k+i+1)_{ref}]^2 + \sum_{i=0}^{H_c-1} \mathbf{W}_{\Delta \mathbf{u}} [\Delta \mathbf{u}(k+i)]^2 + \sum_{i=0}^{H_c-1} \mathbf{W}_u [\mathbf{u}(k+i) - \mathbf{u}(k+i)_{ref}]^2$$

$$\text{Subject to: } \begin{cases} \mathbf{y}_{min} < \mathbf{y}(k+i) < \mathbf{y}_{max} \\ \Delta \mathbf{u}_{min} < \Delta \mathbf{u}(k+i) < \Delta \mathbf{u}_{max}, \text{ For } i = 0, \dots, H_p - 1 \\ \mathbf{u}_{min} < \mathbf{u}(k+i) < \mathbf{u}_{max} \end{cases} \quad (5.6)$$

where \mathbf{W}_u and $\mathbf{W}_{\Delta \mathbf{u}}$ and \mathbf{W}_y are the inputs, inputs increment and outputs weight factors, H_p and H_c are the prediction and control horizon, respectively. The weights set the priority of each variable behaviour to the overall performance. The weights for the controlled outputs (permeate and brine flowrate) were set to one, since each manipulated input (HPP and iSave speed) only affect one output, thus forming two independent control loops. The prediction horizon, H_p , is the future time horizon before which the controller aims to achieve the desired output response. It was selected to cover the process steady-state response to ensure that the entire process dynamics are considered and anticipate constraints violation early enough to allow for corrective action [204]. The control horizon, H_c , is the number of time steps of the control sequence that is computed. It was selected at a small value that would reduce the required computations while providing a robust control action [202]. \mathbf{y}_{ref} is the reference value for the output vector and \mathbf{u}_{ref} is a setpoint for the input vector, which is used if the input is desired to be at a certain value. In this MPC, the inputs are only constrained to minimum, \mathbf{u}_{min} , and maximum values, \mathbf{u}_{max} , in addition to limiting the rate of change of pumps speeds, $\Delta \mathbf{u}$, according to the manufacturer's recommendation. The weight, \mathbf{W}_u , that sets the input to a reference value, \mathbf{u}_{ref} , is set to zero. Overall, the calculation of the control sequence using the objective function is subject to a set of constraints that are specific to the plant's input/output physical limitations. The control parameters, constraints and weights defined for the MPC controller are presented in Table 5.3.

Table 5.3. The Model Predictive Controller tuning parameters.

Controller parameter	Value	
Sample time (k)	0.1 s	
Prediction horizon (H_p)	50 samples	
Control horizon (H_c)	2 samples	
Input constraints	Range	Rate
iSave speed (F_{iSave})	0 - 50 Hz	2 Hz/s
HPP speed (F_{HPP})	0 - 50 Hz	0.5 – 2 Hz/s
Output constraints	Range	Weight (W_y)
Permeate flowrate (Q_p)	0 – 3.5 m ³ /h	1
Brine flowrate (Q_b)	0 - 18 m ³ /h	1

5.4 Results and discussion

5.4.1 Sensitivity analysis

An input disturbance is an uncontrollable input parameter that acts on the system and affects its output response. Thus, the controlled outputs can exhibit different behaviour for the same inputs depending on input disturbances. As such, a vital step in control system design is defining the input disturbances and assessing the controller's ability to maintain a target value despite changes in disturbances. Accordingly, a sensitivity analysis was performed to analyse the influence of initially selected input disturbances, i.e., feed concentration and temperature, on the RO plant operation.

5.4.1.1 Concentration

Fig. 5.5 presents the effect of feed concentration on operating parameters. The feed concentration was varied from 25,000 to 40,000 mg/l with 5000 mg/l increments. The data was collected experimentally from the RO system at a standard feed temperature of 25°C with a $\pm 1^\circ\text{C}$ uncertainty. Fig. 5.5 (a) shows that the feed concentration has an impact on the process pressure, such that the feed pressure required to achieve the same permeate flux increased at higher feed concentrations. The increase in required pressure led to more torque acting on the HPP motor shaft, thus requiring more power and higher SEC for the same permeate flux, which is evident in Fig. 5.5 (b). As for the permeate quality, Fig. 5.5 (c) shows

that the permeate concentration increased for higher feed concentration due to higher salt gradient across the membrane.

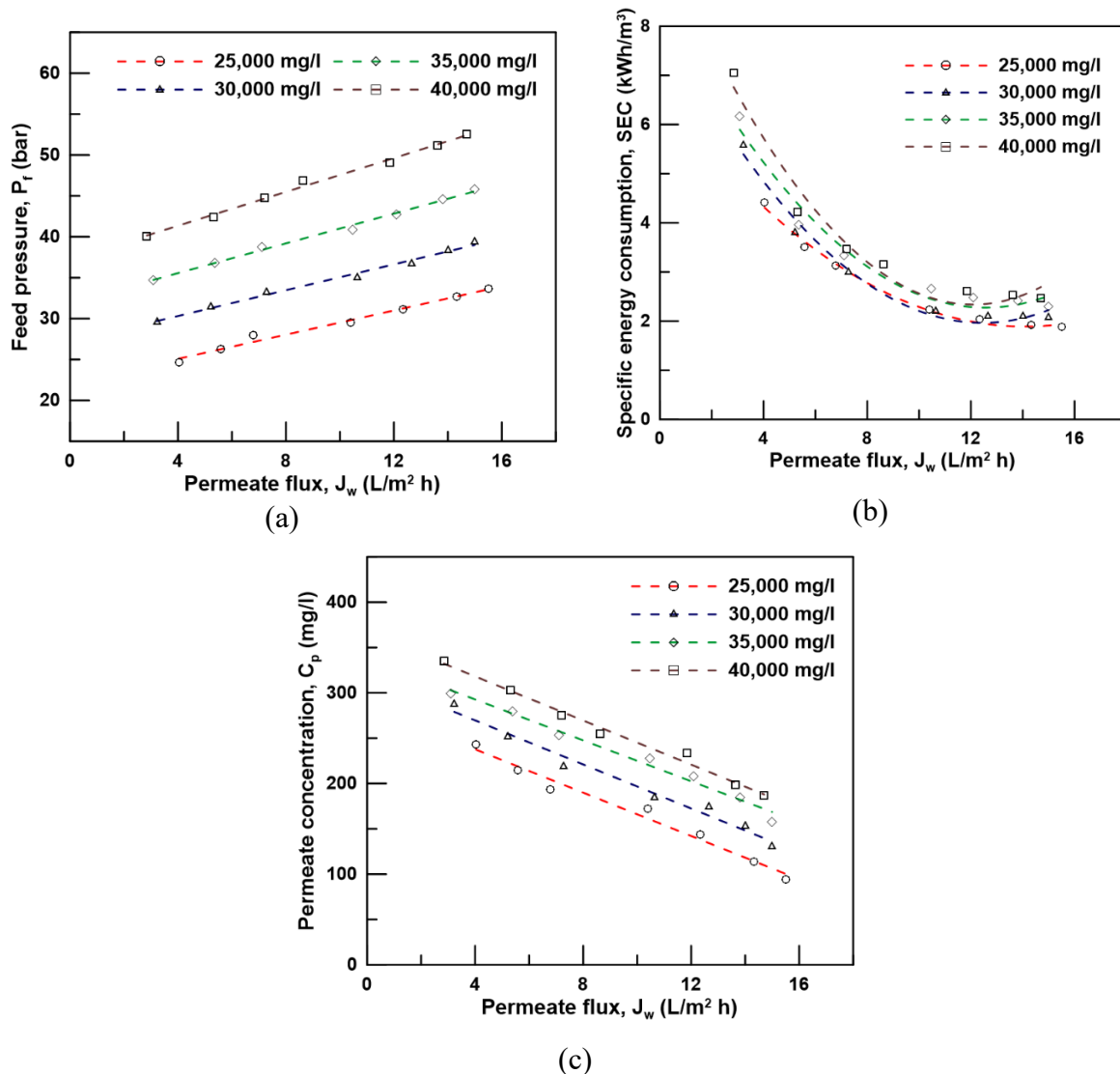


Fig. 5.5. Sensitivity analysis for the effect of feed concentration on a) feed pressure, b) specific energy consumption, and c) permeate concentration.

5.4.1.2 Temperature

The effect of feed temperature on feed pressure and permeate concentration is presented in Fig. 5.6. The feed temperature was varied from 20°C to 30°C, while the feed concentration was maintained constant at 35,000 mg/l. The notion behind including the temperature as an input disturbance is the effect it has on the water and salt permeability of the polymeric membrane. Higher feed temperatures can lead to changes in the physical properties of the membrane structure and possibly, changes in water diffusivity [205]. This was evident from the relationship between permeate flux and feed pressure presented in Fig. 5.6 (a), which showed that, for the same permeate flux, the required feed pressure was reduced at higher

temperatures. As for the permeate quality, Fig. 5.6 (b) shows an increased permeate concentration for the same permeate flux at higher feed temperature.

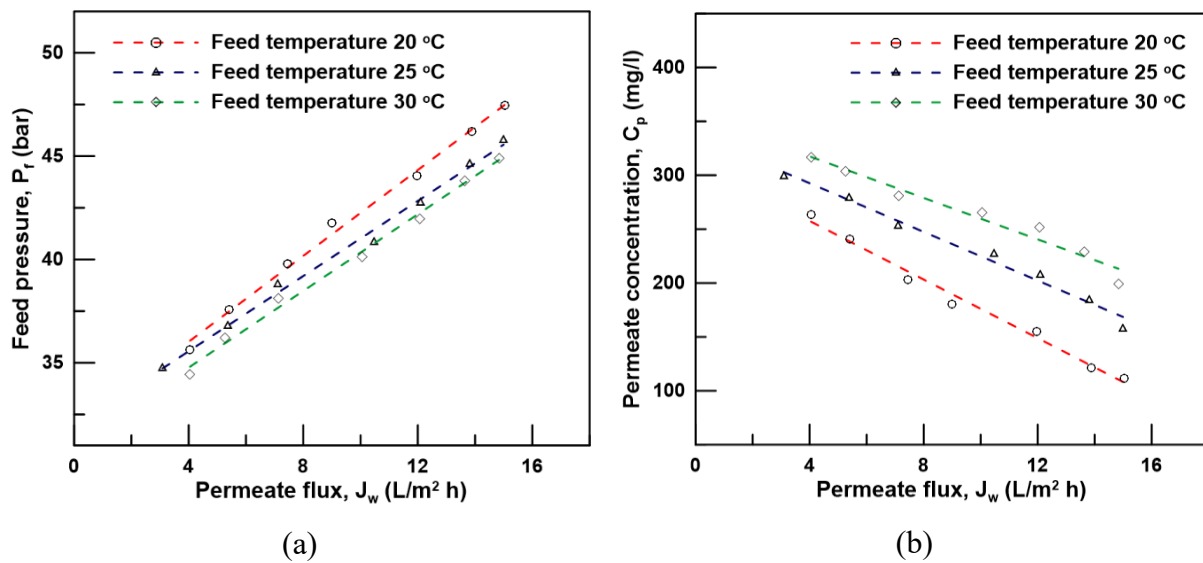


Fig. 5.6. Sensitivity analysis for the effect of feed temperature on a) feed pressure, and b) permeate concentration.

5.4.2 Operational strategy

5.4.2.1 *Selecting a control strategy*

The control strategies investigated were operation at constant recovery, constant brine flowrate or constant feed flowrate. A comparison between the control strategies is presented in Fig. 5.7. Operation at a constant recovery was considered at three recovery ratios (15, 20, and 24%). For operation at constant brine flowrate, the brine flow was maintained at the minimum flowrate, 9.8 m³/h, which allows for pressure higher than 1 bar on the iSave brine discharge [161]. The permeate flowrate was varied independently by manipulating the HPP speed as the brine was maintained constant, achieving variable recovery. For operation using constant feed flow, the permeate and brine flowrates were interchanged to maintain a constant feed flow at 13.3 m³/h, which is the sum of the minimum brine flowrate and maximum permeate flowrate.

In terms of operation range, Fig. 5.7 shows that operation at variable permeate recovery, i.e., constant brine flow and constant feed flow, guaranteed a wider operation range compared to operation at constant recovery. Moreover, the operation range for operating at constant recovery decreased for higher recovery ratios due to a drop in the brine flowrate below the set minimum.

As for the SEC, operating at constant recovery showed higher SEC compared to other strategies due to higher power consumption by the iSave. For operation at variable recovery, the constant brine flowrate strategy achieved the lowest SEC consumption due to minimised brine flowrate and operation at higher recovery ratios. Accordingly, operation with variable permeate recovery and constant brine flowrate was the optimum control strategy for this system configuration, as it allowed the widest operational range at lowest SEC. This finding contrasts with other studies that used constant recovery [33, 79, 188], thus highlighting the advantage of using a test-rig with similar performance to large-scale systems to determine a control strategy better suited to such scale.

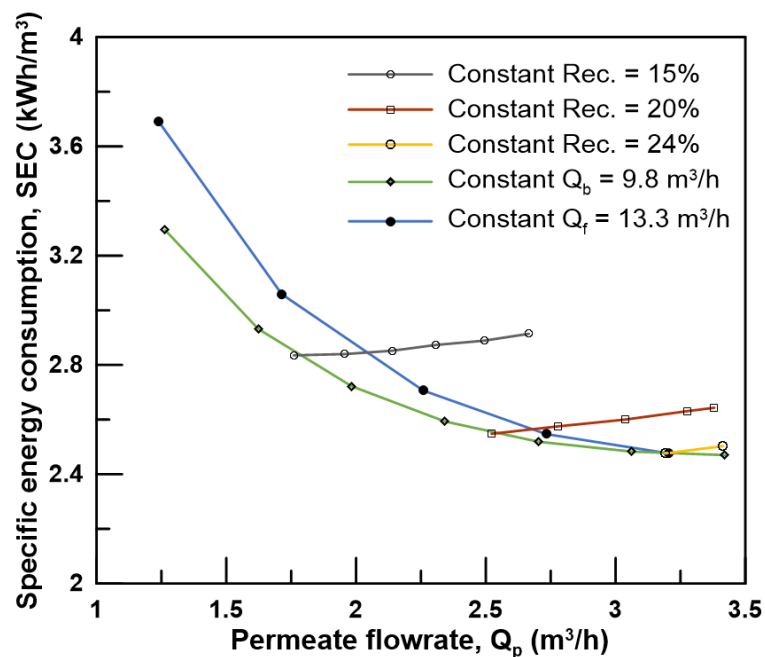


Fig. 5.7. Comparison of possible control strategies.

5.4.2.2 Mapping the controlled parameters

After defining an optimum control strategy, the controlled parameters are mapped with respect to power consumption, presented in Fig. 5.8, for the entire operating range while considering input disturbances, i.e., feed temperature and concentration, and maintaining the brine flowrate at a constant value. The data were calculated from the model at feed concentrations ranging from 30,000 to 40,000 mg/l and temperatures ranging from 20 to 30°C. The fine variation between the concentration and temperature ranges were accounted for by using linear interpolation. The generated operation parameters were then fed to the controller to generate the control signal for the HPP and iSave depending on the error signal. This approach of selecting the process parameters based on a complete overview of the

process inputs (i.e., available power, feed concentration and feed temperature) ensures a match between the RO system energy consumption and available power.

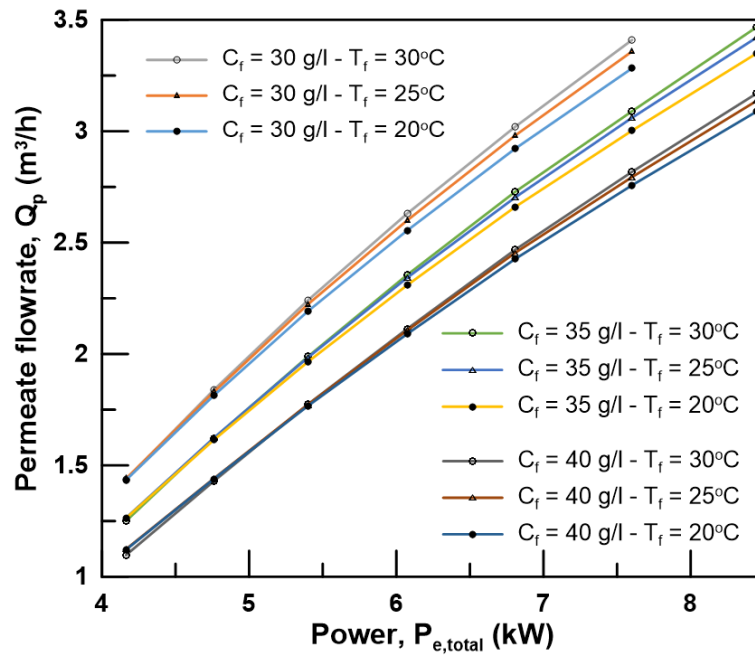


Fig. 5.8. The developed operational strategy based on variable recovery at a constant brine flowrate.

5.4.3 Control system performance analysis

The performance of the PID and MPC controllers are compared in this section. The controllers were assessed based on three criteria: a) tracking a reference signal during a step-change in a controlled variable, b) maintaining a reference signal during a step-change in an input disturbance, and c) cumulative permeate production for the same operating conditions. The control system analysis was performed using the dynamic model of chapter 4.

5.4.3.1 Reference tracking

The controller's ability to track a reference signal was assessed using a step-response test, whereby the simulation was stabilised and a step input of 10% increase in the controlled output was introduced. The step-response test for the PID controlling the HPP and the MPC was performed by introducing a step-change in the permeate flowrate reference signal from 2.57 m³/h to 2.827 m³/h at a feed concentration of 35,000 mg/l and 25°C feed temperature. The results, presented in Fig. 5.9 (a), showed a significant advantage for the MPC controller over the PID. The settling time, time until the error between the actual output and reference signal is within 2%, improved by 47% from 11.95s to 6.33s.

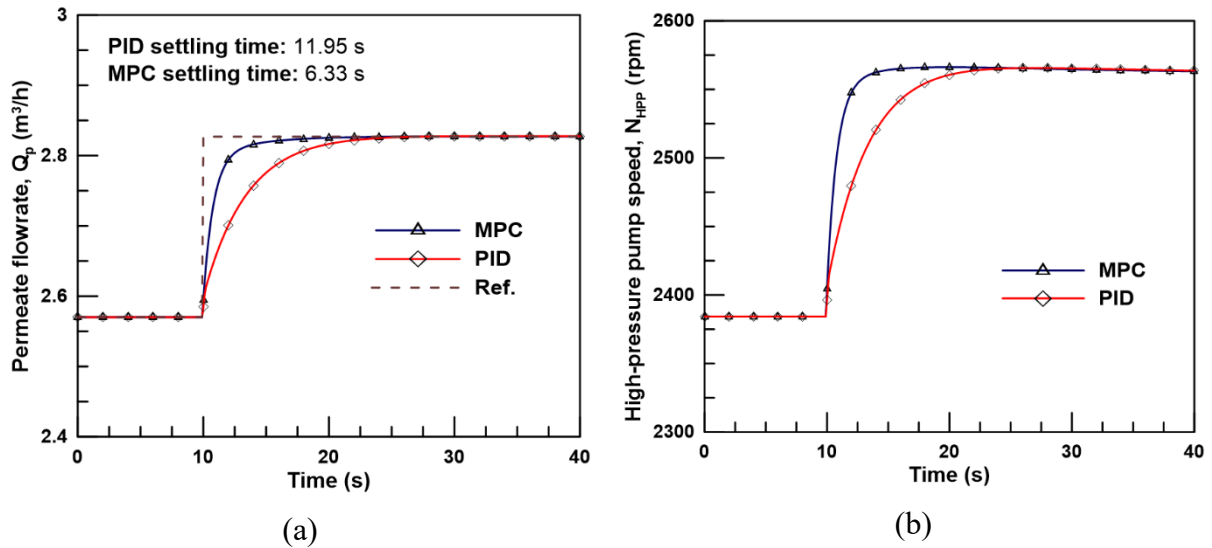


Fig. 5.9. The simulated PID and MPC controller's response to a 10% step change in the reference signal.

The step-response test performed for the MPC and PID controlling the iSave is presented in Fig. 5.10. A 10% step-change in the brine flowrate reference signal was introduced from 10.06 m³/h to 11.06 m³/h at a feed concentration of 35,000 mg/l and 25°C feed temperature. The MPC presented a faster response than the PID controller, improving the settling time by 92.1% from 13.18s to 1.04s.

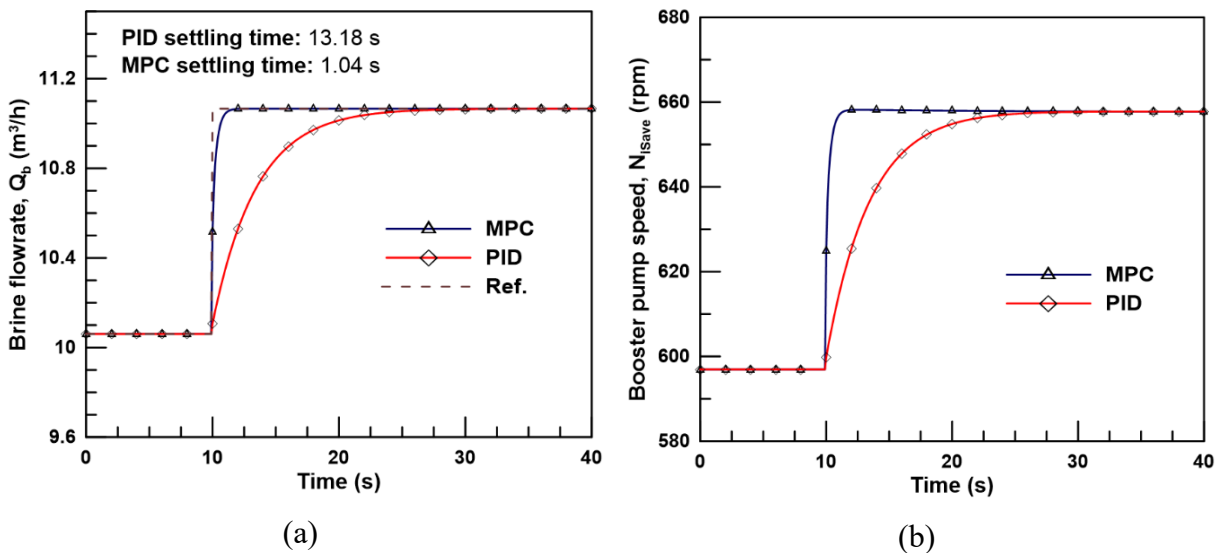


Fig. 5.10. The simulated PID and MPC controller's response to a 10% step change in the reference signal.

5.4.3.2 Disturbance rejection

The ability of the control system to maintain the power consumption at a reference level despite input disturbances is examined in this section. Based on the sensitivity analysis, the input disturbances considered were the feed concentration and feed temperature. Both of

these influence the system pressure leading to a deviation in power consumption relative to available power, if corrective action is not taken. The disturbance rejection tests were performed for both controllers by introducing a 10% step change in feed concentration from 35,000 to 38,500 mg/l at 25°C and a 10% step change in feed temperature from 25°C to 27.5°C at 35,000 mg/l. The controllers were compared for their ability to maintain a power consumption corresponding to a wind speed of 7.5 m/s against changes in disturbances.

Fig. 5.11 shows that the MPC controller offered a faster response to changing the permeate flowrate, such that the settling time improved by 47.2% from 13.3s for the PID to 7.02s for the MPC. However, the value of the power consumption reached steady-state at a similar time for both controllers.

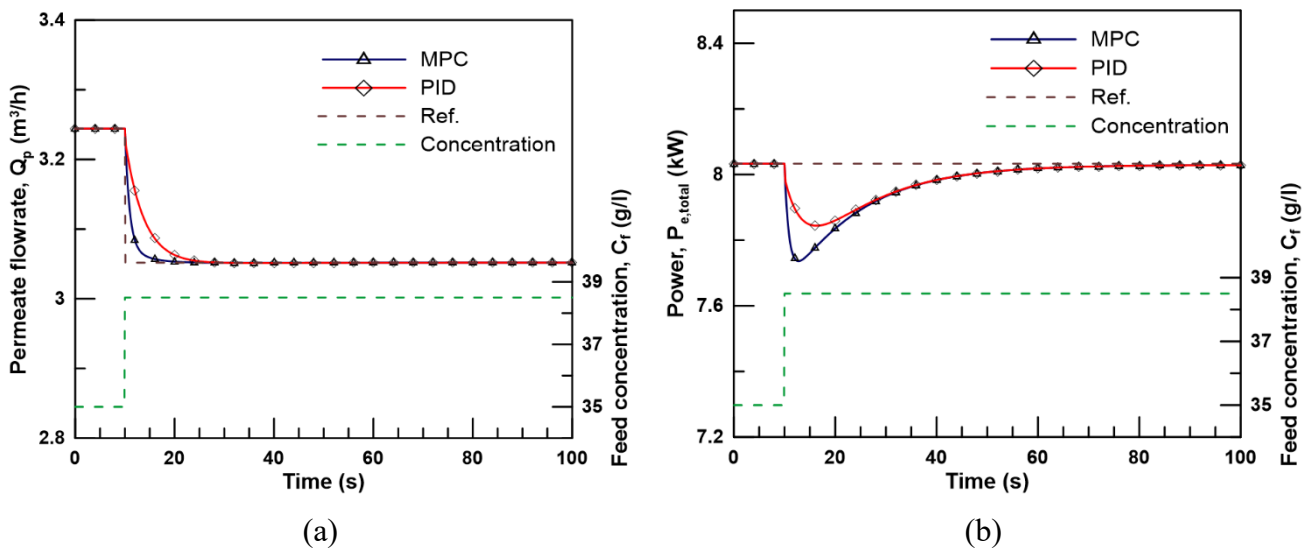


Fig. 5.11. Disturbance rejection test for a step-change in feed concentration presented by a) the permeate flowrate and b) the power consumption. The test is performed at a feed temperature of 25°C.

Fig. 5.12 shows the disturbance rejection test for a step-change in feed temperature. An increase in feed temperature led to an increase in membrane permeability, thus decreasing the required power for the same permeate flux. This allowed increasing the permeate flowrate and maintaining the power consumption at the reference value, thus achieving higher energy utilisation. The MPC showed a faster response to changes in feed temperature, such that the settling time for the permeate flowrate improved by 43.9% from 15.5s using the PID to 8.7s using the MPC. As for the power consumption, presented in Fig. 5.12 (b), the settling time improved from 25.74s using the PID to 19.36s using the MPC.

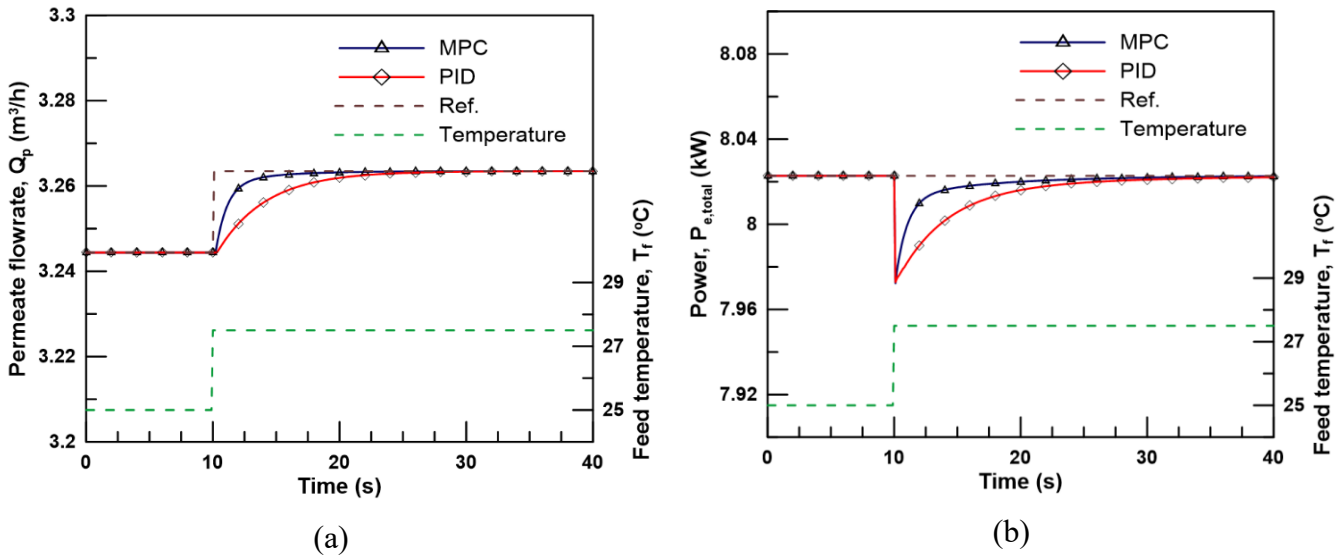


Fig. 5.12. Disturbance rejection test for a step-change in feed concentration presented by a) the permeate flowrate response and b) the power consumption. The test is performed at a feed concentration of 35,000 mg/l.

5.4.3.3 Performance projection

The control systems performance was compared during hourly operation by, a) analysing the match between actual and reference permeate production, and b) comparing the cumulative permeate production for the same input signal. Three wind speed scenarios with distinct wind speed variation were used, as presented in Table 5.4. The three wind speed scenarios were based on a random signal with Gaussian distribution around a mean speed of 6.5 m/s. A high-resolution sample time of 10s was selected for the three scenarios to reflect the wind speed fluctuations. The difference in variation intensity between each signal was subject to a standard deviation representing an increasing percentage of the mean speed as presented in Table 5.4. In addition, a high variation in feed concentration and temperature were introduced for each scenario to include the disturbance rejection performance of both controllers in the assessment. Each scenario was tested for one hour of operation with the same disturbance signal. A sample of the wind speed time-series used in the medium wind-variation scenario is presented in Fig. 5.13.

Table 5.4. Properties of the wind speed input and disturbance signals used for assessing the control systems performance.

Scenario	Signal type	Sample time	Mean	Standard deviation
Low wind-variation				0.325 m/s (5% of mean)
Medium wind-variation	Random	10 seconds	6.5 m/s	0.65 m/s (10% of mean)
High wind-variation	signal with			0.975 m/s (15% of mean)
Feed concentration-variation, C_f	Gaussian distribution		35,000 mg/l	700 mg/l (2% of mean)
Feed temperature-variation, T_f		1 second	25°C	0.5°C (2% of mean)

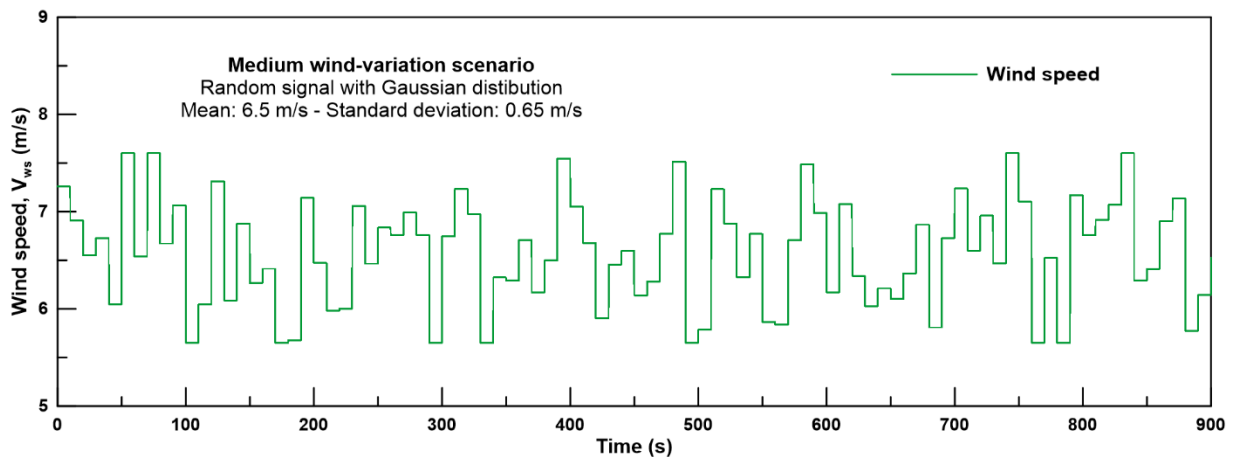


Fig. 5.13. A sample of the wind speed signal used in the medium wind-variation scenario.

Initially, the ability of the controllers to track a reference signal subject to wind speed fluctuations was assessed. The operational strategy defined in Section 5.4.2 was used to generate the permeate flowrate reference signal based on available wind power from each scenario. The PID and MPC controllers applied the control steps while maintaining a change in pumps speeds below 2 Hz/s in accordance with the manufacturers' recommendation [160, 165]. Fig. 5.14 and 5.15 show a sample (15 minutes) of the performance projection for the medium wind-variation scenario compared to the reference signal generated by the operational strategy for the PID and MPC controllers, respectively.

The PID controller showed adequate performance for tracking the reference signal at low wind speed fluctuations. However, there was an evident mismatch between the actual and

reference permeate flowrate in cases of high amplitude wind speed variation, which occurred as a delay in tracking the reference signal or overshoot from the steady-state value. On the other hand, the MPC performance, presented in Fig. 5.15, showed an efficient match between the actual and reference permeate flowrate at different levels of wind speed variation. The MPC showed less delay in tracking the reference signal and minimal overshoot from the steady-state value. The improved performance delivered by the MPC is associated with its predictive ability to test and optimise the control sequence before execution. A similar improvement occurred in the low and high wind-variation scenarios.

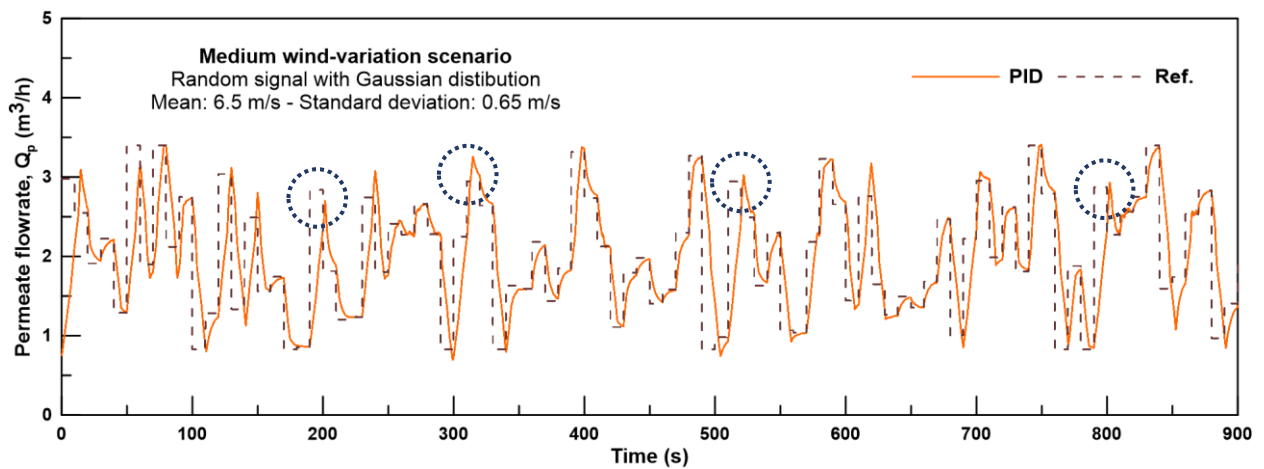


Fig. 5.14. Performance projection of the PID controller reference tracking capability for the input signal defined in the medium wind-variation scenario.

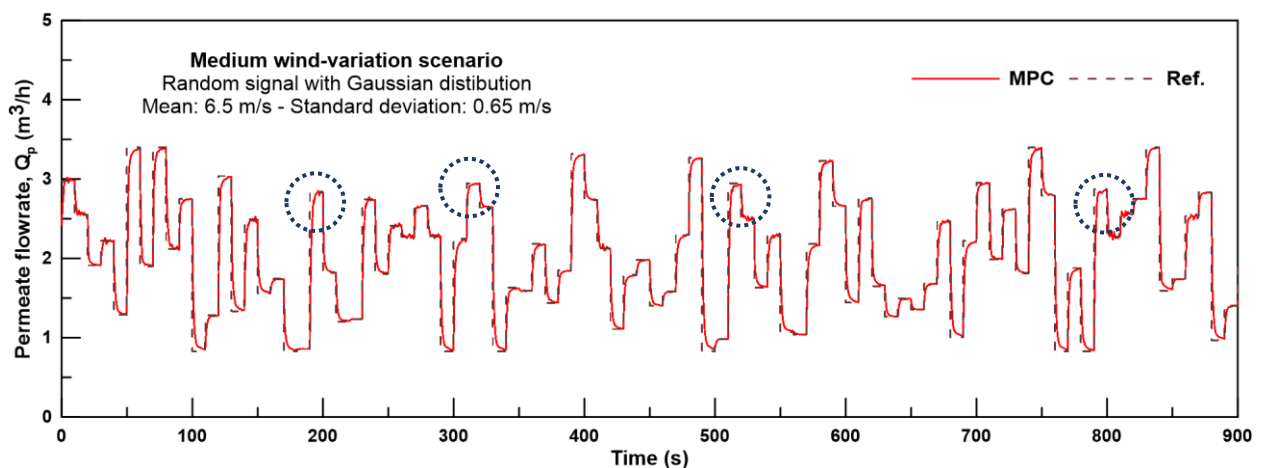


Fig. 5.15. Performance projection of the MPC controller reference tracking capability for the input signal defined in the medium wind-variation scenario.

To quantify the efficiency of the PID and MPC controllers in matching the variable reference signal, their cumulative permeate production for each scenario was compared for one hour of operation. In all three wind speed scenarios, the MPC controller achieved higher permeate

production per hour compared to the PID with varying amounts subject to wind speed fluctuations. Fig. 5.16 presents the improvement percentage in hourly permeate production when the MPC controller was used compared to the PID. The results showed that with increasing wind speed disturbance, the MPC delivered improved performance compared to the PID controller, which translated to higher permeate production and better utilisation of available wind energy. The improvement in permeate production per hour reached 0.31%, 1.76% and 2.35% for the low, medium, and high wind-variation scenarios, respectively. These improvements are considered a step-forward for operating RO systems with variable power, especially considering that the aim is to implement this type of control with medium to large-scale systems with capacities exceeding 40,000 m³/day [11].

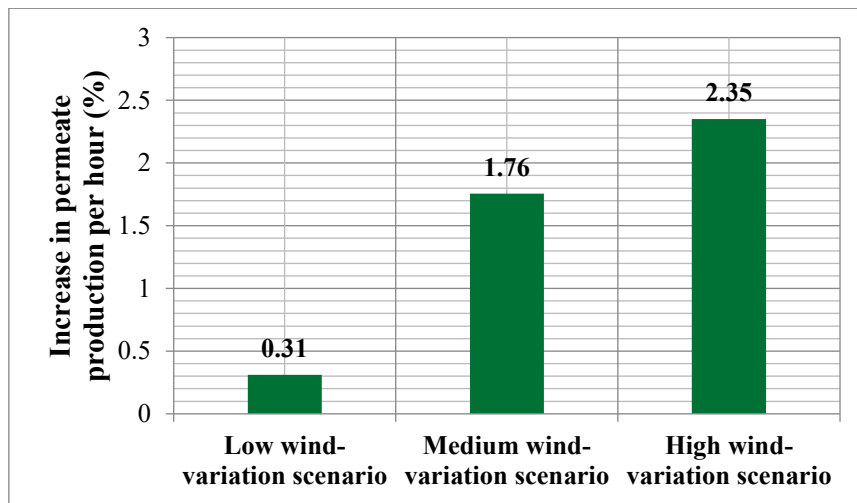


Fig. 5.16. Improvement in cumulative permeate production for one hour of operation due to using a model predictive controller instead of a proportional-integral-differential controller, for three scenarios are detailed in Table 5.4.

5.5 Summary

This Chapter has taken a novel approach to the integration of RO and RE. An optimised variable-speed operation technique has been developed using a RO system with similar characteristics to large-scale plants. The technique defines an operation strategy to optimally vary the RO system power consumption based on rapid power input disturbances from a wind turbine with negligible rotor inertia. In addition, an advanced MPC that delivers fast and robust performance has been developed to implement the optimised operation strategy. The main conclusions are:

- Feed concentration and temperature fluctuations can affect the RO system performance by altering the power consumption for the same HPP and iSave speeds.

This highlights the importance of including the input disturbances in control system design and operation strategy development, especially for systems subject to seasonal variations in feed water temperature and to tidal variations in feed concentration.

- Selection of an optimised operation strategy plays a crucial role in the feasibility of operating RO systems using RE. Operating a RO system based on variable recovery with constant brine flowrate presented the lowest specific energy consumption, indicating best utilisation of available energy, and widest operation range, allowing for permeate production at low power. This finding can be applied to commercial systems using split-feed flow configuration and an isobaric pressure exchanger.
- A RO system operating with variable power from a RE source requires an advanced control system for implementing the mapped control strategy, as highlighted by previous studies [11, 33]. This study has shown that MPC offered superior control compared to a conventional PID controller due to its prediction ability. MPC improved the settling time for a 10% step-change in permeate flowrate by 47%. It also improved the disturbance rejection for a 10% step-change in feed concentration and temperature by 47.2% and 43.9%, respectively. Overall, the MPC gave improved energy utilisation compared to PID control, resulting in a 2.35% increase in hourly permeate production for a Gaussian wind speed distribution with a standard deviation of 15% around a 6.5 m/s mean.
- The operation strategy and control system presented show that variable-speed operation can accommodate rapid fluctuations from a wind RE source to operate a RO system. The ability of the control system to accommodate the wind turbine output indicates that it will also accommodate other RE sources, such as solar, that fluctuate less rapidly. The following chapters will aim to improve the efficiency of RO system modular (on/off) operation to accommodate intermittency of RE sources and substantial power fluctuations.

6 Chapter 6 Wind Speed Prediction Using Neural Networks

6.1 Introduction

The intermittency and fluctuation of RE is a prominent characteristic of their performance. Their random nature and unpredictability pose a challenge for operating large-scale RO systems. As examined earlier, the MPC control system can handle small fluctuations in RE using variable-speed operation. The next step is implementing modular operation by connecting or disconnecting RO units to handle high magnitude RE variation or intermittency. Some studies favoured using solar-PV for modular operation to schedule the RO units operation based on the solar time, a feature unique to solar energy compared to other renewables [47]. However, extending the advantage of a predictable pattern to other RE sources that can be available all day, i.e., wind energy, would be a breakthrough for RE-driven RO. Wind power prediction can be beneficial for both aspects of variable operation, i.e., modular operation and variable-speed operation. Long-term prediction can help with operation scheduling to maintain the standard start-up/shutdown operation procedure during modular operation of RO trains. Short-term prediction can help in smoothing the plant operation against power variation.

The concept of wind speed prediction has been examined by previous studies due to its relevance for wind generation applications such as grid operations and power prediction [206]. Models presented for wind speed prediction included physical models, conventional statistical models, spatial correlation models and Neural Networks [206, 207]. Neural networks, a data-based modelling technique, have been recommended for wind speed prediction for their ability to provide high prediction accuracy for different prediction ranges [208-210]. However, their use in RO applications was limited to modelling the RO modules or integrated into the control system. Using NN wind speed prediction to enhance the performance of wind-driven RO was not previously introduced [11, 187].

Wind speed prediction by NNs can be defined into three categories as follows: immediate short-term within several seconds, short-term prediction in the range of minutes, medium-term in the range of hours and long-term prediction of an entire day. Accurate prediction of wind speed requires special investigation and collection of accurate comprehensive data for prediction [206, 211]. This Chapter aims to present a wind speed prediction algorithm using NNs to be implemented in the operation scheduling and control of RO systems. Initially,

background information on NNs will be given followed by a literature review on applications using NNs for wind speed prediction. Then, the methodology used in this study to develop the NNs is described. This is followed by a results and discussion section and a conclusion to summarise the findings of this chapter.

6.2 Literature review on Neural networks

6.2.1 Background

Artificial NNs are mathematical systems that imitate the structure and function of the human nervous system to model physical systems by using the same mechanism of learning and training. NNs are used in broad applications to provide data-driven modelling when physical models are challenging to derive [211]. A feed-forward NN, which is a widely used type for modelling non-linear systems, consists of a multi-layer structure that includes an input layer, an output layer and one or more hidden layers in between them, as shown in Fig. 6.1 [212, 213]. Each layer consists of elements called ‘neurons’, which are single computation points that form the building block of the NN. The neuron in a specific layer is connected to all neurons in the following layer. This is why NNs are referred to as feed-forward networks [214].

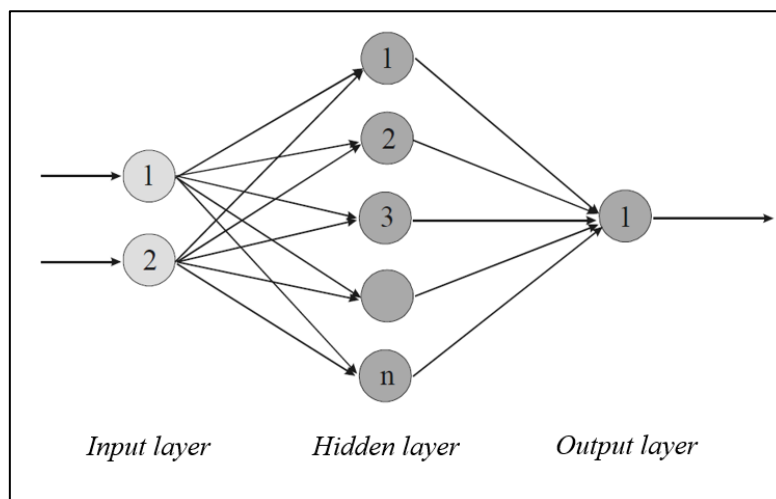


Fig. 6.1. A feed-forward neural network structure [213].

The neuron accepts inputs from single or multiple sources and generates an output, to be passed onto the next layer, based on a simple calculation with a set activation function. A model of a single hidden layer neuron j is presented in Fig. 6.2 [214]. The neuron receives inputs I_i from the previous layer, which is multiplied through a connection with weight w_{ij}

that is specific for the connection between the two neurons. In the neuron, all the weighted signals are added to form the weighted input signal. In addition, a bias b_j is added to the weighted input to shift the transfer function g by a value of b_j . Afterwards, the weighted input signal is passed through the transfer function to generate an output H_j [214]. The transfer function g can be a linear transfer function, step function, hard-limit function, log-sigmoid transfer function, etc. [215].

The network weights are adjusted to train the network to perform specific tasks. This process, described in Fig. 6.3, is called supervised learning. Learning or training is performed until a specific input led to the desired target output. This is done by comparing the actual network output to the target output and adjusting the network weights to minimize the Mean Square Error (MSE), equation (6.1), between the output and target data [212, 215-217].

$$MSE = \frac{1}{N} \sum_{i=0}^N (\text{prediction}_i - \text{target}_i)^2 \quad (6.1)$$

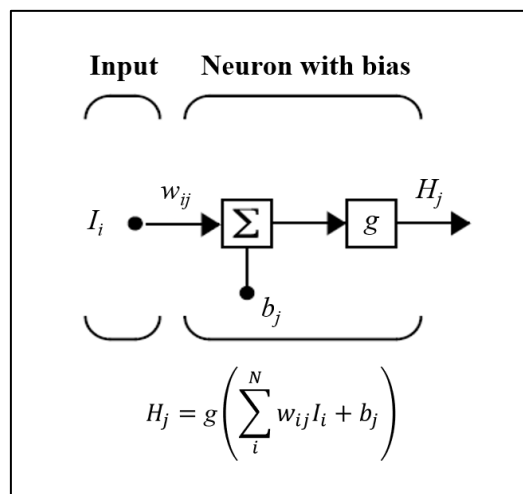


Fig. 6.2. Model of a hidden layer neuron [214].

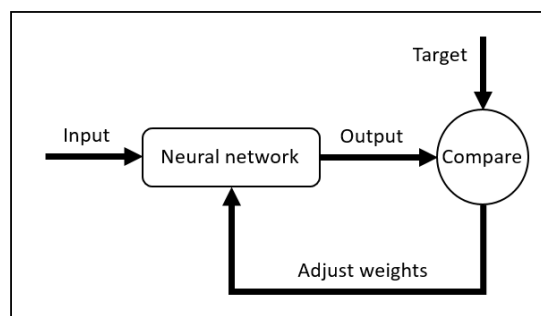


Fig. 6.3. Supervised learning [217].

6.2.2 Wind speed prediction techniques using neural networks

Several studies investigated the use of NNs for wind speed prediction. Philippopoulos and Deligiorgi [218] designed two NNs for predicting hourly wind speed for a complex topography in Chania plain in Greece. The NN algorithm offered higher prediction accuracy than conventional interpolation schemes of wind speed prediction. Azad et al. [211] combined statistical and NN-based approaches to predict hourly wind speed data of an upcoming year. The forecast was applied to two locations in Malaysia and a Mean Absolute Error (MAE) of 0.17 - 0.36 m/s and 0.24 - 0.35 m/s were achieved.

NNs can be used to predict the wind speed in locations that lack measuring equipment using measured data from a nearby location [212, 219, 220]. For instance, Ramasamy et al. [212] used NNs to predict the average daily wind speed in 11 locations in India using measured data from a nearby location. The network inputs were air temperature, air pressure, solar radiation and altitude. The NN achieved a Mean Absolute Percentage Error (MAPE) of 4.55% and a correlation coefficient of 0.98. Similarly, Bilgili et al. [220] developed NN models to predict monthly average wind speeds for multiple regions in Turkey. The NN used wind speed data of neighbouring stations as an input to predict wind speed at a target station. The MAPE for the prediction accuracy varied from 4.49% to 14.13%.

The performance of NNs depends on the type of input data used for prediction. Ü.B. Filik and T. Filik [219] compared the performance of different NNs trained for wind speed prediction while using a different set of metrological data as inputs. The study concluded that using the wind speed, air temperature and pressure achieved the lowest RMSE of 0.6759 m/s for a lead-time of 90 seconds. A NN was used by Mabel and Fernandez [221] to predict the wind energy output of wind farms in Muppandal, India. The NN predicted the wind energy output using the average wind speed, relative humidity, and generation hours as inputs. The NN prediction accuracy was presented by a RMSE of 0.0806 kWh [221].

From the preceding literature review, it was shown that NNs have a high potential to deliver accurate wind speed prediction with different prediction ranges. The NN structure and inputs used would vary depending on the application, prediction range and available data. The timeframe for prediction ranged from average monthly wind speed to prediction in the range of minutes. The inputs to the NNs were either historical wind speed data, wind properties or wind data from reference meteorological stations.

This chapter aims to develop NN algorithms for long-term and short-term wind speed prediction for the same location. Although long-term prediction requires using NN due to the prediction complexity, it is possible to use a simpler modelling technique, e.g., autoregressive model, for short-term prediction due to minor variation in wind speed in that range. However, NN was still used for short-term prediction based on the recommendation of previous studies for its suitability for different prediction ranges and to focus on one solution for wind speed prediction [208-210]. Long-term prediction involves predicting hourly average wind speeds for a full day ahead. This was used to schedule the RO system operation. Short-term prediction involves predicting average wind speed for the upcoming 2 minutes using an input of 5 element timeseries of 2-minute averages representing the past 10 minutes. This was used in guiding the control system according to wind speed variations. The choice of the 2-minutes resolution was based on the time required to complete the shutdown sequence of the RO system. This is explained in detail in Section 7.2.2.

6.3 Wind speed prediction for the wind-RO system

6.3.1 Neural Network design

A feed-forward backpropagation NN is used in this study for predicting wind speed. The selected network type and configuration, presented in Fig. 6.4, has shown adequate performance for approximating different functions in previous studies regarding the convergence time, accuracy and generalization [212, 217]. Network generalization is the ability to generate output from data that was not exposed to the network before. The network consists of three layers: an input layer, a hidden layer, and an output layer. Each layer consists of several neurons and the layers are connected by weighted connections. The neurons receive the inputs from the previous layer and produce an output based on an activation function.

The input layer neurons transmit the input to the hidden layer without alteration such that $I_i = X_i$ [214]. The number of neurons in the input layer is equivalent to the network inputs. As for the hidden layer, it includes a nonlinear hyperbolic tangent sigmoid transfer function, given by equation (6.2), which produces an output in the range (-1 to +1). The nonlinear transfer function allows the NN to approximate both linear and nonlinear relationships. The number of neurons in the hidden layer is determined by trial-and-error, such that the training starts with a few neurons and increases gradually until reaching the lowest error [211]. As for the output layer, a linear transfer function is used so the output can have any value, otherwise,

if a sigmoid transfer function is used the output will be constrained to (-1 to +1) [220]. The number of neurons in the output layer is equivalent to the network outputs.

$$g(x) = \frac{e^x - e^{-x}}{e^x + e^{-x}} \quad (6.2)$$

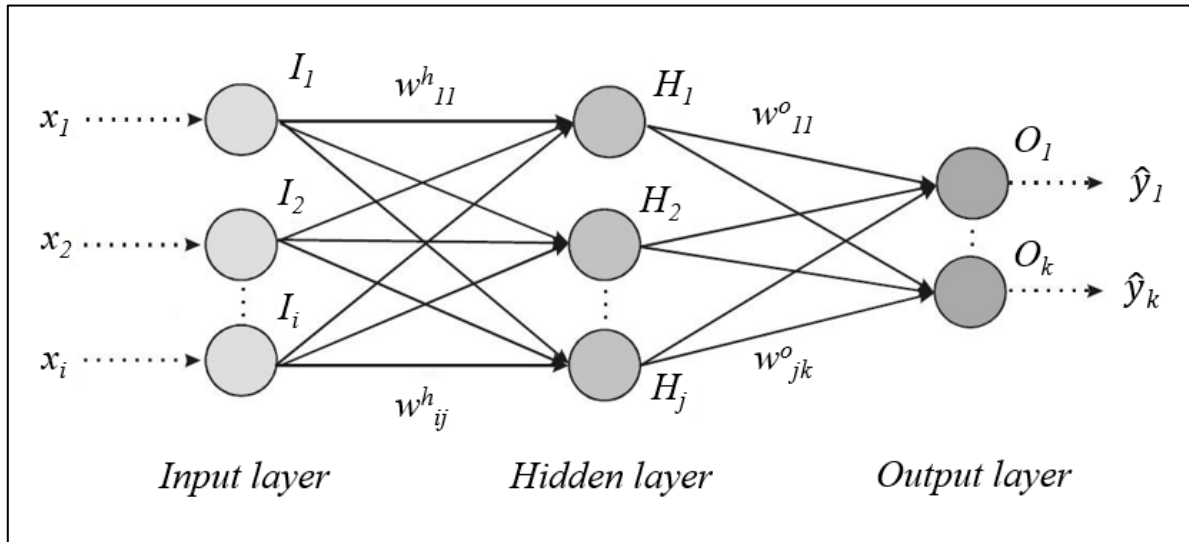


Fig. 6.4. Structure of the three-layer feed-forward backpropagation neural network.

For network training, the Levenberg-Marquardt backpropagation algorithm is used as a training algorithm. Backpropagation is the most used supervised learning technique for multiple layer NNs [217, 222]. It utilises the gradient steepest descent method to correct the weight of the connected neurons to minimize the output error for a given input [213, 223]. The error is calculated at the output layer of the NN, and it propagates back to the input layer, through the hidden layer, hence the name “backpropagation”. Levenberg-Marquardt is a derivation of the backpropagation algorithm that offers faster convergence by accelerating and stabilising the training process [214]. A description of the standard backpropagation algorithm is presented in this study, however, for the sake of being brief, a full description of the Levenberg-Marquardt modification can be found in [216, 224].

6.3.2 Backpropagation training algorithm

In Fig. 6.4, the three-layer NN structure used in this study is presented. X_i is the network input, H_i is the output of the hidden layer, \hat{y}_i is the output of the output layer. The weights between the input and hidden layer are written as w_{ij}^h , such that i refers to the number of the input neuron and j refers to the number of the hidden layer neuron. The weights between the

hidden and output layer are given by w_{jk}^o , such that j and k represent the number of the hidden and output neuron, respectively.

During the training stage, the network is fed several input patterns, each with a specific output combination, such that the training data is a certain number of input/output pairs $\{x_i^p, y_k^p\}$, with p indicating the input/output pattern. The training set can be presented multiple times to the network depending on the convergence. The number of times that the entire training set is presented to the network is referred to as the number of epochs, such that the network weights are updated every epoch [214]. As presented in equation (6.3), the weights of the network are adjusted to minimise the square sum of the error between the network output \hat{y} and desired output y .

$$E(w) = \min \frac{1}{2N} \sum_{p=1}^N \sum_{K=1}^M (\hat{y}_k^p - y_k^p)^2 \quad (6.3)$$

Considering an input x_i^p to the input layer for an input/output pattern p , the input to the hidden layer neuron j is as follows:

$$h_j^p = \sum_i w_{ij}^h x_i^p \quad (6.4)$$

Accordingly, the output of the hidden layer neuron j is given by:

$$H_j^p = g(h_j^p) = g\left(\sum_i w_{ij}^h x_i^p\right) \quad (6.5)$$

where g is the nonlinear hyperbolic tangent sigmoid transfer function used in the hidden layer, presented in equation (6.2). Thus, the input received by the output neuron k from the hidden layer neuron j is as follows:

$$o_k^p = \sum_j w_{jk}^o H_j^p = \sum_j w_{jk}^o g\left(\sum_i w_{ij}^h x_i^p\right) \quad (6.6)$$

and the output of neuron k , which is the actual network output is given by:

$$\hat{y}_k^p = f(o_k^p) \quad (6.7)$$

where f is the linear transfer function included in the output layer.

The weights are adjusted using the gradient descent method. The interconnected weights between the hidden layer and the output layer are modified as follows:

$$\Delta w_{jk}^o = -\eta \frac{\partial E}{\partial w_{jk}^o} = -\eta \frac{\partial E}{\partial \hat{y}_k^p} \frac{\partial \hat{y}_k^p}{\partial o_k^p} \frac{\partial o_k^p}{\partial w_{jk}^o} = -\eta \sum_p (\hat{y}_k^p - y_k^p) H_j^p \quad (6.8)$$

where η is the learning rate that establishes the step size. A low learning rate leads to slower convergence, however, a high rate could lead to a large step size and the minimum might not be found. As for the weights between the input layer and the hidden layer, they are calculated by:

$$\Delta w_{ij}^h = -\eta \frac{\partial E}{\partial w_{ij}^h} = -\eta \frac{\partial E}{\partial H_j^p} \frac{\partial H_j^p}{\partial h_j^p} \frac{\partial h_j^p}{\partial w_{ij}^h} = -\eta \sum_p \sum_k (\hat{y}_k^p - y_k^p) w_{jk}^o \dot{g}(h_j^p) x_i^p \quad (6.9)$$

The Neural Network Fitting Tool developed by MATLAB was used to implement this NN. The network error was monitored by the MSE, calculated using equation (6.1), between the network outputs and the target outputs, for which the network weights were adjusted until the MSE was minimised [225]. The input and target data were normalised in the range of -1 to +1 using a MATLAB mapping function called mapminmax. The wind speed data were randomly divided into three sets. The training data used to adjust the network weights during training constituted 70% of the entire dataset. The validation data used to assess network generalization was 15% of the dataset, such that the network converges and the training stops if generalization stops improving. The testing data that was excluded during training and used to measure the network performance was 15% of the dataset [212]. The accuracy of the NN prediction was presented using the RMSE and correlation coefficient R^2 .

6.3.3 Wind data

The wind data used for this study is six months of wind speed data collected at the University of Bahrain at 12 m height with a one-minute resolution. The data was averaged according to the prediction range, either as one hour average for long-term prediction or 2-minute average for short-term prediction. The wind speed was extrapolated to the wind turbine rotor height of 25 m, to account for changes in the wind speed profile due to surface roughness that is referred to as wind shear, using the wind speed power law as follows [226]:

$$V_{ws,2} = V_{ws,1} \left(\frac{Z_2}{Z_1} \right)^\alpha \quad (6.2)$$

where $V_{ws,1}$ is the actual measured wind speed at height Z_1 , $V_{ws,2}$ is the wind speed at the required height Z_2 , and α is the power-law exponent [227]. The power-law exponent is influenced by the height, season, time of day, surface wind speed, surface roughness and terrain. A study focussing on wind speed variation with height in Bahrain suggested that the appropriate power exponent between 10 m to 30 m would be 0.409 [227, 228].

6.3.4 Long-term prediction

Long-term prediction is forecasting the wind speed for a full day ahead using measured data. A NN was developed to predict the wind speed for the upcoming 24 hours in the form of hourly average timeseries using data measured from the previous day as input. The one-minute resolution data for the six months were converted to hourly averages. The dataset was arranged into input and target column matrices, such that each column included 24 elements representing the input to the NN with the corresponding 24 element output presented in the target matrix. The NN included an input layer with 24 neurons based on the number of inputs, an output layer with 24 neurons based on the number of outputs, and a hidden layer with 10 neurons. Generally, the number of neurons for the hidden layer was defined using trial and error, however, the default value defined in MATLAB of 10 neurons was used. The network structure is presented in Fig. 6.5.

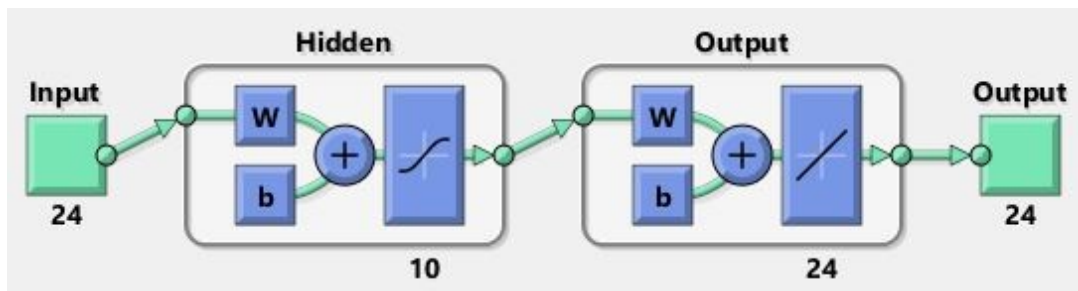


Fig. 6.5. Structure of the long-term prediction neural network.

6.3.5 Short-term prediction

Short-term prediction is forecasting the wind speed in the range of minutes. A NN was developed to predict the average wind speed for the upcoming 2 minutes using an input of 5 element timeseries of 2-minute averages representing the past 10 minutes. The one-minute resolution data for the six months was converted to 2-minute averages. The dataset was

arranged into input and target column matrices, such that each column of the input matrix included 5 elements corresponding to the network inputs, and each column of the output matrix includes one element representing the network output. The NN included an input layer with 5 neurons for the network inputs, a 1 element output layer representing a single output of 2-minute average wind speed. Also, the NN included a hidden layer of 10 neurons based on the default value defined by MATLAB. The network structure is presented in Fig. 6.6.

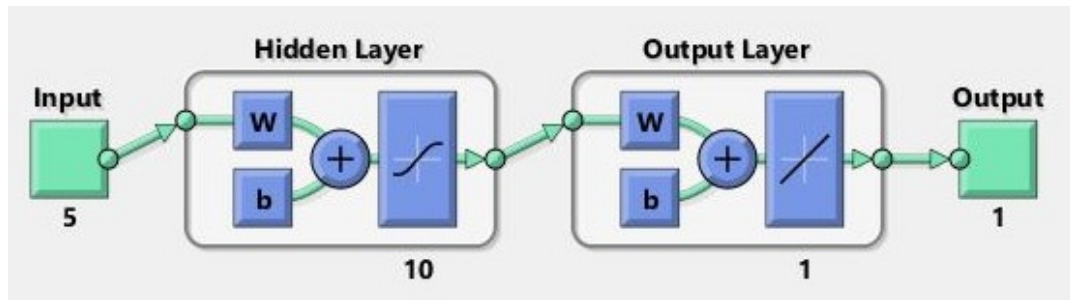


Fig. 6.6. Structure of the short-term prediction neural network.

6.4 Results and discussion

6.4.1 Long-term prediction

6.4.1.1 Error analysis

The accuracy of the NN was determined by investigating the RMSE and correlation between the NN outputs and target data during the training, validation and testing processes. The error analysis during each stage for the long-term prediction NN is presented in Table 6.1. For the training process, the network weights were adjusted until the error between the output and training datasets was minimised. After the training process converged, the RMSE between the output and target data was 1.29 m/s and the R^2 was 0.8, which represented high accuracy and correlation between the network output and target data. The validation error presents the error between the output and target data using the validation data. The network training converged once the validation error ceases to improve. The RMSE and R^2 for the validation process were 1.7 m/s and 0.74 respectively. The network testing was done using 15% of the wind speed samples that were excluded during the training process. The purpose was to represent the actual performance of the network towards new samples. The testing showed good agreement between target and predicted data, presented by a low RMSE of 1.54 m/s and R^2 of 0.64 from the regression analysis.

Table 6.1. Error analysis for the long-term neural network prediction during the development phase

	Samples	RMSE	R ²
Training	126	1.29	0.80
Validation	27	1.70	0.74
Testing	27	1.54	0.64

In Fig. 6.7, the accuracy of the long-term NN is presented using linear regression analysis that estimates the correlation between the target and predicted values for the samples included during training, validation, and testing. For a perfect fit, the data should fall along the Identity line (45° line), meaning that NN outputs are equal to the target values. Considering the long prediction range and limited data, the fit is relatively good for the complete dataset presented by a R² of 0.59. The suitability of this prediction accuracy for RO units operation scheduling was later explored in Section 7.5.2.

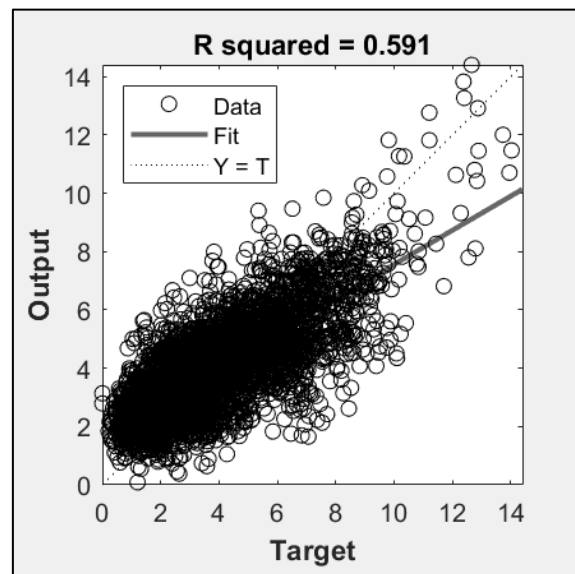


Fig. 6.7. Regression analysis representing the correlation between the long-term neural network outputs and targets dataset during training, validation, and testing.

6.4.1.2 Case studies

The long-term NN was tested using three random days that were excluded from the training dataset to present the network accuracy for different cases studies. For each day, the wind speed timeseries of the previous day was used as input to predict the hourly average timeseries for a full day ahead. The NN prediction compared to the measured data for Days 1,

2 and 3 are presented in Fig. 6.8, 6.9 and 6.10 respectively. The prediction accuracy varied depending on the randomness of wind speed on that day.

For Day 1, the network prediction is considered a good match with the actual value based on a R^2 and RMSE of 0.76 and 1.54 m/s respectively. The NN was successful at predicting the same wind speed pattern as the measured data, however, struggled to predict unusual fluctuations in wind speed at certain hours. For Day 2, the NN offered improved prediction accuracy compared to Day 1 with a R^2 of 0.77 and a RMSE of 1.46 m/s. The NN managed to predict the wind speed pattern accurately and the error between the predicted and measured data was minimal at certain times of the day. As for Day 3, the NN output was a good match for the measured data during the first half of the day, as the wind speed was stable around 9 m/s. The prediction error increased later during the day as the measured wind speed dropped from around 9 m/s to below 2 m/s. However, the NN was successful at predicting the trend in wind speed change along the day, showing a high correlation between measured and predicted data quantified by a R^2 of 0.904.

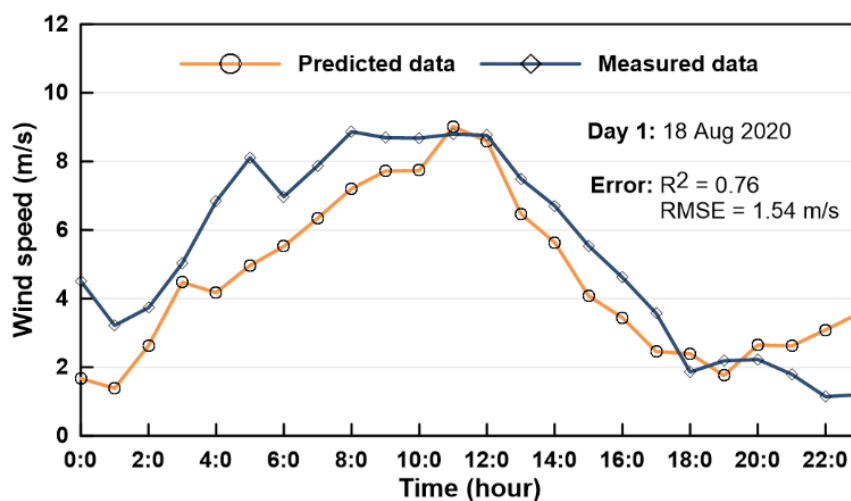


Fig. 6.8. Predicted hourly average wind speed timeseries on 18 August 2020 with respect to measured data.

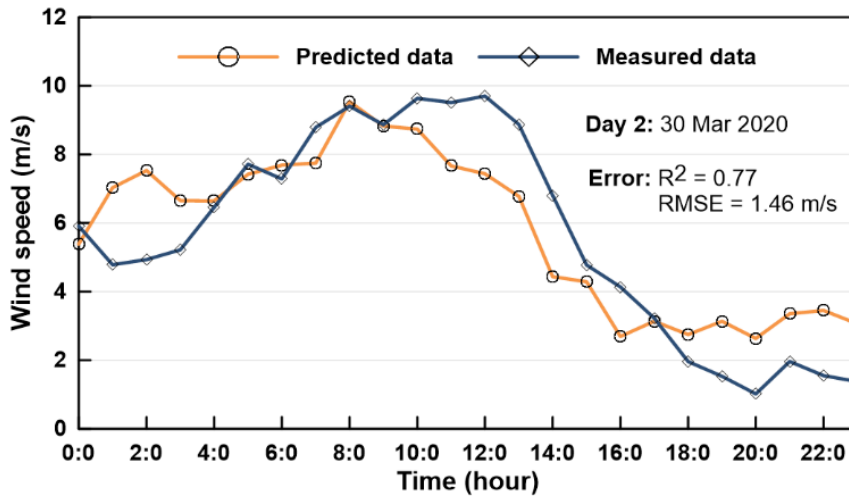


Fig. 6.9. Predicted hourly average wind speed timeseries on 30 March 2020 with respect to measured data.

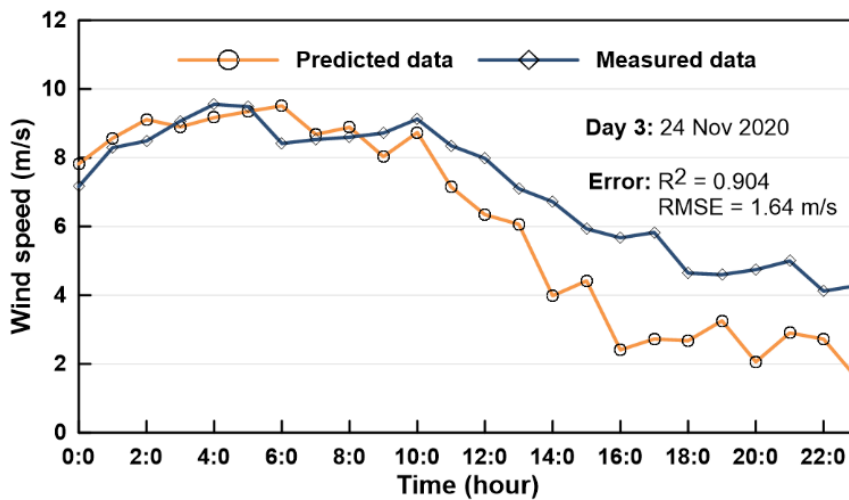


Fig. 6.10. Predicted hourly average wind speed timeseries on 24 November 2020 with respect to measured data.

6.4.2 Short-term prediction

6.4.2.1 Error analysis

The prediction accuracy for the short-term prediction NN is assessed in this section by investigating the RMSE and correlation between the network outputs and target data during the training, validation and testing processes. A summary of the error analysis for each stage is presented in Table 6.2. After the training process converged and the weights of the network are set, the error between the network output and target data from the training dataset was 0.14 m/s and 0.99 for the RMSE and R^2 respectively. As for the error during the validation stage and testing network generalisation, the prediction error was 0.15 m/s for the RMSE and

0.99 for R^2 . Similarly, the prediction error between the network output and target data for the testing dataset was significantly accurate, such that the RMSE and R^2 were 0.15 m/s and 0.99 respectively.

Table 6.2. Error analysis for the short-term neural network prediction during the development phase

	Samples	RMSE	R^2
Training	91201	0.14	0.9958
Validation	19543	0.15	0.9957
Testing	19543	0.15	0.9957

The short-term NN accuracy towards predicting the complete dataset is presented using linear regression in Fig. 6.11. It shows the correlation between the network output and target data for the samples used for training, validation, and testing. The regression analysis showed a high coefficient of determination R^2 0.99, which is represented by the closeness of fit of all the data points relative to the Identity line, on which the NN outputs are equal to the target values.

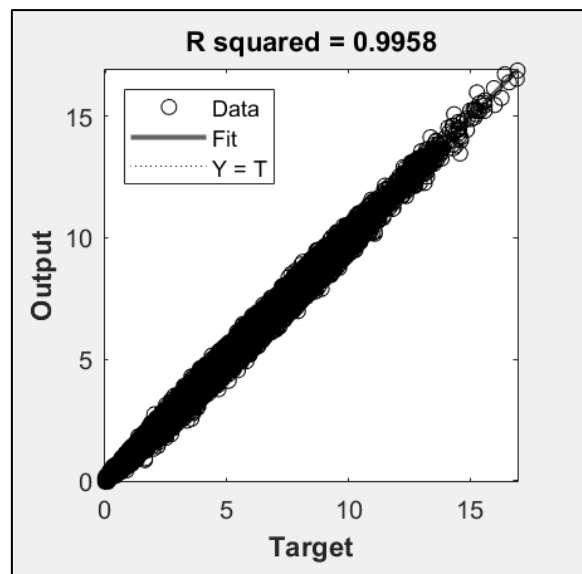


Fig. 6.11. Regression analysis representing the correlation between the short-term neural network outputs and targets dataset during training, validation, and testing.

6.4.2.2 Case studies

The performance of the short-term prediction NN was tested using the data for the three random days excluded from the training dataset. This showcased the network accuracy

towards new inputs and the change in prediction accuracy relative to the randomness of wind speed for each day. The NN prediction of the 2-minute average wind speed compared to the measured data for Day 1, 2 and 3 are presented in Fig. 6.12, 6.13 and 6.14 respectively.

The results showed that the accuracy of the NN prediction improved significantly when using it for short-term prediction in the range of minutes compared to predicting a full day. For the three case studies, the RMSE was approximately 0.2 m/s, which is considered very accurate relative to the stochastic nature of wind speed. As for the correlation between the predicted output and measured wind speed, the NN showed a high correlation for predicting the trend in wind speed change along the day. This was quantified by a R^2 of 0.99, 0.96 and 0.94 for Days 1, 2 and 3 respectively. The NN prediction showed the lowest correlation with measured data for Day 3 due to the increased fluctuations on that particular day.

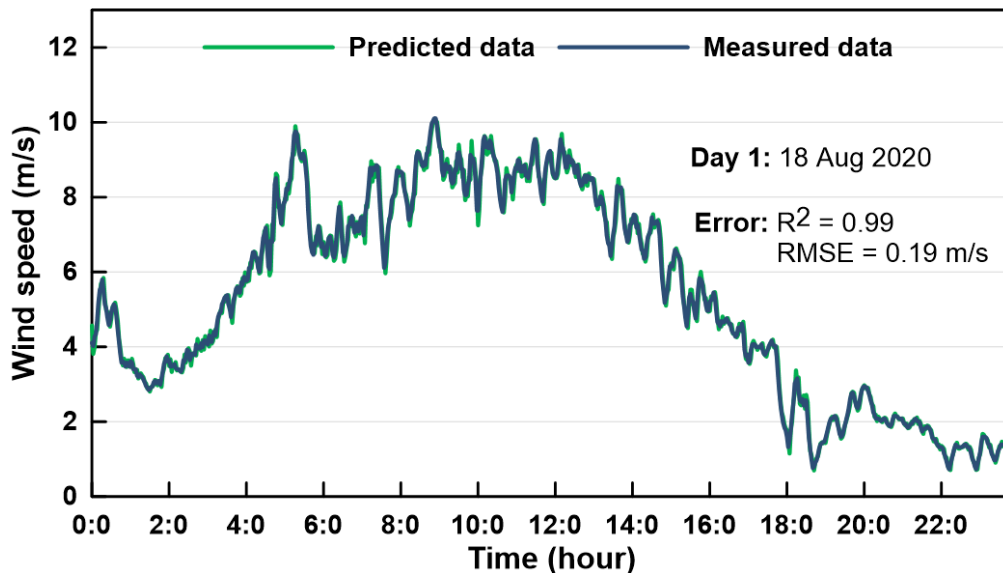


Fig. 6.12. Predicted 2-minute average wind speed timeseries on 18 August 2020 with respect to measured data.

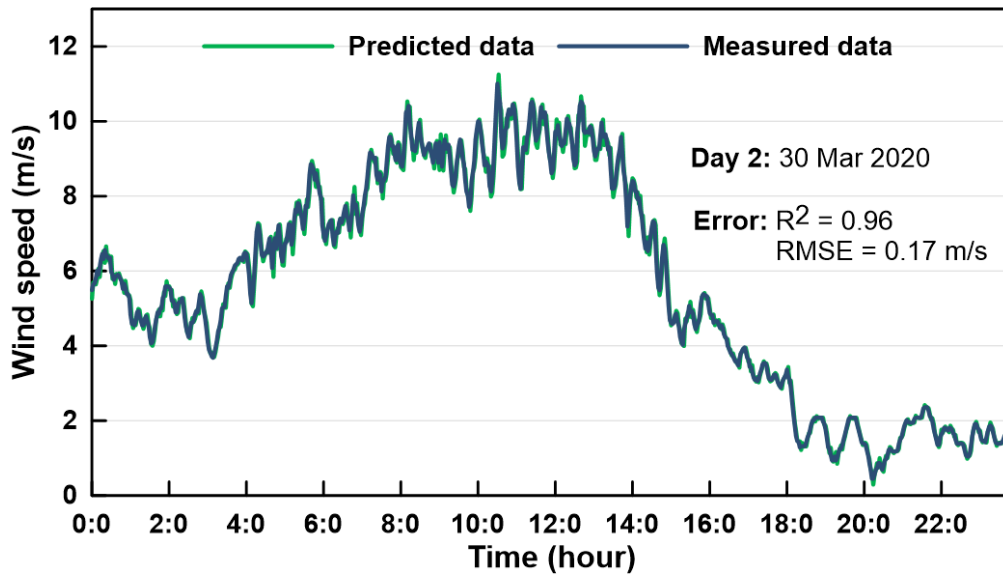


Fig. 6.13. Predicted 2-minute average wind speed timeseries on 30 March 2020 with respect to measured data.

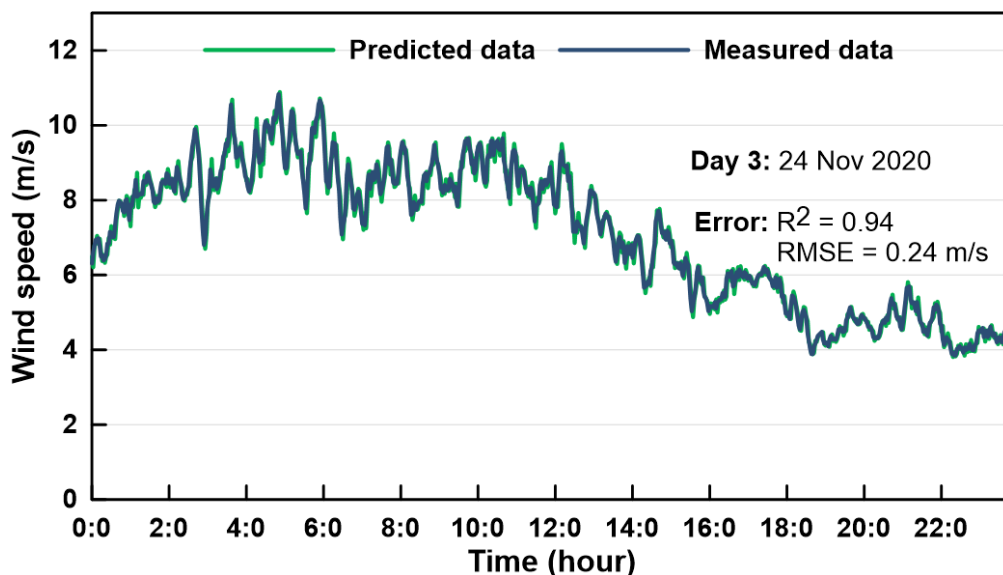


Fig. 6.14. Predicted 2-minute average wind speed timeseries on 24 November 2020 with respect to measured data.

6.5 Summary

Wind speed prediction using NNs has not been considered for RO operations in previous studies. This Chapter showcased the prospects of using NNs for wind speed prediction to be implemented for RE powered RO applications. Three-layer feed-forward backpropagation NNs were developed to provide long-term and short-term wind speed prediction that would integrate with a RO plant scheduling and control. The long-term prediction NN provided

wind speed prediction of a full day ahead wind speed data in the form of hourly averages. The short-term prediction NN predicted wind speed average for 2-minutes ahead using a 5 element timeseries of 2-minute averages as an input. The main conclusions are as follows:

- Long-term prediction of a full day ahead offered relatively high accuracy considering the range of prediction. The NN delivered a good fit between the output and target for the complete dataset presented by a R^2 of 0.59, and a RMSE of approximately 1.5 m/s for testing data. This highlights the potential for using long-term prediction for scheduling the RO system operation.
- Short-term prediction of the average wind speed for 2-minute ahead delivered an impressive prediction accuracy presented by a R^2 of 0.95, thus indicating a high correlation between network output and target data for the complete dataset, in addition to a low RMSE of approximately 0.15 m/s for the testing data.
- The prediction accuracy of the short-term NN was significantly higher than that of the long-term NN. This indicated that the prediction accuracy is inversely proportional to the range of forecast. Moreover, it highlighted the potential of using the predicted wind speed as a reference signal to the control system for predictive control, which is discussed in the next chapter.

7 Chapter 7 Modular operation based on wind power prediction

7.1 Introduction

Modular operation is a variable operation technique for matching the RO load to available energy during high magnitude RE variation [187]. It depends on the RO system modularity, such that RO units/trains are connected/disconnected according to available power. Modular operation is promising for large-scale RO system that includes multiple RO units to handle energy intermittency and considerable power variations while operating with RE [187]. However, there are challenges for safely repeating the start-up and shutdown sequence of RO units based on the random RE variation. This chapter presents a description of the challenges of modular operation and introduces the application of wind speed prediction into RO system scheduling and control as a solution.

7.1.1 Challenges for modular operation

For commercial RO systems, starting up or shutting down a RO unit requires adhering to certain guidelines defined by the membrane and components manufacturers. These guidelines aim to prevent excessive membrane fouling, prevent membrane damage due to excessive loading, and ensure the water quality and productivity are delivered as claimed [142, 143]. RO membrane manufacturers guarantee a working life of around 5 years if the recommended start-up/shutdown procedure and operating conditions are met [64]. RO trains start-up procedure include purging the air out of the membranes using low-pressure water before gradually increasing pressure at a rate of 0.7 bar per second until reaching the set point [142]. The permeate is discarded during this process until it reaches the desired quality [143]. During shutdowns, the RO membranes are flushed using low pressure permeate water or high-quality feedwater to prevent scaling and salt deposition. Membrane flushing takes place until the concentrate conductivity reaches the feed conductivity [138, 142]. Start-up/shutdown procedures consume clean water to flush the membranes, energy to operate the flushing pumps and time wasted that the plant could be producing permeate - all of which are finite in the case of RE powered RO [66, 138]. The time, energy and clean water required for start-up and shutdown are subject to the capacity and design of the RO trains. In addition, large-scale systems require the readiness of auxiliary systems that operates beside the RO trains. These auxiliary systems include pre-treatment processes such as coagulation, flocculation, filtration, antiscalant dosing, water softening, chlorination/de-chlorination, etc. In addition to after-treatment processes such as remineralisation, discharge management, etc.

This shows that the unpredictability of RE variation can be problematic considering that during modular operation using RE, start-up and shutdown of RO trains are more frequent compared to constant operation [33]. Thus, the decision to connect or disconnect a RO train should not be done solely following the changes in available power, however, it requires planning to make sure the recommended start-up and shutdown procedures are followed and to guarantee the readiness of the auxiliary system that operates beside the RO trains.

Scheduling the startup and shutdown procedure for solar-photovoltaic operated RO plants is achievable by using the solar irradiance distribution curve. For wind-powered RO, it is challenging to schedule the RO trains startup/shutdown procedure due to the fluctuation and intermittency of wind speed, wherein a single day there might be several start-up/shutdown cycles for a specific RO train [33]. For modular operation using wind energy to be effective, the RO units modulation cannot be a random process, but rather a precisely managed one [11]. RE forecasting is promising for improving the possibility of operation scheduling for wind-powered RO systems.

7.1.2 Prospects of neural network prediction and RO operation

NNs were suggested by several studies for predicting wind speeds [208-210]; however, their use in wind speed prediction for enhancing the performance of wind-driven RO was not previously introduced [11, 187]. As presented in Chapter 6, NNs were successfully used for predicting wind speeds for long-term and short-term prediction ranges. Long-term prediction of wind energy allows for scheduling the RO trains operation according to energy availability and water demand. This ensures planning to maintain the standard start-up and shutdown sequences; thus, guaranteeing smooth transitions during the on/off cycles, minimising shutdowns, and maintaining equipment lifetime. As for the short-term prediction, it offers the potential to smooth out the RO system operation and maintain the safe shutdown procedure for the RO trains by anticipating sudden drops in available power. Generally, the prospects of using wind energy prediction for wind-powered RO systems have the potential to offer a paradigm shift in how RO systems are operated with RE sources. RE availability prediction can be used with other renewables to further increase the penetration of RE in operating RO and become a standard for operating RO systems with renewables.

To date, the concept of modular operation has not been implemented for large-scale systems due to the challenges mentioned in Section 7.1.1. This chapter aims to present an optimised

modular operation technique to connect/disconnect RO units according to changes in available power while adhering to a standardised start-up/shutdown sequence. It also aims to include wind speed prediction for scheduling and controlling the RO units operations. The modular operation is presented alongside the variable-speed operation, developed in Chapter 6, to allow the RO plant to adapt to various amplitudes of wind power variation. Two solutions based on wind speed prediction are implemented into the modular operation technique as follows:

- Operation scheduling of the RO system is developed using the long-term prediction NN. This is beneficial for the smooth operation of RO units, maintaining the standard start-up and shutdown sequences, and avoiding excessive on/off cycling.
- The short-term wind speed prediction is implemented in the RO system control, such that the predicted averaged wind speed is supplied to the control system as a system input instead of the real-time wind speed. Using an averaged wind speed signal will improve variable-speed control by smoothing out the RO system operation, in addition to anticipating power drops that can lead to a unit shutdown, thus enhancing the efficiency of modular operation. In general, this ‘predictive control’ approach ensures that the control system is always 2 minutes ahead of the wind speed change.

This chapter is structured as follows. Section 7.2 summarises the long- and short-term wind speed prediction NN developed in Chapter 6. Section 7.3 describes a case study for a RO system that includes three RO units of the test-rig presented in Chapter 3. This case study is used in the simulation and analysis of the modular operation technique and developed solutions. Section 7.4 introduces the developed modular operation technique including the guidelines for the start-up and shutdown sequences, rules for modular operation and the algorithm used for its implementation. The results and discussion are presented in section 7.5, where the standardised start-up and shutdown sequences are described, the accuracy of the RO units operation scheduling is assessed, and operation using the short-term wind speed as an input signal ‘predictive control’ is examined. Section 7.6 summarise the findings of this chapter.

7.2 Wind speed prediction using neural networks

NNs are data-based modelling techniques that are used to model physical systems without a predefined mathematical model. They have been recommended by several studies

for wind speed prediction [208-210]. In Chapter 6, two NNs were developed for long-term and short-term speed prediction. The NNs have shown high accuracy for predicting wind speed in terms of predicting the wind speed pattern and the steady-state value. The long-term and short-term NNs are summarised as follows:

7.2.1 Long-term prediction

The long-term prediction NN provided wind speed prediction of hourly averages for a full day ahead, using data collected from the previous day as input. A period of a full day ahead was selected to schedule the daily operation of the RO units beforehand and prepare the auxiliary systems that operate alongside them.

7.2.2 Short-term prediction

The short-term NN was trained to forecast the average wind speed for the upcoming 2 minutes using data of the last 10 minutes as input. It aimed to provide predictive control for the RO system by using the predicted wind speed as the wind speed signal for the control system. In addition, it guarantees that the shutdown procedure is followed without interruption in case of a sudden drop in available power. The selection of the short-term prediction period is subject to the time required to complete the shutdown procedure. Ideally, the short-term prediction horizon should cover the shutdown procedure of a RO train.

7.3 Case study

Assessing the efficiency of modular operation using wind speed prediction requires a RO system that includes multiple RO units to simulate the modularity of large-scale systems. For this study, the system used for investigation consists of three identical RO units connected to the same water tank and powered by a single wind turbine, as presented in Fig. 7.1. The design and performance of each RO unit were based on the test-rig presented in Chapter 3. The RO system description and the control system are presented as follows:

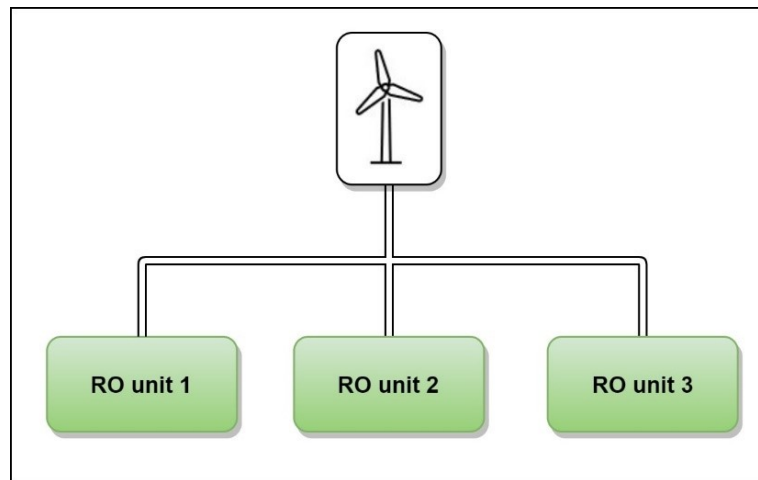


Fig. 7.1. Schematic diagram of the RO plant configuration. The RO plant consists of three RO units driven by a 30 kW wind turbine.

7.3.1 RO system description

As mentioned in Chapter 3, the RO unit consists of two pressure vessels connected in parallel, each vessel contains three 8” RO modules in series. The HPP used is the APP 3.5 axial piston pump manufactured by Danfoss [160]. Moreover, the system includes an isobaric ERD, Danfoss iSave 21 Plus, which recovers energy from the brine [161]. The rated production capacity of the RO unit is 3.2 m³/h at a power consumption of 7.5 kW (at 35,000 mg/l and 25°C). A schematic diagram of the system is shown in Fig. 7.2 and full details on the RO unit design can be found in Chapter 3. The testing and analysis were simulation-based using the RO dynamic model presented in Chapter 4.

The wind turbine used in the simulations to power the three RO units is the Zenia (Ikast, Denmark) ZA30, which is a 3-bladed horizontal axis wind turbine that delivers 30 kW rated power. A simple steady-state model was used to calculate the wind power using the wind turbine power curve, which is presented in Fig. 7.3 [229].

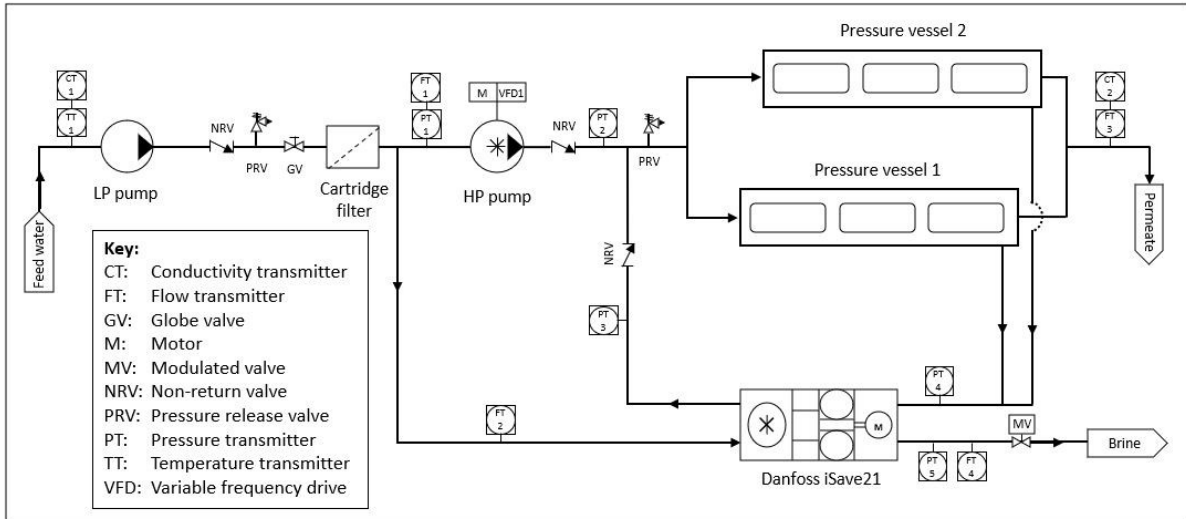


Fig. 7.2. Schematic diagram of the RO unit presented previously in Chapter 3.

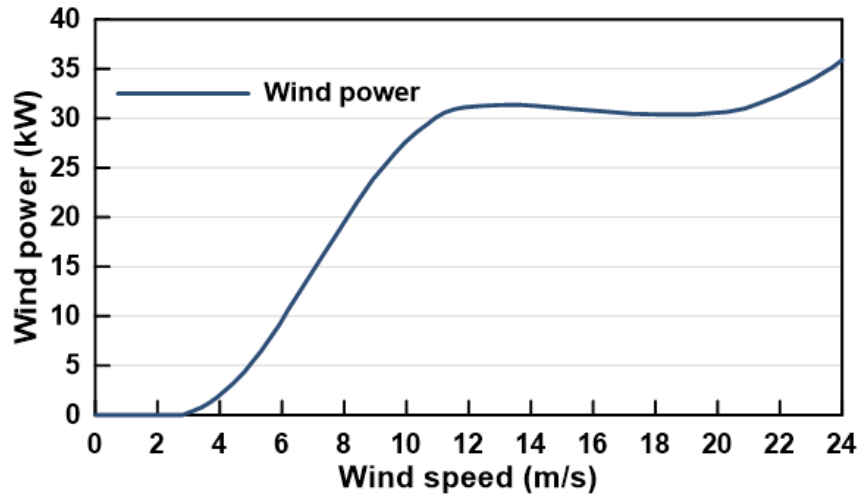


Fig. 7.3. Wind turbine power curve.

7.3.2 Control system

The operational control system for each RO unit uses ‘variable-speed control’ to match the RO plant load to the available wind power. This was achieved by manipulating the HPP and iSave motor speeds using VFDs to vary the operating parameters, i.e., permeate production and recovery ratio, thus varying the RO power consumption. The operating parameters were varied such that the RO unit operates with variable permeate recovery with a constant brine flowrate with changes in wind power. This was found to be the optimum operating strategy for this system configuration as it delivered the widest operation range, guaranteed longest production times, and the lowest SEC offering efficient energy utilisation.

The control system for each RO unit was based on the MPC presented in Chapter 6. It includes a prediction model to predict the plant response to the generated control signal, in addition to an optimiser that adjusts the control signal to minimise the error between the output and target values. The control system was tuned to deliver a fast and robust response towards changes in available power and input disturbances, i.e., feed concentration and temperature. The structure of the MPC is presented in Fig. 7.4. A detailed description of the operation strategy and control system for each RO unit can be found in Chapter 5.

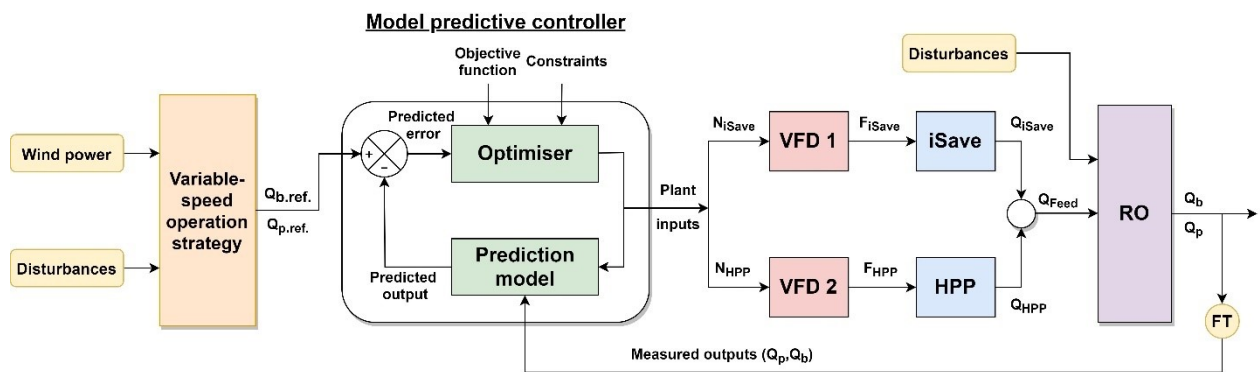


Fig. 7.4. Structure of the Model Predictive Controller. The input disturbances are the feed concentration and feed temperature.

7.4 Modular operation

The development of the modular operation technique used for modulating the RO units operation is presented in this section. The modular operation technique involves making decisions on which RO system is on or off, distributing the power between RO units, and defining the operational state of each unit, i.e., start-up, shutdown or permeate production. The development of the modular operation technique requires the definition of standardised start-up and shutdown sequences and setting the rules and constraints for modulating the RO units operation, which defines the order of connecting or disconnecting the RO units and the power threshold for each units' operation.

7.4.1 Start-up and shutdown sequences

The development of a standardised sequence for the start-up and shutdown of RO systems is essential for efficient operation. Their simplicity and smoothness have a direct impact on the RO system performance, equipment lifetime and product water quality. A well designed start-up and shutdown sequence is more vital for RO systems operating with variable power as they will undergo more start-up/shutdown cycles.

The development of a standardised start-up/shutdown sequence can vary depending on the plant design. It should consider the hydraulic constraints and the recommended operation procedure for the membranes that would guarantee their performance and longevity, in addition to operation constraints for the pumps, such as the constraints on the flowrate, pressure and ramping rates [142]. Moreover, the product quality should be considered in the start-up sequence design. The standard operation sequence for the RO unit used in this study is divided into three stages as follows:

7.4.1.1 *Initial start-up*

The initial start-up is performed after prolonged shutdown or generally when the pressure in the RO system is equivalent to the atmospheric pressure. Its main objectives are purging air from the RO system, controlling the feed pressure ramp rate and ensuring an acceptable permeate quality.

Air purging is an important step of the initial start-up sequence. Generally, air enters the RO system when it is at atmospheric pressure from the pipework and inlet/outlet ports. In other situations, forward osmosis causing water to permeate from the permeate to the brine side can lead to a vacuum being formed on the permeate side and air being drawn into the membrane element. This phenomenon, referred to as permeate suck-back, can be avoided by ensuring enough water volume is available in the permeate line [142]. Air remaining in the elements or the pressure vessels after starting the HPP may lead to excessive forces on the elements in the flow or radial directions causing the fibreglass shell to crack if the feed pressure is increased rapidly. Accordingly, membrane manufacturers recommend that all the air should be properly vented from the RO system.

Pressure and flow changes during the start-up sequence can cause mechanical stresses to the membrane elements. The start-up sequence should maintain a slow feed pressure increase to minimise excessive loading and mechanical stresses on the membranes. Generally, the feed pressure ramp rate can be controlled by either using a VFD to control the HPP speed, valves on the brine reject line or a combination of both, depending on the system design. For the RO system presented in Section 7.3, the feed pressure is directly proportional to the HPP flow, allowing for the pressure ramp rate to be controlled using the HPP VFD. The recommended feed pressure ramp rate by DuPont is slower than 0.7 bar/s to achieve a soft start [142].

Accordingly, the HPP speed increase rate was capped to 0.5 Hz/s during start-up to aim for a smooth start.

At the start of permeation, the permeate quality is not adequate to be collected in the product tank due to high salt passage compared to the permeate flux, causing the permeate flow to have an unacceptably high salt concentration. During start-up, all the permeate is discarded until it reaches an acceptable value below 500 mg/l based on the guidelines of the WHO [79]. The time required for the permeate quality is subject to the plant design. This will be determined experimentally for the RO unit used by noting the average time until the permeate concentration stabilises and reaches a value below the maximum limit of 500 mg/l.

7.4.1.2 *Rolling start-up*

A rolling start for the RO unit can be performed when the system has been shut down for a brief interval and the system pressure is still above atmospheric pressure. This guarantees that air did not leak back into the RO system and air purging is not required before starting the HPP. Defining a rolling start-up sequence is beneficial for increasing the periods of production during short-term shutdowns by reducing the start-up sequence time. The time until the RO unit is depressurised was monitored during experimentation. On average, the RO unit took 21 minutes to de-pressurise and reach atmospheric pressure. This de-pressurisation time is subject to the RO unit design and capacity.

7.4.1.3 *Shutdown*

For the RO unit shutdown, the main objective is to flush the membrane with fresh water to prevent scaling, salt deposition and (forward) osmosis from occurring across the membrane, which can cause the membrane to swell and rupture [120, 142]. The membranes are flushed using low-pressure feedwater to clear the concentrated brine out of the membrane elements and pressure vessels. Membrane flushing takes place until the concentrate conductivity reaches the feed conductivity, thus indicating that all the concentrate was replaced.

7.4.2 **Rules for Modular operation**

After outlining the start-up and shutdown sequences, the rules constituting the modular operation algorithm were defined. This included defining the order for connecting or

disconnecting the RO units and defining the power threshold for the number of operating units. The rules for modular operation are described as follows:

- **Connection – disconnection strategy:** The order for connecting or disconnecting the RO units is based on operating them in sequential order, such that a RO unit operates when the preceding unit has reached full capacity. In addition, the order in which the RO units are disconnected is inverse to the order in which they were connected. For example, in case of a power drop, the first RO unit to be connected is the last to be disconnected. This strategy aims to maximise permeate production by not interrupting the RO units operation and maintaining their production at full capacity as much as possible. Another alternative is distributing the available power across units to keep them operational. Although this would reduce the number of shutdowns and deliver longer periods of operation, it requires further analysis to determine how to allocate power between units and the tradeoff between longer operation, cumulative permeate production and permeate quality. The simple approach of sequentially ramping down units was used in this study.
- **Power threshold:** The power threshold of each RO unit defines the minimum power consumption of a single RO unit that allows for permeate production and operating the HPP, which is 4.09 kW, and the maximum power consumption of a single RO unit, which is 8.48 kW, at the maximum production capacity. This is essential to form the decision to connect or disconnect a RO unit. Generally, a RO unit operates only if there is enough power to run the HPP. The number of operational RO units relative to available power are presented in Table 7.1.

Table 7.1. Number of operational RO units relative to available power.

Power threshold	Number of operational units
Power < 4.09 kW	0 units
Power > 4.09 kW	1 unit
Power > 12.57 kW	2 units
Power > 21.05 kW	3 units

7.4.3 Programming the modular operation algorithm

Lastly, the elements of the modular operation procedure, i.e., standardised start-up/shutdown sequences, power thresholds and rules of connecting/disconnecting the RO

units, were implemented in the control system within the modular operation block to automate the RO units modulation. As presented in Fig. 7.5, the modular operation block receives the available power and the current operational state of each RO unit as an input signal and sends three output signals for each RO unit. The first signal prompts a unit on or off depending on the available power and the power threshold defined in Table 7.1. The second signal is the power allocated for each unit. The third signal defines the operational state of each RO unit, whether it should be in the initial start-up, rolling start-up, permeate production, or shutdown state. For the initial start-up, rolling start-up and shutdown sequences, a separate algorithm in the control system contains the instructions to perform the standardised sequences developed for each operational state. This includes the running time of each pump, the sequence of pumps operation and the pumps' ramp up/ down rate. As for the production stage, the control system used is the MPC controller presented in Section 7.3.2 that operates the RO units at a variable recovery with respect to wind power variation following the variable-speed operation technique.

Fig. 7.6 presents a flowchart describing the algorithm implemented in the modular operation technique block that modulates the RO units operation. Initially, the control system compares the wind power to the power threshold to determine the number of operational RO units. The first RO unit is started followed by the subsequent units if the preceding unit reaches full capacity, as defined in the connection-disconnection strategy. The RO units are disconnected in the opposite order they were connected. Once a RO unit is signalled to start, the shutdown timer is examined to determine whether to initiate the initial start-up or the rolling start-up procedure. As long as there is enough power for permeate production, the RO unit is left operational based on the variable-speed operation technique. Once the available power falls below the threshold for permeate production, the control system sends a signal to the RO unit controller to initiate the shutdown sequence. When the system started the shutdown sequence, a time delay is used to delay changes in the RO unit operational state to ensure that the shutdown sequence is completed successfully without interruption.

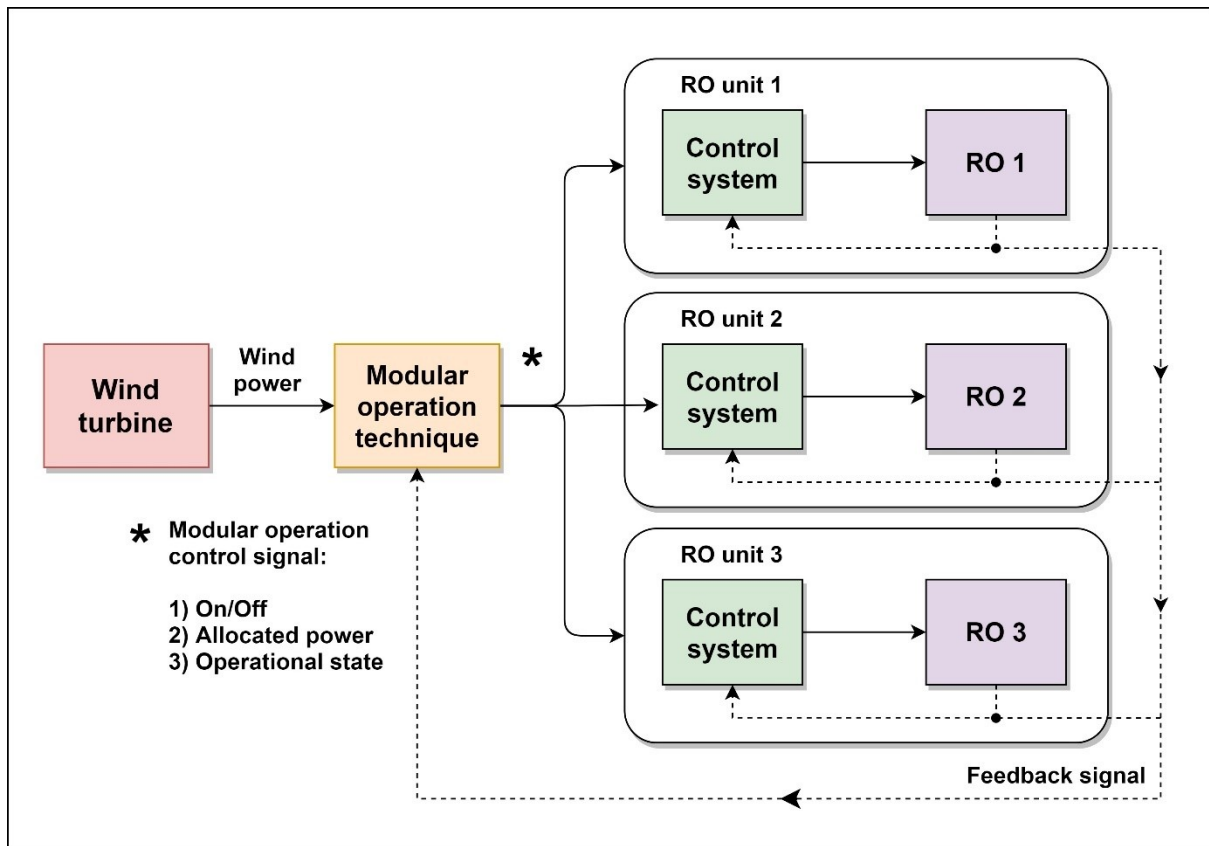


Fig. 7.5. Control system structure after implementing the modular operation technique.

The modular operation technique block identifies if a RO unit is on or off, allocates the power for each unit and prompts the operational state for each unit. Each RO unit includes a separate MPC control system that operates it with variable recovery based on the allocated power. The feedback signal from the RO units to the modular operation technique block includes the operational state of each RO unit.

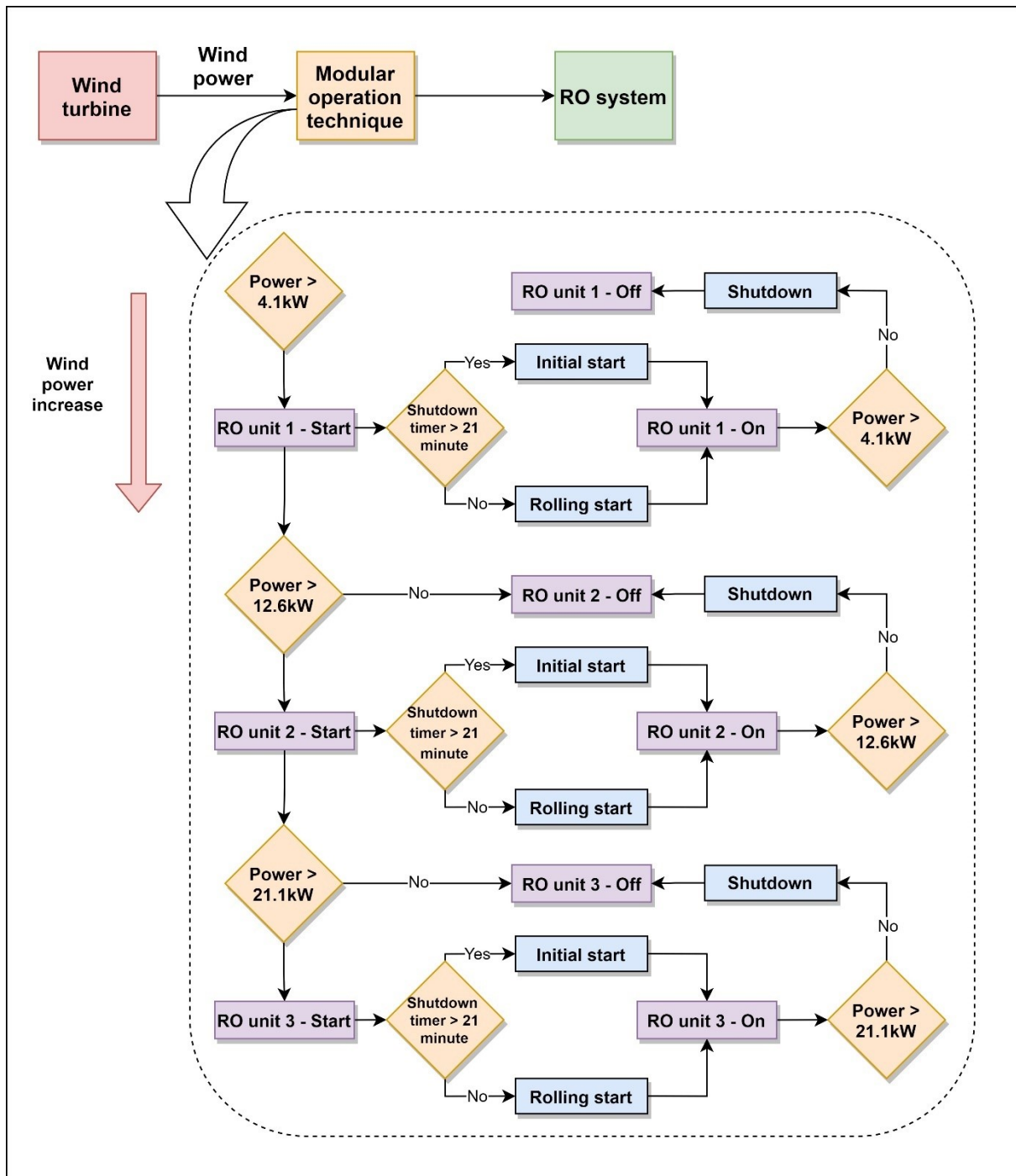


Fig. 7.6. Algorithm for the modular operation procedure.

7.5 Results and discussion

7.5.1 Standardised start-up and shutdown sequences

In this section, the standardised start-up and shutdown sequences, which were developed experimentally for the RO units, are described. The sequences were designed to operate the RO units based on the membrane manufacturers recommendations and the operational guidelines set in the HPP and ERD manuals [160, 165]. The theoretical operation guidelines were implemented experimentally to the RO unit and presented as follows:

7.5.1.1 *Initial start-up procedure*

The developed initial start-up procedure is presented in Fig. 7.7. The first step was operating the LPP to supply feedwater from the feed tank and fill up the RO system. The LPP was left operational for 2 minutes to ensure the entire system was filled with water and to bleed air from the pressure vessels, pipework and iSave. Then, the iSave was started and its motor speed was increased at a rate of 2 Hz/s, based on a maximum rate of 5 Hz/s recommended by Danfoss [165]. The iSave was left operational at a minimum speed of 20 Hz, delivering its minimum flowrate of 9.8 m³/h, for 5 minutes to circulate water through the pressure vessels and vent the air out of the system [165]. After the system fill up and the air venting process were complete, all the air vents were closed and the HPP was started to pressurise the system. The HPP speed was increased to the desired speed at a rate of 0.5 Hz/s to maintain an increase in feed pressure below 0.7 bar/s [142]. Once the HPP reached the desired speed, the permeate was discarded until it reached an acceptable concentration. For the RO unit used in this study, the time until the permeate concentration stabilised at a value below the maximum limit of 500 mg/l was recorded during experimentation to be an average of 7.2 minutes. The entire initial start-up sequence required around 15 minutes to be completed until an acceptable product quality. This time is subject to RO system design and capacity.

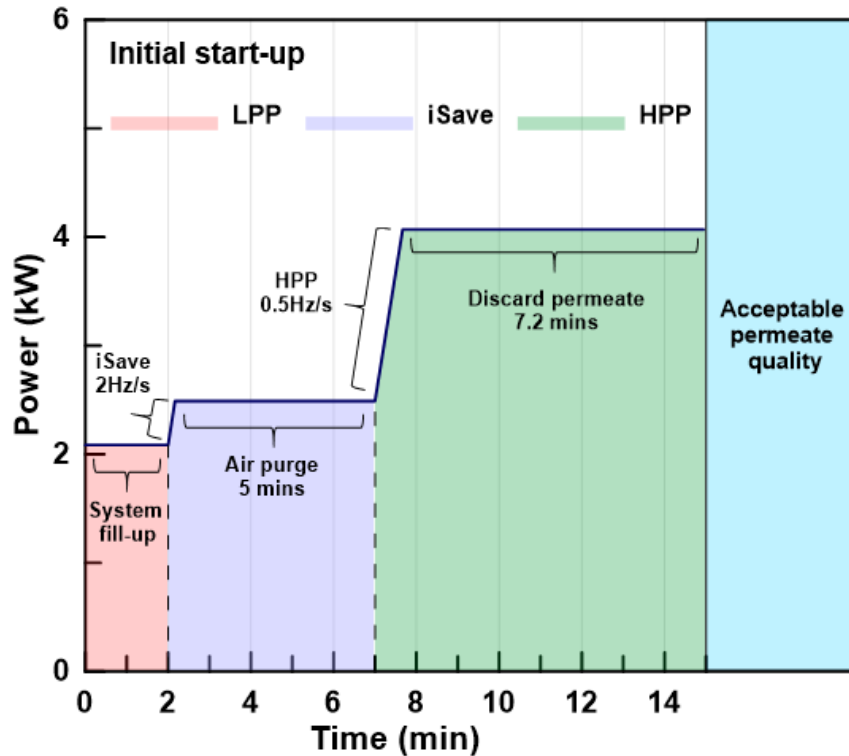


Fig. 7.7. Initial start-up procedure.

7.5.1.2 Rolling start-up procedure

The rolling start-up procedure is presented in Fig. 7.8. It included the same steps as the initial start-up excluding the air purging process. The rolling start-up sequence began with operating the LPP for 30 seconds to ensure steady flow, then the iSave was started at a ramping rate of 2 Hz/s as per the manufacturer's recommendation [165]. The HPP was powered on and ramped at a rate of 0.5 Hz/s to maintain an increase in feed pressure below 0.7 bar/s [142]. After reaching the desired speed, the permeate was discarded until it reached an acceptable concentration. On average, the permeate concentration dropped below 500 mg/l after approximately 5.3 minutes after the HPP is started. The complete rolling start-up sequence required approximately 7 minutes to be completed. This was significantly lower than the initial start-up process, which indicated why it is beneficial to develop more than one start-up procedure depending on the status of the RO system.

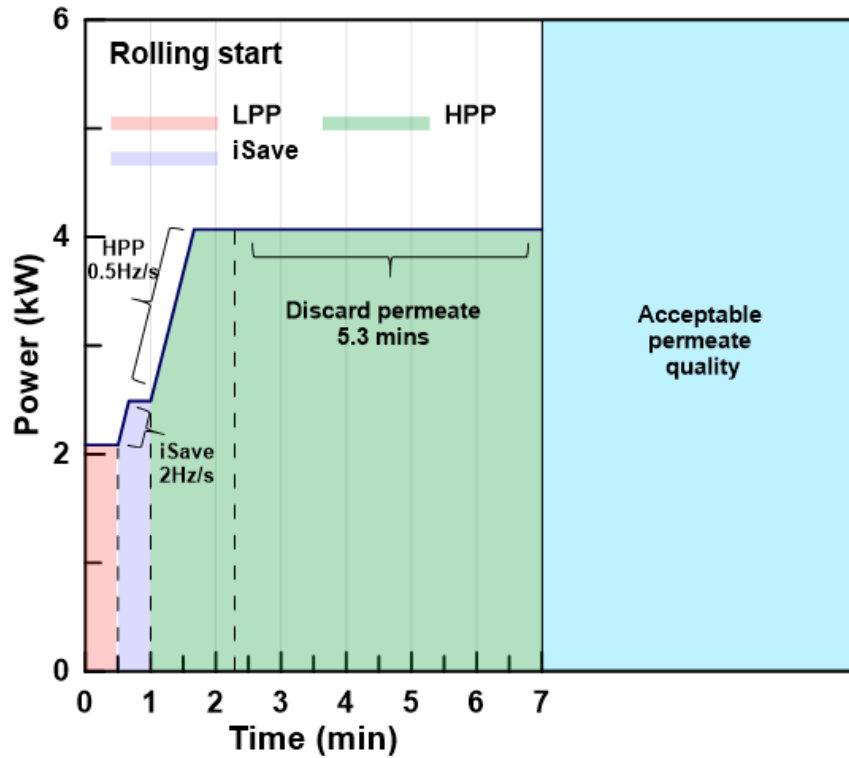


Fig. 7.8. Rolling start-up procedure.

7.5.1.3 Shutdown procedure

The standard shutdown procedure is presented in Fig. 7.9. The HPP was ramped down from the set speed to a complete stop at a fast rate of 2 Hz/s to stop water permeation and allow the pressure to drop below the osmotic pressure. The permeation stopped as soon as the HPP halts completely. The iSave was left operational at a minimum flowrate of 9.8 m³/h for 30 seconds to flush the brine out of the RO elements and pressure vessels. This period was more than enough to replace the full water volume inside the pressure vessels. Then, the iSave was ramped down at a rate of 2 Hz/s and the LPP was turned off after 10 seconds to allow for a smooth shutdown. The complete shutdown sequence required one minute to complete. This showed that there must be an anticipation of a sudden shutdown to guarantee enough power to complete the shutdown sequence.

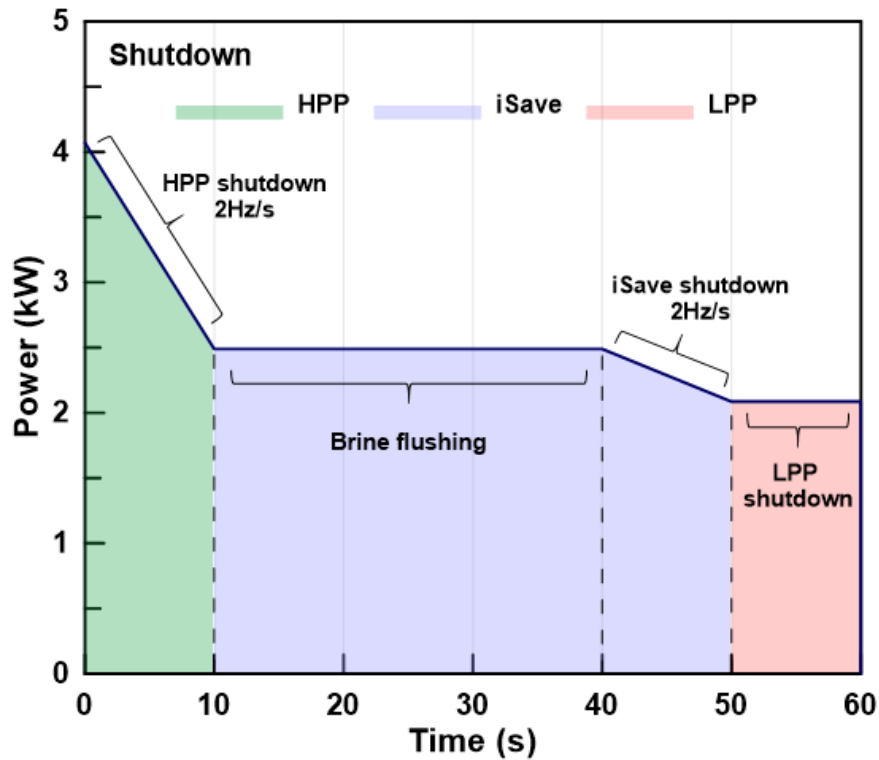


Fig. 7.9. Shutdown procedure.

7.5.2 Operation scheduling using long-term wind speed prediction

This section presents the implementation of long-term wind speed prediction for scheduling the RO units operation. The long-term NN was used for predicting hourly average wind speeds for a full day ahead to estimate the available wind power based on the wind turbine power curve presented in Fig. 7.3. The predicted wind power was then used to estimate the possible number of operational RO units during the day according to the power threshold presented in Table 7.1. This allowed for scheduling the RO units operation while considering a smooth operation profile that minimises unexpected shutdowns. Prior knowledge of the RO units start-up/shutdown cycles can provide a form of reliability similar to operating with constant power in terms of adhering to the standardised start-up/shutdown procedure and guaranteeing the readiness of the auxiliary systems.

In Fig. 7.10, 7.11 and 7.12, the accuracy of estimating the number of operational units along the day is presented by comparing the number of operational RO units using the actual and predicted wind speeds. The comparison was done using wind speed data for three random days that were excluded from the NN training dataset. In addition, a sample of possible scheduling for the RO units is presented for each day based solely on the predicted wind speed. This showcases how wind speed prediction can be used to plan the RO units operation

for a day ahead. The scheduling provided is considered very conservative to guarantee operation without unexpected shutdowns, however, it will not lead to the highest permeate production. The process of scheduling the RO units operation is subject to the operator's decision to assess whether to risk an unexpected drop in power for the sake of higher permeate production.

In Fig. 7.10, the predicted number of operating units is compared to the actual according to the hourly average wind speed for Day 1. During the first hours of the day, the wind power was not sufficient to operate any RO unit. As the wind power increased, the number of operational units increased to a maximum of 3 units during mid-day before it decreased again as the power dropped after 15:00. The bell-shaped pattern is associated with the effect of sea breeze that led to higher wind speeds during mid-day. This applies to Bahrain being an island country with high air temperatures, especially in August. The estimation based on the NN prediction successfully predicted periods of insufficient power to operate any RO unit during the day, specifically the last eight hours. For the remainder of the day, there was an underestimation of the possible number of operational units caused by lower predicted wind speed compared to the actual value. Despite that the underestimation would lead to lower energy utilisation, it would present a smooth operation profile by avoiding sudden power drops. Generally, there was a good correlation between the predicted number of operating units and the actual, represented by a R^2 of 0.78, considering the prediction range of a full day ahead. As for operation scheduling, a scheduling plan for the RO units operation is presented solely based on the predicted wind power. The wind speed prediction had shown the bell-shaped wind speed pattern for the day indicating an increase in wind power during mid-day. Accordingly, a single RO unit would be operated from 06:00 to 08:00, then another will be added to utilise the rise in power near mid-day. The number of units will be reduced gradually during the afternoon in anticipation of a power drop after 15:00.

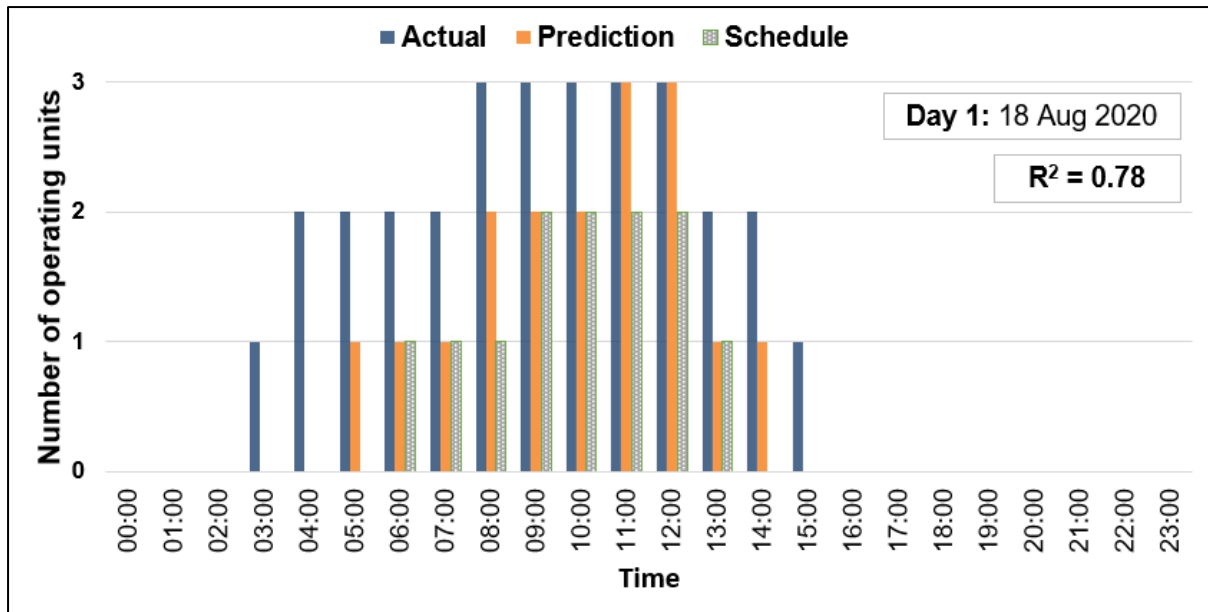


Fig. 7.10. Possible number of operational RO units based on actual and predicted hourly average wind speed on 18 August 2020.

For Day 2, the predicted wind power indicated the possibility of permeate production from the start of the day. The number of operational units based on the predicted power was more than the actual due to an overestimation of the predicted wind speed. The prediction accuracy increased towards mid-day with the predicted number of operational units reaching 3 units. The wind power dropped after 14:00 leading to insufficient power to operate any units, which was predicted successfully by the NN. The correlation between the predicted and actual number of operating units was R^2 0.64. Based solely on the prediction, the RO system can be scheduled to operate a single unit from the period of 01:00 to 04:00 instead of 2 units to allow for any prediction inaccuracies. The number of operating units could be increased to two units as wind power increases towards 08:00. Three units could be operated from 09:00 till 11:00 before ramping down the RO units in anticipation of the power drop after 13:00. As mentioned earlier, this scheduling strategy sets a reserved operation profile that would minimise unexpected shutdown.

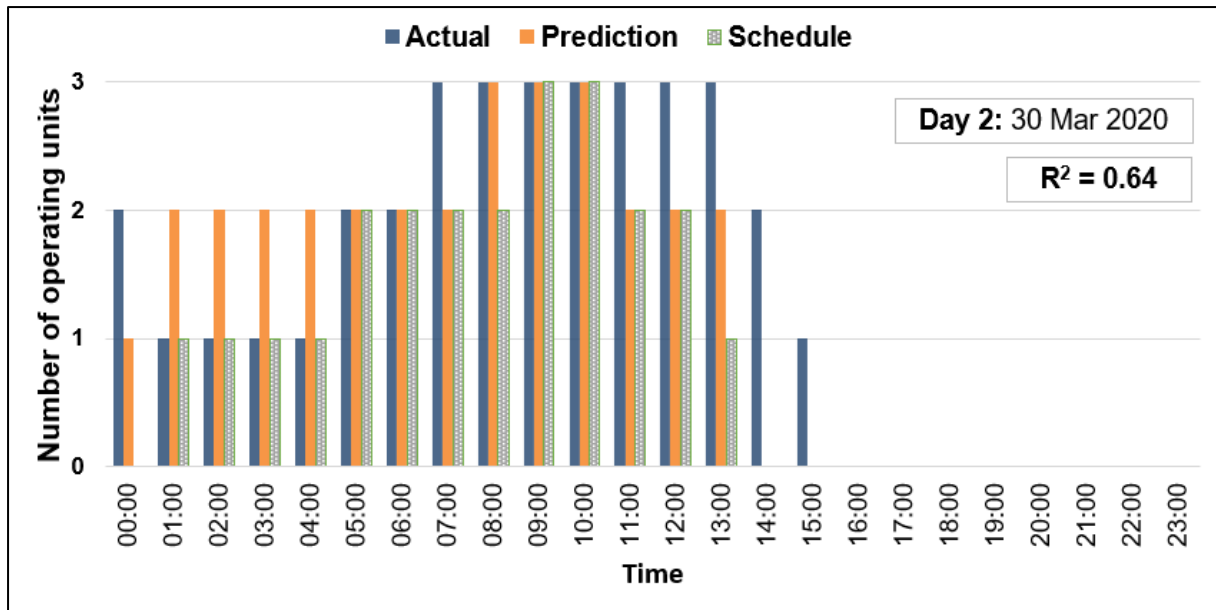


Fig. 7.11. Possible number of operational RO units based on actual and predicted hourly average wind speed on 30 March 2020.

As for Day 3, the high wind speed allowed for two RO units to operate at the start of the day and three units to be operated until 10:00. As the wind speed dropped towards night-time the number of operating RO units decreased. The correlation between the predicted and actual number of operating units was quantified by a R^2 of 0.79. It is noted that the prediction accuracy increased with higher wind power as a result of reaching the maximum power required to operate the 3 units. The estimation of number of operating units accurately predicted the number of operating units from the start of the day till mid-day. As the wind power dropped near the limit of operating 1 unit, the error between the actual and predicted wind speed led to underestimating the wind power at certain times, which is not a disadvantage as operation near the marginal limit of 1 RO unit could result in sudden shutdown due to insufficient wind power. Given the predicted number of operational units a day earlier, an operator could schedule the operation within the period from 01:00 to 10:00 for two units to avoid unscheduled shutdowns. Another operator might schedule 3 units for operation to achieve higher water demand, however, there will be a chance of a shutdown for the third unit in case of a power drop. The selected operation profile will be subject to water demand and the plant operators judgment.

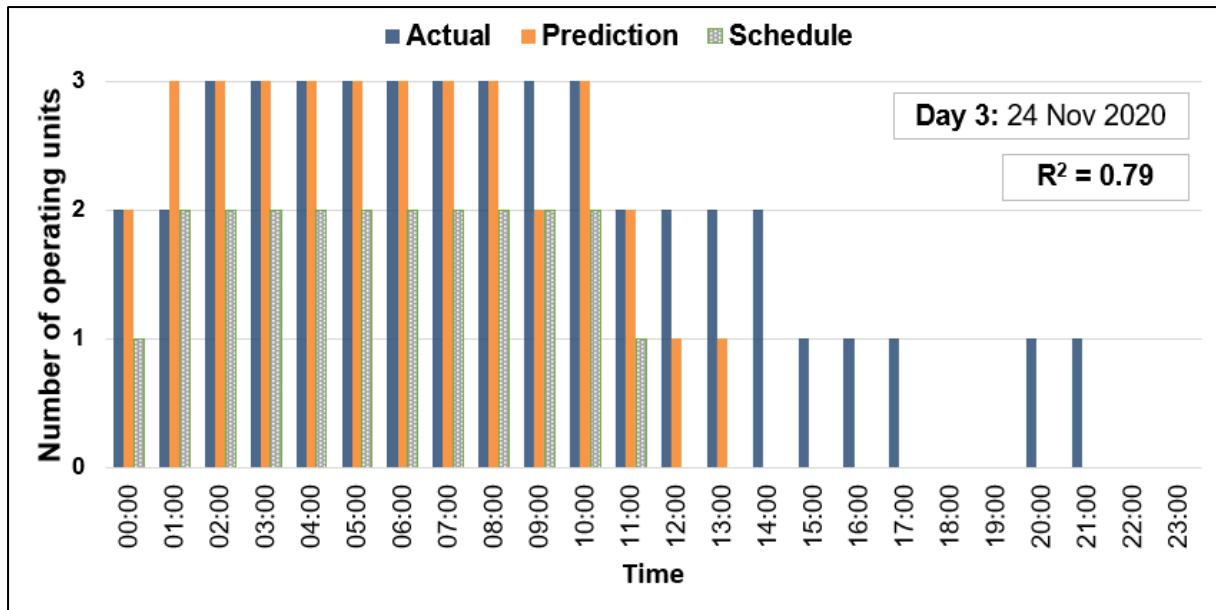


Fig. 7.12. Possible number of operational RO units based on actual and predicted hourly average wind speed on 24 November 2020.

7.5.3 Predictive control using short-term wind speed prediction

The second solution is a predictive control procedure that directly implements the short-term wind speed prediction into the RO system control. The predicted wind speed average for the upcoming 2 minutes was used as the control system input instead of the real-time wind speed signal. As such, the control system generated reference signals to control the RO unit based on the averaged wind speed for the next 2 minutes. In this manner, the RO unit control system was always two minutes ahead of the real-time wind speed variation. Using an averaged wind speed signal would guarantee smoother operation of the RO unit instead of matching the RO unit load to the random wind power variation. In addition, averaging the wind speed signal over a period that covers the time required for the shutdown sequence would guarantee enough energy to perform it without interruption. The high accuracy of the 2-minute average short-term prediction omits the need to operate the RO system with short-term energy storage, e.g., flywheel.

Initially, the short-term NN generated the wind speed average for the next 2 minutes, which was used to calculate the predicted wind power using the wind turbine power curve in Fig 7.4. Then, the predicted wind power was sent to the control system to generate reference signals for the permeate production and brine flowrate to which the motor speeds were controlled, thus, matching the RO plant load to the predicted average power. The modular operation procedure presented in Section 7.4 was implemented, such that the RO units are

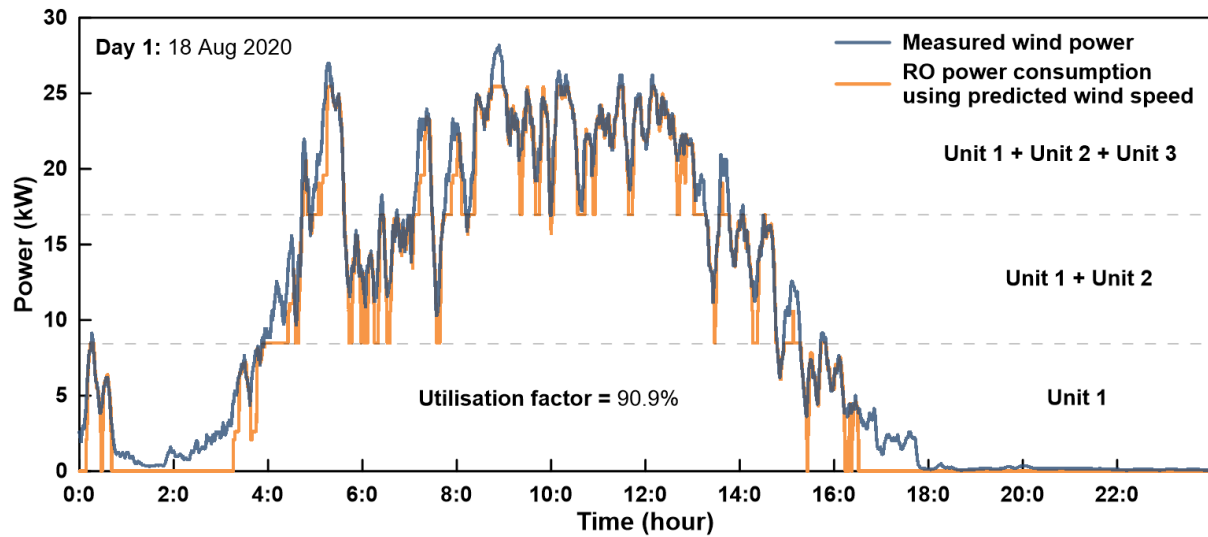
started or shut down depending on the available wind power and the defined power threshold for each unit. To test the performance delivered by the presented predictive control procedure, the RO units load based on the wind speed prediction was compared to the real-time wind power for three random days that were excluded from the NN training.

In Fig. 7.13 (a), the RO system power consumption based on the 2-minute averaged wind speed signal is compared to the real-time measured wind power. The figure highlights the start-up and shutdown of the RO units along the day. Using the predicted wind power average as the input for the control system provided more stable performance than the control system reacting to the real-time power variation. In addition, the high accuracy delivered by the short-term NN meant that the control system can accurately track real-time wind power changes. This meant that the RO plant load matched with the available wind power while securing a two-minute lead time to account for sudden changes in available power. In addition, the implementation of the modular operation technique by switching the RO units on/off ensured the RO system can accommodate wide changes in available power. The combination of modular operation and predictive control using the short-term wind speed prediction offered high utilisation of the available energy such that the ratio between the RO plant energy consumption and the energy generated by the wind turbine, named the utilisation factor, was 90.9%. This translated to high cumulative permeate production by the end of the day. Fig. 7.13 (b) presents the rate of permeate production along the day for the RO system. The figure highlights the periods of permeate production for each RO unit subject to the start-up/shutdown cycles. By using the predicted wind power as the control system input, along with using the modular and variable-speed operation, the RO system produced 78 m³ for Day 1 of fresh water at a 147.1 mg/l concentration.

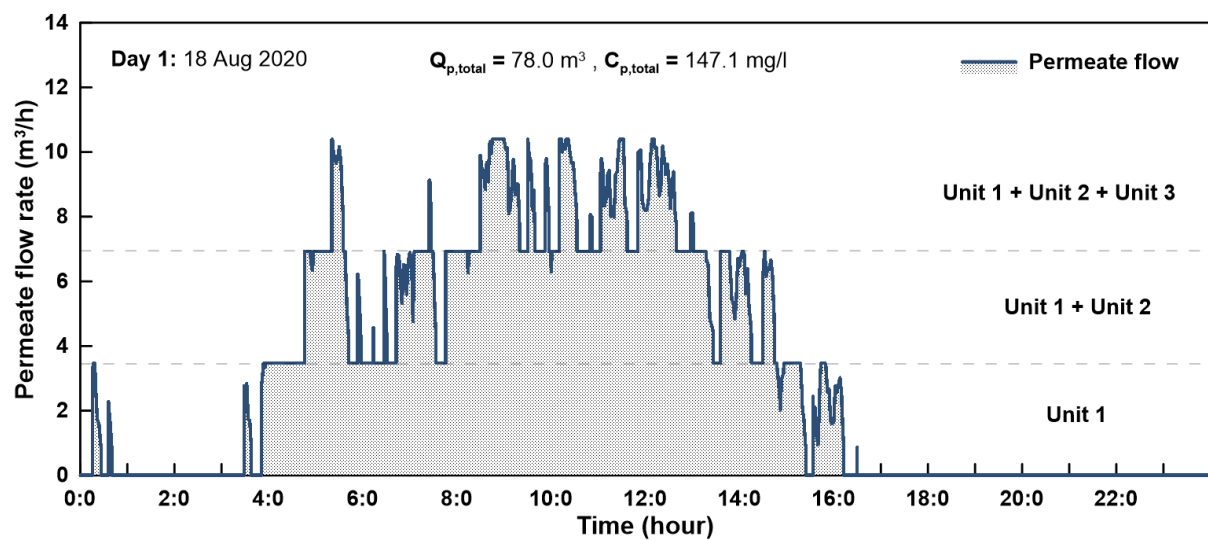
The only disadvantage noticed in Fig. 7.13 (a) is the short duration start-ups for the RO units, especially for unit 3, due to power drop below the operation threshold. However, implementing the modular operation procedure in addition to defining a standard start-up/shutdown sequence, ensured that these short-duration start-up/shutdown cycles were performed as smoothly and safely for the RO units as possible. Moreover, these short-duration start-ups can be avoided by using the long-term prediction, described in Section 7.5.2, for scheduling the RO units operation in advance.

Similar performance was noticed for Days 2 and 3 presented in Fig. 7.14 and 7.15. The energy utilisation factor for Days 2 and 3 were 91.5% and 91.4%, respectively. As for total

permeate production, the RO system produced a total of 91.5 m³ of fresh water at 145.1 mg/l NaCl concentration for Day 2 and 123.4 m³ at a 145.5 mg/l concentration for Day 3. A summary of the RO system performance for Days 1, 2 and 3 is presented in Table 7.2.



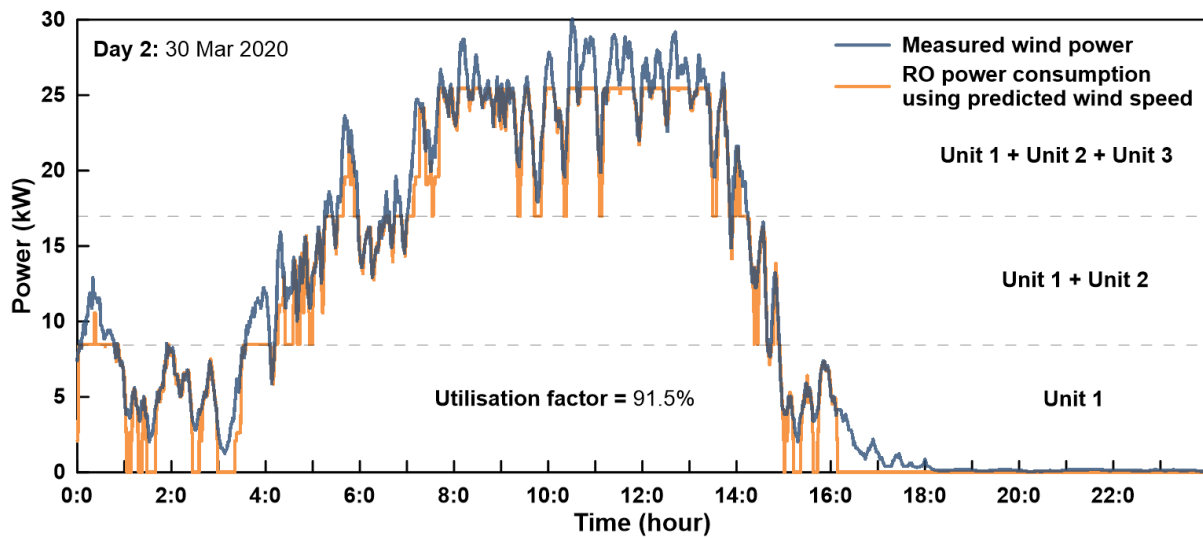
(a)



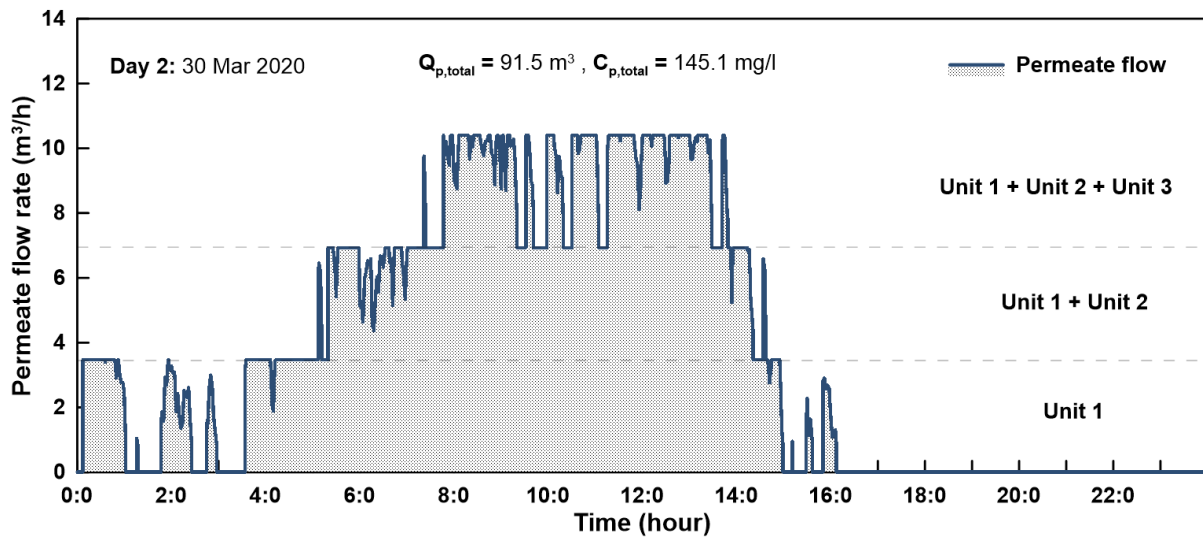
(b)

Fig. 7.13. The RO units operation using the predicted wind power from the short-term neural network as the power input for the control system.

The modular and variable-speed operation strategies are implemented to vary the RO units load according to the predicted wind power. The figure presents a) a comparison between the RO system power consumption and real-time wind power, and b) the rate of permeate production during Day 1.



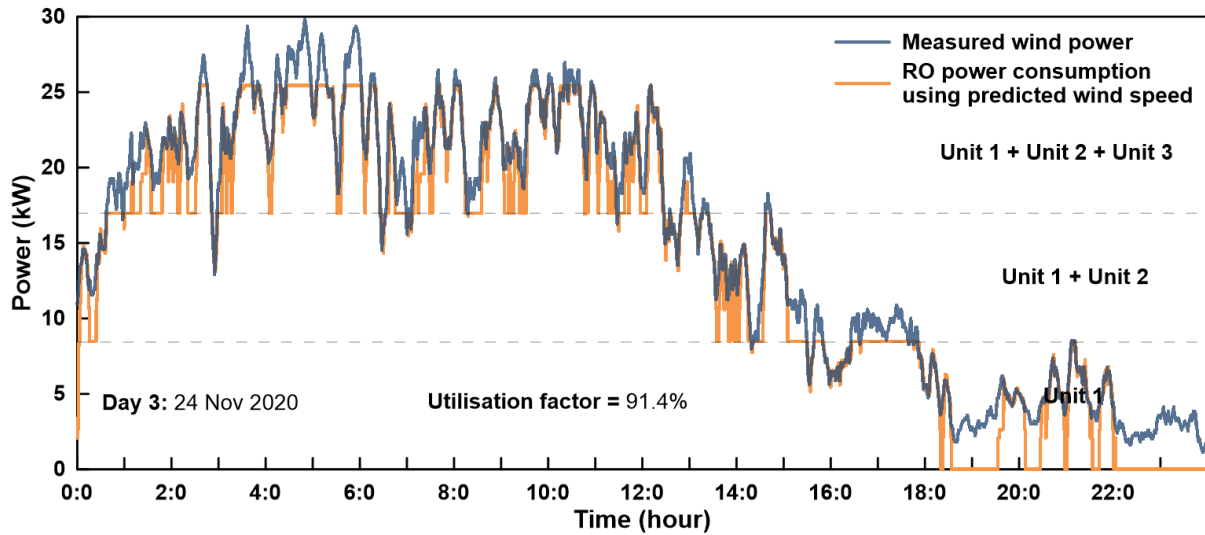
(a)



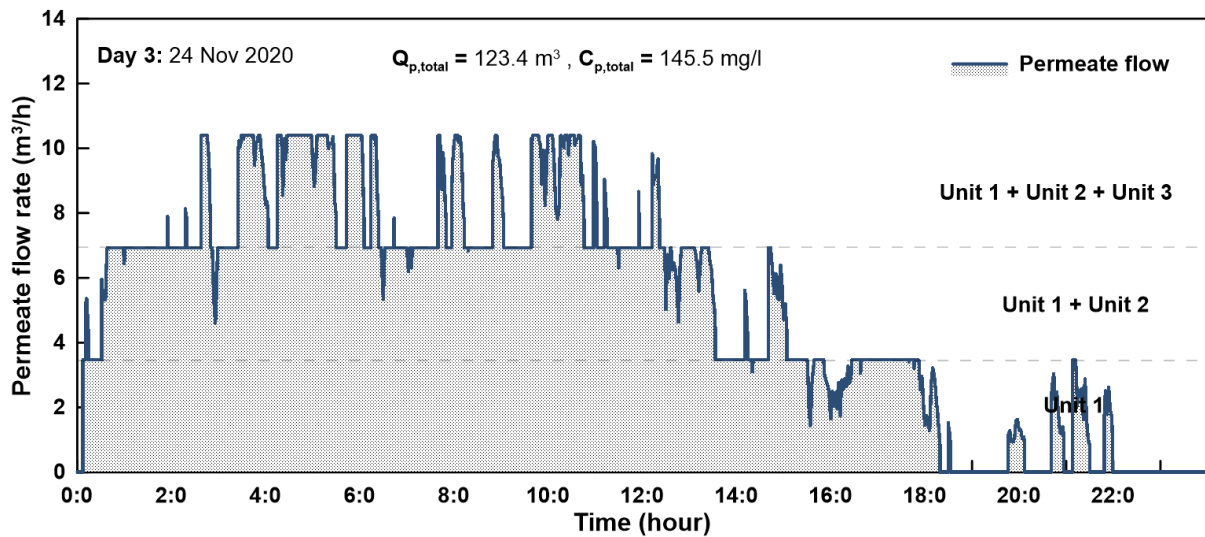
(b)

Fig. 7.14. The RO units operation using the predicted wind power from the short-term neural network as the power input for the control system.

The modular and variable-speed operation strategies are implemented to vary the RO units load according to the predicted wind power. The figure presents a) a comparison between the RO system power consumption and real-time wind power, and b) the rate of permeate production during Day 2.



(a)



(b)

Fig. 7.15. The RO units operation using the predicted wind power from the short-term neural network as the power input for the control system.

The modular and variable-speed operation strategies are implemented to vary the RO units load according to the predicted wind power. The figure presents a) a comparison between the RO system power consumption and real-time wind power, and b) the rate of permeate production during Day 3.

Table 7.2. Summary of the RO system performance for Days 1, 2 and 3.

	Total wind energy (MJ)	RO energy consumption (MJ)	Permeate production (m³/day)	Permeate quality (mg/l)	Energy utilisation (%)
Day 1	855.1	777.3	78	147.1	90.9
Day 2	965.0	883.2	91.5	145.1	91.5
Day 3	1313.0	1200.0	123.4	145.5	91.4

7.6 Summary

This chapter presented a modular operation technique that uses wind speed prediction for operation scheduling and predictive control of the RO units. Two solutions were introduced based on the long-term and short-term wind speed prediction to improve the efficiency of modular operation. Initially, the long-term prediction was used to schedule the daily operation of the RO units. Secondly, the short-term prediction was used as the wind speed signal for the control system, such that the control system predictively generated a reference signal and was always ahead of the actual wind speed change. The modular operation technique was presented alongside the variable-speed operation technique and the MPC control system developed in Chapter 5, thus forming a complete load management technique for matching the RO load to wind power variation. A RO system consisting of multiple RO units was used in the analysis to reflect the modularity of large-scale systems. The tests were performed using the wind speed time-series for three random days that were excluded from the NN training. The conclusions are presented as follows:

- The development of a standardised start-up/shutdown sequence can vary depending on the plant design. A standardised start-up and shutdown sequence was developed experimentally using guidelines set by the membrane manufacturers and operation limitations for the pumps that ensure smooth and efficient operation during the start-up/shutdown cycles. The operating sequences included the running time of each pump, the sequence of pumps operation and the pumps' ramp up/ down rate. The initial start-up and rolling start-up sequences required approximately 15 and 7 minutes to be completed, respectively. The shutdown sequence required around one minute to

be completed, indicating the necessity to anticipate power drops to guarantee an uninterrupted shutdown sequence.

- The long-term wind speed prediction was used for scheduling the RO units operation to operate according to a smooth operation profile that minimises unexpected shutdowns. The number of operating units according to the predicted hourly-average wind speeds was compared to the actual for Days 1, 2 and 3. A good correlation was achieved indicated by R^2 of 0.78, 0.64, and 0.79 for Days 1, 2 and 3, respectively. In addition, a sample schedule was presented for the RO units, based solely on the predicted wind speed, that delivered a conservative and smooth operation profile without risking an unexpected shutdown.
- The two-minute average wind speed generated by the short-term NN was used as the wind speed signal for the control system. As such, the control system predictively generated reference signals for the permeate and brine flowrates based on the averaged wind speed. The comparison between the RO system power consumption based on the predicted wind speed signal and the real-time measured wind power indicated that using the predicted wind speed average led to a smoother operation profile than the control system reacting to the real-time power variation. In addition, the RO plant load matched with the real-time available power due to the high accuracy of the short-term wind speed prediction, while securing a two-minute lead time to account for sudden changes in wind speed and available power.
- The combination of variable-speed operation and modular operation, enhanced using predictive control via the short-term wind speed prediction, presented a complete load management technique that matches the RO load to wind energy variations. Overall, it offered high utilisation of the available energy, such that the energy utilisation factor, was 90.9%, 91.5% and 91.4% for Days 1, 2, and 3, respectively. This translated to high cumulative daily permeate production of 78 m³, 91.5 m³ and 123.4 m³ for Days 1, 2 and 3, respectively.

8 Chapter 8 Conclusions

8.1 Introduction

This chapter summarises the research findings and highlights the original contributions arising from this work. Responses to individual objectives are presented to summarise the research activities and outcomes. The extent to which the overall aim was achieved is assessed by examining the original contributions of this study. Lastly, recommendations for further development are outlined.

8.2 Responses to the objectives

- **Objective 1:** Review published literature to identify state of the art regarding RE-driven RO desalination, in addition to identifying technical challenges and potential solutions for large-scale implementation (Chapter 2).

The literature review indicated that variable operation by directly connecting the RO system to a RES, without backup systems, has shown feasible performance compared to RO systems operating with constant power. The findings of the literature review helped identify points of potential improvements for RE powered-RO and conceptualise the objectives for this thesis. They are presented as follows:

- a) Previous studies used small-scale systems as a proof-of-concept for operating RO systems using RE. Although these systems presented a good platform to develop and analyse their proposed solutions, they do not reflect operation characteristics or include equipment similar to large-scale systems to guarantee that their technology is suitable to such scale.
- b) Maintaining the performance and lifetime of the RO modules during variable operation was an important point raised in previous studies. This indicated the need to operate the system within the safe operating limits and based on the manufacturer's recommendations during load variation.
- c) An advanced control system that can deliver fast and robust performance is required to operate the RO systems using variable power for matching the RO plant load to the RE fluctuations. Limited studies were found that specifically discussed the control system of RE powered RO plants.

- d) The execution of modular operation requires the development of a standardised start-up/shutdown sequence that guarantee the smoothness of the modulation cycles and maintain the recommended operating procedure. In addition, modular operation would subject the RO units/trains to multiple start-ups/shutdowns during the day due to RE variation. This highlighted the need to schedule the RO units' operation to avoid their random connection/disconnection.
- **Objective 2:** Design, build and test an RO pilot plant at an industrial scale having comparable performance to large-scale systems to develop solutions transferable to such scale (Chapter 3).

A RO test-rig was designed and built at Aston University as a platform for testing the operation of RE-driven RO systems. The test-rig was arranged in a split-feed flow configuration by splitting the feed between a HPP and an isobaric ERD. In addition, it utilised commercial equipment used in large-scale RO systems to reflect their capability for operating with variable power. The plant rated production capacity is 3.2 m³/h.

- **Objective 3:** Develop and validate a dynamic model that predicts the dynamic behaviour of the developed RO system (Chapter 4).

A dynamic model was developed for the RO system that included the solution-diffusion theory and the concentration polarisation theory to describe the RO membrane performance, in addition to individual models for the components of the pumping system. The prediction accuracy of the model steady-state output and dynamic response were validated using experimental data from the RO system. The model accurately predicted the transient change in permeate flowrate, feed pressure, and permeate concentration, such that the error between the predicted and measured data remained within a 5% margin along a 10% step-change in the HPP rotational speed. The model was used for the development and testing of the solutions presented throughout this study.

- **Objective 4:** Present an optimised variable-speed operation technique to vary the RO operation parameters according to available power (Chapter 5).

Selection of an operation strategy, to optimally vary the RO system load according to the available power and input disturbances, is essential for the feasibility of operating RO systems using RE. Multiple operational strategies were explored in this study for varying the

operating parameters. The investigation considered operation at constant recovery, operation at constant brine flowrate, and operation at a constant feed flow. The operation strategy is selected to provide the widest operation range at the least SEC. The results revealed that operation at variable recovery with constant brine flowrate delivered the lowest specific energy consumption, indicating best utilisation of available energy, and widest operation range, allowing for permeate production at low power. This original finding can be applied to commercial systems using split-feed flow configuration and an isobaric pressure exchanger.

- **Objective 5:** Design and implement an advanced control system based on MPC and compare its performance to a conventional PID controller (Chapter 5).

Operating a RO system using variable power from a RE sources requires a control system delivering fast and robust performance. An advanced control system based on MPC was designed and compared to a conventional PI controller. The MPC controller improved the settling time for a 10% step-change in permeate flowrate by 47% compared to the PI controller. Moreover, the disturbance rejection improved by 47.2% and 43.9% for a 10% step-change in feed concentration and temperature, respectively. The MPC offered better energy utilisation indicated by a 2.35% increase in hourly permeate production for a defined wind speed time-series.

- **Objective 6:** Develop a wind speed prediction algorithm using NNs for forecasting long- and short-term changes in wind speed (Chapter 6).

Two NNs were developed to provide long- and short-term wind speed prediction for use in RO plant scheduling and control. The NNs were trained using wind speed data spanning six months for a site in the Kingdom of Bahrain. The long-term NN predicted the hourly average wind speed for a full day ahead and delivered a good fit between the output and target data for the complete dataset presented by a R^2 0.59. and a RMSE of approximately 1.5 m/s. As for the short-term NN, it predicted the average wind speed for 2 minutes ahead using wind data of the previous ten minutes. It delivered a high prediction accuracy presented by a R^2 0.95, indicating an impressive correlation between the network output and target data, and a low RMSE of approximately 0.15 m/s. The accuracy delivered by the long-term and short-term NNs highlighted their potential in scheduling the operation of RO systems, which was explored in the next objective.

- **Objective 7:** Develop a modular operation technique to connect/disconnect RO units, while following a standardised start-up/shutdown sequence, according to changes in available power. The technique utilises wind speed prediction in scheduling the RO units' start-up/ shutdown sequence and parameters variation (Chapter 7).

Two solutions were presented based on the long-term and short-term NNs. Initially, the long-term prediction was used to schedule the daily operation of the RO units. This was done by estimating the number of operational units along the day based on the predicted power and generating a schedule for the RO units operation that maintained a smooth operation profile and minimised unnecessary repetition of the start-up/shutdown cycle. For assessing this solution, the estimated number of operating units according to the predicted hourly-average wind speeds was compared to the actual and a good correlation was achieved of a R^2 0.78, 0.64, and 0.79 for Days 1, 2 and 3, respectively. In addition, a sample schedule was presented that ensures a conservative operation of the RO units while avoiding unexpected shutdowns. For the second solution, referred to as 'predictive control', the two-minute average wind speed signal generated by the short-term NN was used as the input wind speed signal for the control system. This led to a smoother operation profile than reacting to the real-time power variation while securing a two-minute lead time to account for sudden changes in wind speed and available power. The RO plant load matched the real-time available power due to the high accuracy of the short-term wind speed prediction.

Combining variable-speed operation and modular operation, while using the predictive control supported by the short-term wind speed prediction, presented an efficient load management technique that matched the RO load to wind energy variations. Overall, it offered high utilisation of the available energy indicated by a utilisation factor of 90.9%, 91.5% and 91.4% for Days 1, 2 and 3, respectively. This led to a high cumulative daily permeate production of 78 m³, 91.5 m³ and 123.4 m³ for Days 1, 2 and 3, respectively.

8.3 Overview and original contributions

This section presents an overview of the overall aim in the context of describing the original contribution towards achieving it. This thesis aimed to optimise the operation of RE-driven RO and thus pave the way for large-scale implementation. The original contributions arising from this work are as follows:

- The current state-of-the-art and technical challenges in using RE as the main driver of large-scale RO plants were identified. Several reviews covered progress in driving RO plants with RE. However, the technical challenges for the direct operation of large-scale RO plants using RE were not discussed specifically [11].
- Variable operation was recognised as the procedure for directly connecting the RO plant to the RE source. It is essential to allow the RO system to accommodate the RE variation. As national grids become more dependent on RE, there will be a necessity to manage the connected loads rather than the current practice of changing the power output of the fossil-fuelled powered plants.
- A RO test-rig with similar design and performance characteristics to large-scale systems was used to develop solutions transferable to such scale. This is a fundamental contribution by this research as previous studies used small-scale systems that did not reflect the performance of utility-scale systems.
- An investigation was performed to determine the optimum control strategy for implementing variable-speed operation of the RO system. Operating the RO system based on variable recovery with constant brine flowrate presented the lowest specific energy consumption, indicating best utilisation of available energy and widest operation range, and allowing for permeate production at low power. This original finding applies to commercial systems using split-feed flow configuration and an isobaric pressure exchanger.
- An advanced control system is developed for implementing the mapped control strategy and operating the RO system using fluctuating power. The MPC offered superior control compared to a conventional PID controller, due to its prediction ability, in terms of maintaining the controlled output at the reference value and suppressing output variation due to changes in disturbances. The introduction of MPC in RE powered-RO applications fulfils a knowledge gap highlighted by [11, 33] for the necessity of advanced control systems for such applications.
- A modular operation technique was developed to handle high magnitude variations in RE by connecting/disconnecting RO units according to the change in available power. Standardised start-up and shutdown sequences were developed for the RO system

described in Chapter 3 based on the guidelines of the equipment manufacturers to maintain safe/smooth operation during the start-up/shutdown sequence.

- Another novel contribution was implementing wind speed prediction using NN into RO system modular operation. Wind speed prediction allowed for scheduling the RO units operation based on a forecast of available wind power for a full day ahead, thus minimising unnecessary start-up/ shutdown cycles. Furthermore, the concept of predictive control by controlling the RO system based on the averaged wind speed prediction provided smooth operation and secured enough reaction time to perform the shutdown procedure.

Powering RO systems using RE is essential for decarbonising water production. It has the potential to improve the sustainability of RO desalination and reduce its reliance on fossil fuels, thus allowing for more deployment. The benefits of RO-driven RO can extend to two communities. Countries that have enough resources to meet their water demand through RO can reduce their operational cost and environmental footprint. On the other hand, developing countries with limited resources can meet their water demand by investing in RO with lowered operational costs.

8.4 Recommendations for future work

Although this thesis provided a load management technique that can be used to power RO systems using RE, more aspects require investigation.

Several studies had different outcomes on the effect of flow and pressure variation on membrane performance. An investigation is required that spans the membrane lifetime to give a definitive conclusion on how/if the membrane performance and lifetime would be affected. This was not possible during this study due to time limitations.

Another aspect to consider is the effect of flow and pressure fluctuations on mixing between the feed and brine streams within the ERD. Mixing between the two streams can lead to an increase in osmotic pressure, thus increasing the power consumption. This requires additional sensors to be installed for the pilot plant described in Chapter 3.

The strategy used in modular operation for disconnecting/ ramping down the RO units during a power drop requires further investigation. Alternatives such as power distribution for maintaining units operation can reduce the number of shutdowns. However, this requires

detailed analysis to determine the method of distributing power between units and the trade-off between longer operation, cumulative permeate production and permeate quality.

Another potential improvement is using hybrid RE sources for stabilising the power input to the RO systems. This can help improve operational reliability and allow operation for extended periods. However, the economic feasibility and performance efficiency of using hybrid RE is subject to the optimised selection and sizing of the RE sources.

In addition, the majority of previous studies have focused on either solar or wind energy as alternatives to fossil fuels. This is justified as solar and wind energy are considered mature renewables. However, wave energy can also be a feasible option for powering RO systems, especially due to its high energy density and that RO systems are mostly located in coastal areas.

Another topic to consider is the development of short-term energy storage that can smooth the power fluctuation from the RE source and improve operation stability. Storage systems such as flywheels, hydraulic accumulators and supercapacitors have been presented in previous studies, however, require further improvement for use with large-scale RO systems.

It is also worth mentioning that the environmental impact of discharging highly saline brine from large-scale RO plants is concerning. Currently, the desalination industry is moving towards zero liquid discharge for minimising brine water. This extends to benefiting from the brine by extracting valuable minerals, e.g., Lithium, Magnesium and Boron, that are present in high concentrations compared to seawater. Future studies should aim to improve the zero liquid discharge technology and its integration with RE powered-RO.

Lastly, the solutions presented in this study should be implemented on a large-scale system, whether through simulations or experimentally, to analyse its efficiency for directly coupling the RO system to the RES and to showcase the economic and environmental feasibility of variable operation. This requires collaboration with industrial partners to provide data for modelling and validation, and possibly allow for testing on their systems.

9 References

1. Mekonnen, M.M. and A.Y. Hoekstra, *Four billion people facing severe water scarcity*. Science Advances 2016. **2**: p. 6.
2. UNWWAP, *UN world water development report 2017. Wastewater: The Untapped Resource*. 2017: Paris.
3. UN-Habitat, *World Cities Report*. 2016.
4. WHO. *World health organization - Drinking water facts*. June 2018 [cited 2018 4 June].
5. Gökçek, M. and Ö.B. Gökçek, *Technical and economic evaluation of freshwater production from a wind-powered small-scale seawater reverse osmosis system (WP-SWRO)*. Desalination, 2016. **381**: p. 47-57.
6. IDA, *IDA desalination yearbook 2016-2017*. 2017.
7. Ghaffour, N., T.M. Missimer, and G.L. Amy, *Technical review and evaluation of the economics of water desalination: Current and future challenges for better water supply sustainability*. Desalination, 2013. **309**: p. 197-207.
8. Amy, G., et al., *Membrane-based seawater desalination: Present and future prospects*. Desalination, 2017. **401**: p. 16-21.
9. IDA, *IDA Water Security Handbook 2018 -2019*, in *Water Desalination Report*. 2018, International Desalination Association.
10. Lee, H.-J., et al., *Designing of an electrodialysis desalination plant*. Desalination, 2002. **142**: p. 267-286.
11. Mito, M.T., et al., *Reverse osmosis (RO) membrane desalination driven by wind and solar photovoltaic (PV) energy: State of the art and challenges for large-scale implementation*. Renewable and Sustainable Energy Reviews, 2019. **112**: p. 669-685.
12. Alkaisi, A., R. Mossad, and A. Sharifian-Barforoush, *A Review of the Water Desalination Systems Integrated with Renewable Energy*. Energy Procedia, 2017. **110**: p. 268-274.
13. Eltawil, M.A., Z. Zhengming, and L. Yuan, *A review of renewable energy technologies integrated with desalination systems*. Renewable and Sustainable Energy Reviews, 2009. **13**(9): p. 2245-2262.
14. Mathioulakis, E., V. Belessiotis, and E. Delyannis, *Desalination by using alternative energy: Review and state-of-the-art*. Desalination, 2007. **203**(1-3): p. 346-365.
15. IDA, *IDA Desalination Yearbook 2017–2018*. 2017.
16. Abdelkareem, M.A., et al., *Recent progress in the use of renewable energy sources to power water desalination plants*. Desalination, 2018. **435**: p. 97 - 113.
17. Voutchkov, N., *Energy use for membrane seawater desalination – current status and trends*. Desalination, 2018. **431**: p. 2-14.
18. Zarzo, D. and D. Prats, *Desalination and energy consumption. What can we expect in the near future?* Desalination, 2018. **427**: p. 1 - 9.
19. Shahzad, M.W., et al., *Energy-water-environment nexus underpinning future desalination sustainability*. Desalination, 2017. **413**: p. 52-64.
20. Voutchkov, N., *Desalination Engineering: Planning and Design*. 2013, United States: McGraw Hill.
21. González, D., J. Amigo, and F. Suárez, *Membrane distillation: Perspectives for sustainable and improved desalination*. Renewable and Sustainable Energy Reviews, 2017. **80**: p. 238-259.
22. IRENA and IEA-ETSAP, *Water Desalination Using Renewable Energy: Insights for policy makers*. 2013.
23. Cheah, S.F., *Photovoltaic Reverse Osmosis Desalination System*, in *Desalination and water purification research and development*. 2004, ITN Energy Systems, Inc. .
24. Kim, J., et al., *A comprehensive review of energy consumption of seawater reverse osmosis desalination plants*. Applied Energy, 2019. **254**: p. 113652.
25. Raluy, R.G., L. Serra, and J. Uche, *Life cycle assessment of desalination technologies integrated with renewable energies*. Desalination, 2005. **183**(1-3): p. 81-93.

26. Roberts, D.A., E.L. Johnston, and N.A. Knott, *Impacts of desalination plant discharges on the marine environment: A critical review of published studies*. Water Research, 2010. **44**(18): p. 5117-5128.
27. Subramani, A., et al., *Energy minimization strategies and renewable energy utilization for desalination: a review*. Water Res, 2011. **45**(5): p. 1907-20.
28. Shemer, H. and R. Semiat, *Sustainable RO desalination – Energy demand and environmental impact*. Desalination, 2017. **424**: p. 10-16.
29. REN21.2016, *Renewables Global Status Report 2016*. 2016.
30. Reichelstein, S. and M. Yorston, *The prospects for cost competitive solar PV power*. Energy Policy, 2013. **55**: p. 117-127.
31. Fu, R., et al., *U.S. Solar Photovoltaic System Cost Benchmark: Q1 2017*. 2017, National Renewable Energy Laboratory.
32. Bolinger, M. and R. Wiser, *Understanding wind turbine price trends in the U.S. over the past decade*. Energy Policy, 2012. **42**: p. 628-641.
33. Carta, J.A., et al., *Preliminary experimental analysis of a small-scale prototype SWRO desalination plant, designed for continuous adjustment of its energy consumption to the widely varying power generated by a stand-alone wind turbine*. Applied Energy, 2015. **137**: p. 222-239.
34. Ali, A., et al., *Membrane technology in renewable-energy-driven desalination*. Renewable and Sustainable Energy Reviews, 2018. **81**: p. 1-21.
35. Subiela, V.J., J.A. Carta, and J. González, *The SDAWES project: lessons learnt from an innovative project*. Desalination, 2004. **168**: p. 39-47.
36. Council, N.R., *Review of the desalination and water purification technology roadmap*. 2004, National Academy of Sciences.
37. *World Energy Resources: Hydropower*, in *World Energy Resources report*. 2016, World Energy Council.
38. Witte, T., S. Siegfriedsen, and M. El-Allawy, *WindDeSalter Technology Direct use of wind energy for seawater desalination by vapour compression or reverse osmosis*. Desalination, 2003. **156**.
39. Liu, C.C.K., et al., *Experiments of a prototype wind-driven reverse osmosis desalination system with feedback control*. Desalination, 2002. **150**: p. 277-287.
40. Peñate, B., et al., *Assessment of a stand-alone gradual capacity reverse osmosis desalination plant to adapt to wind power availability: A case study*. Energy, 2011. **36**(7): p. 4372-4384.
41. Liu, C.C.K., *Wind-powered reverse osmosis water desalination for Pacific islands and remote coastal communities*, in *Reclamation: Managing water in the west*. 2009, U.S. Department of the Interior. Bureau of Reclamation.
42. Koroneos, C., A. Dompros, and G. Roumbas, *Renewable energy driven desalination systems modelling*. Journal of Cleaner Production, 2007. **15**(5): p. 449-464.
43. Gude, V.G., N. Nirmalakhandan, and S. Deng, *Renewable and sustainable approaches for desalination*. Renewable and Sustainable Energy Reviews, 2010. **14**(9): p. 2641-2654.
44. Manju, S. and N. Sagar, *Renewable energy integrated desalination: A sustainable solution to overcome future fresh-water scarcity in India*. Renewable and Sustainable Energy Reviews, 2017. **73**: p. 594-609.
45. Rodríguez, L.G., *Desalination by wind power*. Wind Engineering, 2004. **28**: p. 453-466.
46. Astariz, S. and G. Iglesias, *The economics of wave energy: A review*. Renewable and Sustainable Energy Reviews, 2015. **45**: p. 397-408.
47. Ghaffour, N., et al., *Renewable energy-driven desalination technologies: A comprehensive review on challenges and potential applications of integrated systems*. Desalination, 2015. **356**: p. 94-114.
48. Bundschuh, J., et al., *State-of-the-art of renewable energy sources used in water desalination: Present and future prospects*. Desalination, 2021. **508**: p. 115035.
49. Okampo, E.J. and N. Nwulu, *Optimisation of renewable energy powered reverse osmosis desalination systems: A state-of-the-art review*. Renewable and Sustainable Energy Reviews, 2021. **140**: p. 110712.

50. Mohamed, E.S., et al., *A direct coupled photovoltaic seawater reverse osmosis desalination system toward battery based systems — a technical and economical experimental comparative study*. *Desalination*, 2008. **221**(1-3): p. 17-22.
51. Helal, A.M., S.A. Al-Malek, and E.S. Al-Katheeri, *Economic feasibility of alternative designs of a PV-RO desalination unit for remote areas in the United Arab Emirates*. *Desalination*, 2008. **221**(1-3): p. 1-16.
52. Ahmed, F.E., R. Hashaikeh, and N. Hilal, *Solar powered desalination – Technology, energy and future outlook*. *Desalination*, 2019. **453**: p. 54-76.
53. Siddiqi, A. and L.D. Anadon, *The water–energy nexus in Middle East and North Africa*. *Energy Policy*, 2011. **39**(8): p. 4529-4540.
54. Marzooq, M., M. Alsabbagh, and W. Al-Zubari, *Energy Consumption in the Municipal Water Supply Sector in the Kingdom of Bahrain*. *Computational Water, Energy, and Environmental Engineering*, 2018. **07**(03): p. 95-110.
55. Alsayegh, O., S. Alhajraf, and H. Albusairi, *Grid-connected renewable energy source systems: Challenges and proposed management schemes*. *Energy Conversion and Management*, 2010. **51**(8): p. 1690-1693.
56. Shafiullah, G.M., et al., *Potential challenges of integrating large-scale wind energy into the power grid—A review*. *Renewable and Sustainable Energy Reviews*, 2013. **20**: p. 306-321.
57. Gude, V.G., *Energy storage for desalination processes powered by renewable energy and waste heat sources*. *Applied Energy*, 2015. **137**: p. 877-898.
58. Qiblawey, H., F. Banat, and Q. Al-Nasser, *Laboratory setup for water purification using household PV-driven reverse osmosis unit*. *Desalination and Water Treatment*, 2009. **7**(1-3): p. 53-59.
59. Abbey, C. and G. Joos, *Supercapacitor Energy Storage for Wind Energy Applications*. *IEEE Transactions on Industry Applications*, 2007. **43**(3): p. 769-776.
60. Sharon, H. and K.S. Reddy, *A review of solar driven desalination technologies*. *Renewable and Sustainable Energy Reviews*, 2015. **41**: p. 1080-1118.
61. Pestana, I.d.I.N., et al., *Optimization of RO desalination systems powered by renewable energies. Part I: Wind energy*. *Desalination*, 2004. **160**: p. 293-299.
62. García Latorre, F.J., S.O. Pérez Báez, and A. Gómez Gotor, *Energy performance of a reverse osmosis desalination plant operating with variable pressure and flow*. *Desalination*, 2015. **366**: p. 146-153.
63. Cabrera, P., et al., *Artificial neural networks applied to manage the variable operation of a simple seawater reverse osmosis plant*. *Desalination*, 2017. **416**: p. 140-156.
64. Carta, J.A., J. González, and V. Subiela, *Operational analysis of an innovative wind powered reverse osmosis system installed in the Canary Islands*. *Solar Energy*, 2003. **75**(2): p. 153-168.
65. Freire-Gormaly, M. and A.M. Bilton, *Experimental quantification of the effect of intermittent operation on membrane performance of solar powered reverse osmosis desalination systems*. *Desalination*, 2018. **435**: p. 188-197.
66. Abufayed, A.A., *Performance characteristics of a cyclically operated seawater desalination plant in Tajoura, Libya*. *Desalination*, 2003. **156**: p. 59-65.
67. Ma, Q. and H. Lu, *Wind energy technologies integrated with desalination systems: Review and state-of-the-art*. *Desalination*, 2011. **277**(1-3): p. 274-280.
68. Lai, W., et al., *Effects of wind intermittence and fluctuation on reverse osmosis desalination process and solution strategies*. *Desalination*, 2016. **395**: p. 17-27.
69. Kumar, Y., et al., *Wind energy: Trends and enabling technologies*. *Renewable and Sustainable Energy Reviews*, 2016. **53**: p. 209-224.
70. Bilstad, T., et al., *Wind-powered RO desalination*. *Desalination and Water Treatment*, 2014: p. 1-5.
71. McKenna, R., P. Ostman v.d. Leye, and W. Fichtner, *Key challenges and prospects for large wind turbines*. *Renewable and Sustainable Energy Reviews*, 2016. **53**: p. 1212-1221.
72. Willis, D.J., et al., *Wind energy research: State-of-the-art and future research directions*. *Renewable Energy*, 2018. **125**: p. 133-154.

73. Zhang, Y., et al., *A hybrid energy storage system with optimized operating strategy for mitigating wind power fluctuations*. *Renewable Energy*, 2018. **125**: p. 121-132.
74. Rahal, Z., *Wind powered desalination*. 2001, Loughborough University: <https://dspace.lboro.ac.uk/2134/7466>.
75. Bognar, K., R. Pohl, and F. Behrendt, *Seawater reverse osmosis (SWRO) as deferrable load in micro grids*. *Desalination and Water Treatment*, 2013. **51**(4-6): p. 1190-1199.
76. Miranda, M.S. and D. Infield, *A wind powered seawater reverse-osmosis system without batteries*. *Desalination*, 2002. **153**: p. 9-16.
77. Miranda, M.d.S., *Small-scale wind-powered seawater desalination without batteries*. 2003, Loughborough University: <https://dspace.lboro.ac.uk/2134/10708>.
78. Moreno, F. and A. Pinilla, *Preliminary experimental study of a small reverse osmosis wind-powered desalination plant*. *Desalination*, 2005. **171**(3): p. 257-265.
79. Pohl, R., M. Kaltschmitt, and R. Holländer, *Investigation of different operational strategies for the variable operation of a simple reverse osmosis unit*. *Desalination*, 2009. **249**(3): p. 1280-1287.
80. Carta, J.A. and P. Cabrera, *Optimal sizing of stand-alone wind-powered seawater reverse osmosis plants without use of massive energy storage*. *Applied Energy*, 2021. **304**: p. 117888.
81. Thomson, M. and D. Infield, *Laboratory demonstration of a photovoltaic-powered seawater reverse-osmosis system without batteries*. *Desalination*, 2005. **183**(1-3): p. 105-111.
82. Bilton, A.M., L.C. Kelley, and S. Dubowsky, *Photovoltaic reverse osmosis — Feasibility and a pathway to develop technology*. *Desalination and Water Treatment*, 2012. **31**(1-3): p. 24-34.
83. Manolakos, D., et al., *Technical and economic comparison between PV-RO system and RO-Solar Rankine system. Case study: Thirasia island*. *Desalination*, 2008. **221**(1-3): p. 37-46.
84. Bilton, A.M., et al., *On the feasibility of community-scale photovoltaic-powered reverse osmosis desalination systems for remote locations*. *Renewable Energy*, 2011. **36**(12): p. 3246-3256.
85. Forstmeier, M., W. Feichter, and O. Mayer, *Photovoltaic powered water purification — challenges and opportunities*. *Desalination*, 2008. **221**(1-3): p. 23-28.
86. Ahmad, N., et al., *Modeling, simulation and performance evaluation of a community scale PVRO water desalination system operated by fixed and tracking PV panels: A case study for Dhahran city, Saudi Arabia*. *Renewable Energy*, 2015. **75**: p. 433-447.
87. Richards, B.S. and A.I. Schafer, *Design considerations for a solar-powered desalination system for remote communities in Australia*. *Desalination*, 2002. **144**: p. 193-199.
88. Thomson, M. and D. Infield, *A photovoltaic-powered seawater reverse-osmosis system without batteries*. *Desalination*, 2002. **153**: p. 1-8.
89. Riffel, D.B. and P.C.M. Carvalho, *Small-scale photovoltaic-powered reverse osmosis plant without batteries: Design and simulation*. *Desalination*, 2009. **247**(1-3): p. 378-389.
90. Kelley, L.C. and S. Dubowsky, *Thermal control to maximize photovoltaic powered reverse osmosis desalination systems productivity*. *Desalination*, 2013. **314**: p. 10-19.
91. Kumarasamy, S., S. Narasimhan, and S. Narasimhan, *Optimal operation of battery-less solar powered reverse osmosis plant for desalination*. *Desalination*, 2015. **375**: p. 89-99.
92. Almarshoud, A.F. and E. Adam, *Towards VLS-PV deployment in Saudi Arabia: Challenges, opportunities and recommendations*. *Energy Policy*, 2018. **114**: p. 422-430.
93. Zaihidee, F.M., et al., *Dust as an unalterable deteriorative factor affecting PV panel's efficiency: Why and how*. *Renewable and Sustainable Energy Reviews*, 2016. **65**: p. 1267-1278.
94. Syafiq, A., et al., *Advances in approaches and methods for self-cleaning of solar photovoltaic panels*. *Solar Energy*, 2018. **162**: p. 597-619.
95. Moharram, K.A., et al., *Influence of cleaning using water and surfactants on the performance of photovoltaic panels*. *Energy Conversion and Management*, 2013. **68**: p. 266-272.
96. Vyas, H., et al., *Modus operandi for maximizing energy efficiency and increasing permeate flux of community scale solar powered reverse osmosis systems*. *Energy Conversion and Management*, 2015. **103**: p. 94-103.
97. Ntavou, E., et al., *Experimental evaluation of a multi-skid reverse osmosis unit operating at fluctuating power input*. *Desalination*, 2016. **398**: p. 77-86.

98. Soric, A., et al., *Eausmose project desalination by reverse osmosis and batteryless solar energy: Design for a 1m³ per day delivery*. Desalination, 2012. **301**: p. 67-74.
99. Clarke, D.P., Y.M. Al-Abdeli, and G. Kothapalli, *The effects of including intricacies in the modelling of a small-scale solar-PV reverse osmosis desalination system*. Desalination, 2013. **311**: p. 127-136.
100. Salama, L. and K.Z. Abdalla, *Design and analysis of a solar photovoltaic powered seawater reverse osmosis plant in the southern region of the Gaza Strip*. DESALINATION AND WATER TREATMENT, 2019.
101. Ghafoor, A., et al., *Techno-economic feasibility of solar based desalination through reverse osmosis*. Desalination, 2020. **485**: p. 114464.
102. Saleem, M.W., et al., *Design and cost estimation of solar powered reverse osmosis desalination system*. Advances in Mechanical Engineering, 2021. **13**(6): p. 16878140211029090.
103. Al-Rousan, N., N.A.M. Isa, and M.K.M. Desa, *Advances in solar photovoltaic tracking systems: A review*. Renewable and Sustainable Energy Reviews, 2018. **82**: p. 2548-2569.
104. Maleki, A., F. Pourfayaz, and M.H. Ahmadi, *Design of a cost-effective wind/photovoltaic/hydrogen energy system for supplying a desalination unit by a heuristic approach*. Solar Energy, 2016. **139**: p. 666-675.
105. Maleki, A., M.G. Khajeh, and M.A. Rosen, *Weather forecasting for optimization of a hybrid solar-wind-powered reverse osmosis water desalination system using a novel optimizer approach*. Energy, 2016. **114**: p. 1120-1134.
106. Hossam-Eldin, A., A.M. El-Nashar, and A. Ismaiel, *Investigation into economical desalination using optimized hybrid renewable energy system*. International Journal of Electrical Power & Energy Systems, 2012. **43**(1): p. 1393-1400.
107. Weiner, D., et al., *Operation experience of a solar- and wind-powered desalination demonstration plant*. Desalination, 2001. **137**: p. 7-13.
108. Mokheimer, E.M.A., et al., *Modeling and optimization of hybrid wind-solar-powered reverse osmosis water desalination system in Saudi Arabia*. Energy Conversion and Management, 2013. **75**: p. 86-97.
109. Spyrou, I.D. and J.S. Anagnostopoulos, *Design study of a stand-alone desalination system powered by renewable energy sources and a pumped storage unit*. Desalination, 2010. **257**(1-3): p. 137-149.
110. Kershnan, S.A., J. Rheinlander, and H. Gabler, *Seawater reverse osmosis powered from renewable energy sources - hybrid wind/photovoltaic/grid power supply for small-scale desalination in Libya*. Desalination, 2002. **153**: p. 17-23.
111. Mentis, D., et al., *Desalination using renewable energy sources on the arid islands of South Aegean Sea*. Energy, 2016. **94**: p. 262-272.
112. Smaoui, M. and L. Krichen, *Control, energy management and performance evaluation of desalination unit based renewable energies using a graphical user interface*. Energy, 2016. **114**: p. 1187-1206.
113. Li, Q., et al., *Integration of reverse osmosis desalination with hybrid renewable energy sources and battery storage using electricity supply and demand-driven power pinch analysis*. Process Safety and Environmental Protection, 2017. **111**: p. 795-809.
114. Gökçek, M., *Integration of hybrid power (wind-photovoltaic-diesel-battery) and seawater reverse osmosis systems for small-scale desalination applications*. Desalination, 2018. **435**: p. 210-220.
115. Maleki, A., *Design and optimization of autonomous solar-wind-reverse osmosis desalination systems coupling battery and hydrogen energy storage by an improved bee algorithm*. Desalination, 2018. **435**: p. 221-234.
116. Khiari, W., M. Turki, and J. Belhadj, *Power control strategy for PV/Wind reverse osmosis desalination without battery*. Control Engineering Practice, 2019. **89**: p. 169-179.
117. Elmaadawy, K., et al., *Optimal sizing and techno-enviro-economic feasibility assessment of large-scale reverse osmosis desalination powered with hybrid renewable energy sources*. Energy Conversion and Management, 2020. **224**: p. 113377.

118. Ibrahim, M.M., et al., *Performance analysis of a stand-alone hybrid energy system for desalination unit in Egypt*. Energy Conversion and Management, 2020. **215**: p. 112941.
119. Cabrera, P., et al., *Wind-driven SWRO desalination prototype with and without batteries: A performance simulation using machine learning models*. Desalination, 2018. **435**: p. 77-96.
120. Rahal, Z., *Wind Powered Desalination 2001*, Loughborough University: <https://dspace.lboro.ac.uk/2134/7466>.
121. Rodgers, V.G.J. and R.E. Sparks, *Effect of transmembrane pressure pulsing on concentration polarization*. Journal of Membrane Science, 1992. **68**(1): p. 149-168.
122. Winzeler, H.B. and G. Belfort, *Enhanced performance for pressure-driven membrane processes: the argument for fluid instabilities*. Journal of Membrane Science, 1993. **80**(1): p. 35-47.
123. Al-Bastaki, N. and A. Abbas, *Use of fluid instabilities to enhance membrane performance: a review*. Desalination, 2001. **136**(1): p. 255-262.
124. Al-Bastak, N.M. and A. Abbas, *Periodic Operation of a Reverse Osmosis Water Desalination Unit*. Separation Science and Technology, 1998. **33**(16): p. 2531-2540.
125. Peñate, B. and L. García-Rodríguez, *Energy optimisation of existing SWRO (seawater reverse osmosis) plants with ERT (energy recovery turbines): Technical and thermoeconomic assessment*. Energy, 2011. **36**(1): p. 613-626.
126. Stover, R.L., *Seawater reverse osmosis with isobaric energy recovery devices*. Desalination, 2007. **203**(1-3): p. 168-175.
127. Woodcock, D.J. and I. Morgan White, *The application of Pelton type impulse turbines for energy recovery on seawater reverse osmosis systems*. Desalination, 1981. **39**: p. 447-458.
128. Peñate, B. and L. García-Rodríguez, *Current trends and future prospects in the design of seawater reverse osmosis desalination technology*. Desalination, 2012. **284**: p. 1-8.
129. Mirza, S., *Reduction of energy consumption in process plants using nanofiltration and reverse osmosis*. Desalination, 2008. **224**: p. 132-142.
130. Flowsolve Inc. - DWEER. [cited 2018 30 May].
131. Schneider, B., *Selection, operation and control of a work exchanger energy recovery system based on the Singapore project*. Desalination, 2005. **184**: p. 197-210.
132. Energy recovery Inc. - PX pressure exchanger. [cited 2020 25 Oct].
133. Paulsen, K. and F. Hensel, *Introduction of a new Energy Recovery System—optimized for the combination with renewable energy*. Desalination, 2005. **184**(1-3): p. 211-215.
134. Peñate, B., J.A.d.l. Fuente, and M. Barreto, *Operation of the RO Kinetic® energy recovery system: Description and real experiences*. Desalination, 2010. **252**: p. 179-185.
135. Paulsen, K. and F. Hensel, *Design of an autarkic water and energy supply driven by renewable energy using commercially available components*. Desalination, 2007. **203**(1-3): p. 455-462.
136. Ghermandi, A. and R. Messalem, *Solar-driven desalination with reverse osmosis: the state of the art*. Desalination and Water Treatment, 2009. **7**: p. 285-296.
137. Spectra watermakers - Clark pump. [cited 2018 30 May].
138. Thomson, M., *Reverse-Osmosis Desalination of Seawater Powered by Photovoltaics Without Batteries*. 2003, Loughborough University: <https://dspace.lboro.ac.uk/2134/10701>.
139. Stover, R.L. and B. Andrews, *Isobaric Energy-Recovery Devices: Past, Present, and Future*. IDA Journal of Desalination and Water Reuse, 2013. **4**(1): p. 38-43.
140. Gude, V.G., *Energy consumption and recovery in reverse osmosis*. Desalination and Water Treatment, 2012. **36**(1-3): p. 239-260.
141. Xu, E., et al., *Computational Fluid Dynamics Simulation of Brine–Seawater Mixing in a Rotary Energy Recovery Device*. Industrial & Engineering Chemistry Research, 2014. **53**(47): p. 18304-18310.
142. DUPONT, *FILMTEC - Reverse Osmosis Membranes - Technical Manual*.
143. Toray, *Operation, maintenance and handling manual*. 2005, Toray membranes.
144. Alatiqi, I., H. Ettouney, and H. El-Dessouky, *Process control in water desalination industry*. Desalination, 1999. **126**: p. 15-32.
145. Palacín, L.G., *Modelling, simulation and advanced control of small scale reverse osmosis desalination plants*. 2014, University of Valladolid.

146. Sobana, S. and R.C. Panda, *Identification, Modelling, and Control of Continuous Reverse Osmosis Desalination System: A Review*. Separation Science and Technology, 2011. **46**(4): p. 551-560.
147. Alatiqi, I., H. Ettouney, and H. El-Dessouky, *Process control in water desalination industry: an overview*. Desalination, 1999. **126**: p. 15-32.
148. Janghorban Esfahani, I., et al., *Control performance evaluation of reverse osmosis desalination system based on model predictive control and PID controllers*. Desalination and Water Treatment, 2016. **57**(55): p. 26692-26699.
149. Seborg, D.E., T.F. Edgar, and D.A. Mellichamp, *Process dynamics and control*. 2004: Wiley.
150. Abbas, A., *Model predictive control of a reverse osmosis desalination unit*. Desalination, 2006. **194**(1-3): p. 268-280.
151. Garcia, C.E., D.M. Prett, and M. Morari, *Model Predictive Control: Theory and Practice - a Survey*. Automatica, 1989. **25**: p. 335-348.
152. Robertson, M.W., et al., *Model based control for reverse osmosis desalination processes*. Desalination, 1996. **104**.
153. Qi, W., J. Liu, and P.D. Christofides, *Supervisory predictive control for long-term scheduling of an integrated wind/solar energy generation and water desalination system*. IEEE Transactions on control systems technology, 2012. **20**(2): p. 504-512.
154. Salazar, J., F. Tadeo, and C. de Prada, *Predictive Control of Microgrids with Mixed Sources for Desalination in Remote Areas*. IFAC-PapersOnLine, 2016. **49**(27): p. 244-249.
155. Al-Shayji, K.A. and Y.A. Liu, *Predictive modeling of large-scale commercial water desalination plants: Data-based neural network and model-based process simulation*. Ind. Eng. Chem. Res., 2002. **41**: p. 6460-6474.
156. Abbas, A. and N. Al-Bastaki, *Modeling of an RO water desalination unit using neural networks*. Chemical Engineering Journal, 2005. **114**(1-3): p. 139-143.
157. Libotean, D., et al., *Neural network approach for modeling the performance of reverse osmosis membrane desalting*. Journal of Membrane Science, 2009. **326**(2): p. 408-419.
158. Salgado-Reyna, A., et al., *Artificial neural networks for modeling the reverse osmosis unit in a wastewater pilot treatment plant*. Desalination and Water Treatment, 2013: p. 1-11.
159. Shaalan, H.A., *Artificial neural network modeling of reverse osmosis process*, in *Department of Chemical Engineering*. 2012, Loughborough University.
160. Danfoss. *Danfoss APP pumps*. 2021 [cited 2021 May]; Available from: <https://www.danfoss.com/en-gb/products/hpp/pumps/high-pressure-pumps-for-reverse-osmosis-applications/app-pumps/>.
161. Danfoss. *Danfoss iSave 21 Plus*. 2021 [cited 2021 April]; Available from: <https://www.danfoss.com/en/products/energy-recovery-devices/hpp/energy-recovery-devices-for-reverse-osmosis-applications/isave-21-plus/#tab-overview>.
162. Danfoss. *Filter solutions for Danfoss high-pressure pump and energy recovery devices*. 2021 [cited 2021 June 2021]; Available from: <https://assets.danfoss.com/documents/173977/AI317041322125en-000201.pdf>.
163. Pikalov, V., et al., *Demonstration of an energy recovery device well suited for modular community-based seawater desalination systems: Result of Danfoss iSAVE 21 testing*. Desalination and Water Treatment, 2013. **51**(22-24): p. 4694-4698.
164. Stover, R.L., *Development of a fourth generation energy recovery device. A 'CTO's Notebook'*. Desalination, 2004. **165**: p. 313-321.
165. Danfoss. *Danfoss iSave 21 - Installation, operation and maintenance manual*. 2021 [cited 2021 April]; Available from: <https://www.danfoss.com/en/products/hpp/energy-recovery-devices/energy-recovery-device-for-small-to-medium-swro-applications/isave-21-plus/>.
166. Fischer, G. *e-Diastar*. 2021 [cited 2021 June 2021]; Available from: <https://www.gfps.com/en-vn/products-solutions/innovation/e-diastar.html>.
167. Omega. *FPB100 series paddlewheel flow meter*. 2021 [cited 2021 September]; Available from: <https://www.omega.com/en-us/flow-instruments/flow-meters/paddlewheel-flow-meters/p/FPB100-Series>.
168. RS-components. *RS PRO IPS Series pressure sensors*. 2021 [cited 2021 September]; Available from: <https://uk.rs-online.com/web/p/pressure-sensors/7975005/>.

169. Omega. *CDTX-2851 Integral mount conductivity transmitters*. 2021 [cited 2021 September]; Available from: <https://www.omega.com/en-us/control-monitoring/air-soil-liquid-and-gas/water-quality-transmitters/cdtx-2850-series/p/CDTX-2851>.
170. Walton, N.R.G., *Electrical Conductivity and Total Dissolved Solids—What is Their Precise Relationship?* Desalination, 1989. **72**(3): p. 275-292.
171. SYXTHSENSE. *TEAT-LL fluid temperature transmitter*. 2021 [cited 2021 September]; Available from: <https://www.syxthsense.com/sensors/teat-ll/fluid-temperature-transmitter,-4..20ma/>.
172. HOBUT. *HOBUT CT132TRAN current transmitter*. 2021 [cited 2021 September]; Available from: <https://www.hobut.co.uk/ct132tran-current-sensor-current-transducer/>.
173. Wijmans, J.G. and R.W. Baker, *The solution-diffusion model: a review*. Journal of Membrane Science, 1995. **107**: p. 1-21.
174. Wijmans, J.G. and R.W. Baker, *The solution-diffusion model: a review*. Journal of Membrane Science, 1995. **107**(1): p. 1-21.
175. Kim, Y.M., et al., *Overview of systems engineering approaches for a large-scale seawater desalination plant with a reverse osmosis network*. Desalination, 2009. **238**(1): p. 312-332.
176. Kim, S. and E.M.V. Hoek, *Modeling concentration polarization in reverse osmosis processes*. Desalination, 2005. **186**(1): p. 111-128.
177. Kim, J.S., J. Chen, and H.E. Garcia, *Modeling, control, and dynamic performance analysis of a reverse osmosis desalination plant integrated within hybrid energy systems*. Energy, 2016. **112**: p. 52-66.
178. Al-Obaidi, M.A. and I.M. Mujtaba, *Steady state and dynamic modeling of spiral wound wastewater reverse osmosis process*. Computers & Chemical Engineering, 2016. **90**: p. 278-299.
179. DUPONT. *FilmTec SW30HRLE-400 Element Data sheet*. 2021 [cited 2021 April]; Available from: <https://www.dupont.com/content/dam/dupont/amer/us/en/water-solutions/public/documents/en/45-D00967-en.pdf>.
180. Avlonitis, S.A., M. Pappas, and K. Moutesidis, *A unified model for the detailed investigation of membrane modules and RO plants performance*. Desalination, 2007. **203**(1-3): p. 218-228.
181. Kim, J., K. Park, and S. Hong, *Application of two-stage reverse osmosis system for desalination of high-salinity and high-temperature seawater with improved stability and performance*. Desalination, 2020. **492**: p. 114645.
182. Park, K., et al., *Design, modelling and optimisation of a batch reverse osmosis (RO) desalination system using a free piston for brackish water treatment*. Desalination, 2020. **494**: p. 114625.
183. Van Gauwbergen, D. and J. Baeyens, *Macroscopic fluid flow conditions in spiral-wound membrane elements*. Desalination, 1997. **110**(3): p. 287-299.
184. Xylem. *LOWARA CEA - End suction centrifugal pumps*. 2021 [cited 2021 May]; Available from: <https://www.xylem.com/en-uk/brands/lowara/lowara-products/cea-stainless-steel-threaded-centrifugal-pumps/>.
185. Energy, R. *E-10 HAWT - 10kW Small Wind Turbine for On-Grid & Off-Grid Power Systems*. 2021 [cited 2021 March]; Available from: <https://www.ryse.energy/10kw-wind-turbines/>.
186. Gambier, A., *Dynamic modelling of the rotating subsystem of a wind turbine for control design purposes*. IFAC PapersOnLine, 2017(50): p. 9896-9901.
187. Mito, M.T., et al., *Prospects of wind power prediction and variable operation in optimizing wind-powered reverse osmosis operation*, in *International Desalination Association. World Congress on Desalination and Water Reuse 2019, Crossroads to Sustainability*. 2019, International Desalination Association (IDA): Dubai, United Arab Emirates.
188. Loutatidou, S., et al., *Wind-powered desalination for strategic water storage: Techno-economic assessment of concept*. Desalination, 2017. **408**: p. 36-51.
189. Richards, B.S., et al., *Renewable energy powered membrane technology: Safe operating window of a brackish water desalination system*. Journal of Membrane Science, 2014. **468**: p. 400-409.
190. Thomson, M. and D. Infield, *Laboratory demonstration of a photovoltaic-powered seawater reverse-osmosis system without batteries*. Desalination, 2005. **183**(1): p. 105-111.

191. Kiam Heong, A., G. Chong, and L. Yun, *PID control system analysis, design, and technology*. IEEE Transactions on Control Systems Technology, 2005. **13**(4): p. 559-576.
192. Korsane, D.T., V. Yadav, and K.H. Raut, *PID Tuning Rules for First Order plus Time Delay System*. International journal of innovative research in electrical, electronics, instrumentation and control engineering, 2014. **2**(1).
193. Sen, R., et al., *Comparison Between Three Tuning Methods of PID Control for High Precision Positioning Stage*. Journal of Metrology Society of India, 2014. **30**(1): p. 65-70.
194. Nagy, T., et al., *Flexible and efficient solution for control problems of chemical laboratories*, in *Computer Aided Chemical Engineering*, A.A. Kiss, et al., Editors. 2019, Elsevier. p. 1819-1824.
195. Zhao, W., et al. *Implement and performance comparison of three turning methods of PI controller parameters for buck converter based on MATLAB/Simulink*. IET Conference Proceedings, 2021. 982-989.
196. MathWorks. *PID Tuner*. 2021 [cited 2021 September]; Available from: <https://www.mathworks.com/help/control/ref/pidtuner-app.html>.
197. Qin, S.J. and T.A. Badgwell, *A survey of industrial model predictive control technology*. Control Engineering Practice, 2003. **11**(7): p. 733-764.
198. Cutler, C. and B.L. Ramaker, *Dynamic matrix control??A computer control algorithm*, in *Joint Automatic Control Conference*. 1980: San Francisco, CA. p. 72.
199. Lundström, P., et al., *Limitations of dynamic matrix control*. Computers & Chemical Engineering, 1995. **19**(4): p. 409-421.
200. Prett, D.M. and C.E. García, *Fundamental Process Control*, ed. D.M. Prett and C.E. García. 1988: Butterworth-Heinemann. 1-5.
201. Torreglosa, J.P., et al., *Energy dispatching based on predictive controller of an off-grid wind turbine/photovoltaic/hydrogen/battery hybrid system*. Renewable Energy, 2015. **74**: p. 326-336.
202. Bemporad, A., M. Morari, and N.L. Ricker, *Model Predictive Control Toolbox: User's guide*. 2014: MathWorks.
203. Ljung, L., *Perspectives on system identification*. Annual Reviews in Control, 2010. **34**(1): p. 1-12.
204. Maurath, P.R., et al., *Predictive controller design by principal components analysis*. Industrial & Engineering Chemistry Research, 1988. **27**(7): p. 1204-1212.
205. Goosen, M.F.A., et al., *Effect of feed temperature on permeate flux and mass transfer coefficient in spiral-wound reverse osmosis systems*. Desalination, 2002. **144**(1): p. 367-372.
206. Wu, Y.-K. and J.-S. Hong. *A literature review of wind forecasting technology in the world*. in *Proc. IEEE Lausanne Power Tech*. 2007. Lausanne, Switzerland.
207. Lei, M., et al., *A review on the forecasting of wind speed and generated power*. Renewable and Sustainable Energy Reviews, 2009. **13**(4): p. 915-920.
208. Noorollahi, Y., M.A. Jokar, and A. Kalhor, *Using artificial neural networks for temporal and spatial wind speed forecasting in Iran*. Energy Conversion and Management, 2016. **115**: p. 17-25.
209. Sfetsos, A., *A comparison of various forecasting techniques applied to mean hourly wind speed time series*. Renewable Energy, 2000. **21**: p. 23-35.
210. Colak, I., S. Sagiroglu, and M. Yesilbudak, *Data mining and wind power prediction: A literature review*. Renewable Energy, 2012. **46**: p. 241-247.
211. Azad, H.B., S. Mekhilef, and V.G. Ganapathy, *Long-term wind speed forecasting and general pattern recognition using neural networks*. IEEE Transactions on sustainable energy, 2014. **5**(2): p. 546-553.
212. Ramasamy, P., S.S. Chandel, and A.K. Yadav, *Wind speed prediction in the mountainous region of India using an artificial neural network model*. Renewable Energy, 2015. **80**: p. 338-347.
213. Rumelhart, D.E., G.E. Hinton, and R.J. Williams, *Learning representations by back-propagating errors*. Nature, 1986. **323**(6088): p. 533-536.
214. Roffel, B. and B. Betlem, *Process Dynamics and Control: Modeling for Control and Prediction*. 2007: Wiley.

215. Haykin, S.O., *Neural Networks and Learning Machines*. Third ed. 2008: Prentice Hall.
216. Hagan, M.T., H.B. Demuth, and M.H. Beale, *Neural Network Design*. 1996: PWS.
217. Demuth, H. and M. Beale, *Neural Network Toolbox: For Use with MATLAB®*. 4 ed. 2002: The MathWorks, Inc.
218. Philippopoulos, K. and D. Deligiorgi, *Application of artificial neural networks for the spatial estimation of wind speed in a coastal region with complex topography*. *Renewable Energy*, 2012. **38**(1): p. 75-82.
219. Filik, Ü.B. and T. Filik, *Wind Speed Prediction Using Artificial Neural Networks Based on Multiple Local Measurements in Eskisehir*. *Energy Procedia*, 2017. **107**: p. 264-269.
220. Bilgili, M., B. Sahin, and A. Yasar, *Application of artificial neural networks for the wind speed prediction of target station using reference stations data*. *Renewable Energy*, 2007. **32**(14): p. 2350-2360.
221. Carolin Mabel, M. and E. Fernandez, *Analysis of wind power generation and prediction using ANN: A case study*. *Renewable Energy*, 2008. **33**(5): p. 986-992.
222. Basheer, I.A. and M. Hajmeer, *Artificial neural networks: fundamentals, computing, design, and application*. *Journal of Microbiological Methods*, 2000. **43**(1): p. 3-31.
223. Lee, T.-L., *Back-propagation neural network for long-term tidal predictions*. *Ocean Engineering*, 2004. **31**(2): p. 225-238.
224. Hagan, M.T. and M.B. Menhaj, *Training feedforward networks with the Marquardt algorithm*. *IEEE Transactions on Neural Networks*, 1994. **5**(6): p. 989-993.
225. Jung, J. and R.P. Broadwater, *Current status and future advances for wind speed and power forecasting*. *Renewable and Sustainable Energy Reviews*, 2014. **31**: p. 762-777.
226. Manwell, J.F., J.G. Mcgowan, and A.L. Rogers, *Wind energy explained. Theory, design and application*. Second ed. 2009: Wiley.
227. Jowder, F.A.L., *Wind power analysis and site matching of wind turbine generators in Kingdom of Bahrain*. *Applied Energy*, 2009. **86**(4): p. 538-545.
228. Alvi, S.H. and Y.A. Abdalla. *Variation of wind speed with height in Bahrain*. in *Proceedings of the intersociety energy conversion engineering conference*. 1989.
229. *Zenia ZA30 wind turbine*. [cited 2021 23 April].

Appendix A RO system design drawings

A.1 Frame design

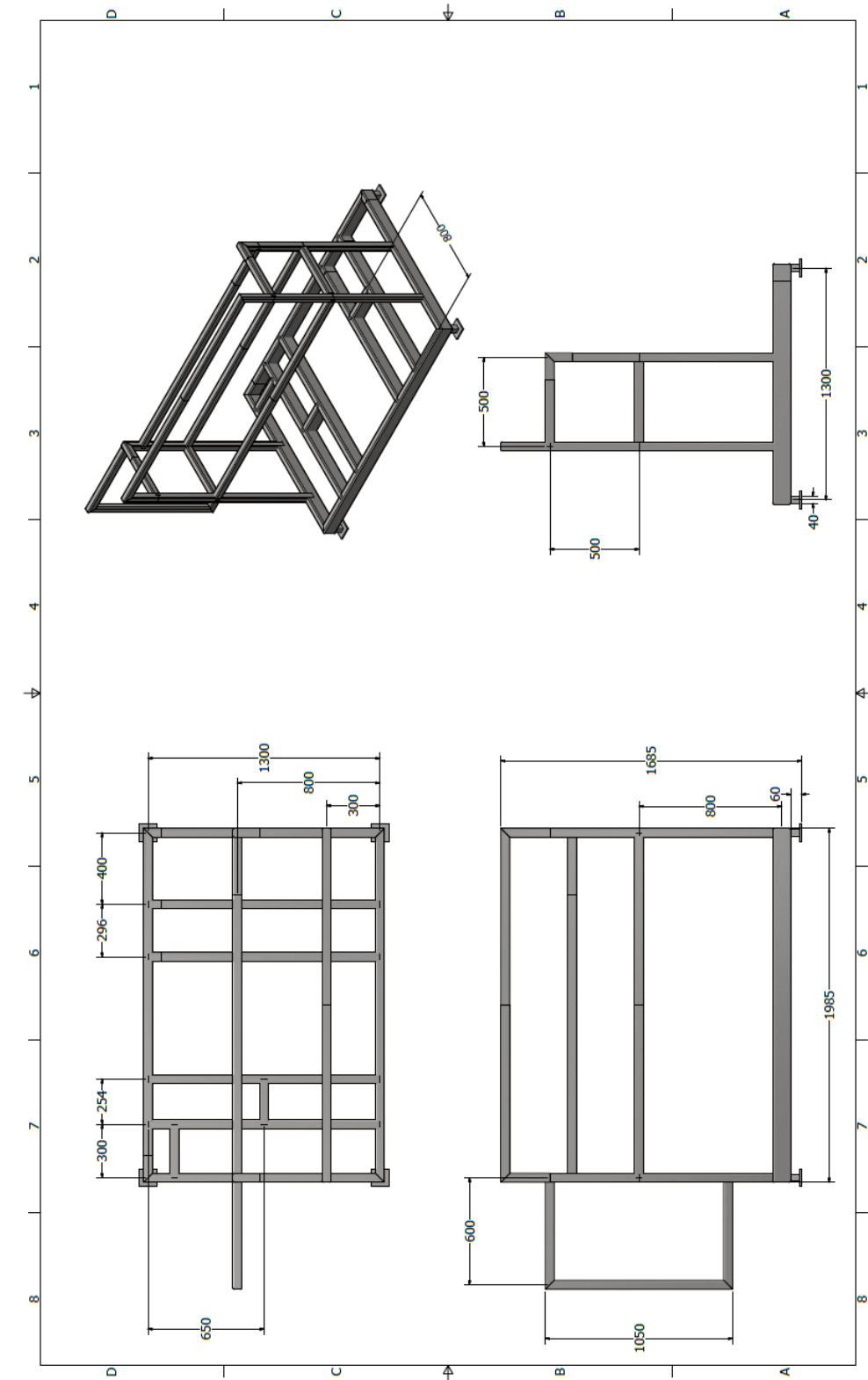


Fig. A.1. Frame design.

A.2 RO system assembly

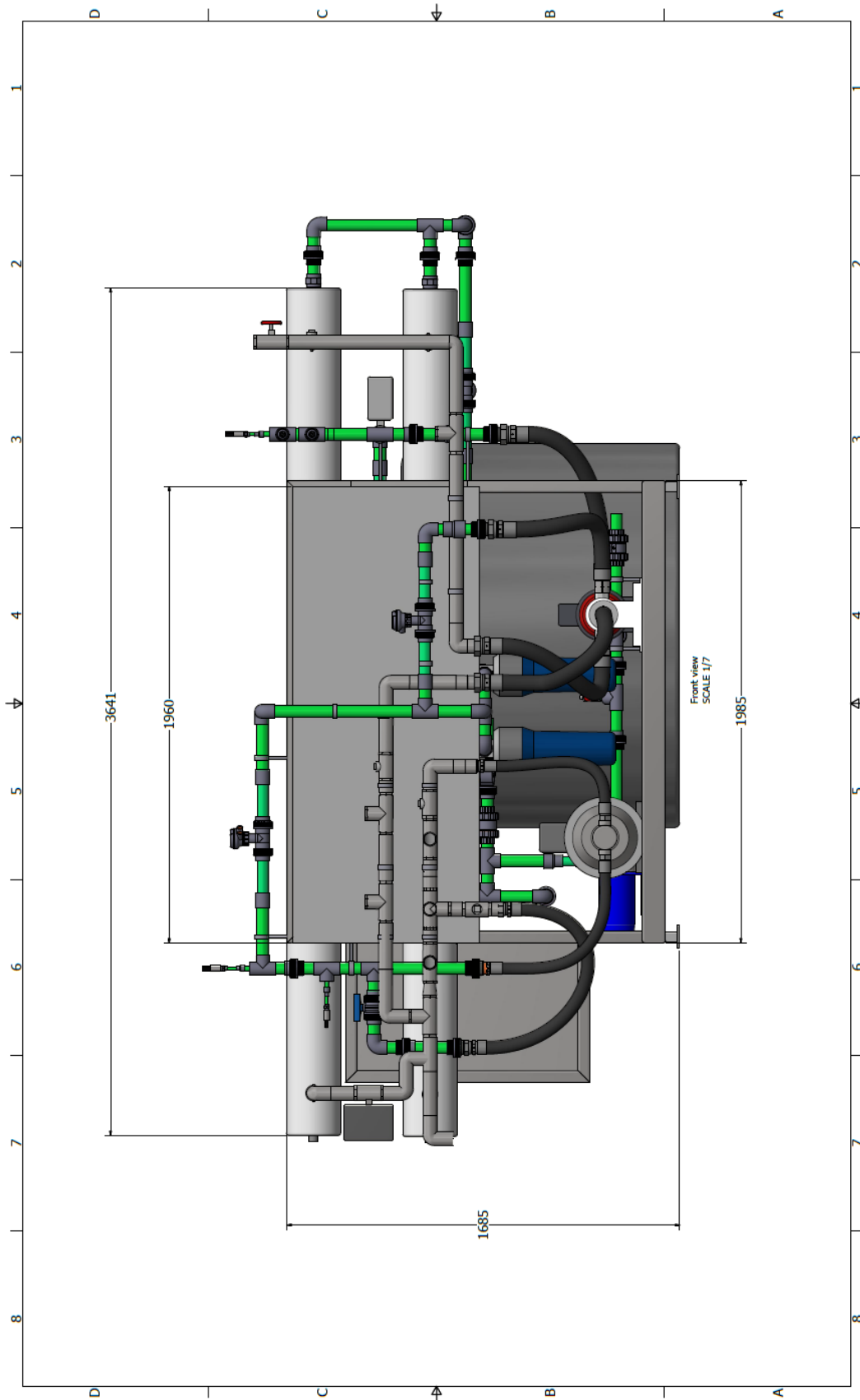


Fig. A.2. Front view of the RO system.

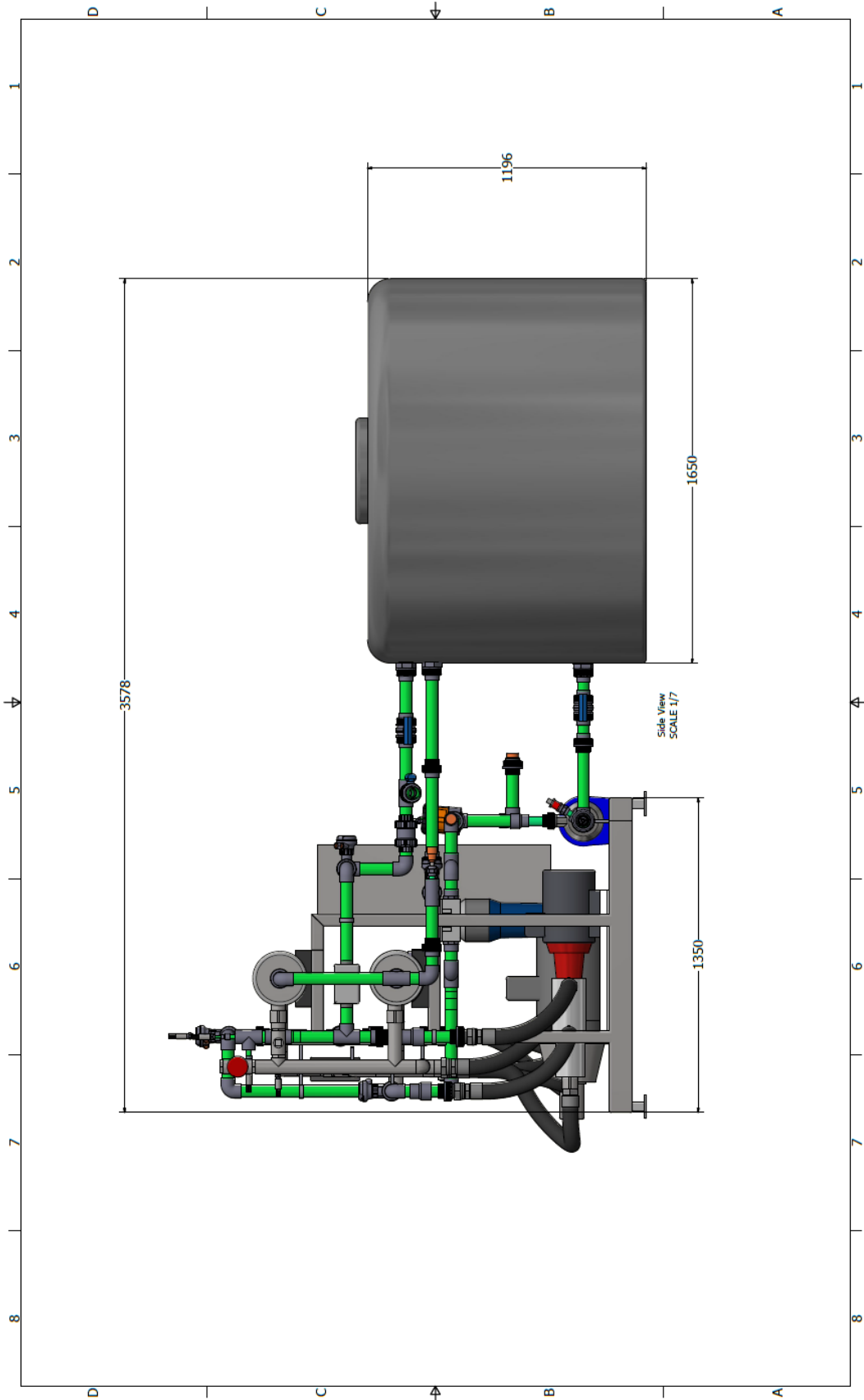


Fig. A.3. Side view (right) of the RO system.

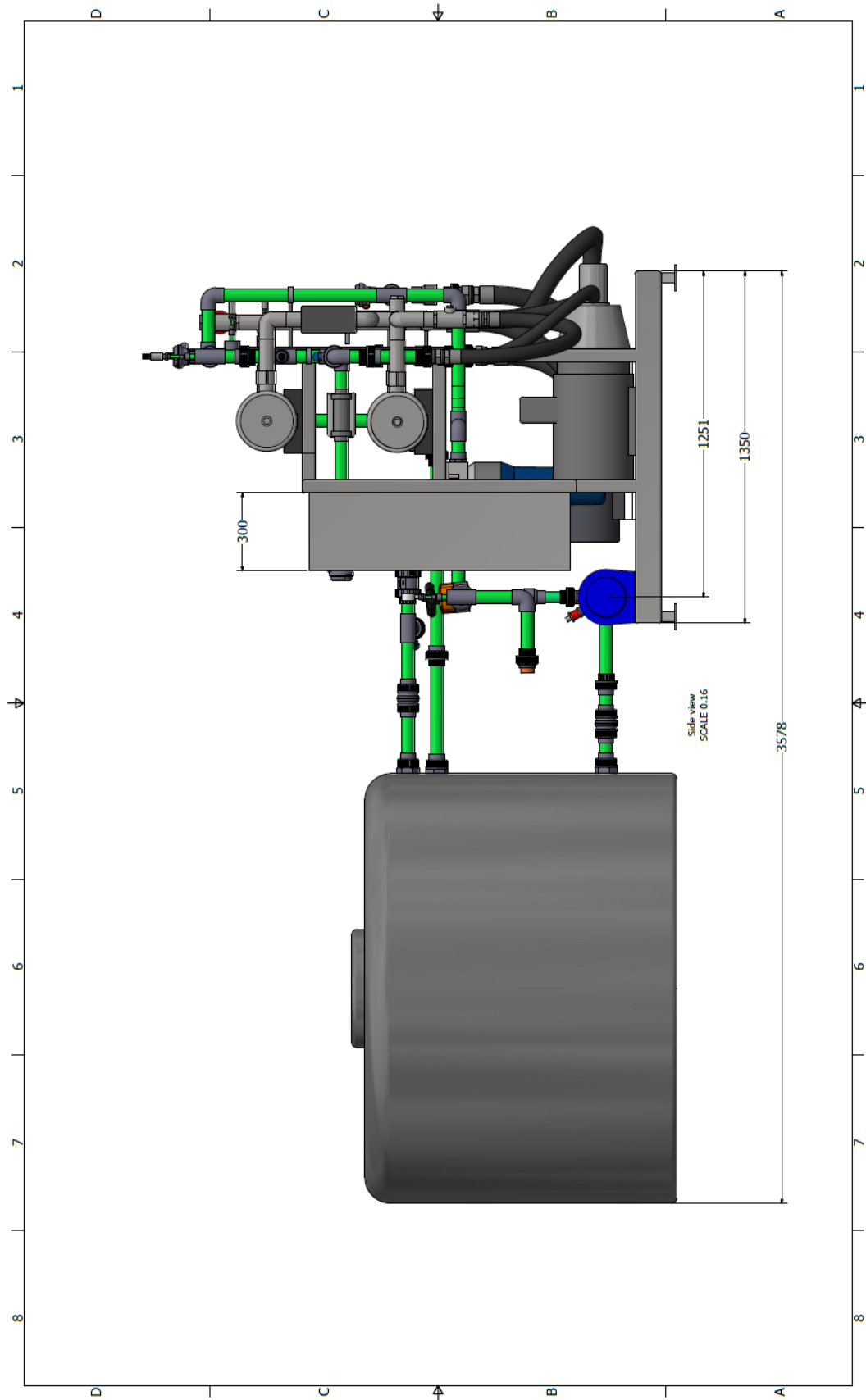


Fig. A.4. Side view (left) of the RO system.

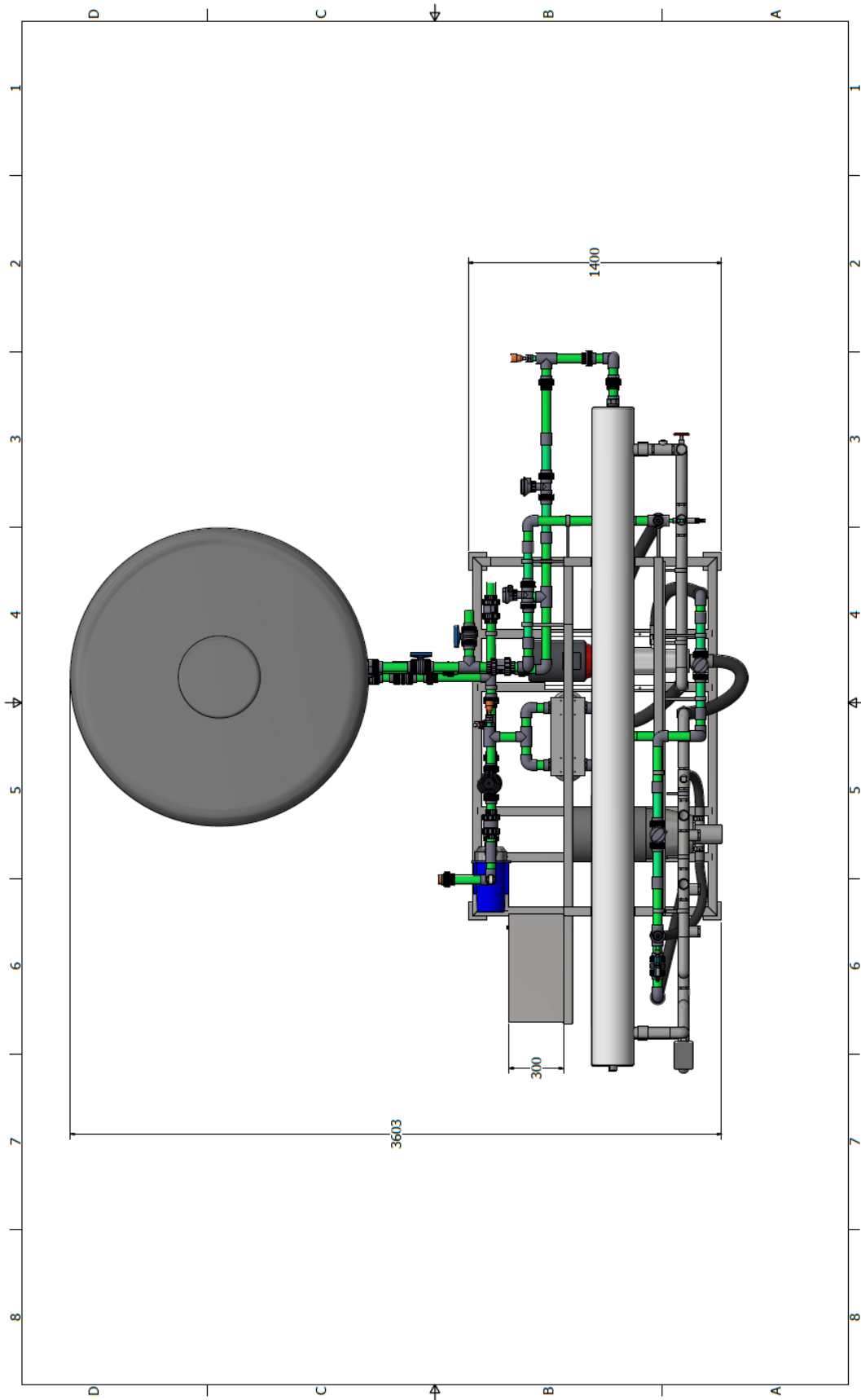


Fig. A.5. Plane view of the RO system.

A.3 Process and instrumentations diagram

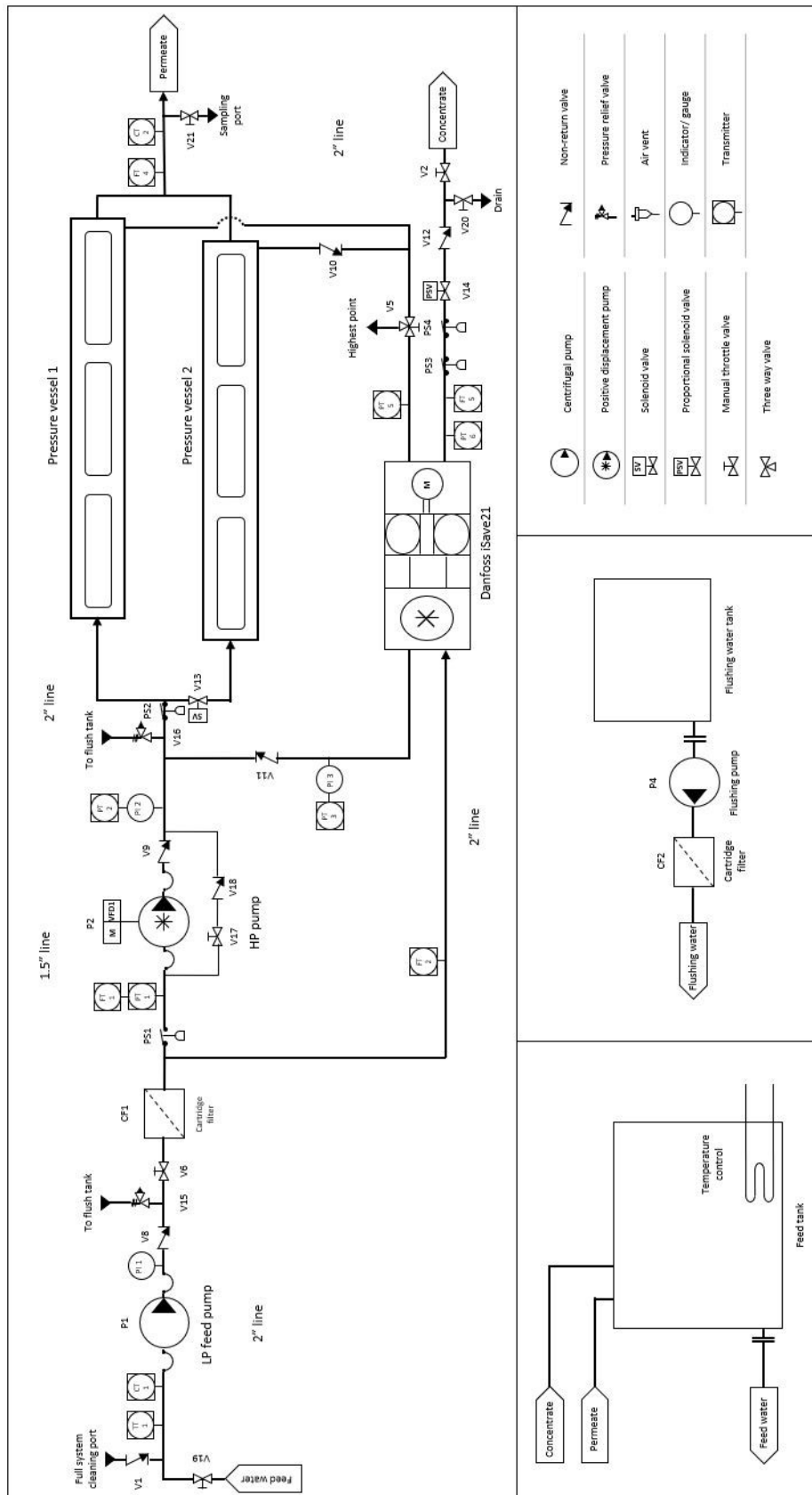


Fig. A.6. Process and instrumentations diagram of the RO system.

Appendix B Electrical panel design drawings

B.1 High-voltage power circuit

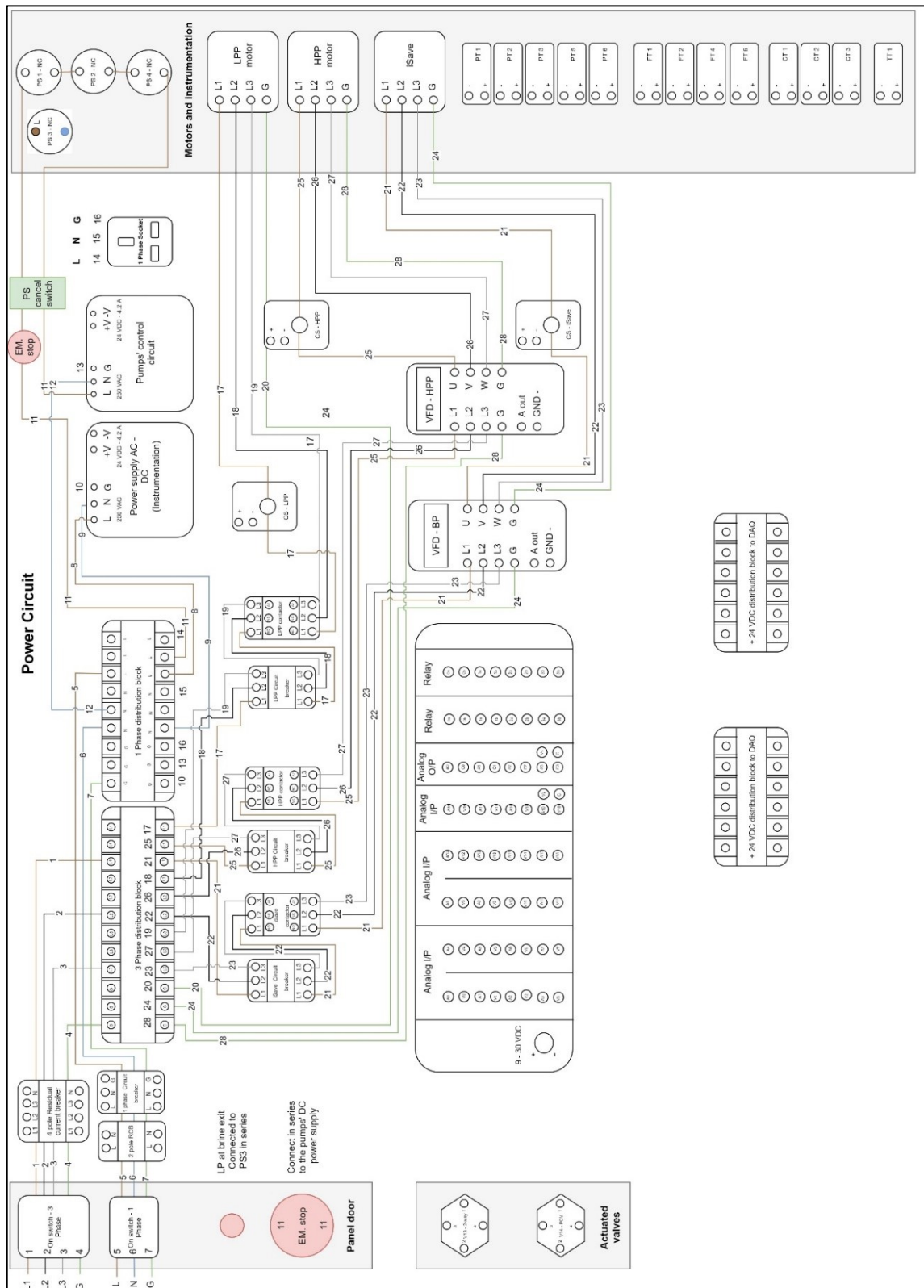


Fig. B.1. High-voltage power circuit.

B.2 Low-voltage control circuit

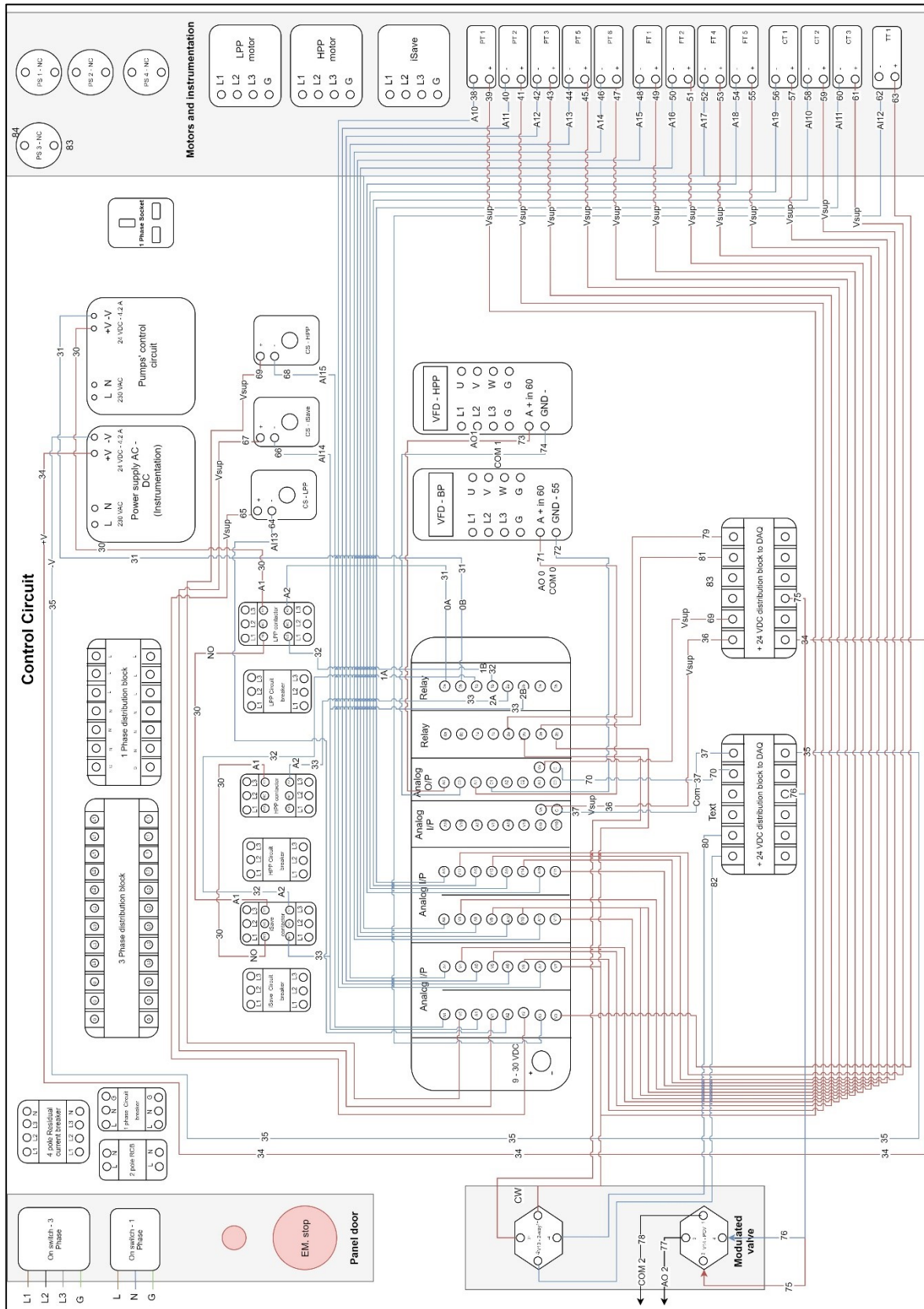


Fig. B.2. Low-voltage control circuit.

B.3 NI DAQ chassis terminals

Table B.1. NI DAQ chassis terminal

DAQ card	terminal	Function
NI 9482 – Relay (1)	0A – 0B	On/Off LPP (31)
	1A – 1B	On/Off iSave (32)
	2A – 2B	On/Off HPP (33)
	3A – 3B	-
NI 9208 – Current input	Vsup	+ve DC supply (36)
	Com	-ve DC supply (37)
	A10	PT 1 (38)
	A11	PT2 (40)
	A12	PT3 (42)
	A13	PT5 (44)
	A14	PT6 (46)
	A15	FT1 (48)
	A16	FT2 (50)
	A17	FT4 (52)
	A18	FT5 (54)
	A19	CT1 (56)
	AI10	CT2 (58)
	AI11	CT3 (60)
AI12	TT1 (62)	
AI13	CS1 – LPP (64)	
AI14	CS2 – iSave (66)	

	AI15	CS3 – HPP (68)
NI 9265 – Current output	Vsup	+ve DC supply (69)
	Com	-ve DC supply (70)
	AO 0	VFD iSave (+ve) (71)
	COM 0	VFD iSave (-ve) (72)
	AO 1	VFD HPP (+ve) (73)
	COM 1	VFD HPP (-ve) (74)
	AO 2	Modulated valve (77)
	COM 2	Modulated valve (78)
	AO 3	-
	COM 3	-
NI 9482 – Relay (2)	0A – 0B	Isolation valve (on) (79)
	1A – 1B	Isolation valve (off) (81)
	2A – 2B	Modulated valve (Open)
	3A – 3B	Modulated valve (Close)

Appendix C Sensors calibration

C.1 Flowmeter

Ω OMEGA[®]

Test Certificate

<u>Part information</u>	<u>Calibration equipment used</u>
Part number: FP8501A/20	Unit ID: RS-01
Body/Rotor/Pin: Polypro/Black PVDF/Titanium	Cal due date: 02/21/2020
Serial number: 61912191748	
Test date: 12/21/2019 5:58:37 AM	

<u>Test conditions</u>				
Test media:	Water			
Temperature:	21.7°C			
Test location:	PFL3			

Flow Velocity (ft/s)	Flow Velocity (m/s)	Reynolds Number	Sensor Frequency (Hz)	Linearity (%)
1.32	0.40	15936.08	14.62	-0.44
3.74	1.14	45097.38	43.09	-0.53
5.57	1.70	67087.92	65.42	-0.23
7.41	2.26	89283.70	87.47	-0.13
9.28	2.83	111756.43	110.22	0.14
11.11	3.39	133872.32	131.32	-0.13
12.97	3.95	156261.06	154.88	0.53
14.79	4.51	178122.12	175.11	-0.01
16.64	5.07	200414.75	197.62	0.24
19.65	5.99	236697.77	232.41	-0.13

Fig. C.7. Flow sensor calibration.

C.2 Pressure sensors

Calibration Data - Do Not Discard

Type	797-5021		
Serial No.	612346	Zero	3.98
Range	0 TO 100 BAR G	Span	16.02
Output	4 - 20MA / 2-WIRE	NL&H	0.06242%

Fig. C.2. Pressure sensor calibration.

C.3 Conductivity sensors

The feed and permeate conductivity sensors were calibrated based on a single-point calibration using a 12,880 $\mu\text{S}/\text{cm}$ NIST compliant conductivity solution.

Table C.1. Conductivity sensor calibration.

Sensor	Target value ($\mu\text{S}/\text{cm}$)	Sensor reading ($\mu\text{S}/\text{cm}$)	Actual Error (% of reading)	Rated accuracy (% of reading)
Feed conductivity	12,880	13078.9	+1.54	$\pm 2\%$
Permeate conductivity	12,880	12987.7	+0.84	$\pm 2\%$